Photodetectors Based on Colloidal Quantum Dots

by

David C. Oertel

B.A. in Chemistry and Mathematics
Oberlin College
Oberlin, Ohio
2001

Submitted to the Department of Chemistry
in partial fulfillment of the requirements for the degree of

Doctor of Philosophy

at the

MASSACHUSETTS INSTITUTE OF TECHNOLOGY

June 2007

© Massachusetts Institute of Technology 2007. All rights reserved.

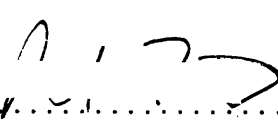Author . . . .
Department of Chemistry
May 9, 2007

Certified by. . . . .
Moungi G. Bawendi
Professor of Chemistry
Thesis Supervisor

Accepted by . . . .
Robert W. Field
Chairman, Department Committee on Graduate Students
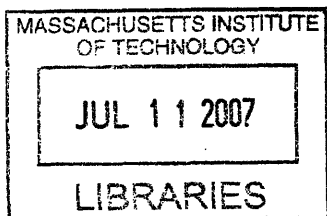
This doctoral thesis has been examined by a committee of the Department of Chemistry as follows:

....

Professor Andrei Tokmakoff
Thesis Committee Chairman

....

Professor Moungi G. Bawendi
Thesis Adviser
Thesis Committee Member

....

Professor Robert W. Field
Thesis Committee Member

Photodetectors Based on Colloidal Quantum Dots

by

David C. Oertel

B.A. in Chemistry and Mathematics

Oberlin College

Oberlin, Ohio

2001

Abstract

Inspired by recent work demonstrating photocurrent enhancement in quantum-dot (QD) solids via post-deposition chemical annealing and by recent successes incorporating single monolayers of QDs in light-emitting devices (QD-LEDs), we set out to develop thin-film, layered photodetectors in which the active layer is a chemically annealed QD solid. This thesis reports initial steps in this development.

Chapters 1 and 2 contain introductory material. In Chapter 3, we demonstrate a layered QD photodetector (QD-PD) in which the active layer is a 200-nm thick film of CdSe QDs annealed with n-butylamine. These "thick-slab" devices, active in the visible spectrum, represent a minimal transformation from the transverse channel test structures employed for more fundamental studies to a layered, sandwich geometry. The thick-slab design exhibits a number of desirable characteristics, including near-unity internal quantum efficiency and a 50-kHz bandwidth. More complex QD-PD designs, allowing the successful incorporation of much thinner QD solids, are discussed in Chapter 4, and these devices provide insight into the zero-bias operation of thick-slab QD-PDs.

The final three chapters of the thesis focus on PbSe QDs, this group's initial material of choice for accessing the short-wavelength-IR spectral window. Initial study of PbSe QDs as a material for QD-PDs is described in Chapter 5. Chapter 6 discusses an ^{31}P-based NMR investigation of the mechanism of PbSe monomer formation, allowing for rational "doping" of syntheses to increase chronically low yields. Finally, Chapter 7 discusses a brief assessment of the suitability of PbSe QDs for in vivo imaging.

Thesis Supervisor: Moungi G. Bawendi
Title: Professor of Chemistry

Acknowledgments

Bob Field and Moungi Bawendi have been my research advisers during my time at MIT. My leaving the Field Group in Spring, 2003, was difficult for both Bob and me, and I would like to thank Bob for handling the situation with uncommon grace. I would also like to thank Moungi for welcoming me into his group in May, 2003; my work since that time is the subject of this thesis. Moungi has been unwavering in his financial support and patience. Vladimir Bulović has been an informal adviser to me during my time in the Bawendi Group, and I thank him for his friendly enthusiasm.

The members of both the Bawendi and Bulović Groups have been helpful and have generally been the kinds of upstanding colleagues one hopes for. In particular, Alexi Arango in the Bulović Group was willing to share his lab experience and supplies. Venda Porter and, more recently, Scott Geyer always knew more about transport in QD solids than I did and were generous with their insight. I enjoyed interaction with Brent Fisher, who was innovative with his humor in light conversation but was also most sincere. John Zimmer was a valued labmate and friend with whom I had countless conversations about chemistry, baseball, golf, religion, and ditch-digging, among other things. His attention to and appreciation of detail was uncommon at MIT. I have greatly enjoyed spending time with Chemistry Department graduate-student colleagues and good friends Joe Loparo and Brian Yen since first working together on problem sets during Fall, 2001. Their friendship and interpretation of the graduate experience has made things here more entertaining, if nothing else.

I have had the good fortune to discover some uncommon resources at MIT. In particular, I enjoyed Toby Bashaw's IAP courses on welding and blacksmithing and

value greatly the educated exposure to these important topics. Fred Coté and Mark Belanger served as head instructors at the Edgerton Center Student Shop in Building 44. Their helpfulness, coupled with the fine quality and condition of the available equipment, contributed to some of most fulfilling days I had at MIT.

The Dudley House Orchestra at Harvard provided musical recreation for me each semester since Spring, 2002. The Dudley House music directors, most recently and impressively Drew Schroeder, have given their time, energy, and skill to make this a very successful volunteer group.

My most substantial and meaningful growth at MIT likely came through my involvement with the House Council at the Sidney-Pacific Graduate Residence, in which I became involved almost accidentally (and solely for the purpose of housing) during Spring, 2002. These sorts of hands-on leadership and management experiences are not easy to come by and are of great value, and the friendships that I made are too numerous to cite here. I especially would like to thank Ronak Bhatt, who served as an adviser and mentor for me in a number of positions I held at S-P. More than anyone else I know, Ronak has the ability to quickly identify critical issues and the essential strategy in response to a problem. S-P Housemaster Roger Mark has served as a mentor to me as much as any faculty member at MIT; Roger's sincerity and advice have always been available. Roger and Dottie's warmth and generosity has been a gift.

Finally, I thank my family for their supreme love and trust that served as a beacon through the long, foggy night at MIT.

Contents

List of Figures

13

15

List of Tables

THIS PAGE INTENTIONALLY LEFT BLANK

Chapter 1

Introduction I: Overview

In simplest terms, photodetectors are devices in which incident photons create an electronic change that can then be read by measurement instrumentation, from which information about the original incident photons can in turn be drawn. While often hidden to the casual observer, photodetectors play important roles in commerce, industry, and research. Small (four- or six-element) photodiode arrays read reflected laser light in CD players while much larger two-dimensional silicon-based CCD arrays containing millions of pixels play a critical role in digital photography. Detectors made with III-IV semiconductor materials and sensitive to $\lambda = 1.3$ μm and $\lambda = 1.55$ μm, two wavelengths with favorable dispersion in silica, are used extensively in fiber-optic communications. Finally, photodetectors based on a broad array of materials and operating principles enable spectroscopy over a wide spectral range from the visible into the IR (photoconductors and photovoltaics) and extending to the far IR (bolometers).[1]

The development of photodetectors has often occurred concurrently with the development of understanding of their constituent materials. For example, the development of photodiodes (and also their close relatives, light-emitting devices) has been intertwined with developments in the understanding of the theory and manipulation of solid-state semiconductor materials. The research that constitutes the bulk of this thesis concerns developing photodetectors based on a relatively new material set, colloidal semiconductor nanocrystals, or quantum dots (QDs), and is strongly driven

by the recent surge in nanotechnology research. While numerous challenges must be overcome for such devices to become practical, this research represents first steps toward potentially useful devices based on new materials and using unconventional fabrication methods.

The remainder of this overview begins with a brief discussion of how recent successes in QD-related research motivate the present work. Possible QD-PD uses are discussed at some level of abstraction along with much more concrete challenges. The chapter concludes with a thesis overview.

1.1 Background and Motivations

1.1.1 Nanotechnology

The United States Patent and Trademark Office defines a "nanostructure"[2] as an entity that

(a) Has at least one physical dimension of approximately 1-100 nanometers; and

(b) Possesses a special property, provides a special function, or produces a special effect that is uniquely attributable to the structure's nanoscale physical size.

Defined this way, manifestations of man-made nanotechnology have had a presence in society for thousands of years, with documented instances including hair dye based on PbS nanoparticles during Greco-Roman times,[3] glass stains based on nanocrystalline silver compounds,[4] and carbon nanotubes found in forged Damascus steel[5]. However, only in recent years have refinements in synthetic techniques, coupled with the widespread availability of appropriate analytical methods, allowed for significant appreciation of unusual behavior at the nanoscale, fueling the rapid growth of explicit nanotechnology-related research that has taken place over the last decade. Figure 1-1 shows the rise in funding of research classified as nanotechnology-related, summed across the major federal granting agencies.[6]

The development of research involving colloidal semiconductor nanocrystals has mirrored this more general trend. The advent of high-quality CdSe QD syntheses via
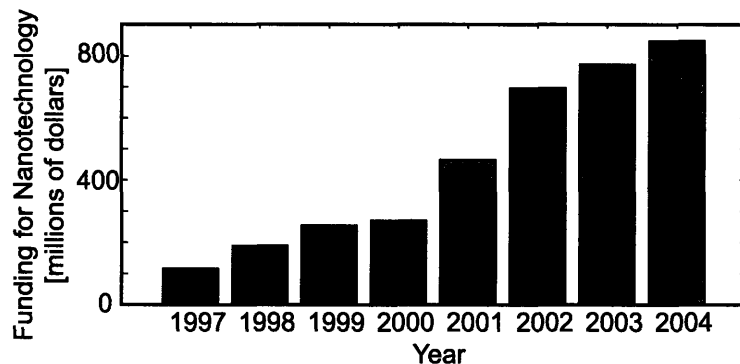
Figure 1-1: Government funding of nanotechnology research, 1997-2004, summed across funding agencies. Data are from Ref. [6].

pyrolysis of organometallic precursors in the early 1990s[7] (and, later, more controlled approaches using metal salts[8, 9]) have made possible a deeper physical exploration of these particles. As predicted theoretically,[10] colloidal semiconductor nanocrystals exhibit qualitatively different densities of states than those of corresponding bulk material, and these discrete, atom-like energy-level structures give rise to unusual absorption and emission spectra that are tunable with QD size. (Thorough discussions of quantum confinement exist elsewhere.[11, 12]) With a narrow size distribution ($\sigma < 5\%$ can routinely be achieved synthetically), ensembles of QDs exhibit well-defined absorption features, with appreciable oscillator strength condensed in the band-edge transition, typically with a FWHM $\sim$ 25 meV. Such a size distribution, coupled with well-passivated, relatively trap-free particle surfaces, gives rise to an emission peak that is Gaussian and roughly the same width (Fig. 1-2).

As high-quality QD syntheses were first developed and in the years immediately following, QD research focused heavily on optical spectroscopy of this new fluorophore material set. Elucidation of electronic band-edge states was carried out with fluorescence line-narrowing and photoexcitation luminescence studies,[14] and many ensemble studies, including those focused on the Stark effect[15] and Auger recombination[16, 17] followed. Single nanocrystal spectroscopy was developed,[18] enabling examination of blinking characteristics[19] and surface-enhanced emission[20]. Today, fundamental spectroscopic studies of QDs (both in single-dot and ensemble regimes) continue, with investigations of effects such as ordered multiphoton

21
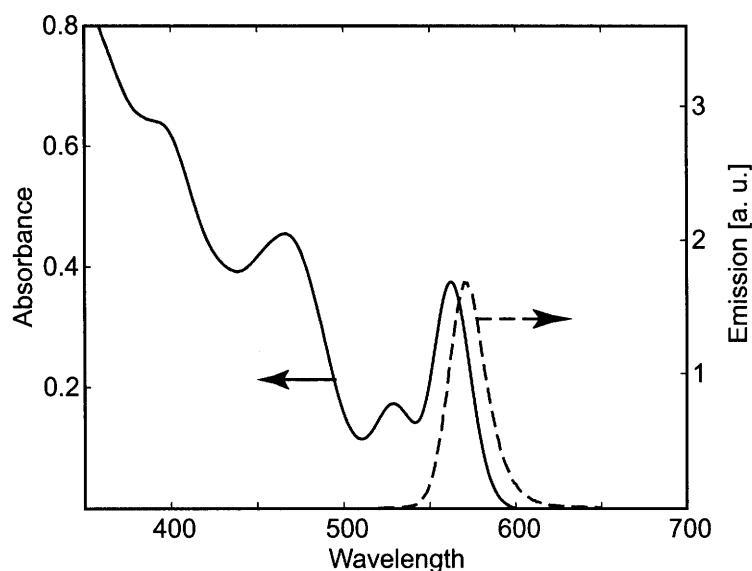
Figure 1-2: Absorption (solid) and emission (dashed) spectra for CdSe QDs, prepared using the cadmium oleate synthetic method outlined in Appendix A.[13] While discrete-like features are evident, the absorption spectrum is continuous and increases to the high-energy side of the band edge.

emission[21] and carrier multiplication[22, 23].

However, more recently, this group (along with peer groups) has evolved such that a large portion of the research portfolio now is oriented toward quasi-real-world applications of QDs. These applications largely fall into the broad categories of biological imaging and of photonics and optoelectronics and are primarily driven by three unique properties of QDs:

- Unlike their organic dye counterparts, QDs have absorption spectra that are continuous to the high-energy side of the band gap, allowing for multiplexed excitation—efficient excitation of spectrally distinct emitters using a single excitation source.

- QDs are robust emitters and do not readily photobleach.

- Optical characteristics of QDs are determined by their semiconductor cores, whereas chemical compatibility is determined by organic passivating ligands on the particle surfaces. Insofar as ligand exchange is possible for a particular system, chemical and optical properties are decoupled.

22

Biological Imaging. The photostability of fluorophores is of critical importance biological imaging applications, and QDs are of interest because of the high, robust fluorescence efficiencies and broad tunability. This is particularly relevant in the near-IR, where the few fluorophores that are available readily photobleach.[24] In one example of in vivo imaging using QDs dispersed in solution, InAs QDs synthesized to emit at $\lambda \sim 750$ nm and ligand exchanged for compatibility with an aqueous, biological environment were injected into a rat subcutaneously. Using a broad-band white light source, multiple lymph nodes (relevant to cancer treatment) were imaged with a silicon CCD array equipped with a long-pass filter.[25]

In another demonstration, QDs were functionalized to be compatible with a silica sol-gel chemistry, and a layer of QD-silica matrix was deposited on existing, monodisperse silica spheres. This produced silica spheres ~ 1 μm in diameter containing QDs emissive in the visible spectrum. Two sets of spheres containing two different sizes (different colors) of QDs were injected into a mouse and were simultaneously imaged using multiphoton scanning microscopy with a single two-photon excitation source, revealing blood flow in the brain of a mouse.[26] These two examples in the area of biological imaging both exploit all three key properties of QDs listed above.

Lasing. The robustness of QDs as fluorophores and the relative temperature-independence of gain[27] make QDs attractive lasing media. In this case, again, functionalizing QD surfaces to be compatible with sol-gel chemistries has enabled the successful incorporation of QDs with high luminescence efficiency into titania and silica matricies both in distributed-feedback[28, 29] and whispering-gallery-mode[30] cavities, and these structures exhibit optically pumped lasing. Electrically pumped lasing from colloidal QDs has yet to be achieved, however.

1.1.2 QD-Containing Light-Emitting Devices

The most prominent optoelectronic application of QDs, particularly relevant to this work, has been the incorporation of QDs into organic light emitting device structures to produce emissive hybrid organic-inorganic devices that have come to be known as QD-LEDs.[31, 32] These devices are directly related to traditional organic-light-
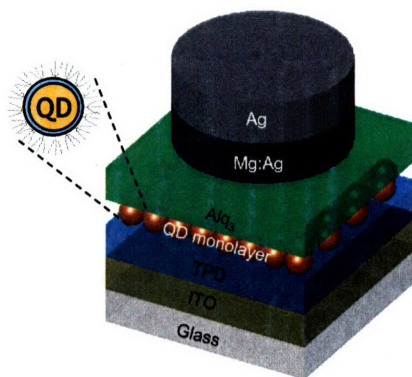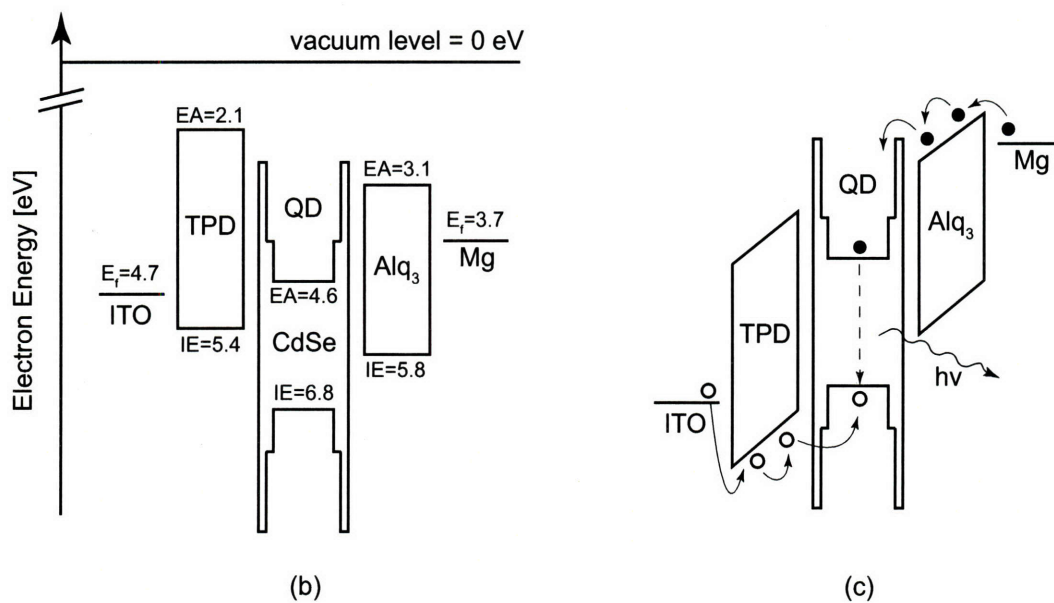
Figure 1-3: Cartoon cutaway of basic layered QD-LED device (a) shows its similarity to the existing OLED class of organic electronic devices. Energy-band structures of QD-LED in open-circuit (b) and forward-bias (c) conditions. Panel (c) depicts direct charge injection into QDs, understood to be one of two mechanisms (along with Förster transfer) through which excitons arise on QDs. Layer widths not drawn to scale. Panel (b) adapted from Ref. [31].

emitting-device (OLED) architectures,[33] in which charge is injected from two electrodes (at least one of which is transparent) into two molecular organic semiconductor materials with distinct electron- and hole-mobility characteristics. In OLEDs, charge recombines at the interface of these two organic layers, giving rise to electroluminescence, the spectrum of which is usually strongly characteristic of the lower-band-gap molecular semiconductor.[34] QD-LEDs share the same essential architecture [see cutaway cartoon in Fig. 1-3(a) and energy band structure in Fig. 1-3(b)], except that a monolayer of QDs is inserted at the critical charge-recombination interface. During operation, charge is injected in the host organic layers as in an OLED, as shown in Fig. 1-3(c). However, through some combination of direct charge injection (onto QDs) and Förster transfer of nearby excitons to QDs from the nearby host organic materials,[35] QD-LEDs produce electroluminescence (EL) with a spectrum that is largely characteristic of the photoluminescence (PL) spectrum of the constituent QDs.[31, 32] Despite the fact that these devices constitute an opto*electronic* use of QDs, however, this application again relies squarely on the outstanding optical properties of QDs—the narrowness of QD emission spectra, high luminescence efficiency, and the ability to decouple surface chemistry from spectral tunability. Put another way, QDs do not serve an appreciable charge transport role in this device architecture.

The critical consequence of the close correspondence between QD-LED EL and the PL of the constituent QDs is that QD-LED EL spectra can be much narrower than phosphor or organic counterparts, giving rise to individual QD-LEDs with very "saturated" colors [Fig. 1-4(a)]. QD-LED arrays can be anticipated, with individual pixels like those in Fig. 1-4(c) having either red, green, or blue emission, thus creating an RGB display. Because of the color saturation of each individual pixel, a QD-LED RGB display can render more colors that are perceptible to the human eye than existing technologies, as indicated by the triangles superimposed on the CIE diagram in Fig. 1-4(b). This increase in color saturation is the primary driver of the QD-LED technology, which forms the basis for the start-up company QD Vision, Incorporated.[1]

---

[1]Founded in 2004 by Seth A. Coe-Sullivan and Jonathan S. Steckel.
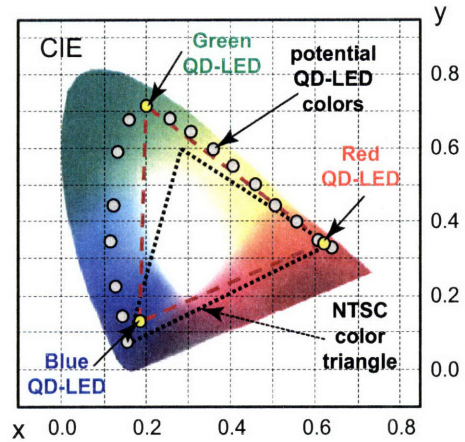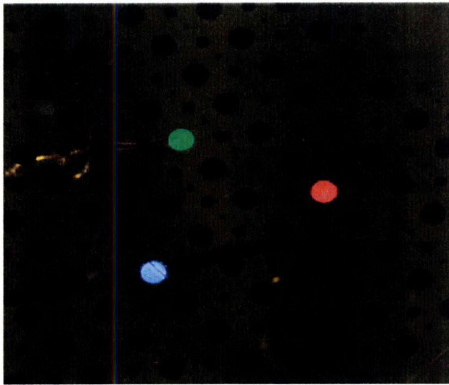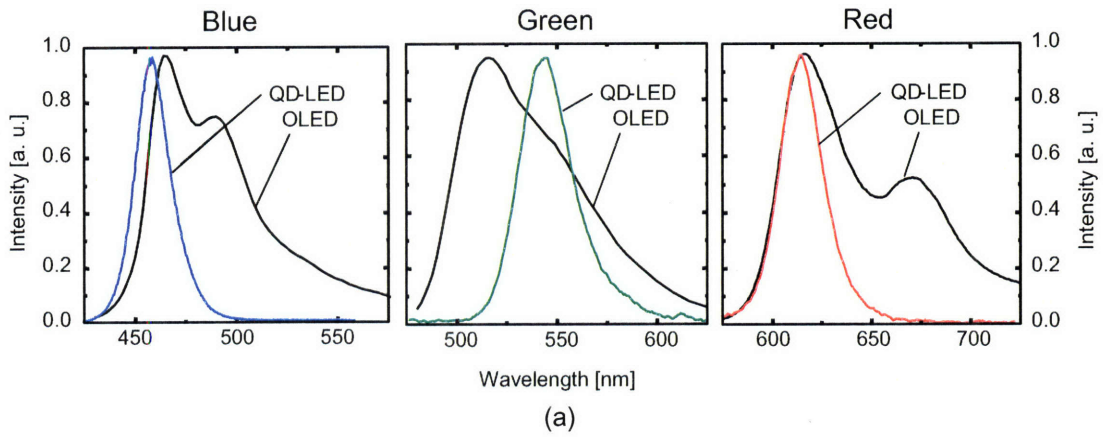
Figure 1-4: Comparison of (a) of red, green, and blue QD-LED emission spectra to those of OLEDs, emphasizing the superior color saturation (narrowness of emission features). RGB displays based on individual red, green, and blue QD-LED pixels (b) are predicted to enable displays capable of rendering more colors that are perceptible to the human eye compared to existing technologies (c).
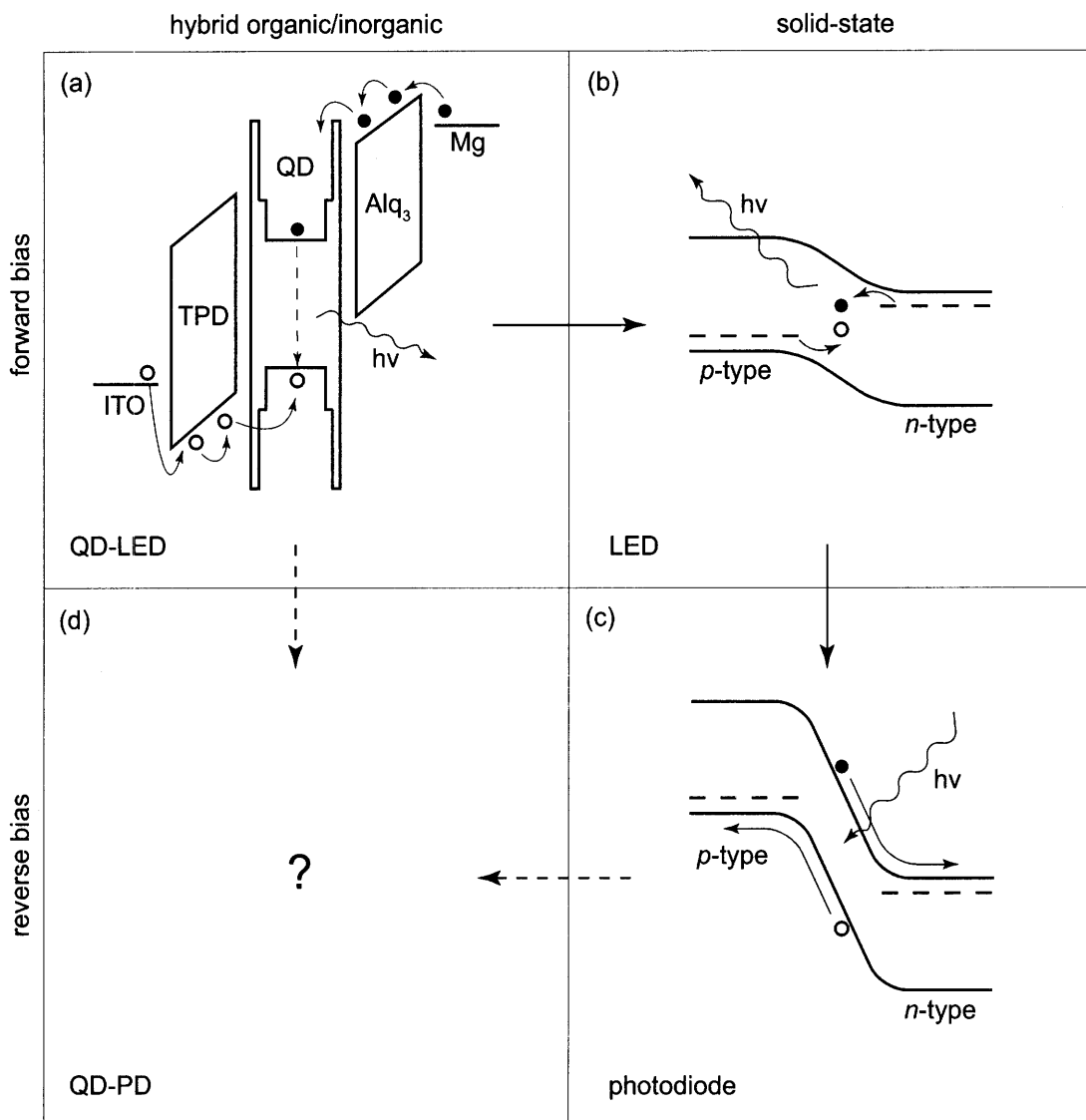
Figure 1-5: Matrix of hybrid organic/inorganic and solid-state devices. The energy-level structure of QD-LED under forward bias (a) is similar to (b), which depicts the band structure of a solid-state p-n junction under forward bias. In both, electrons are injected from the n-type side and holes from the p-type side, and their recombination produces electroluminescence. Panel (c) shows a similar p-n junction, this time under reverse bias, which acts as a photodiode. Photoexcitons absorbed in the depletion region between the p- and n-type sides are immediately dissociated and collected with high efficiency. How can hybrid organic/inorganic photodetectors (d) be achieved?

QD-LEDs, then, represent the merging of a new material set, QDs, with existing unconventional OLED processing techniques to enable potentially superior emissive devices with simplified, scalable fabrication, and potentially on flexible substrates.

1.2 QD-Containing Photodetectors

It is evident that the band diagram in Fig. 1-3(b), reproduced in Fig. 1-5(a), is strikingly similar to a solid-state p-n junction under forward bias [Fig. 1-5(b)], widely explained in references such as Ref. [36], acting as an LED. And, of course, a p-n junction in reverse bias can act as a photodiode [Fig. 1-5(c)]. Thus, the following question arises: Can we just reverse-bias an existing QD-LED and create a working QD-based photodetector (QD-PD)? More broadly, can the same combination of novel materials and unconventional processes that enables QD-LEDs be used to produce promising QD-PDs?

Before addressing this question, it is worth considering whether making photodetectors based on colloidal quantum dots is even a worthwhile idea.

1.2.1 Why QD-PDs?

QD-PDs based on colloidal QDs are an interesting prospect for many of the same reasons that make QD-LEDs appealing. Presumably, their fabrication, like that of QD-LEDs, could take advantage of the solution-processibility of QDs and would be simplified, scalable, and potentially adapted to a continuous roll-to-roll manufacturing process. QD-PDs could also be deposited on flexible substrates as well as rigid ones, perhaps enabling large, wearable detector arrays at a sufficiently low cost. The potential to position thin QD layers of small band gap between much thicker host layers of much higher band gap could enable direct analogs to more expensive solid-state p-i-n counterparts in the IR spectral region.

As with QD-LEDs, another strong motivation for developing QD-PDs is the potential to tune spectral characteristics of the QD-PD with size of constituent QDs. However, in this case, instead of exhibiting narrow, saturated electroluminescence,
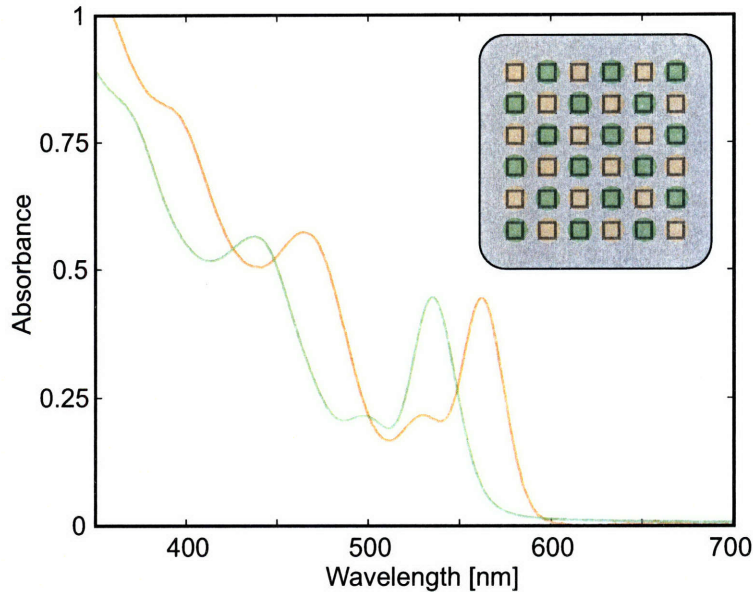
Figure 1-6: Photodetector pixels containing one of two sizes of QDs would have different photoresponse spectra (roughly proportional to the absorbance spectra shown), and a device in which pixels are patterned in a checker-board-like pattern (inset) could be used to produce an image with some spectral selectivity, or color recognition.

the differing absorption spectra of varying sizes of constituent QDs would give rise to different spectral responses of different photodetectors. The simplest manifestation of this would be a pixel array in which two different sizes of QDs (Fig. 1-6) are patterned with a checker-board-like array (Fig. 1-6, inset). An array of detectors with different spectral characteristics, analogous to the three types of cones in the human eye,[37] could enable simple spectral selectivity, or a basic color vision, in the visible or in the IR spectral regions.[2]

1.2.2 Potential Wavelength Ranges of Interest

In this section, we address the question: Given that QD-PDs can be produced, how could these devices be used? We make the assumptions that (1) the QD-PD response spectrum will be roughly proportional to constituent QD absorption near the QD

---

[2]This same sort of selectivity can be achieved by adding filters to existing detectors and is not alone a compelling reason to pursue development of QD-PDs. However, there is motivation in the potential for achieving spectral selectivity with reduced complexity in process (cost).
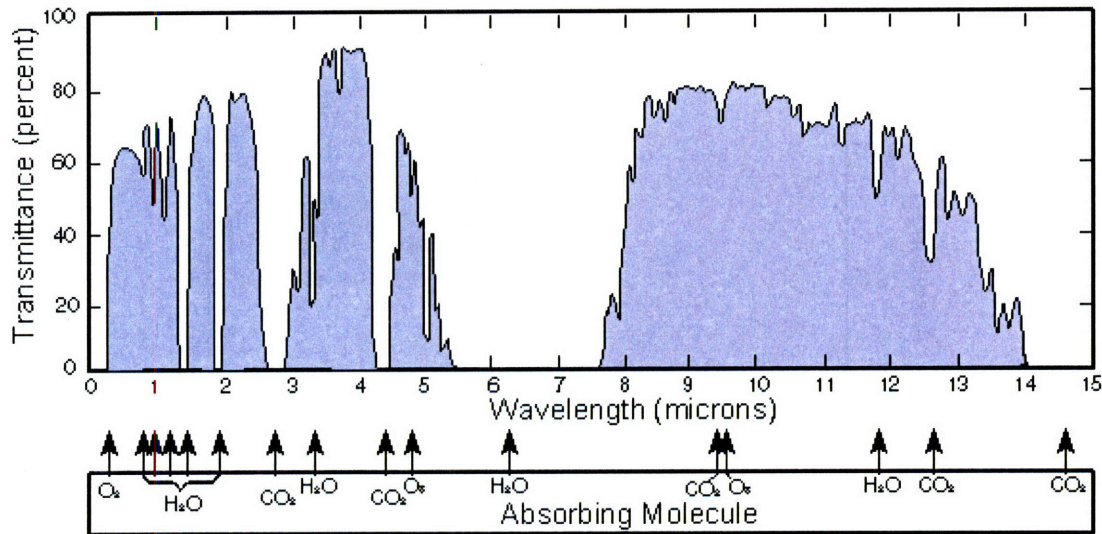
Figure 1-7: The transmission spectrum of the atmosphere for $\lambda < 15$ μm. Adapted from Ref. [39].

band-edge, where the features are most dependent on QD size and (2) the bandwidth of QD-PDs will certainly be no larger than those of current organic photodetectors.[3] Figure 1-7 shows the atmospheric spectrum, relevant to this section, with the three wavelength ranges discussed below indicated.

Visible and near-IR spectrum (400 nm $< \lambda <$ 1.0 μm). To this point, QD research has overwhelmingly focused on materials (most notably CdSe) with band gaps tunable with size over this range of the spectrum. However, existing silicon photodiodes are active for $\lambda < 1.0$ μm, covering this entire range. Silicon detectors operate at room temperature, have excellent overall external quantum efficiency η_{eqe}, are sufficiently fast, and are already widely integrated into commercial applications at low cost, both in single-element and array form. It is unlikely that QD-PDs could gain much traction in the visible spectrum.

Mid-IR (2.5 μm $< \lambda <$ 12.0 μm). This wavelength range contains two atmospheric "windows" (3 μm $< \lambda < 5$ μm and 8 μm $< \lambda < 10$ μm, as can be seen in Fig. 1-7) of interest to the military for thermography or ground-to-air or ground-to-

---

[3]While there is one report of a wide-bandwidth ($f_{3\mathrm{dB}}$ = 430 MHz), 64-layer organic photodetector,[38] most organic and polymer photodetectors are understood to have < 20 MHz bandwidth.

satellite communications. While thermal detection systems often do use multichannel systems to gather rough thermal radiation spectra, the spectral windows used are, in general, much larger than the range over which one can easily tune QD absorption features.[39] In other words, multichannel QD-PD systems used for thermal sensing would likely have to consist of different QD materials, not different sizes of QDs of the same material, and would thus fail to exploit the unique size-tunability of QDs.

Unfortunately, the 3 μm $< \lambda <$ 5 μm range has proven difficult to access from a QD synthesis standpoint and the 8 μm $< \lambda <$ 12 μm range has yet to be attempted. The bulk band gap of PbSe is 0.27 eV ($\lambda \sim$ 5 μm), but owing to the large exciton Bohr radius of this material, QDs with a band edge 3 μm $< \lambda <$ 5 μm would have to be 20 nm or more in diameter, well beyond the size range accessible by standard colloidal nanocrystal syntheses. Though InSb, with bulk band gap 0.17 eV (λ = 7.3 μm), is a better candidate to exhibit a confined band-gap tunable across 3 μm $< \lambda <$ 5 μm with synthetically accessible particle sizes, syntheses of InSb are exceedingly difficult and to this point have been elusive. Post-doc Frédéric Dumestre undertook the InSb QD synthetic challenge for many months in 2004 using a method analogous to InAs syntheses,[40, 25] but ultimately was only able to produce polydisperse particles and nanoribbons (Appendix B). Hence, this wavelength range cannot currently be achieved via band-edge absorption in existing colloidal QD materials.

Short-wavelength-IR (1 μm $< \lambda <$ 2.5 μm). The short-wavelength-IR (SW-IR) corresponds to photon energies below the silicon band gap and can be accessed synthetically using well-known PbSe QD (1.1 μm $< \lambda <$ 2.5 μm)[41, 32] and PbS QD (700 nm $< \lambda <$ 1.7 μm) syntheses[42]. Based on wavelength range alone, there are two potential applications:

1. **Fiber-optic communications.** One potential application driving the development of QD-PDs in this range is fiber-optic communications, in which the important wavelengths λ = 1.3 μm and λ = 1.55 μm are easily accessible with both PbS and PbSe QDs. While this application is feasible for QD-PDs with regard to spectral window, the frequency response of QD-PDs is likely to compare very unfavorably to existing optical communications receivers, which have
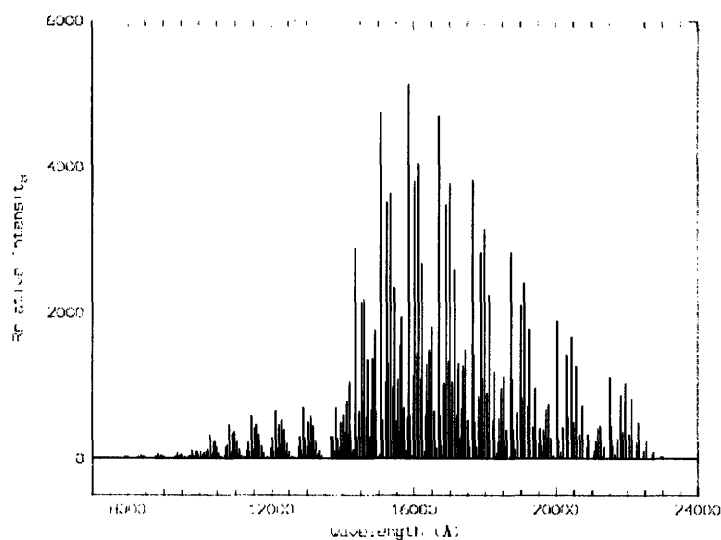
Figure 1-8: Calculated vibrational emission (with $\Delta v = 2$ to 5) of nigh-sky OH radical emission. Reproduced from Ref. [43]. (©2000 Springer-Verlag.)

bandwidths on the order of GHz. This bandwidth is well beyond even the 430 MHz bandwidth demonstrated by a very specialized organic photodetector.[38] No QD-PD faster than 50 kHz (Chapter 3) has been reported.

2. **Night vision using atmospheric nightglow.** One of the more feasible potential applications of QD-PDs appears to be night vision imaging using atmospheric nightglow. Nightglow, which occurs primarily in the 1.4 μm $< \lambda <$ 2.1 μm spectral window, results primarily from vibrational emission from OH radicals in a 6 to 10-km thick atmospheric layer $\sim$ 87 km in altitude.[43] In this layer, OH is formed in a reaction between ozone and atomic hydrogen, and the thermodynamics are such that nascent OH can be populated up to the $X^2\Pi_i$ $v = 9$ level.[44] Currently, InGaAs detectors, with a broad response spectrum from 1.0 μm $< \lambda <$ 1.8 μm are used for night-glow based night vision. However, fast refresh rates are not needed for this application (frequencies as low as 30 Hz suffice), and using pixels containing QDs of different sizes could enable IR absorbance- or reflectance-based "color" vision. QD-PDs operating in the SW-IR could provide value for this application if they prove to have

detectivities[4] on the same order as common InGaAs detectors.

Of the three wavelength ranges considered in this simple preliminary analysis, only 1.0 μm $< \lambda <$ 2.5 μm seems to contain an application where colloidal QD-based detectors may have a realistic application. However, owing to the familiarity with materials and ease of work in the visible range, the 400 nm $< \lambda <$ 1.0 μm is also a reasonable place to work for early development of QD-PDs.

1.2.3 QD-LED under Reverse Bias

QD-PDs might indeed have benefits in cost and utility, particularly in the 1.0 μm $< \lambda <$ 2.5 μm range, and we return to the question of how an absorptive QD-based optoelectronic device can be realized [Fig. 1-5(d)]. Can an existing QD-LED, simply placed under reverse bias, serve this role? Figure 1-9(a) and (b) shows cartoon cutaways of QD-LEDs operating in forward and reverse bias, respectively. While a monolayer is sufficient to produce saturated QD emission, a device like that shown in Fig. 1-9(b) will work very poorly because of exceedingly weak QD monolayer absorption.[5] Figure 1-9(c) shows that band-edge QD monolayer absorption efficiency $\eta_{abs} \approx 0.01$, which places a severe limit on the overall device efficiency η_{eqe}.[6] To ease this absorption limitation, more layers of QDs must be added,[7] depicted in the cartoon cutaway closeups in Fig. 1-9(d) and (e), and by doing this, a device is created in which QDs now must be considered a *charge-transport layer* as well as optical layer.

To realize a QD layer with a dual optical and transport role, we exploit a longstanding fundamental study in our group devoted to understanding charge transport in close-packed CdSe films.[46, 47, 48] Specifically, post-deposition, solution-phase

---

[4]See Appendix C for a brief discussion of the detectivity metric, or D^*.

[5]An additional problem with simply reversing the bias on a QD-LED, not emphasized here, is that the energy levels of materials in QD-LEDs are engineered to facilitate charge *injection* and not charge *extraction*. This problem is more easily solved than the more fundamental absorption limitation.

[6]For organic and hybrid organic-inorganic hybrid photodetectors, it is useful to think of overall external quantum efficiency as the product $\eta_{eqe} = \eta_{abs}\eta_d\eta_{cc}$, where η_{abs} is absorption efficiency, η_d is exciton dissociation efficiency, and η_{cc} is charge collection efficiency.

[7]A precisely engineered cavity may allow for considerable absorption enhancement, but (1) this is quite difficult to achieve in practice and (2) the spectral photocurrent response of such a device would be a convolution of the QD absorption and cavity enhancement.
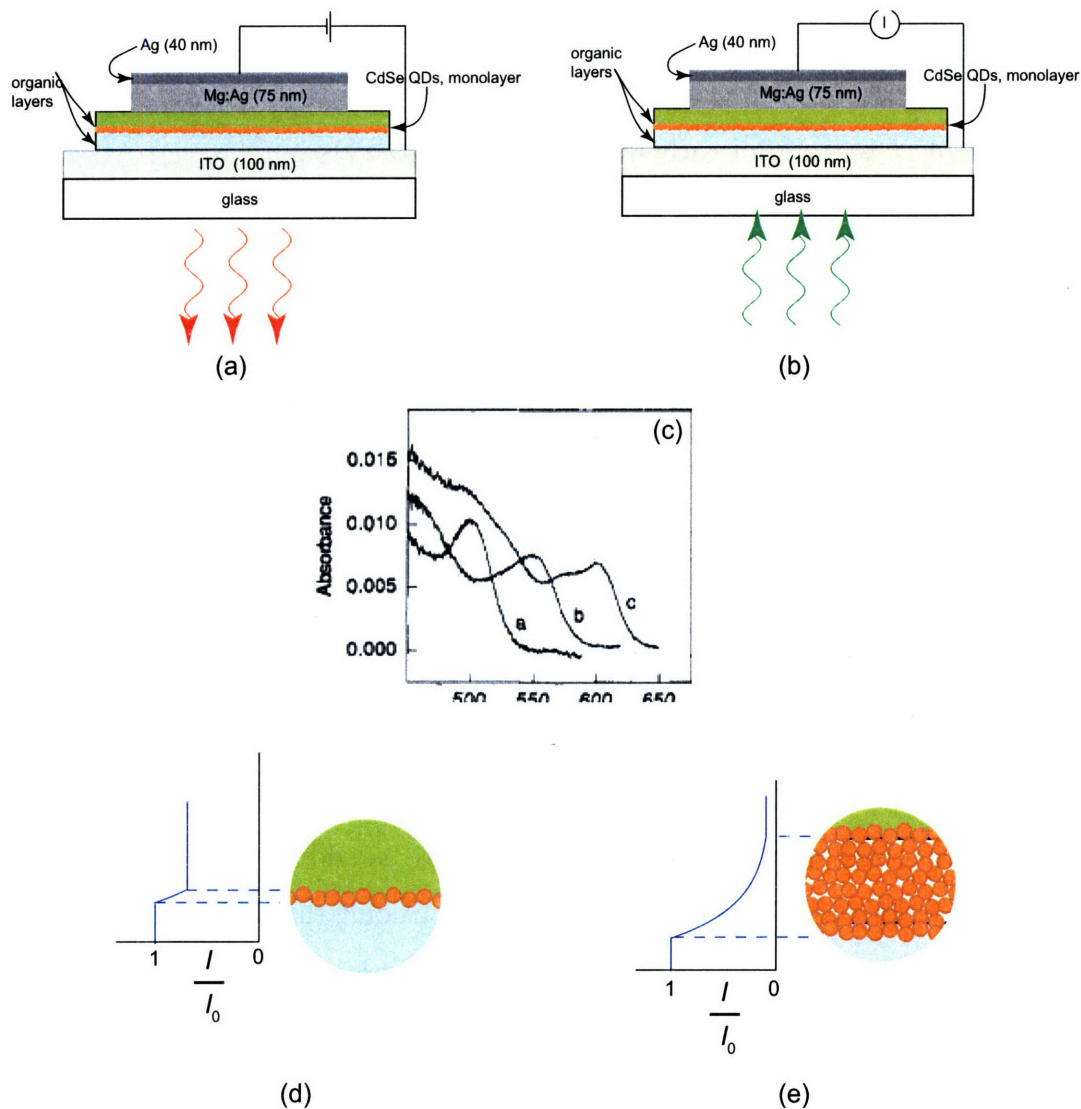
Figure 1-9: Cutaway cartoons of QD-LED in forward (a) and reverse (b) bias. The external quantum efficiency η_{eqe} of the would-be photodetector in (b) is limited by very low absorption ($\eta_{\mathrm{abs}} \approx 0.01$ at the absorption band edge), shown in panel (c). Microscopic cartoon views of the absorption of a single monolayer and a thicker layer are contrasted in panels (d) and (e), respectively. Panel (c) is reproduced from Ref. [45]. ©American Chemical Society.

34

chemical treatments, first explored in an electrochemical cell setup,[49] have recently led to the development of procedures through which unity internal quantum efficiency has been observed in test structures.[48] These annealing procedures—in essence in situ cap exchanges, further discussed in § 2.1 and § 3.2 (the latter of which discusses our adaptation for layered structures)—enable QD solids to be incorporated into functional, layered QD-PDs.

In this thesis, we seek to use the general fabrication and deposition methods learned in QD-LED development in conjunction with recent improvements in transport in QD solids to produce QD-PDs containing thick layers of QDs. While the 1.0 μm $< \lambda <$ 2.5 μm range holds the most eventual promise, our strategy is to use the canonical material CdSe, active in the visible range, to develop device architectures before incorporating IR-active QD materials such as PbSe or PbS, about which much less is known.

1.2.4 Challenges

A number of challenges exist, both relating to the specific goals of this research and much more general to the development QD-based optoelectronic devices.

Materials and processes. Broadly speaking, this work involves combining new materials and new processes to find combinations that may eventually have real utility. The great range of materials, device designs, and processes that we can consider is both a source of freedom and of a very large parameter space. For example, different QD materials can be considered for use across the same wavelength range. PbSe and PbS both are active in the 1.0 μm $< \lambda <$ 2.5 μm. QD deposition methods include single spin casts, multiple spin casts, stamping, and even printing. Devices may include one of or both quasi-n-type and quasi-p-type blocking layers, as is discussed in Chapter 4. These layers can be organic semiconductors, or they can be sputtered or sol-gel-deposited metal oxides. Parameter space increases exponentially as more options are considered.

Throughput. High throughput is critical for making progress in this area of research both for screening through the different combinations of materials and pro-

cesses mentioned above and, perhaps more importantly, for optimizing the various processes that contribute to a finished device. Because we are a small-scale, batch-mode academic lab, and the project has had at most two students focusing on it an one time, it is much more difficult to develop the kind of consistency in process seen in industrial settings. Compounding this problem is the relative scarcity of QDs. While they are easily made on the scale of a tenth of a gram, one QD preparation may produce as few as two devices. This high material cost discourages making structures of diagnostic value only, which further hinders morphological understanding of devices.

Logistics. Though trivial by some definitions, simple logistics also pose a challenge to this work. A total of four labs in three buildings have been used to synthesize and process QDs and then produce and characterize QD-PDs. Retrieval of forgotten equipment or supplies comes at a steep price. The synthesis of the QDs notwithstanding, all work has been done on shared equipment managed and run by students. This can produce numerous aborted device runs owing to unexpected scheduling conflicts and improperly working equipment. While not unique to this project, these logistical challenges severely impede throughput, critical to screening and optimizing device configurations.

1.3   Thesis Overview

The following chapter provides an introduction to existing work in the areas of charge transport in QD solids and QD-based photovoltaics and photodetectors, the first of which is an important part of the foundation for the work discussed in Chapters 3-5. The remainder of this thesis consists of five chapters and three appendices. Chapters 3 and 4 focus on work toward initial, exploratory devices based on CdSe QDs (active in the visible spectrum). Chapter 3 is an expansion of the research reported in Ref. [50] focusing on making the simplest possible layered QD-PD. More complex multilayer structures are discussed in Chapter 4, and work reported in Ref. [51] is contained in this chapter.

Chapter 5, 6, and 7 focus on the PbSe QD material set and its possible applica-

tions. Chapter 5 discusses initial efforts to understand transport in PbSe QDs and to incorporate this material in layered QD-PDs. Chapter 6 discusses the synthesis of PbSe QDs at a more mechanistic level and contains work reported in Ref. [52]. An evaluation of PbSe QDs as a fluorophore material for biological imaging is included in Chapter 7. Brief concluding remarks follow. Finally, three appendices provide information on narrow topics and are referenced in the main text where appropriate.

THIS PAGE INTENTIONALLY LEFT BLANK

Chapter 2

Introduction II: Existing Work

This chapter, which represents the second portion of the introductory material, provides background regarding (1) charge transport in QD solids and (2) QD-containing photovoltaics and photodetectors. The former reviews work leading up to and including the recent development of methods that significantly improve charge transport in QD solids. The latter describes existing work on QD-containing absorptive devices related to the QD-based photodetectors whose development is described in this thesis. The two main sections of this chapter reflect these two topics.

2.1 Charge Transport in QD Solids

The prospect of using colloidal QDs in devices such as LEDs, lasers, photodetectors, electromodulators, and photovoltaics has driven considerable interest in understanding the transport of charge in semiconductor nanocrystal materials. While a few early studies have involved single-quantum-dot devices,[53, 54] most of the work in this area has focused on transport in three-dimensional QD solids, the kinds of ensembles potentially of use in practical, macroscale devices. Interest in electronic properties of QD solids was also driven by the novelty of these "artificial solids," created from constituent "aritificial atoms."[55, 56, 57]

Owing to their hard-sphere repulsion, van der Waals attraction, and narrow size distributions ($\sigma < 5\%$), colloidal QDs can be self-organized into 3D QD crystals with

long-range order through gentle destabilization of a QD dispersion.[58] In order to create such structures, QDs must first go through several cycles of precipitation with a non-solvent followed centrifugation and redispersion in solvent. (The details of this process affect significantly the electronic properties of the resulting QD solid.[59]) Following this step, QDs are typically dispersed in a mixture of two solvents with differing vapor pressures, and thin films are cast onto substrates, allowing 3D QD solids to be integrated into optoelectronic devices. QD solids exhibiting some long-range order can be drop-cast on pre-wired bar electrodes to produce a transverse structure.[46, 47] Alternatively, QD solids (likely with less long-range order) can be spin-cast in the fabrication of layered structures.[60]

Quantum-dot solids are typically highly insulating in their nascent state (regardless of degree of long-range order) owing to long-chain surface-passivating ligands. There is very little red-shift of absorption and emission features between QDs dispersed in solution and QD solids, further suggesting minimal electronic overlap of low-energy excited states.[58] In this section, we discuss early studies of these insulating solids and the methods developed subsequently to substantially improve the conductivity of these solids. Finally, we discuss how judicious application of these methods can lead to practical device applications, such as a recently reported thin-film transistor based on PbSe QDs.[61]

2.1.1 Early CdSe QD Transport Studies

Early studies were performed primarily on CdSe QD solids passivated by tri-n-octylphosphine (TOPO) ligands, either as drop-cast films on bar electrode or as spin-cast layers in a layered sandwich-type device. A close-packed film of TOPO-capped QDs exhibits a core-to-core spacing of ~ 1.1 nm,[47] and the very low conductivity observed in these films ($\sim 10^{14}$ S cm^{-1} [62]) is attributed both to the long aliphatic barriers between cores and the availability of traps within the film. Because of the low intrinsic carrier concentrations in CdSe, studies of transport in CdSe QDs have often relied on charge generation through photoexcitation and subsequent exciton ionization.

Ginger et al. studied charge transport in 200-nm thick films of TOPO-capped CdSe

QDs using the layered structure: ITO/CdSe QDs (200 nm)/M, where M = Al, Ca, or Au.[60] Devices containing Al or Ca had rectifying *I-V* curves and behaved similarly to each other, while the device containing Au did not show rectification, implying that (1) only Al and Ca could inject electrons into the conduction level in CdSe QDs, and (2) the behavior of the Al and Ca devices was determined by the QD solid, not by the electrode work function. The Al- and Ca-containing devices also displayed some photovoltaic response. Lengthy photocurrent decays were observed and fit with stretched exponentials, and sequential cycling of voltage in the dark reduced the current level which could then be "restored" by exposure to light higher in energy than the CdSe band gap. It was calculated that the number of charges extracted from a device was a factor of a 10^3 larger than the number of photons incident. These observations led the authors to propose a space-charge-limited conduction (SCLC) model in which deep traps were numerous enough that, with time, the SCLC condition throughout the film is reached. Morgan et al. also explored dark currents in CdSe QD but used a markedly different geometry in which films were drop-cast on an inverted field-effect-transistor structure with Au electrodes.[63] The only signal above the noise floor (~ 0.1 pA) measured were current *transients* in response to voltage steps, which exhibited a power law decay with time (over $\sim 10^2$ to 10^3 seconds) dependent on applied field and not channel width. Another interesting observation was that far more charge flowed from source to drain than could have been trapped in the sample. As a result, the authors proposed that there was a thin (~ 100 nm) space-charge layer near the injecting contact which behaves as a Coulomb glass. The current transients observed result from extraction of carriers from the space-charge region over time.[63] Novikov et al. recently have proposed a "conduction channels" model based on Lévy statistics that accounts for the current transients seen by both Ginger and Morgan.[64]

While current-voltage analysis has provided some insight into the difficulty with which injected charge moves through CdSe solids, charge migration can be imaged directly using electrostatic force microscopy (EFM), used previously to study electrostatics and blinking of single QDs.[65] Figure 2-1 shows two electrodes beneath a
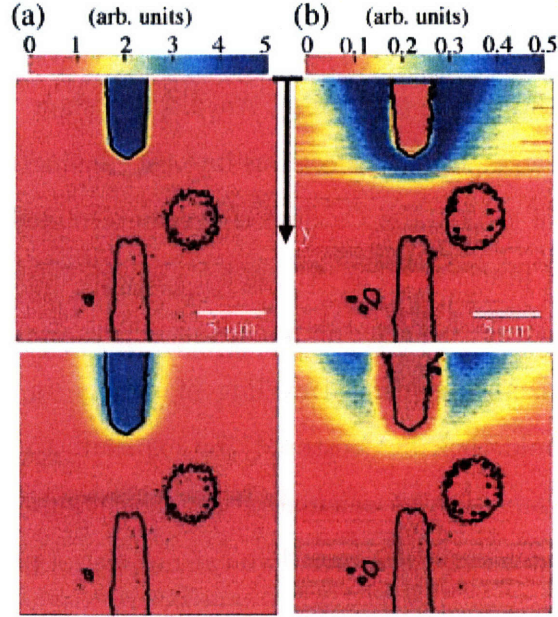
Figure 2-1: EFM images of (a) charging and (b) discharging events. The upper pane of (a) was taken immediately after the application of $V_{dc} = 40$ V, and the lower pane is after 40 minutes at this potential. The upper pane of (b) was taken immediately after the voltage was switched off following 1 hr of charging at $V_{dc} = 40$ V. The lower pane of (b) was recorded 9 min later. (Reproduced from Ref. [66]. ©2003 American Institute of Physics.)

200-nm thick film of TOPO-capped CdSe QDs. The bottom drain electrode can be seen only in the electrode contour outline superimposed on the EFM image, showing very poor conduction. Based on the time over which charge spread throughout QD films, diffusion constants were calculated to be $\sim 3 \times 10^{-3}$ μm s^{-1}, corresponding to a resistance of $\sim 3 \times 10^{18}$ Ω/square.[66]

Photoconductivity in nascent CdSe QD films drop-cast on inverted FET structures with Au electrode was studied in depth by Leatherdale et al.[46, 47] This work is particularly significant because of its insightful modeling of the photoexciton ionization event, which was found to determine largely current-voltage characteristics. As was the case with previous work, measurements were carried out at in vacuo and at low temperature ($T < 77$ K). While a large field ($\sim 10^6$ V cm^{-1}) was applied across the film, light with $\hbar\omega \leq E_g$ (E_g is the QD band gap) was incident on the sample. Some fraction of photoexcitons were ionized by the field and subse-
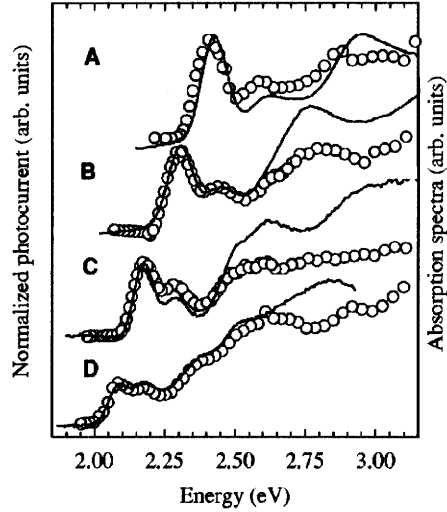
Figure 2-2: Far above the band edge, non-radiative decay is more efficient, resulting in reduced photocurrent. Four sizes of CdSe QDs are shown: A 1.75 nm; B 2.06 nm; C 2.5 nm; D 3.0 nm. (Reproduced from Ref. [47]. ©2000 American Physical Society.)

quently were extracted from the film. The intensity dependence of photocurrent was observed to be linear[47] (Ginger observed near-linear behavior[60]), suggesting essentially monomolecular charge recombination within the film. Figure 2-2 shows the agreement, which is expected, between band-edge absorption features and photocurrent (PC) response spectra. The departure of the PC response from the absorption profile at energies far above the band edge is expected owing to reduced radiative efficiency.[47, 67]

While the magnitude of I-V characteristics decreased with increasing temperature, the shape—a quasi exponential, suggesting some sort of tunneling mechanism—did not, indicating that charge transport in this regime was not thermally activated. In addition, PL quenching increased under increasingly high fields. These observations are consistent with a model in which charge generation efficiency (or exciton dissociation efficiency) η_d depends on competition between geminate recombination and field-dependent exciton ionization. This competition can be expressed as

$$\eta_d(F, T) = \frac{k_F(F, T)}{k_F(F, T) + k_r(T) + k_{nr}(T)}, \tag{2.1}$$

and with relatively low ionization rate (k_F), this can be factored to $\eta_d = \tau(T)k_F(F)$,

43

where $1/\tau = k_r + k_{nr}$. Here, $\tau(T)$ is most strongly temperature dependent through k_{nr}, and $k_F(F)$ is a field-dependent ionization rate independent of temperature, suggesting a tunneling process. Accordingly, Leatherdale et al. proposed a two-site resonant tunneling model. Unlike Onsager-type models, this model can explain charge separation for cases in which the Coulomb energy of the initial exciton is much greater than kT. Further, the transport in QD solids should be enhanced substantially if the width of the tunnel barrier (aliphatic surface-passivating ligands) between QDs can be reduced.

In general, nascent CdSe QD films in the solid state, even at low temperature, at which non-radiative decay rates are suppressed, show poor conductivities and transport properties that are defined by significant trapping within the film and poor ionization efficiency. In the next section, we discuss methods used to improve transport in QD solids by alleviating these problems.

2.1.2 Methods of Improving Conductivity

Several methods have been used to enhance the conductivity properties of QD solids. Thermal annealing and chemical treatments primarily have the effect of bringing QD cores closer together, facilitating more facile tunneling of charge. Doping, when used in tandem with chemical treatments, can increase film conductivities by orders of magnitude, especially when done in an electrochemical cell, in which trap sites on QDs are passivated by an inert electrolyte solution.

Thermal Annealing

Thermal annealing has been used to increase conductivity in CdSe[62] and PbSe[68] QD solids. (Distinct from thermal annealing is sintering, a more extreme process in which quantum confinement is lost. Reports of sintering are numerous, including one report of "all-inorganic" thin-film transistors with field effect mobilities up to $1 \text{ cm}^2 \text{ V}^{-1} \text{ s}^{-1}$.[69]) Drndić et al. annealed TOPO-capped CdSe QDs, after deposition on a transverse channel between parallel Au electrodes, at temperatures in excess of
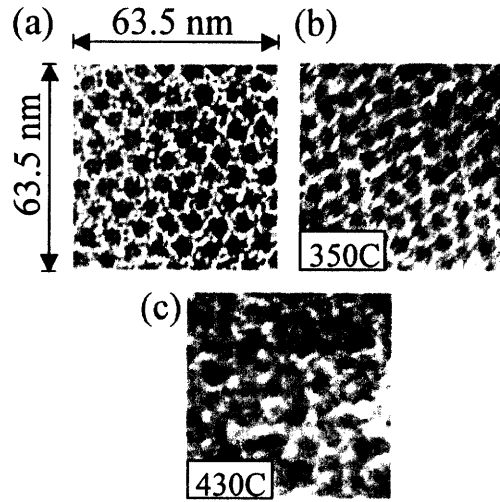
Figure 2-3: TEM of CdSe QD solids after different annealing temperatures. Panel (a) shows a nascent QD film with cores spaced by ~ 1.1 nm; (b) shows QD film annealed at 350 °C with cores spaced by ~ 0.6 nm; (c) shows QD film annealed at 430 °C in which cores have been sintered. (Reproduced from [62]. ©2002 American Institute of Physics.)

110 °C in a forming-gas environment. Treatment at 400°C led to sintering of particles and severe degradation of features in the absorption spectrum.[62] Figure 2-3 shows TEM images of a nascent CdSe films, in which cores are spaced by ~ 1.1 nm, a film annealed at 350 °C for tens of minutes, in which cores, still well-defined, are spaced by only ~ 0.6 nm, and a film annealed at 430 °C, in which the QDs are no longer distinct.[62]

Films annealed at 350 °C have increased conductivity both in the dark and under photoexcitation. While the dark current increased by roughly 400-fold, which is consistent with a model in which tunneling is proportional to $\exp\left(-\alpha d\right)$, where $\alpha^{-1} \sim 0.1$ nm for alkanes and d is the distance between cores,[47] the photocurrent, particularly at low field, increased by three orders of magnitude.

PbSe flims have also been thermally annealed at 420 K to reduce core spacing from ~ 3 nm to ~ 2 nm, and EFM in tandem with TEM were used to image charging patterns and its correspondence to film morphology.[68] While charging and discharging prior to annealing was qualitatively similar to what was observed with EFM in nascent CdSe QD films,[66] post-annealing charging was almost instantaneous, show-

ing greatly enhanced transport. However, TEM micrographs show a strong correspondence between charging and morphological defects, such as cracking, in annealed films. While these annealing procedures did increase exciton ionization efficiency and charge transport in both CdSe and PbSe, their benefits are balanced by increased dark currents and morphological defects.

Chemical treatments

Solution-phase "chemical treatments" of QD films have shown great utility in enhancing conductivity either by cross-linking[49] or simply by reducing core-to-core spacing.[48] Treatments exhibiting cross-linking were first shown by Guyot-Sionnest and coworkers to be of utility in doping experiments carried out in an electrochemical cell (discussed below).[49] In some ways, these treatments can be thought of an in situ ligand exchange. The general process for chemically treating films involves briefly ($\sim$ 1 min) exposing the nascent QD film to a dilute solution of the ligand of interest dissolved in a solvent, such as acetonitrile, in which the film is insoluble. This is followed by baking at $\sim$ 70 °C, well below temperatures required for thermal annealing of QD films, to drive off excess solvent.

Jarosz et al. studied the effects of a wide range of ligand treatments on CdSe QD films drop-cast on inverted FET structures with Au electrodes.[48] Among these were ligands that were both monodentate and bidentate (capable of cross-linking) and that were both conjugated and unconjugated. GAXS analysis suggests that interparticle spacing is in general reduced, sometimes significantly, by these treatments. In an extreme case, treatment with n-butylamine reduced core-to-core spacing from $\sim$ 1.1 nm to 0.2 nm.[48] One important outcome of this work was that the most successful treatments, some of which were monodentate, not only increased the magnitude of the photocurrent seen in these devices, but they changed qualitatively behavior seen in the I-V curves. Unlike what is observed for nascent CdSe QD solids, in which the I-V relationship is everywhere quasi-exponential, which relects the dependence of exciton ionization efficiency on field strength,[47] three distinct regions were identified: (1) at low fields, the curve was roughly exponential, representing sub-unity exciton

ionization efficiency, (2) at moderate fields, a region of linear dependence of current on voltage was observed, and (3) at high fields, saturation was observed, representing unity internal quantum efficiency of device (because the Au electrodes are blocking contacts for CdSe, only primary photoconductivity was observed.) Chemical treatments hence provide access to regimes (2) and (3), representing recombination-time limited and transit-time limited conduction, respectively, which had not observed previously in QD solids. Access to these regimes has enabled extraction of transport metrics such as $\mu\tau$ products.

The utility of chemical treatments is general and not limited to CdSe QDs. CdTe QD films, treated with n-butylamine and studied in a setup identical to that studied above, display secondary photoconductivity with photoconductive gains as high as 10 because Au electrodes are able to inject holes, the majority carrier, into the film.[70] In addition, intrinsic dark conductivity is observed and has been analyzed.

Recently, a layered CdSe QD photodetector produced with n-butylamine-treated films was reported,[50] in addition to an IR-sensitive PbS QD photodetector in which QDs are cap-exchanged with n-butylamine prior to casting,[71] which has a similar effect.

Doping

The prospect of creating n-type or p-type QDs adds another dimension of control to 2D and 3D arrays. Despite recent success doping Mn into ZnSe QDs,[72] doping QDs during synthesis is generally challenging. As a result, a number of efforts have turned to doping QDs post-synthesis, either in solution,[73, 74] after casting into arrays,[75] or using an electrochemical cell.[76, 77]

Chemical doping. CdSe, CdS, and ZnO QDs have been doped n-type while dispersed in solution by introducing the radical biphenyl anion, and the charged QDs were analyzed optically while still in solution.[73, 74, 78] Evidence of doping included (1) partial bleach of the absorption feature corresponding to the $1S_h - 1S_e$ transition accompanied by (2) the appearance of an IR absorption feature corresponding to $1S_e - 1P_e$ and (3) a PL quenching associated either with the Auger mechanism or by

hole trapping by charged surface states. Bleaching and the accompanying IR feature typically disappeared on the order of hours, and after many hours, PL recovery were observed.[79]

CdSe QDs have also been doped n-type in the solid state.[75] Dark conductviity was measured in real time as potassium metal was evaporated on a CdSe film drop-cast on a channel between a pair of gold electrodes, resulting in electrons being injected from the low-work-function metal into the $1S_e$ QD level. Conductivity increased by more than three orders of magnitude during the potassium deposition and remained high after evaporation was complete. The appearance of an IR transition is evidence of the presence of electrons in the $1S_e$ state.[75]

Another example of solid-state doping in CdSe was achieved in a layered charging device with the structure ITO/PAH-PAA (15.5 monolayers)/CdSe QD (20 nm)/Al.[80] Both electrons and holes could be injected into the device, and under appropriate bias, and corresponding fluorescence quenching and band-edge absorbance bleach were observed.[80] Fluorescence was modulated 20% to 30% of its magnitude on the timescale of tens of milliseconds. Larger fields were needed to inject electrons into the QD layer when overcoated (CdSe)ZnS QDs were used rather than bare CdSe nanparticles.[80]

Electrochemical cells and electrochemical doping. CdSe QD solids can also be doped n-type using an electrochemical cell.[49, 79, 81] QDs are deposited on a Pt or Au disk and are placed in a cell (with electrolyte and organic solvent that does not dissolve the film) along with a Pt wire counter electrode and Ag pseudoreference electrode. By applying negative cell potentials, electrons are injected into the QDs. Studying conductivity of QD solids in electrochemical cells has two notable advantages over studies in the solid state: (1) traps in films are passivated by the inert electrolyte solution and (2) counterions enable intimate gating of the QD film as opposed to gating at a distance of hundreds of nanometers, as is the case with inverted FETs. The potentials at which the bleach occurs are dependent on the size of the QDs but typically range from 0.5 V to -1.5 V. The $1S_e - 1P_e$ IR absorption band and the bleach of the $1S_h - 1S_e$ absorption feature are observed, consistent with n-type doping
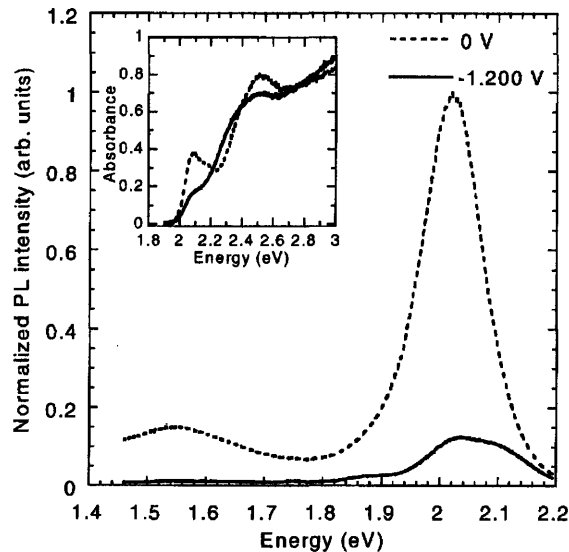
Figure 2-4: Emission quench and $1S_h - 1S_e$ absorption bleach (inset) for undoped CdSe QD (dotted line) and those in which electrons have been injected into the $1S_e$ level (solid line). (Reproduced from Ref. [81]. ©2002 Amierican Institute of Physics.)

with biphenyl anion in solution or K^+ in the solid state. These absorption features can be modulated on the minute timescale, as can be the PL quench. Figure 2-4 shows emission quench and $1S_h - 1S_e$ absorption bleach (inset) for undoped CdSe QD (dotted line) and those in which electrons have been injected into the $1S_e$ level (solid line).[81] Analogous effects have been studied extensively in ZnO QDs in a similar gated electrochemical cell configuration.[82, 83, 84]

While these first demonstrations of electrochemical responses were qualitative only,[79, 81] studies done using films chemically treated prior to placement in the electrochemical cell have allowed quantitative results and switching on much faster timescales.[49] When CdSe QD films were treated with various cross-linker molecules, such as 1,7-heptanediamine, 4,4'-biphenyldithiol, or 1,6-hexanedithiol, a number of benefits were observed: (1) charging/discharging of films occurred on much faster timescales than observed in untreated analogs; (2) electrochemical responses observed were quantitative, allowing electrons injected per QD to be calculated;[49] (3) electrons were injected into higher-energy states (above $1S_e$) than in previous work;[79, 81] and (4) films were more robust both mechanically and electrochemically, and could be cycled thousands of times without significant degredation.

Most recently, electron *and* hole injection have been achieved with PbSe QD films in an electrochemical cell.[85] Because PbSe has a smaller band gap than CdSe, both electron and hole states are within the range accessible with stable electrochemical injection. While the hole bleach is observed, it is not complete (90 % for the $1S_h - 1P_h$ versus 100% for the $1S_e - 1P_e$ electron bleach), and hole injection is not possible into states higher in energy than $1S_h$.[85]

Variable-range hopping. The greatly enhanced conductivities afforded by electrochemical doping and chemical treatments together have made possible the observation of effects not previously observed in QD solids, such as variable-range hopping (VRH), which was recently observed in charged CdSe and PbSe QD solids.[76, 77] In experiments carried out in an electrochemical cell, QD solids made from pyridine-capped CdSe were deposited on a pair of Pt interdigitated electrodes spaced by ~ 5 μm. Films cross-linked with 1,4-phenylene were electrochemically doped n-type, at which point the temperature was lowered, freezing the electrolyte solution below 200 K. When the cell was stored at $T < 160$ K, the doping remained stable on the time scale of days.[76]

Depending on the temperature, systems with strong Coulomb interactions can either exhibit low-field conductance with temperature dependence $\log G \propto T^{-1/2}$ or $\log G \propto T^{-1/4}$. While the crossover from Efros-Shklovskii to Mott regimes for typical amorphous materials are often on the order of 1 K, it is estimated to be much higher on the order or 400 K in CdSe[76] and 1400 K in PbSe[77] in quantum-confined systems. Yu et al. observe such behavior for CdSe below 120 K.[76] Wehrenberg et al. show ES-VRH for n-type PbSe QDs between 4.2 K and 135 K.[77]

2.1.3 Enabling New Devices

Recently, n- and p-channel transistors with PbSe QD solids treated with hydrazine have been demonstrated.[61] PbSe was chosen because narrow distributions in particle energies were achievable synthetically (distribution in $1S_h - 1S_e$ transition energies less than 40 meV), the large exchange coupling owing to the large Bohr radius of PbSe, and the low charging energy of the array owing to the very large PbSe dielectric
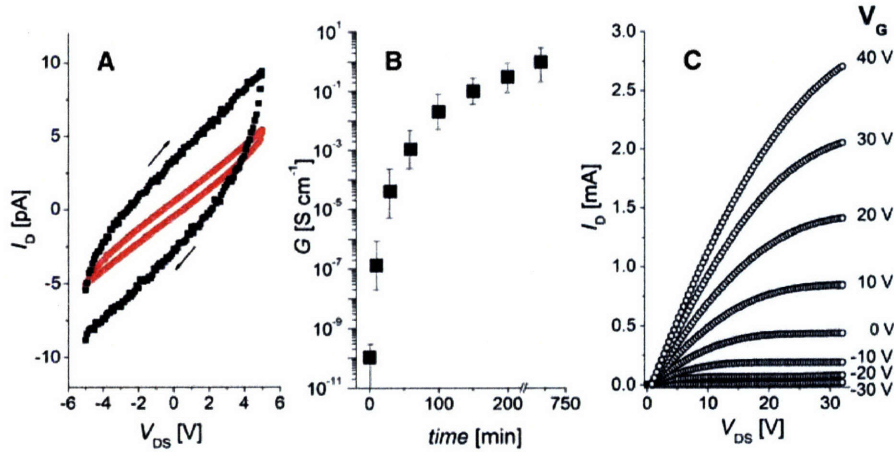
Figure 2-5: Panel A shows I_D versus V_{DS} prior to treatments. Different scan rates show some hysteresis. Panel B shows the improvement of conductance with exposure time to hydrazine. Panel C shows plot of I_D versus V_{DS} as a function of V_G. (Reproduced from Ref. [61]. ©2005 American Association for the Advancement of Science.)

constant. Care was taken to produce arrays displaying long-range order in three dimensions, confirmed with GISAXS. While nascent films had conductivities in the range of 10^{-11} S cm^{-1} and displayed no gate modulation, devices exposed to 1 M hydrazine in acetonitrile behaved as n-FETs with current modulation of over 10^3 and conductance < 1 S cm^{-1}. Figure 2-5 shows source-drain I-V characteristics before hydrazine treatment, improvement of conductance with treatment time, and a plot of I_D versus V_{DS} as a function of V_G. Heating the QD films (100 °C) or exposing them to vacuum first turns the films ambipolar and then into p-FETs. Electron microscopy and X-ray scattering showed that, as a result of the hydrazine treatment, QDs became more closely spaced (~ 1.1 nm down to ~ 0.3 nm), consistent with previous work.[48] Hydrazine treatments also been shown to dramatically increase the conductivity of PbS, PbTe, CdSe, and InP arrays.[61, 86] It should be noted that Talapin et al. also observe variable range hopping in their PbSe TFTs. Interestingly, they fit their low-field conductance to a Mott VRH model ($\nu = 1/4$), citing a much larger value (~ 250) for the dielectric constant of bulk PbSe.[61]

51

2.2 QD Photovoltaics and Photodetectors

There has been considerable interest in the incorporation of colloidal QDs and other quantum-confined semiconductor structures into photodetectors (PDs) and photovoltaics (PVs) owing to their broad spectral tunability and ease of processing. QDs made from the II-VI materials CdS, CdSe, and CdTe can be tuned in the visible, while IV-VI materials such as PbS and PbSe exhibit band-edge responses in the IR, even beyond $\lambda = 2000$ nm. Band-edge photocurrent is proportional to the QD absorption spectrum, and arrays of PDs containing QDs of slightly different sizes could enable color vision or rough spectroscopy either in the visible or near IR, though this prospect is complicated by the continuous and increasing absorption features QDs above E_g. Some theoretical analyses point out potential advantages in QD-based devices; in particular, conversion of "hot" photogenerated carriers to enhance photocurrents or photovoltages may be readily achieved in QDs in than in bulk inorganic semiconductors.[87] Nozik proposes three broad QD-PD designs that may be of interest: (1) QD arrays in *p-i-n* cells in which a thin, ordered lattice of QDs (serving the role of the intrinsic layer) exhibits miniband transport; (2) QD sensitized nanocrystalline TiO$_2$ cells, in which QDs play the role of dye in a Grätzel-like cell;[88] (3) QD/polymer matrix cells, in which QDs and polymers are dispersed together to form a bulk type-II heterojunction. The least progress has been made toward method (1), in part because of the very poor transport in QD solids that until very recently was observed. Some progress has been made toward approach (2) in the form of film photosensitization with PbS and CdSe clusters[89, 90, 91] and even colloidally grown InP QDs adsorbed onto TiO$_2$.[92] However, the most active and promising area of research has been overwhelmingly approach (3), on which we shall focus in this section of the review.

Though we do make a mild categorization of QD-PDs and QD-PVs in this review, we do not claim a strong distinction between QD-PDs and QD-PVs. In the solid-state semiconductor regime PDs are optimized for wavelength range and speed and PVs for power efficiency and spectral overlap with the solar spectrum, QD-PDs and

QD-PVs are much newer technologies and quantum efficiency is perhaps the metric most often emphasized in both. QD-PDs and QD-PVs are often made from very similar QD-polymer composites. We know of no QD devices in which photocurrent yield is constant with increasing "reverse bias," which is in general the case for solid-state p-n or p-i-n diodes. Wavelength response is at times a point of emphasis, and to our knowledge, bandwidth response has only been measured once for a QD-PD or QD-PV.[50] Generally speaking, we shall consider a device to be a QD-PD if (1) its photocurrent action spectrum arises solely from QD absorption, (2) its photocurrent action spectrum consists of the spectrally separated absorption of a polymer and QD, or (3) the device has particularly notable wavelength response characteristics. QD-PVs, then, are devices in which (1) the photocurrent action spectrum has good overlap with the solar spectrum and (2) reported measurements include fourth-quadrant metrics such as I_{sc}, V_{oc}, fill factor (FF), and power conversion efficiency eta under solar radiation.

2.2.1 QD-PVs

For over a decade, nanocrystal-polymer blends have been an active area of research in the pursuit of low-cost, flexible, efficient photovoltaic devices. In their simplest form, PVs made from a thick (100s of nm) polymer layer containing QDs doped at high weight percentage between two electrodes, usually one of which is transparent.[93] Typically, both polymer and QDs have appreciable absorption in the visible solar spectrum, and excitons are created in both. QD-polymer blends often constitute a bulk type-II heterojunction, and charge separation occurs throughout the film at QD-polymer interfaces. Subsequently, charges migrate through the two phases (holes through the polymer and electrons through the less continuous QD network) and are collected at the electrodes. These are direct analogs to the well-established MEH-PPV/C_{60} composite PVs[94] or recent bulk type-II PVs reported in the organic electronics literature.[95]

Exciton Transfer and Charge Separation

While early studies in this area focused on a system in which CdS QDs were grown in situ by exposing a Cd precursor dissolved in poly(N-vinylcarbazole) (PVK) to H_2S gas.[96, 97] Greenham et al. were the first to study the charge separation properties of CdS and CdSe QDs colloidally grown and subsequently dispersed in polymers (MEH-PPV).[98, 93] Both TOPO and pyridine capped QDs were used in MEH-PPV with varying weight percentage. Charge separation at QD/MEH-PPV interfaces occurred when the difference in electron affinities (or ionization potentials) was larger than the exciton binding energy. Some fraction of photogenerated excitons were transferred from MEH-PPV to CdSe via Förster transfer, followed by hole transfer from the QD to polymer nearby.[98] In both cases, charge transfer occurred more quickly than the polymer exciton decay rate (100 to 1000 ps) or QD exciton decay rates, which is a necessary condition for this composite to be useful for PVs. Figure 2-3 depicts three pathways through which charge can separate at a QD/polymer interface. (a) shows a $\pi - \pi^*$ transition resulting in an exciton on the polymer chain, followed by electron donation to the $1S_e$ level of a QD. (b) depicts an exciton on the polymer transferred via a Förster mechanism to the QD, followed by hole transfer to the polymer. (c) shows the same separation process as in (b), but the QD is directly excited by incident light. In all cases, it is presumed that exciton decay times are longer than charge separation times.

QD-PVs were produced with the a blend of MEH-PPV and pyridine-capped CdSe QDs sandwiched between electrodes, and external quantum efficiencies reached 12%. The authors concluded that at low wt %, increasing QD doping level improves both charge separation and transport, but at high wt %, only transport is enhanced.[98]

More extensive studies have been carried out on QD-polymer blends to probe the sensitivity of QD-polymer charge transfer on QD and polymer energy levels.[99, 100, 101] CdSe QDs of three sizes, each with different conduction and valence levels, were used in blends with MEH-PPV and two related polymers, MEH-CN-PPV and DHeO-CN-PPV. Charge transfer was observed in all systems (with the excep-
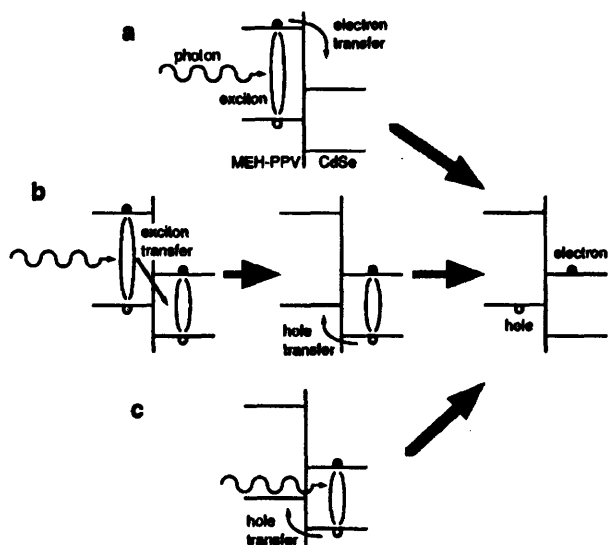
Figure 2-6: Depiction of three pathways through which charge can separate at a QD/polymer interface. (a) shows a $\pi - \pi^*$ transition resulting in an exciton on the polymer chain, followed by electron donation to the $1S_e$ level of a QD. (b) depicts an exciton on the polymer transferred via a Förster mechanism to the QD, followed by hole transfer to the polymer. (c) shows the same separation process as in (b), but the QD is directly excited by incident light. In all cases, it is presumed that exciton decay times are longer than charge separation times. (Reproduced from Ref. [98]. ©1996 American Physical Society.)

tion of blends with DHeO-CN-PPV, in which bulky alkyl groups are suspected to prevent intimate contact between QDs and polymer chains), demonstrating the generality of charge transfer in these systems. Photoinduced absorption of QD/polymer blends showed only a weak dependence on temperature above $T > 150$ K in contrast to the pure polymer, indicating the presence of polarons on polymer chains and confirming charge separation at QD/polymer interfaces.[99, 100] (Recently, excitation transfer from polymer to nanocrystals has been studied both theoretically[101] and experimentally[102] with a focus on QD/polymer-based EL devices.[103]) While charge transfer at semiconductor/polymer interfaces can be achieved through multiple pathways (Fig. 2-6), its presence is critical for devices based on QD/polymer blends.

QD-PV Devices

The first QD-PVs were based on QD/polymer composites like those discussed in 2.1.1, and reasonable results were obtained. One early QD-polymer device consisted of CdSe QDs and MEH-PPV.[98] Under AM1.5 with intensity well under one sun, power conversion efficiency was only 0.2%. At higher intensity ($50 \, \text{mW cm}^{-2}$), two PV metrics (I_{sc}, FF) deteriorated, and a sublinear photocurrent dependence on intensity indicated charge buildup in electron-percolation networks. This performance-limiting drawback of QD-PVs led researchers to consider new elongated materials for use in PVs (discussed below).

Despite their limitations, QD-PVs continue to receive attention in more exploratory work with new systems. One new system is the ZnO QD-PV developed by Beek et al. in which nontoxic ZnO particles are blended with poly(2-methoxy-5-(3',7'-dimethyloctyloxy)-1,4-phenylene vinylene) (MDMO-PPV) or P3HT.[104, 105] These ZnO QDs are prepared ligand-free using sol-gel techniques and were readily dissolved in polymer solutions. Because ZnO QDs absorb only at very blue and shorter wavelengths, most absorption of the solar spectrum is due to the polymer alone. Under AM1.5 radiation, the MDMO-PPV devices showed $V_{oc} = 814$ mV, FF = 0.59, and $\eta = 1.6\%$, which compares favorably to $\eta = 0.42\%$ for a TiO_2 QD-polymer blend QD-

PV recently reported.[106] Watt et al. have demonstrated a QD-PV device fabricated using a new synthetic method. PbS are synthesized in the presence of MEH-PPV, leading to a composite in which PbS QDs are embedded in MEH-PPV without the normal capping ligand barrier.[107] While QDs produced in this way are much less monodisperse than those created in normal colloidal syntheses, QD monodispersity is not paramount in PV systems. Single-wavelength EQE reached 1.1% and power conversion under AM1.5 illumination was 0.7%.

NR-PV Devices

Electron transport through a dispersed QD matrix was identified as a limiting factor the efficiency of QD-PVs. As a result, semiconductor nanorods (NRs) introduced as components in PV devices. NRs have one dimension (the length of the rod) over which charge can be separated within the nanoparticle. In addition, after charge has been separated at a semiconductor/polymer interface, electrons have to hop between fewer nanoparticles to be extracted from the device. The first NR-PVs contained NRs with a very modest aspect ratio (< 2) blended with MEH-PP15V.[108] EQE under ~ 0.5 mW cm^{-2} at $\lambda = 514$ nm was for these devices was 16% compared to 4% for the control made with approximately spherical QDs, and fill factor also increased substantially from 0.26[98] in previous QD-PV efforts to 0.49.[108] Further improvement was realized by using NRs with much higher aspect ratio (> 10) and length (70 nm) and through the replacement of MEH-PPV with poly-3-hexylthiophene (P3HT), in which hole mobilities can be as high as 0.1 cm^2 V^{-1} s^{-1}.[109] Longer NRs exhibited diminished solubilities but could be dispersed along with dissolved polymer in a binary pyridine/chloroform mixture. (In related work, special "electroactive surfactants"[110] and amine-functionalized P3HT variants[111] have been created to increase the solubility and mixing of NRs with P3HT chains.) NR-PVs made with longer NRs exhibited peak EQEs over 50% and AM1.5G power efficiency $\eta = 1.7$%.[112] In addition to fitting I-V characteristics to a modified Shockley equation, Huynh et al. measured shunt resistance and device metrics such as photoconductance, V_{oc}, and FF as a function of intensity.[113] The latter analysis suggested that transport within
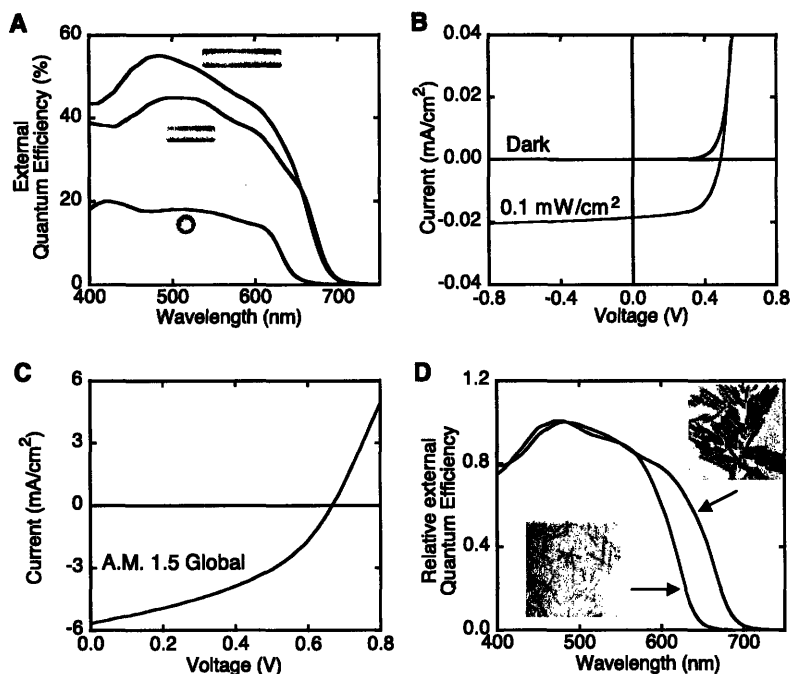
Figure 2-7: (A) Improvement of NR-QD EQE with increasing NR aspect ratio. (B) *I-V* curves for a NR-PV in the dark and under low intensity light. (C) The fourth quadrant of NR-PV under AM1.5G, showing poorer FF than in pane (B). (D) A comparison of EQE spectra for NRs of different diameters (shown in TEM micrographs, inset) showing that rods with larger diameters cover a larger portion of the spectrum. (Reproduced from Ref. [112]. ©2002 American Association for the Advancement of Science.)

the device is limited by hole mobility in the polymer phase and not electron hopping between NRs. Sublinear current dependence on intensity was explained through a combination of bimolecular recombination and photoconductivity at high charge density (the latter of which could be eased by blocking layers). Results also suggest that device thicknesses greater than 150 nm-200 nm provide no EQE benefit owing to significant increases in series resistance.[113] Figure 2-7 shows (A) the improvement of NR-PV EQE with increasing NR aspect ratio, (B) *I-V* curves for a NR-PV in the dark and under low intensity $\lambda = 514$ nm light, (C) the fourth quadrant of NR-PV under AM1.5G, and (D) a comparison of EQE spectra for NRs of different diameters (shown in TEM micrographs, inset) showing that rods with larger diameters cover a larger portion of the spectrum.

"All-inorganic" NR-PVs, containing no organic or polymer layer in their final form,

58

have also been reported. CdTe and CdSe NRs were spin-coated sequentially, giving rise to a type-II heterojunction bilayer.[114] In this design, CdTe is the hole-transport material, and the device exhibits strong rectification. After treatment with $CdCl_2$ in methanol and brief sintering at 400 °C, the photoresponse increased by two orders of magnitude, and power conversion efficiencies as high as $\eta = 2.9\%$ were observed. This is an excellent extension of the work of Schulz et al., in which CdTe thin films were created by sintering CdTe nanoparticles.[115] These all-inorganic NR-PVs, no longer containing well-defined nanocrystals, showed minimal degredation over more than 10 hours of AM1.5G exposure.[114]

New PV Strategies

One limiting factor in NR-PVs is that some appreciable fraction of NRs lie perpendicular to the direction of current flow and electron-percolation pathways hence are not optimized.[116] Two new strategies described below, the first involving new kinds of nanocrystals and the other involving new ways to produce polymers, may increase the orientation of percolation pathways. CdSe tetrapods,[117] quantum-confined structures extending in three dimensions, may provide a way to further reduce hopping events required for charge extraction. Sun et al. demonstrated a tetrapod-based PV in which CdSe tetrapods nearly 80 nm in height (made up of four branches 5 nm × 50 nm) were used in combination with the polymer OC_1C_{10}-PPV.[116, 118] Direct comparison with NR/polymer devices was made with 86 wt % nanocrystal loading, and the photocurrent response of the tetrapod device was higher by nearly a factor of two. In addition, power conversion efficiency for the tetrapod was at AM1.5, and quantum efficiency for these devices decreased less severely with an increase in incident intensity than did NR-QDs, suggesting the existence of fewer trapped electrons at "dead ends" of percolation pathways.[116]

The growth of nanometer-size polymer "brushes" from transparent electrodes is another new strategy to orient percolation channels parallel to current flow.[119] Snaith et al. demonstrate significant uptake of small (< 3 nm) CdSe QDs between poly(triphenylamine acrylate) brushes ∼ 100 nm in length grown from an ITO sub-

strate, creating a composite of swollen brushes in which the QDs-to-polymer weight ratio is 2:1. The vertically oriented polymers strands and QD-filled interstices define percolation pathways, and monochromatic EQEs is as high 20%. An open-circuit voltage of 850 mV suggest these structures warrant further investigation for PV applications.[119] An inverse fabrication approach to building a similar structure, in which CdS semiconductor wires were grown on a Ti substrate followed by spin-coating with MEH-PPV, has also been shown, but with power conversion efficiency of only 0.60%.[120]

2.2.2   Carrier Multiplication

Another potential strategy for increasing the power efficiency of QD-based photo-voltaics is though carrier multiplication (CM). In CM, the absorption of photons of energy higher than $2E_g$ give rise to more than one exciton instead of relaxing thermally to the lowest excited state. Although this effect has very low efficiency in bulk semiconductors,[87] it has recently been observed in a number of QD semiconductor materials owing to strong Coulomb interactions.[22, 23, 121, 122] When limited to one exciton per photon absorbed across the solar spectrum, the maximum power efficiency of a solar cell is $\eta = 44\%$ when $E_g = 1.1$ eV. However, if CM could be fully exploited in PVs, the upper limit in power efficiency could be as high as $\eta = 65\%$ with $E_g = 0.3$ eV.[123]

Klimov and coworkers were the first to observe carrier multiplication in PbSe through pump-probe transient absorption measurements.[22] As expected, a fast biexciton component (~ 40 ps) on top of the slow exciton decay in the band-edge bleach was induced using high pump powers (with the average number of electron-hole pairs $N_{e-h} = 1.6E_g$). However, a similar fast component with essentially the same time constant was seen at lower pump energies (average number of electron-hole pairs per QD $N_{e-h} \geq 2.9Eg$) but with photons of sufficiently high energy ($\hbar\omega \geq 2.9E_g$). These initial results were attributed to "impact ionization," an inverse Auger-like process, in which a highly excited electron with $\hbar\omega = 2E_g$ relaxes to the lowest excited level with the effect of exciting another valence electron. In this framework, the higher-than-

expected onset of CM at $2.9E_g$ rather than $2 \sim 2.0E_g$ can be explained by an even division of energy in excess of E_g between the electron and hole of the exciton.[22]

Subsequently, the observation of quantum efficiency greater than 300% with $\hbar\omega = 4E_g$ was reported along with the observation of CM in PbS.[23] Ellingson et al. offer a contrasting explanation for CM in which multiple carriers arise through a coherent evolution of a single exciton state into multiple exciton states. In this model, the ratio of dephasing rates for single-exciton and multiexciton states determines CM efficiency. Despite the expectation that there would be oscillations in the multiexciton rise times, no such behavior was observed clearly.

Most recently, CM has been observed in CdSe and with quantum efficiency as high as 700% in PbSe.[121, 123, 124] The CM threshold for CdSe was found to be $2.5E_g$ (less than the $2.9E_g$ value for PbSe), which can be attributed to the dissimilarity of electron and hole effective masses in CdSe.[121] The observation of CM in both CdSe and PbSe (materials with significantly different energy structures and carrier relaxation characteristics) along with the apparent speed of CM (50-200 fs) in comparison to the much slower Auger-like processes (100s of picoseconds), suggests that CM is a phenomenon very general to QDs and is not dependent on an Auger-like process. Schaller et al. proposed that formation of multiexciton states is instantaneous via virtual single exciton states.[124] Like the theory of Ellingson et al., this theory relies on Coulomb coupling. However, the virtual-state theory does not require Coulomb coupling to be strong relative to the dephasing rate; rather, it requires only high spectral densities of high-energy single-exciton states and multi-exciton states and not precise resonances between them. Figure 2-8 depicts (a) the timescales of different processes in the most recent understanding of CM and (b) representative data, showing the development of CM in a CdSe sample.

One caveat regarding the implementation of CM in devices is that charge separation must be faster than Auger recombination rates. Perhaps for this reason, there has yet to be widespread exploitation of this mechanism in QD-PVs, though one recent report includes possible evidence of CM in a layered MEH-PPV:PbSe QD composite photodetector.[125]
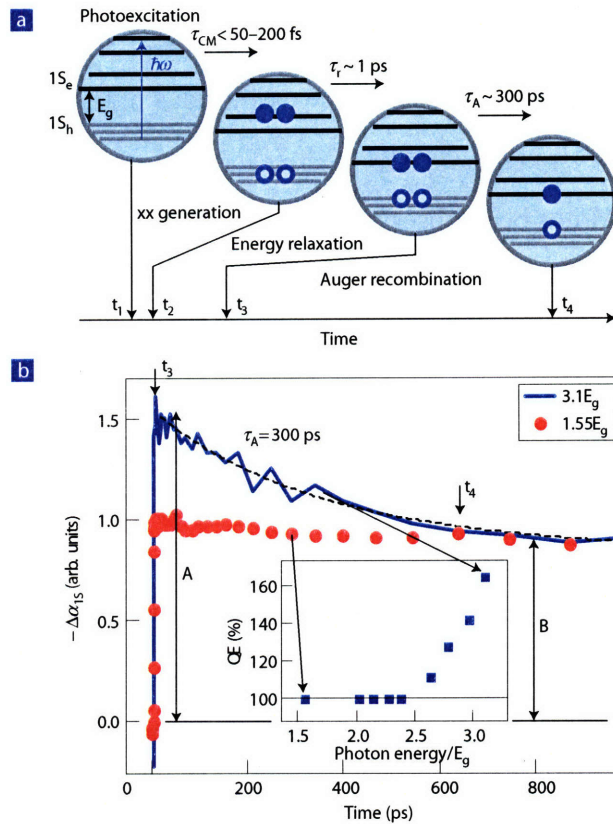
Figure 2-8: (a) Following photoexcitation, very fast CM is followed by thermal relaxation to the band edge states. Auger relaxation becomes a factor on the timescale of 100s of picoseconds. (b) Comparison of low-power absorption bleach at $1.55E_g$ and $3.1E_g$, showing the unmistakable fast component at the higher energy. Inset: The CM threshold (at which point QE begins to exceed 100%) for CdSe is shown to be $\sim 2.5E_g$ (Reproduced from Ref. [124]. ©2005 Nature Publishing Group.)

2.2.3 QD-PDs

The development of QD-PDs, as we have defined them, has been less active than for PVs because (1) the potential payoff for cheap, efficient PVs is much greater, (2) Si PDs (active in the visible spectrum) are likely impossible to eclipse with QD-PDs, and (3) QDs active beyond $\lambda = 1000$ nm, such as PbSe and PbS, are less stable than CdSe QDs.[126] Ginger et al. produced layered QD-PDs, active in the visible spectrum, of composition ITO/CdSe QD (200 nm)/X, where X = Al, Ca, and Au to study more fundamental transport physics in 3D QD solids. While these devices showed PC action spectra that closely mirrored QD absorption and showed zero-bias quantum efficiency of ~ 2 to 3% at the band edge, device exhibited poor transport and persistent photoconductivity. More recently, a similar device, ITO/PEDOT:PSS/CdSe QD (200 nm)/Ag was produced with an n-butylamine treated CdSe layer, which showed a similar spectral response in the visible ($\lambda = 550$ nm). These detectors exhibited a 3dB frequency bandwidth of 50 kHz,[50] which compares favorably to slower reponse times inferred from reports of previous work.[60, 127]

QD-PDs active in the IR have attracted considerable interest, in part owing to the suitability of PbS and PbSe for the $\lambda = 1.3$ μm and $\lambda = 1.55$ μm communication bandwidths. McDonald et al. first showed PbS-polymer composite QD-PDs (ITO/PPV/MEH-PPV: PbS QD/Mg) with band-edge responses ranging from $\lambda = 950$ to 1350 nm.[127, 128] In similar devices, the surface-passivating ligands on PbS have been exchanged from oleate groups (18-carbon chains) to octylamine ligands (8-carbon chains) prior to mixing with polymer. This processing strategy has improved device performance substantially over similar previous devices, with EQE values reported to have increased a factor of 600 to 0.15% with monochromatic excitation near the band edge. In the most recent device in this series, a device of structure ITO/PEDOT:PSS/P3OT/PbS QD (200 nm)/Al was produced (P3OT = poly-3-octylthiophene). In this device, PbS QDs were ligand-exchanged with n-butyamine prior to casting (a process very similar in effect to chemical treatments after casting), and EQE values of nearly 0.5% were reported at $\lambda = 1260$ nm.[71] This

is the first (and to our knowledge, only) example of an IR-active QD-PD in which the active layer is a QD solid rather than a QD-polymer blend. Recently, QD-PDs based on a blend of PbSe QDs (capable of being tuned to even longer wavelengths than PbSe) in PVK have been demonstrated, with spectral responses at $\lambda = 1500$ nm and efficiencies similar to devices made with MEH-PPV-PbS QD blends.[129, 130]

Chapter 3

Photodetectors Based on Treated CdSe QD Films

The chapter reports the development of a layered QD-PD architecture containing CdSe QDs. While development is done in the visible region, the goal of this work is to produce a platform that can be used with a variety of QD materials to produce QD-PDs active in a range of spectral regions. Because of the small absorption efficiency of a QD monolayer at the absorption band edge ($\eta_{abs} \approx 0.01$ [45]) [Figure 1-9(c)], it was clear that a qualitatively thicker layer of QDs would be required to achieve appreciable η_{eqe}. Solution-phase chemical annealing (see § 2.1 and § 3.1), developed during the last five years, has been shown to greatly improve conductivity in QD solids,[49, 48] and this was our method of choice for realizing reasonable absorption efficiencies without making devices prohibitively resistive. (A previous study demonstrated simple, thick film QD-PDs, but performance was hindered by high trap density.[60])

Though QD-containing photovoltaics based on bulk type-II heterojunctions have been demonstrated with some success,[108] our strategy differs for a number of reasons: (1) our primary interest is photodetection, for which device response spectra that mirror QD excitation manifolds are most desirable; (2) QD-polymer blend devices are already well developed for CdSe QDs (active in the visible); and (3) while QD-polymer type-II heterojunctions work well for QDs with band gaps similar to those of most polymers, it is not obvious (and indeed perhaps not likely) that this
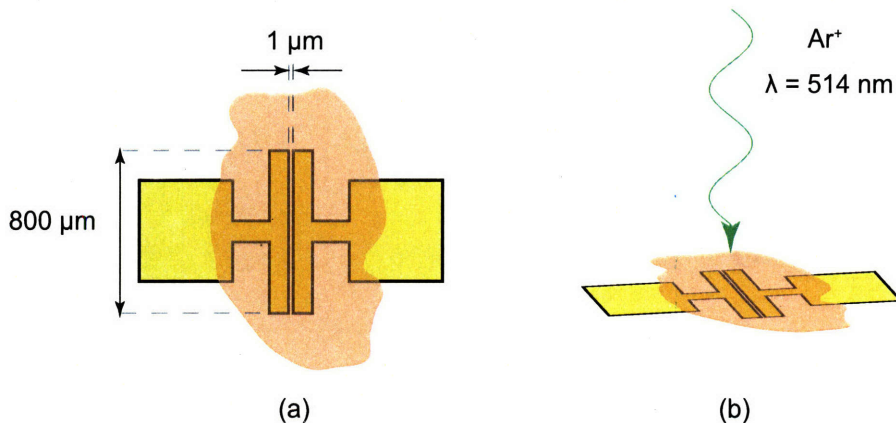
Figure 3-1: Top-down (a) and 3D (b) views of the transverse channel geometry used extensively for fundamental QD studies. After being wired to a DIP chip carrier, QD solids are drop cast from 9:1 hexane:octane, filling the 100-nm deep channel between electrodes with glassy QD solid. Device area is 800 μm^2.

mechanism will work with IR-active QDs with much smaller band gaps.

Thus, we set out to make a fairly direct transformation from the transverse channel geometry to a layered geometry, with an obvious difference being an increase in device area by $> 10^3$. The following sections describe the construction and characterization of such a device.

3.1 Solution-Phase Chemical Annealing

Considerable work has been done with the goal of improving the transport properties of QD solids, and these efforts are discussed in some depth in § 2.1. In this brief section, we discuss only the consequences of post-deposition treatment of CdSe QD solids with acetonitrile containing 0.1-M n-butylamine, which proved to be the most effective treatment procedure in Ref. [48]

In general, current-voltage characteristics measured for nascent CdSe QD solids as shown in Fig. 3-1 display exponential-like behavior for all voltages, similar to the plot corresponding to the region marked (i) in Fig. 3-2. This behavior is consistent with inefficient exciton dissociation ($\eta_d < 1$). However, after treatment with n-butylamine, the shape of I-V curves is qualitatively different, and this behavior is primarily at-

66
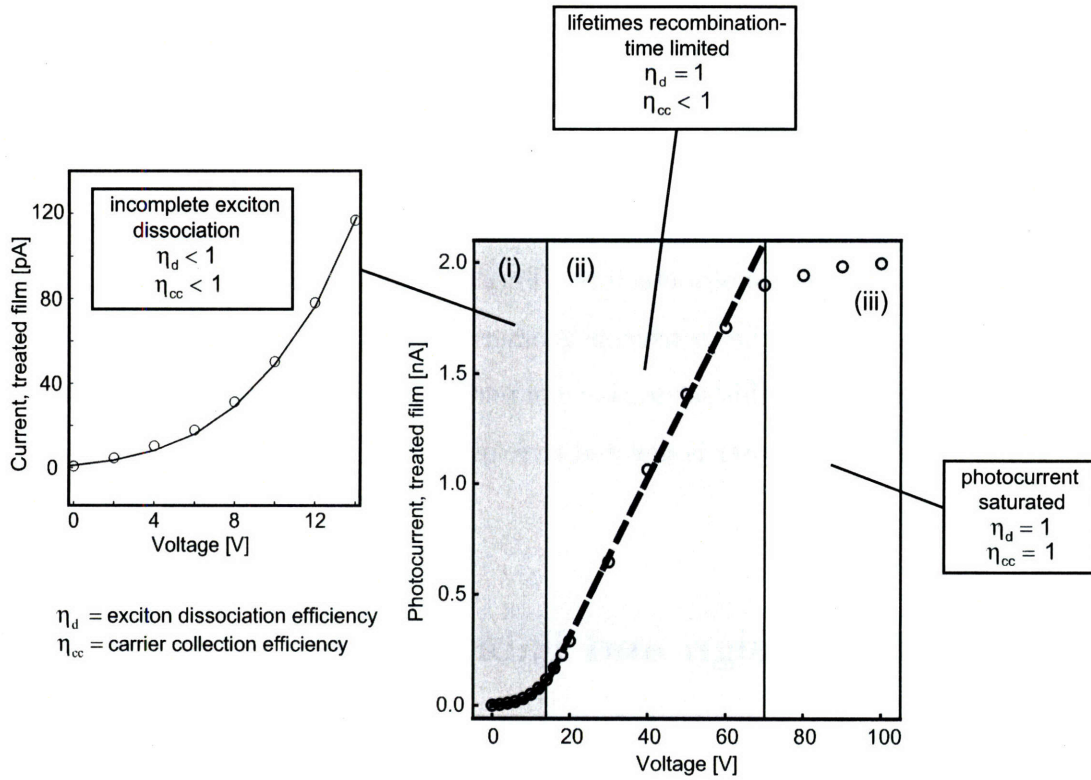
Figure 3-2: Current-voltage characteristics of n-butylamine-treated CdSe QD solids, measured in the transverse channel geometry.[131] In region (i), I-V characteristics are identical in shape to what is everywhere observed in I-V characteristics of nascent films ($\eta_d < 1$). A linear current-voltage relationship is present in region (ii), consistent with unity exciton dissociation efficiency but recombination-time-limited carrier lifetimes (charge-collection efficiency $\eta_{cc} < 1$). At $|V| > 70$ V (iii), current saturation is observed, which corresponds to unity internal quantum efficiency η_{iqe} in which carrier lifetimes are transit-time limited. Adapted from Ref. [48].

tributed to the significant reduction in core-to-core spacing between individual QDs in the solid.[48] As Fig. 3-2 shows, three distinct qualitative regimes become evident in the treated solids over the same voltage range in which regime (i) completely dominated prior to treatment. For small applied voltages, η_d is still less than unity, and the same exponential-like shape is observed. However, at moderate voltages (ii), a linear regime emerges, interpreted as unity exciton dissociation efficiency η_d, but with charge collection efficiency $\eta_{cc} < 1$, indicative of lifetimes being recombination-time limited. At still higher applied voltage, regime (iii) emerges, in which current saturation is observed. Here, both η_d and η_{cc} are unity. However, $\eta_{iqe} = \eta_d \eta_{cc}$, so in this

regime, unity internal quantum efficiency η_{iqe} is, in fact, observed.

This result is significant. The observation of unity quantum efficiency in the transverse channel geometry suggests that, unlike highly resistive nascent CdSe QD solids in which $eta_d \ll 1$, treated QD solids are a sensible material to consider incorporating in layered photodetectors. Furthermore, the fields at which current saturation is observed in the transverse geometry correspond to ~ 10 V in a layered structure, indicating that this saturation can perhaps be achieved at sensible voltages. The remainder of this chapter is devoted to exploiting this material in a new, layered geometry.

3.2 Device Design and Fabrication

Choices in materials and deposition techniques were strongly influenced by conventions in the Bulović Group and by practical constraints. The final device structure developed is written in shorthand as glass/ITO/PEDOT:PSS/CdSe QD/Ag, where slashes separate successively deposited layers, read from left to right.

3.2.1 Choice and Deposition of Layers

Glass/ITO. Layered optoelectronic device structures require at least one transparent electrode (to allow light coupling into or out of the device), and glass coated with indium-tin oxide (ITO) is widely used to meet this requirement in the visible spectrum. In general, we purchased ITO glass on which ITO (115 nm) had already been sputtered, with sheet resistance of 55 Ω/square. The ITO was patterned as needed using a photolithography procedure and then cleaned, as described elsewhere.[132] Immediately before further use, substrates were subjected to UV-ozone treatment for 5 min.[1]

PEDOT:PSS. The water-based polymer suspension of poly-3,4-ethylenedioxy-thiophene doped with polystyrene sulfonate (PEDOT:PSS) was deposited on the

---

[1]This final cleaning step has since been superseded in the LOOE (Laboratory of Organic Optics and Electronics) by exposure to oxygen plasma for 5 min, which is thought to be far more effective.
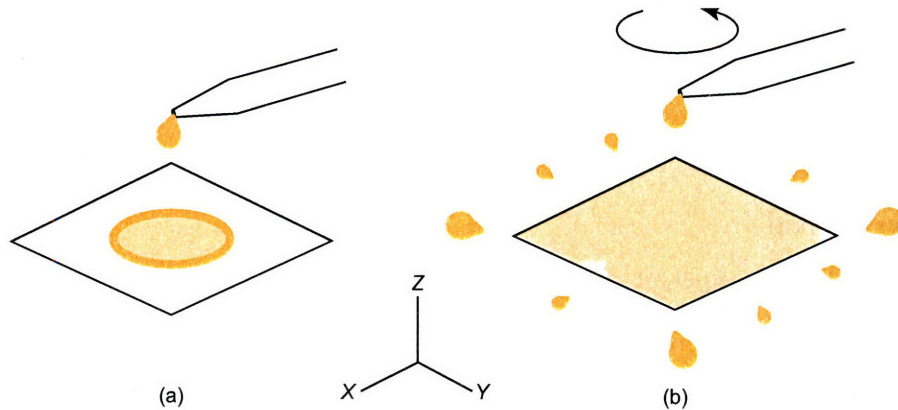
Figure 3-3: Two common methods for depositing spin-cast films. Panel (a) shows drop casting, in which there is minimal waste but limited control and anisotropy in the XY plane. Panel (b) shows spin-casting, in which one achieves uniformity in the XY plane but at the expense of a great deal of material ($> 99\%$ wasted).

glass/ITO substrate via spin casting. The reasons for doing this were threefold: (1) PEDOT:PSS coatings planarize the ITO electrode; (2) PEDOT:PSS increases the work function of the ITO electrode from ~ 4.7 eV to ~ 5.2 eV;[133] (3) PEDOT:PSS appears to facilitate better wetting of the QD layers spun from organic solvents. PEDOT:PSS (Baytron P VP AI 4083) was used as purchased and was spin-cast onto a glass/ITO substrate (3 000 RPM, 10 000 RPM/s) after filtration through a 0.45-μm PVDF syringe filter. Baking at 110 °C cross-linked the PEDOT:PSS layer.[2] This procedure resulted in PEDOT:PSS films 40 nm in thickness, as shown in the inset profile in Fig. 3-4. Glass/ITO/PEDOT:PSS substrates were then introduced into a nitrogen environment, and all subsequent fabrication steps were done either in nitrogen or vacuum.

CdSe QD deposition. At the time that we began this project, the two developed methods for depositing close-packed films of QDs were drop casting and spin casting. Drop casting, used in the preparation of transverse channel devices, has the advantages of simplicity and limited material consumption. However, the thickness of a drop-cast film is highly non-uniform, often exhibiting a thick ring around the edge.[3] Spin casting, in which over 99% of the QDs are thrown off the substrate as

[2]This procedure has since been superseded by one employing low-resistance Baytron P VP CH 8000, which is spin-cast (4 000 RPM, 1 000 RPM/s) and then baked (120 °C, 15 min).

[3]As in a coffee stain.

waste, provides added control and isotropy in the XY plane of the device but at the expense of very high material consumption. However, because lateral uniformity is important in layered structures, we chose to use the much more wasteful spin-coating deposition method.

Following an established QD synthesis and processing protocol (Appendix A), a concentrated solution of CdSe QDs in chloroform was prepared. (QDs were not overcoated because the higher-band-gap shell layer in core-shell structures increases the distance through which charge must tunnel to move from one QD core to a neighbor, which was thought to decrease the QD film conductivity.[4]) This solution was then filtered through a 20-nm filter and spin-cast air-free (using a spin-coater inside a glove box). The spin coater was always set to 3 000 RPM with 10 000 RPM/s acceleration. Choice of solvent proved to be critical to the successful creation of high-quality QD films. Figure 3-5 shows optical microscope images of QD films spin-cast from hexane and chloroform. The hexane film exhibits pinholes that compromise layered structures of our design. Other solvents, including hexane:octane (9:1) and toluene led to similarly poor films. Films spin-cast from chloroform were often of sufficient quality.

More recently, stamping[134] and ink-jet printing have been developed as methods for deposition of close-packed films of QDs. Stamping, typically using a PDMS stamp coated with parylene-C, has been used primarily for depositing a monolayer of QDs in at the interface of electron- and hole-transport layers in QD-LEDs. Stamping is not particularly appealing for QD-PDs (employing thick films) for two reasons: (1) stamping a thick film (tens of "monolayers") often leads to a cracked or smeared film, (2) stamping still involves a spin-coating step(s), and hence does not avoid the wasteful spin-coating process. One possible variant of the stamping method would be a sequential stamping approach in which many (10-20) thin layers of QDs are stamped, perhaps separated by treatment steps. Though this method would represent no material savings, an added advantage might be increased device yield—pinholes in indi-

---

[4]More recently, interest in studying conductivity through close-packed solids of overcoated QDs has returned, and it appears that conductivity in overcoated QDs is *not* impeded by the shell of larger band gap, so long as the shell is not to thick and not cracked.
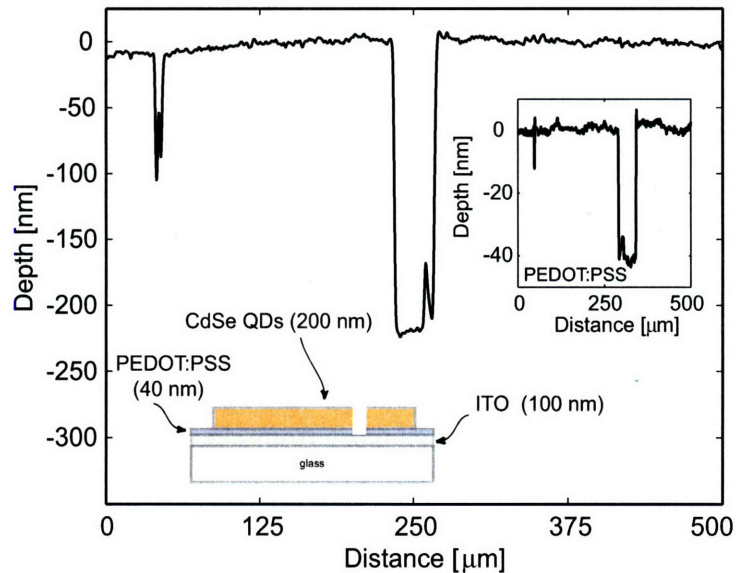
Figure 3-4: Profile of scratch in glass/ITO/PEDOT:PSS/CdSe QD structure, showing total depth of 220 nm. Inset profile shows PEDOT:PSS layer alone to have a depth of 40 nm.

vidual layers would rarely be aligned throughout the device, preventing catastrophic shorting.

Ink-jet printing of QDs has recently been made easy through a collaboration between the LOOE and a major ink-jet printer manufacturer that has developed a more research-friendly print-head platform. The print head has since been interfaced with an XYZ stage for programmable delivery. This technique makes possible very direct delivery of QDs in small volumes (~ 2 to 80 pL) with resolution of ~ 25 μm. Using this technology, it would be possible to print layer after layer of QDs (again, perhaps chemically treating in between depositions) with a minimal amount of wasted QD material. The primary drawback is that the preparation of a single device substrate would take many hours (in comparison to the one-minute spin routine currently employed to produce a spin-cast film).

Treatment with *n*-butylamine. Immediately following spin casting, films were treated with ~ 0.1 M *n*-butylamine in acetonitrile. Entire glass/ITO/PEDOT:PSS/-CdSe QD structures were submerged vertically, and care was taken not to scratch the
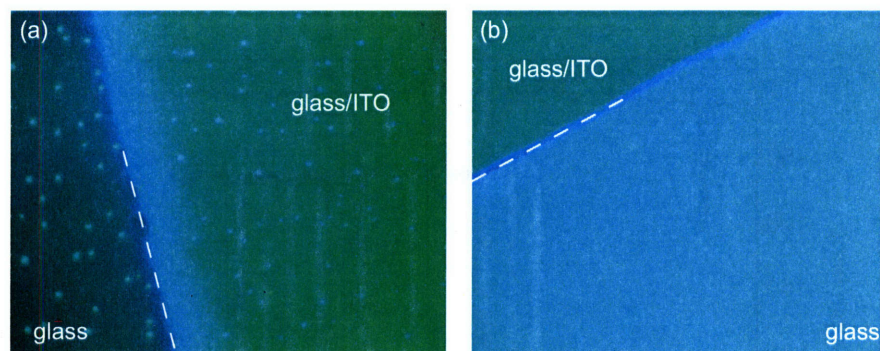
Figure 3-5: Optical microscopy of close-packed CdSe film on patterned glass/ITO substrates deposited via spin-casting . A CdSe QD film spin-cast from hexane exhibits pinholes (a) while a corresponding film spin-cast from chloroform (b) is free of such defects. Dotted lines indicate the edge of the ITO under the film.

QD films. After exposure for 10 minutes, the substrates were rinsed with acetonitrile and baked for 1 hr at 70 °C, a temperature at which solvent is expelled but organic caps are understood to be unaffected.[48] A decrease in mean interparticle spacing, measured by glancing-angle X-ray scattering (GAXS), from 1.1 nm to less than 0.5 nm as a result of this treatment has been reported.[48]

CdSe QD films were made noticeably more mechanically robust by this chemical treatment. While the height of nascent CdSe QD films could not be measured using profilometry (the stylus, even at the lightest weight, gouged the film), treated films were reproducibly measured using a KLA/Tencor P10 profilometer, as shown in Fig. 3-4, in which the height of the film after treatment was found to be nearly 200 nm.[5]

Top Ag electrode. Silver was the material of choice for the top electrode for both practical and functional reasons. Low-work-function materials such as Mg, Ca, or Li are often used in OLEDs or QD-LEDs,[31] where cathodes must be capable of electron-injection. In general, such behavior is not needed in a charge extraction device, though at least one example using these low-work-function materials does exist in the literature.[60] Au offers a large work function and good stability in air during testing, but evaporation of gold requires current levels in excess of the safe range of the LOOE thermal evaporator. Ag was hence a good choice in terms of

---

[5]We found that films significantly thinner than 200 nm often contained pinholes. Films thicker than 200 nm would likely lower the IQE and the 3-dB frequency for our device, and films significantly thicker than 200 nm would likely exhibit cracking.

stability and work function offset (~ 1 eV) with PEDOT.

The top Ag electrode was evaporated in the LOOE integrated materials deposition system (described extensively in [135]), which allows for introduction into the evaporator without exposure to air. Dynamic vacuum ($< 5 \times 10^{-6}$) Torr was maintained during evaporation, in which a 600 Å layer of Ag was deposited at a rate of ~ 2 Å/s. After evaporation, devices were stored in a nitrogen environment until testing. With all equipment and chemistry working properly, the yield of individual device pixels was $\lesssim 50\%$.

3.2.2 Patterning

While the previous section outlined construction of the device in the Z direction of the device, this section summarizes how various layers were patterned in the XY plane. Ten well-defined device areas on a 0.495" $\times$ 0.495" substrate were defined by patterning both the ITO and Ag layers, as shown in Fig. 3-6(a). The ITO pattern was defined photolithographically and the Ag with a shadow mask during evaporation,[135] and the resulting pixels were 1.22 mm^2 in area.[132]

In addition to defining ten device pixels, these masks also provide 12 spots near the edge of the substrate (three on each side) for electrical contact. Two contact the ITO "bus" directly, while the other ten each connect to a distinct pixel. These ten pads were aligned with ITO islands underneath. During device fabrication, the QD film was purposely compromised on top of these ITO pads to allow direct Ag-ITO contact, providing a more robust edge contact pads [inset to Fig. 3-6(a)]. A "measurement block" machined from delrin was fashioned to both hold and electrically contact the device substrate simultaneously. This block, depicted in Fig. 3-6(b), facilitated consistency and ease in the device measurements discussed in 3.3.

3.2.3 Energy Structure

Figure 3-7 shows the proposed energy-level diagram of our QD-PDs. Though the position of the ionization potential and electron affinity for CdSe QDs relative to vac-

contact point for
Au pin held in
measurement block

isolated ITO pad
for better pin contact

Ag top
electrode

ITO bus

1/2"

■ ITO - sputtered and etched
■ QDs - spun
■ Ag - evaporated

final device area 1.22 mm^2

(a)

3"

1.5"

(b)
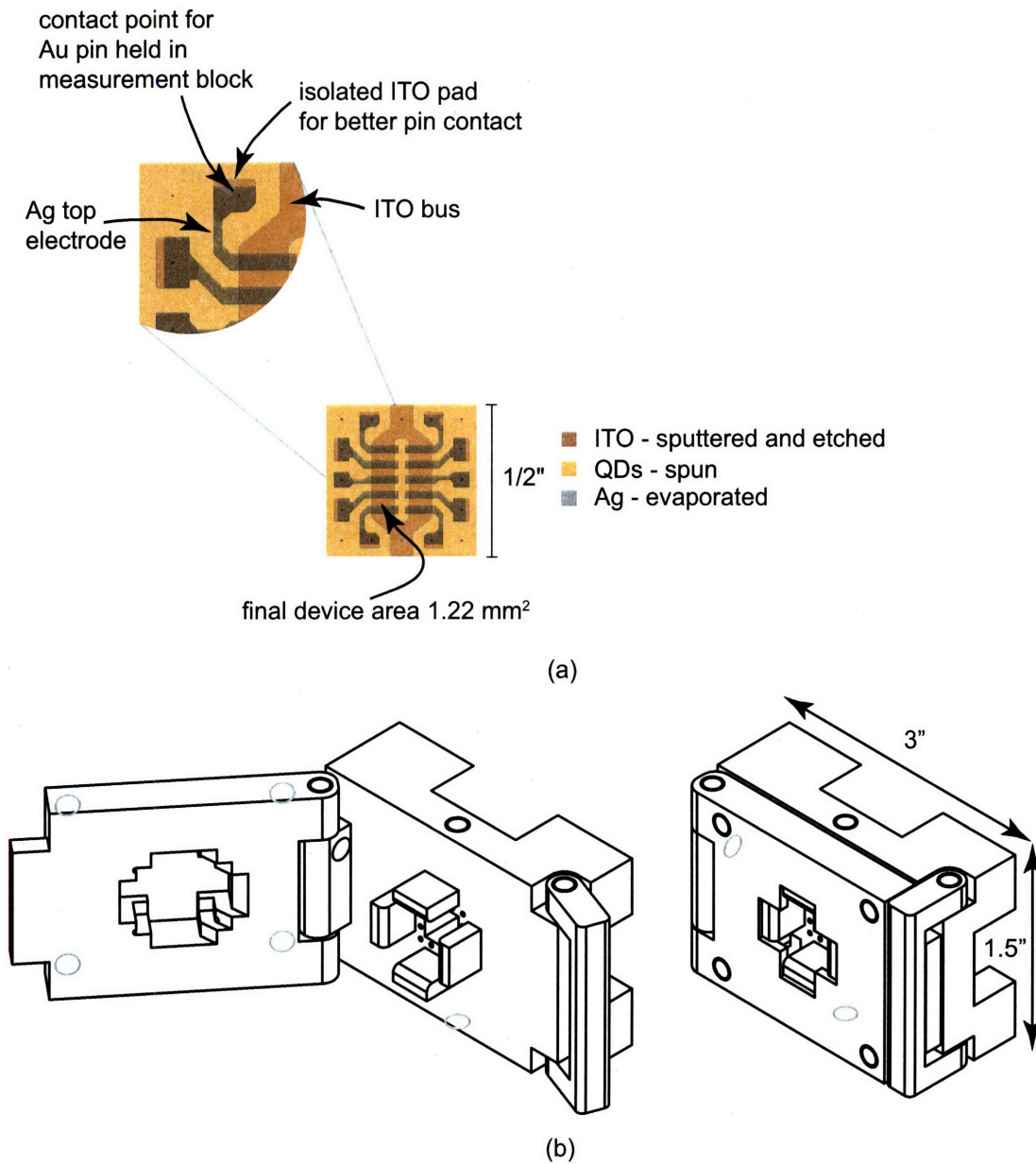
Figure 3-6: QD-PD pattern and device measurement block. Panel (a) depicts a top-down view of QD-PD substrate, with inset showing in detail electrode overlap. Panel (b) shows the delrin device measurement block in its open and closed positions.
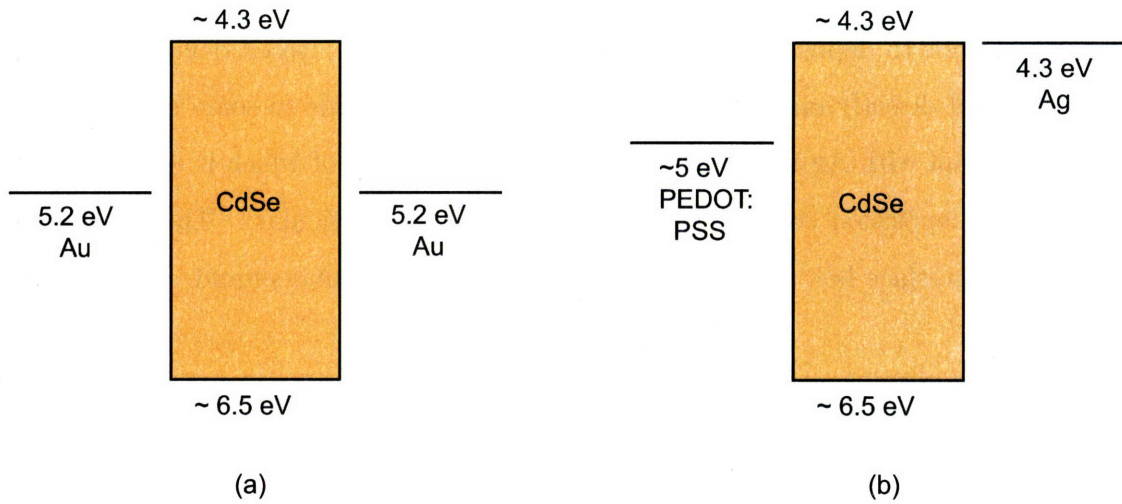
Figure 3-7: Energy structures for transverse and layered structures. Panel (a) depicts the proposed energy-level structure for the transverse channel device, with symmetric noninjecting Au contacts. The proposed energy-level structure of the layered QD-PD is shown in (b), with asymmetric electrodes, separated by ~ 0.7 eV.

uum has not previously been measured, the theoretically predicted electron affinity is likely near 4.3 eV,[136] close to the work function of the Ag electrode. The work function of the PEDOT:PSS-coated ITO electrode is significantly larger at ~ 5 eV,[133]. (Not depicted in Fig. 3-7 are the aliphatic ligands of large band gap that stabilize the surface of each QD but through which photogenerated charge must tunnel.)

While the essential electrode/QD/electrode design of the transverse channel geometry was preserved in our layered structure, our electrode materials and the nature of the interfaces is much changed. Figure 3-7(a) shows the energy structure of the transverse channel geometry. The Au electrodes are symmetric and both lie well below the CdSe valence band, making them blocking contacts. This has led to the observation of primary photocurrent only in this structure and limits internal quantum efficiency to $\eta_{iqe} \leq 100\%$.[48] In contrast, the layered device [Fig. 3-7(b)] has asymmetric electrodes, one of which (Ag) is expected to lie very close to the CdSe valence level. The asymmetry is expected to give rise to a built in field (photovoltaic behavior) and the alignment may allow for the observation of secondary photoconductivity (recently observed for CdTe QD solids in the channel geometry[70]).

The interfaces are somewhat simple in the channel geometry in which all metal is

deposited prior to deposition of the QDs. However, in the layered device, "hot" Ag is evaporated directly onto the CdSe QDs, which likely leads to some impregnation of the QD film with Ag nanoparticles, an effect the extent of which is dependent on the precise deposition conditions (the growth rate, in particular). This makes the QD/metal interface less reproducible and more difficult to understand.

3.3 Characterization of QD-PDs

When characterizing exploratory photodetectors, the specific application of which is not defined, there is no single set of device metrics which stands out as appropriate. Further, metrics reported in the literature for organic photodetectors or even QD-containing devices vary broadly (Chapter 2), providing limited guidance. However, there are four general areas of performance, somewhat fundamental, that will go a long way toward characterizing any potential photodetector:

- **Spectral response.** Over what spectral range do incident photons give rise to photocurrent? Does this pattern mirror the absorption of the constituent QDs?

- **Quantum efficiency.** How many electrons of photocurrent are collected per incident photon?

- **Bandwidth.** How quickly can incident light be modulated without appreciable decrease in output signal?

- **Detection limit.** How small can input intensity be and still be detected with sufficient certainty?

In this section, we evaluate these and other metrics.

While most QD photoconductivity studies in the channel geometry have been performed at 77 K, all measurements of these QD-PDs were done at room temperature. We discovered early on that, consistent with what was observed in the test geometry, photoconductivity in QD solids treated with n-butylamine was much less temperature-dependent than in nascent films, presumably owing to the decrease in

k_{nr} and increase in k_F effected by the treatment. Room-temperature testing was chosen because it is much easier to facilitate experimentally and is representative of most real-world operating conditions. Devices were tested in air, but they were stored in a nitrogen environment between fabrication and characterization. Testing usually occurred within a day of fabrication, and all measurements employed the measurement block described in § 3.2. We have not performed long-term stability studies of these devices, though experience has shown that the device lifetime in air is less than one week is similarly short in a nitrogen environment after some transient exposure to air.

3.3.1 Quantum Efficiency

Photocurrent excitation spectrum. External quantum efficiency (EQE), $\eta_{eqe}(\lambda)$, for QD-PDs was measured using a lock-in amplifier, a calibrated silicon photodetector, and wavelength-scanned monochromatic light generated by a Xe lamp and monochromator, as shown in Fig. 3-8(a).

Figure 3-9 shows agreement between the $\eta_{eqe}(\lambda)$ and the absorbance spectrum of constituent QDs in hexane, suggesting that the entirety of the photoresponse is from excitation of the QDs and subsequent exciton dissociation. At zero bias, the EQE is 0.13% at $\lambda = 560$ nm and more than 0.20% on the high-energy side of the band edge. Possible reasons for the relative decrease in η_{eqe} at higher photon energies include absorption from the PEDOT:PSS layer and more efficient nonradiative exciton decay within the QD film. Figure 3-10 shows photocurrent spectra under nonzero bias, recorded as shown in Fig. 3-8(b). Care was taken to ground only the lock-in so as not to create a ground loop. Biases as large as -6 V were applied, resulting in an EQE of 15% at $\lambda = 560$ nm. Some device instability is evident between $\lambda = 425$ nm and $\lambda = 475$ nm in the photocurrent spectrum taken at -6 V.

Internal quantum efficiency calculation. In order to calculate device internal quantum efficiency (IQE), absorption of the film was measured. Because of the likelihood of cavity effects and reflection off the Ag electrodes, this was more accurately done in situ than using a stand-alone QD film cast on a glass/ITO/PEDOT:PSS
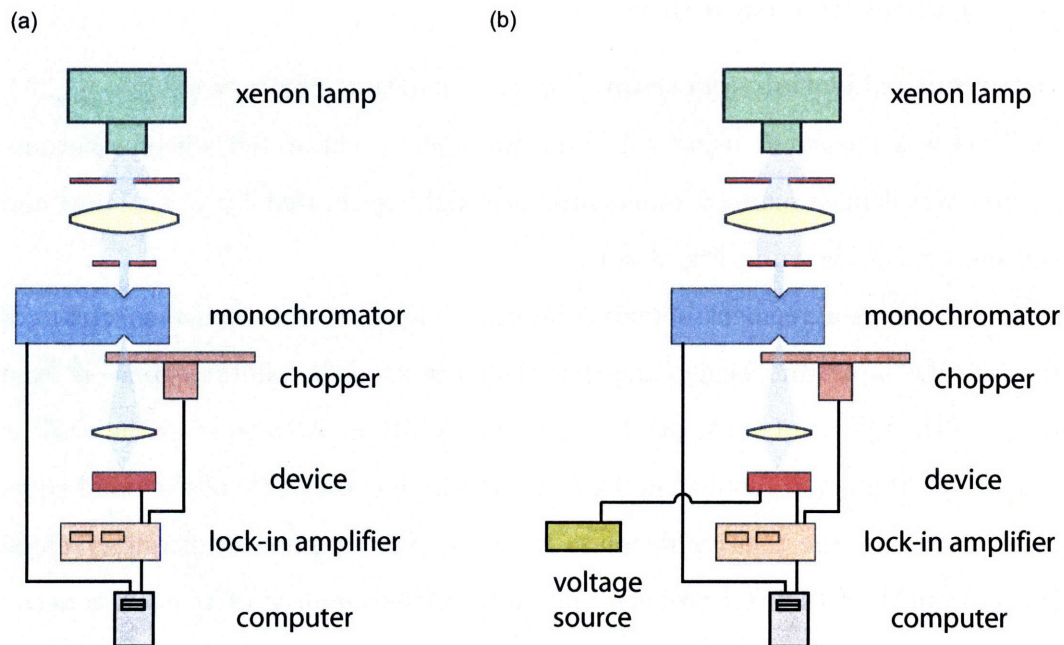
Figure 3-8: Setups for zero-bias and biased EQE measurements. Panel (a) shows the zero-bias measurement setup, with Xe lamp, monochromator, chopper, and lock-in being key elements. In panel (b), a voltage source was added to allow $\eta_{\mathrm{eqe}}(\lambda)$ to be measured at nonzero bias. Care was taken to avoid the creation of a ground loop.
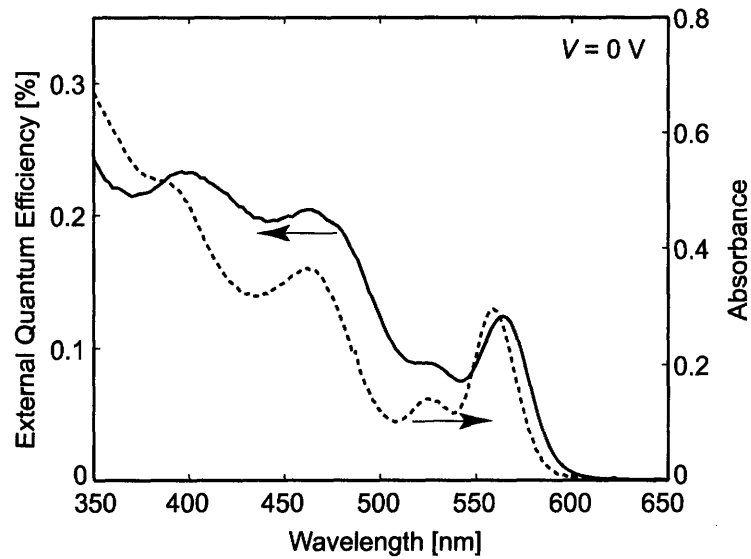
Figure 3-9: Plot of the external quantum efficiency (solid line) of a QD-PD at $V = 0$ V as a function of wavelength and the absorbance spectrum (dashed line) of the constituent QDs in hexane.
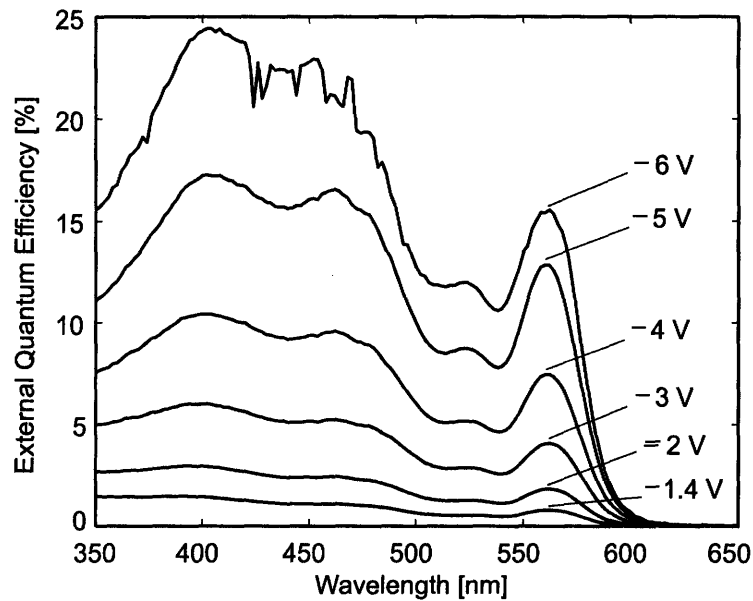
Figure 3-10: EQE spectrum of a QD-PD with different biases applied to the Ag electrode relative to ITO.

79

	η_{iqe} [%]	$\eta_{\text{eqe}}(\lambda = 560 \text{ nm})$ [%]
$V = 0$ V	0.6 ± 0.1	0.13
$V = -6$ V	70 ± 10	15

Table 3.1: Comparison of η_{iqe} and η_{eqe} at voltage extremes for CdSe QD-PD.

substrate. Using a calibrated silicon photodetector, light transmission and reflection from the device were measured. Using $A = 1 - T - R$, the percent device absorption as a function of wavelength was computed, shown by the solid line in Fig. 3-11(a). While the spectrum is not ideal, $\eta_{\text{eqe}} \sim 20\%$ at the band edge, which allows us to calculate internal quantum efficiencies in Table 3.1 [by taking the ratio of the bottom two traces in Fig. 3-11(b)]. Note that while η_{eqe} is strongly dependent on both incident wavelength and applied voltage, η_{iqe} [Fig. 3-11(c)] is roughly independent of wavelength and dependent on voltage only.

3.3.2   *I-V* Characteristics and Device Stability

Current-voltage characteristics and time-dependent photocurrents were recorded with a semiconductor parameter analyzer (Agilent 4156c), monochromatic laser source (Ar^+, $\lambda = 514$ nm line) and neutral density filter wheel used for attenuation. Two of the four independent source-measure units (SMUs) available on the parameter analyzer were used (one held at ground, the other swept in voltage). An alternative arrangement would have been to use only one of the SMUs available. Triaxial cable with inner ground sheath floating was connected to unshielded leads (several inches in length) that were clipped to the contact pin leads of the measurement block.[6] No effort was made to minimize external noise in this setup.

Figure 3-12 shows the photocurrent stability of the device at zero bias over a two-minute span. After 10 s, the device was exposed to 110 mW cm^{-2} illumination at $\lambda = 514$ nm. The photoresponse shows good stability, with charging effects modulating the magnitude of the current response within $\pm 5\%$.

---

[6]Trompeter Electronics triaxial-to-coaxial adapters ADBJ77-E2-PL20 were used to facilitate this. Using other adapters may create a floating outer sheath on the triaxial side and the buildup of dangerously high capacitive charge.
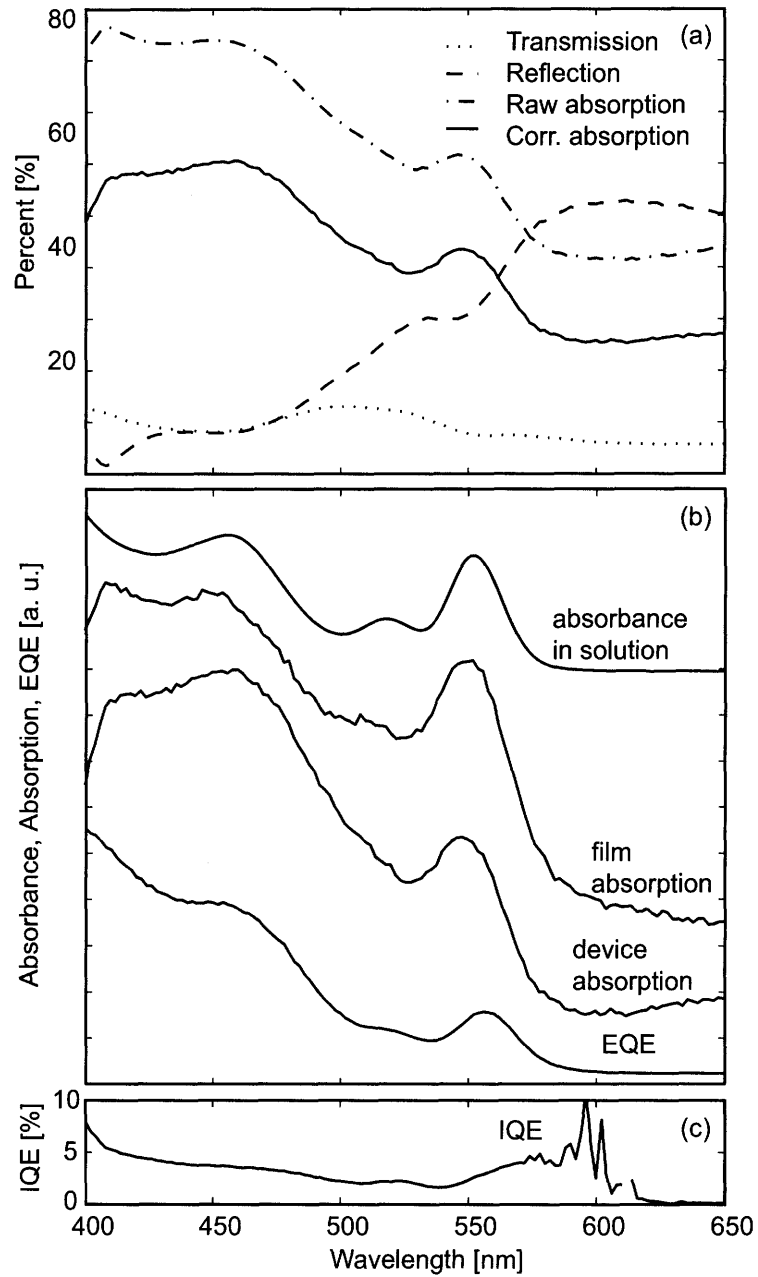
Figure 3-11: Measurement of in situ absorption η_{abs} of QD-PD. Panel (a) shows transmission, reflectance, and the resulting raw and corrected (based on "blank" device) spectra. Panel (b) compares in situ device absorption with absorbance of the same QDs in solution, the absorption of a film on glass, and $\eta_{eqe}(\lambda)$ for the device. The calculated η_{iqe} is shown in (c) and is not strongly dependent on wavelength.

Typical I-V characteristics in the dark (dashed line) and under illumination (solid line) are shown in the inset to Fig. 3-12, where the voltage on the abscissa corresponds to the voltage applied to the Ag electrode with respect to the ground ITO electrode. Devices typically experienced irreversible breakdown when the applied bias exceeded the range of -6 V to 1 V. While hysteresis independent of the rate of voltage sweep was observed under illumination (with the larger V_{oc} seen with the upward voltage sweep), there was appreciable photocurrent in steady-state operation at $V = 0$ V. The photocurrent to dark current ratio, I_{photo}/I_{dark}, is $\sim 10^2$ and reaches a maximum of 6×10^3 at $V = 0$ V. The I_{photo}/I_{dark} maximum is due to the very low dark current level at $V = 0$ V.

Figure 3-13 shows a linear-linear plot of the photocurrent voltage shown in the inset of Fig. 3-12. Unlike the experiments done in the transverse geometry, no "saturation" ($\eta_d = 1$, $\eta_{cc} = 1$) is observed, and it even appears that no "linear" region ($\eta_d = 1$, $\eta_{cc} < 1$) is present. As voltage is made more negative, photocurrent continues to increase at an increasing rate. Consistent with the energy-level structure shown in Fig. 3-7, it appears that charge injection could be playing a role (secondary photoconductivity). Further evidence of this might be the two subtle kinks (marked with asterisks) at approximately -1 V and -2.5 V, which could correspond to the onset of first electron and then hole injection. While the former is reasonable, the inset at the upper left shows the rather large (~ 1.5 eV) barrier injected holes would have to overcome.

3.3.3 Intensity Dependence of Photocurrent

Systematic study of the dependence of device response on excitation intensity is seldom reported in the literature, and for this reason, such studies were not a focus of our QD-PD characterizations. However, some intensity vs. photocurrent data were recorded by adjusting a neutral density filter wheel over two orders of magnitude while recording I-V curves described above. This provided us with three-dimensional current density vs. applied voltage vs. excitation intensity data.

Bimolecular carrier dynamics. Jarosz et al. observed bimolecular transport
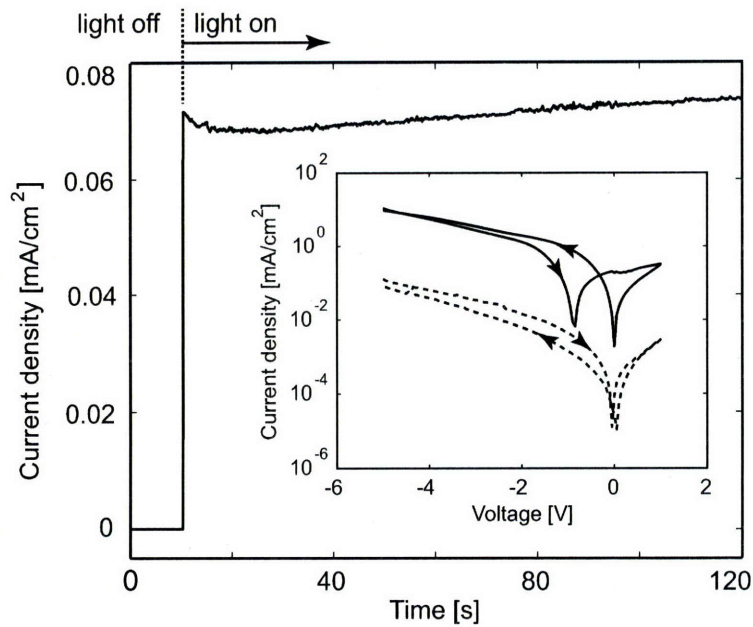
Figure 3-12: Current response of QD-PD when exposed to 110-mW cm^{-2} illumination at $\lambda = 514$ nm, showing signal modulation due to charging within $\pm 5\%$. [Inset: Magnitude of current density vs. voltage plots for QD-PD in the dark (dotted line) and under 110 mW cm^{-2} illumination at $\lambda = 514$ nm (solid line). Positive voltage corresponds to the Ag electrode biased positive with respect to ITO.]
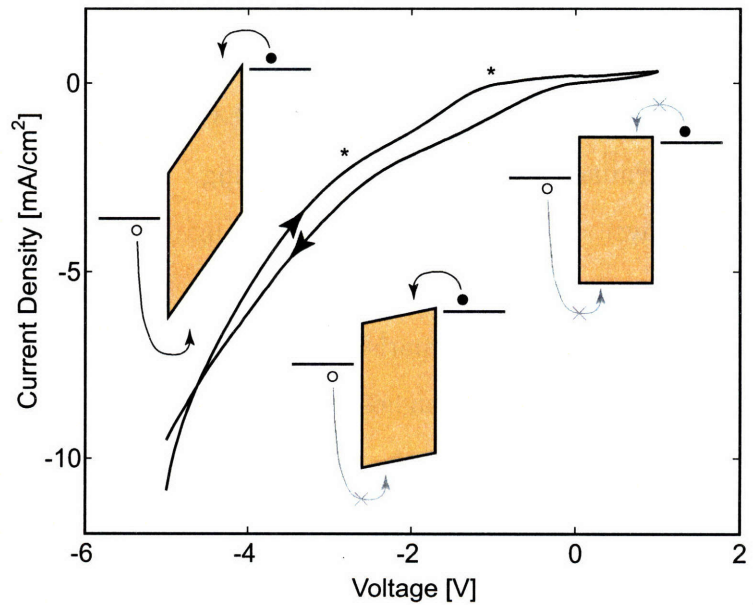
Figure 3-13: A linear-linear I-V plot reveals kinks, marked with asterisks, at ~ -1 V and ~ -2.5 V. One possible explanation for these are first electron and then hole injection (with increasingly negative voltage), as indicated by the inset cartoons.

dynamics by analyzing intensity vs. photocurrent data recorded for close-packed CdSe films in the transverse bar electrode geometry.[59] Films of poor quality exhibited trap density (N_t) much larger than free carrier density (n), leading to the observation of monomolecular transport dynamics. However, careful, air-free preparation led to films with N_t and n being on the same order. In their analysis, Jarosz et al. begin with the charge generation equation

$$\frac{dn}{dt} = G - (N_t + n)nb,$$ (3.1)

where G is the rate of carrier photogeneration, and b is a normalized recombination efficiency. For the equilibrium case, using the steady-state approximation, this can be simplified to

$$I = \frac{1}{2\alpha}\left(-\beta + \sqrt{\beta^2 + 4\alpha E}\right),$$ (3.2)

where I is photocurrent at a given voltage. One can then find the relative trap density from

$$\frac{n}{N_t} = \frac{\alpha}{\beta}I.$$ (3.3)

Figure 3-14 shows a log-log plot of our current density vs. excitation intensity data for the QD-PDs discussed here fitted to Eq. 3.3 with $\alpha = 0.013 \pm 0.004$ and $\beta = 0.12 \pm 0.03$, determined using least-squares fitting.[7] The current density value for each point is the average in the -3 V to -5 V range, in which the shape of the I-V curves is invariant with varying excitation intensity. (The figure inset shows the linear-linear data for more direct comparison with data in Ref. [59].) The resulting ratio α/β is 0.11 ± 0.03, which at the highest intensity (2.13 mW cm^{-2}) gives $n/N_t = 1.0 \pm 0.3$. This value is consistent with the values for untreated films in Ref. [59] and is consistent with what has been observed in the transverse bar electrode geometry for n-butylamine-treated CdSe films.[8]

Hysteresis trends with incident intensity. One unsatisfying feature of Fig. 3-

---

[7]The attentive reader will notice that while Jarosz et al. fit absolute current versus intensity, current *density* versus intensity is fit here. These fits lead to different values for α and β, but their ratio remains unchanged.

[8]Private correspondence with Venda J. Porter.
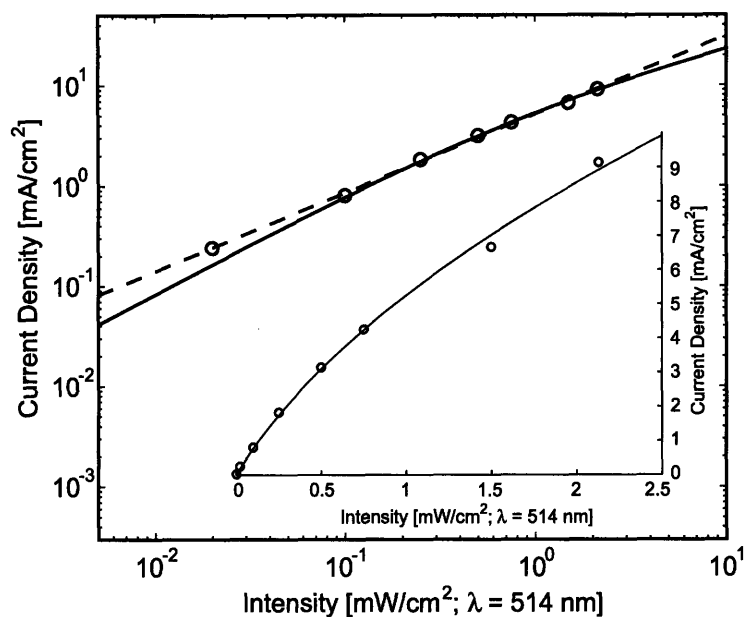
Figure 3-14: Dependence of photocurrent on excitation intensity. Data, shown in open circles, are fit with the equation $I = \frac{1}{2\alpha}\left(-\beta + \sqrt{\beta^2 + 4\alpha E}\right)$, where E is intensity, $\alpha = 0.013$ and $\beta = 0.12$ (solid line) and $I = I_0 E^\gamma$ with $I_0 = 2.59$ and $\gamma = 0.78$ (dashed line). (Inset: Linear-linear plot of solid line fit, showing resemblance to analogous fits in Ref. [59].)
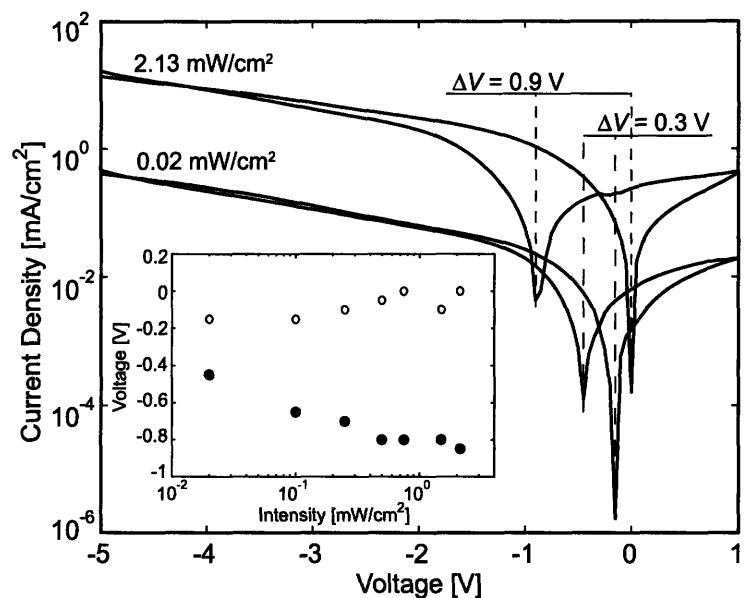
Figure 3-15: I-V plots with $E = 2.13$ mW/cm^2 and $E = 0.02$ mw/cm^2 showing markedly different hysteresis behavior. The inset displays V_{oc} as a function of intensity, which suggests that the V_{oc} values observed on the upward voltage sweep are representative of the steady-state V_{oc} value.

85

12 is the considerable hysteresis, represented by the difference of nearly 1 V between V_{oc} and the upward voltage sweep and V_{oc} on the downward voltage sweep. By comparing entire I-V curves at different excitation intensity, the two most extreme of which are shown in Fig. 3-15, it is evident that the hysteresis in open circuit voltage ΔV_{oc} increases from 0.3 V to 0.9 V as intensity increases from 0.02 mW cm^{-2} to 2.13 mW cm^{-2}. The inset to Fig. 3-15 shows clearly that this increase is mostly accounted for by the trend in V_{oc} on the upward (solid circles). V_{oc} is expected to decrease with the logarithm of intensity,[51] suggesting that the V_{oc} values observed on the upward voltage sweep are representative of steady-state V_{oc} values.

3.3.4   Bandwidth Determination

In a previous report, CdSe QD photodetectors of sandwich geometry displayed persistent photocurrent of significant magnitude for hundreds of seconds after exposure to the excitation source ceased.[60] As a result of the reduced charge trapping of the chemically treated QD films, our devices display no such persistent photocurrent. QD-PD bandwidth was measured (Fig. 3-16) in the frequency domain using laser light ($\lambda = 514$ nm) sinusoidally modulated in intensity with an acousto-optic modulator and a lock-in amplifier (Signal Recovery 7280, bandwidth > 1 MHz). Figure 3-17 shows the normalized photocurrent (top) and phase (bottom) response from 1 Hz to 1 MHz for a device at $V = 0$ V. The 3-dB rolloff occurs at ~ 50 kHz and 20 dB/octave rolloff behavior to observed to the high-frequency side.

An HP 4192A LF impedance analyzer in the Akinwande Lab at the MIT Microsystems Technology Lab (MTL) was used to measure equivalent resistance and capacitance values for our QD-PDs. A series resistance-capacitance model was used, and measurements were done at 1 kHz on several device pixels exposed to low-level ambient light. The measured capacitance was found to be $C = 377 \pm 4$ pF. Based on these measurements, we would expect that the capacitance of device, coupled with the resistance of our measurement electronics circuitry, to impose an upper bandwidth limit on the order of $1/(50 \ \Omega \times 377 \text{ pF}) \sim 5$ MHz on the bandwidth of the measurement system. This suggests that the 50-kHz bandwidth observed is a property of the
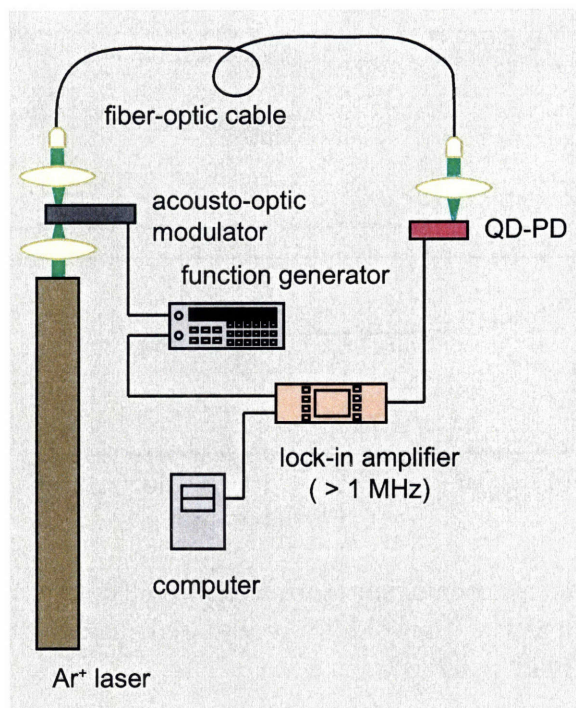
Figure 3-16: Experimental setup for bandwidth determination. A wide-bandwidth lock-in amplifier, function generator, and acousto-optic modulator allow sinusoidal intensity modulation to be swept over a wide range of frequency.

device and *not* the measurement electronics. The bandwidth of our device is likely limited by carrier recombination lifetime within the QD film.

A slightly preferable method of determining bandwidth is to measure directly the transient photocurrent decay after exposure to a femtosecond (or even picosecond) laser pulse.[95] The 1-kHz $\lambda = 400$ nm system at the MIT Institute for Soldier Nanotechnologies (ISN) was used with our detector, both at zero bias and under bias with a battery. However, the (poorly shielded) cable and sample holder were susceptible to interference from the Pockels cells in the laser system, preventing the observation of transient signal. Owing to success in the frequency domain, determination of bandwidth in the time domain was not pursued further.

3.3.5 Detection Limit

The detection limit of the system (device and measurement electronics) was determined at $V = 0$ V, where we found I_{photo}/I_{dark} to be highest. Using an Agilent 4156c
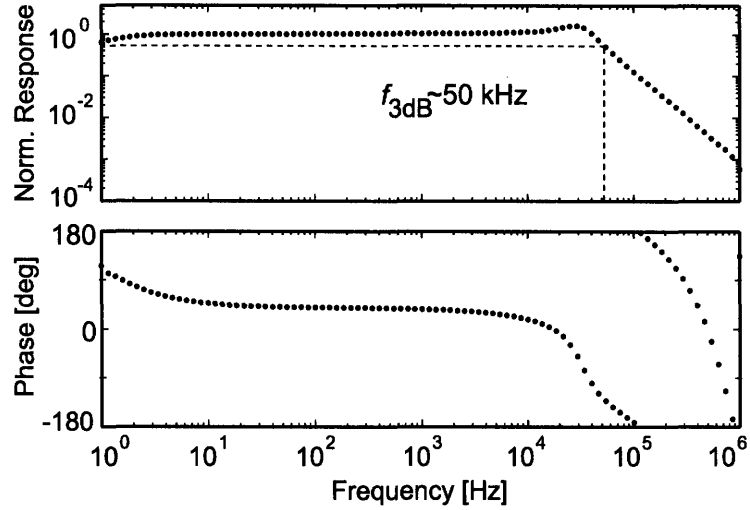
Figure 3-17: Normalized photocurrent (top) and phase (bottom) response at $V = 0$ V as a function of frequency of sinusoidally modulated incident light at $\lambda = 514$ nm. The 3-dB rolloff occurs at ~ 50 kHz.

parameter analyzer, the current response as a function of time was measured while manually modulating the incident light ($\lambda = 514$ nm) at < 1 Hz. We determined the detection limit to be ~ 10 μW cm^{-2} using the 3-σ metric

$$i_{\text{min}} = \bar{i}_{\text{dark}} + 3\sigma_{\text{dark}}, \tag{3.4}$$

where i_{min} is the minimum detectable signal and $\bar{i}_{\text{dark}}$ and σ_{dark} are the mean and standard deviation of device readings in the dark, respectively. Figure 3-18 displays the response of the device to modulated light over several orders of magnitude, and a histogram at the right of Fig. 3-18(d) shows that the photo signal and dark signal distributions are separated by roughly three standard deviations for 10-μW cm^{-2} excitation.

3.3.6   QD-PD response to Voltage Step

Under constant illumination at $\lambda = 514$ nm, the bias applied to the device was stepped between -0.5 V and -1.0 V with a Standford Research DS 535 function generator at a frequency well below the 50-kHz 3-dB bandwidth. This represented a step from what was found to be a steady-state $V_{\text{oc}} \approx -0.5$ V to a reverse bias
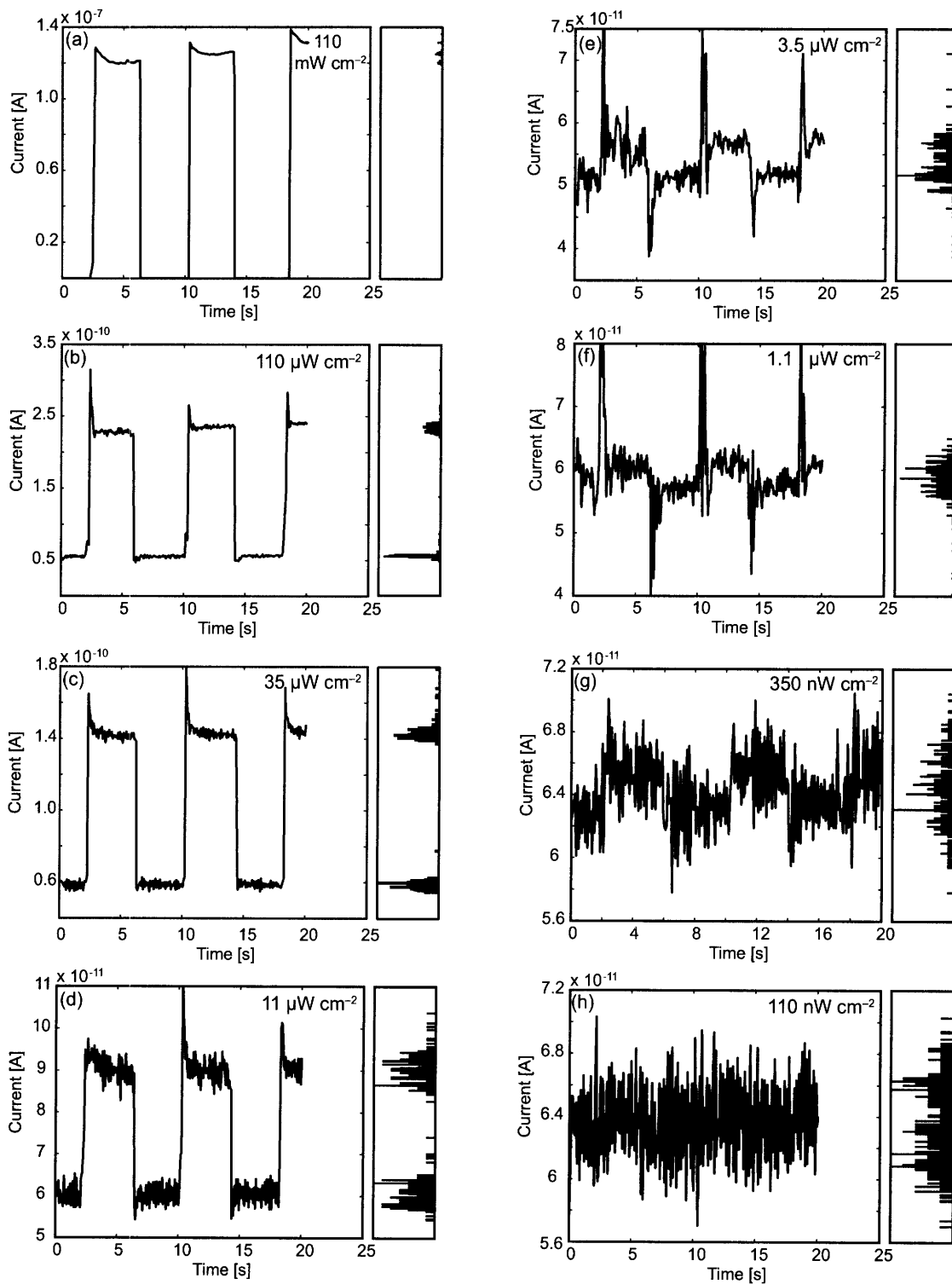
Figure 3-18: Zero-bias photocurrent response to different intensities of $\lambda = 514$ light modulated by hand: (a) 110 mW cm^{-2}; (b) 110 μW cm^{-2}; (c) 35 μW cm^{-2}; (d) 11 μW cm^{-2}; (e) 3.5 μW cm^{-2}; (f) 1.1 μW cm^{-2}; (g) 350 nW cm^{-2}; (h) 110 nW cm^{-2}. Histograms to aid in the application of the 3-σ metric are shown at the right of each plot.
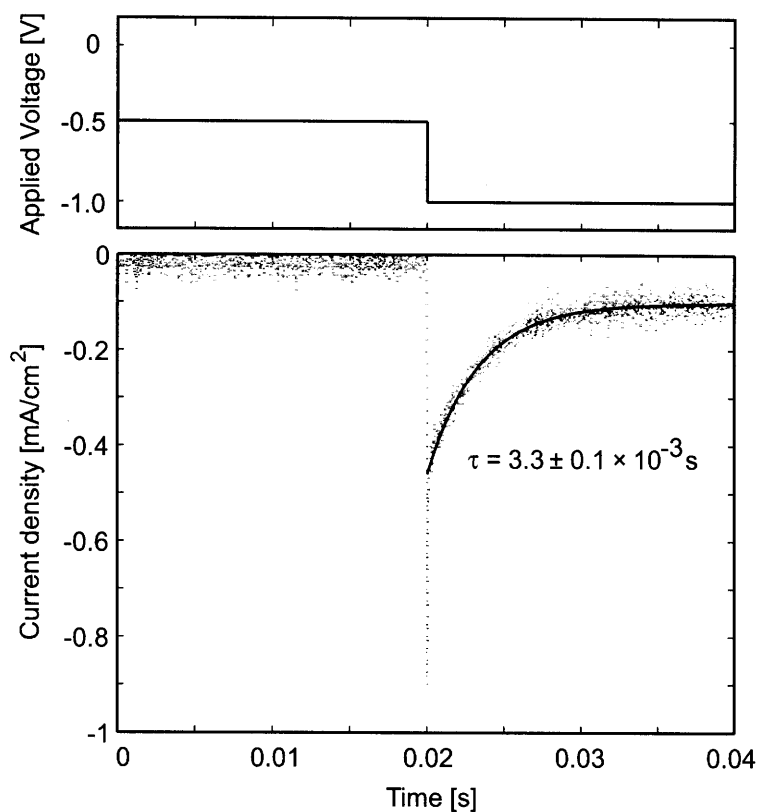
Figure 3-19: Device response (bottom panel) under constant illumination (λ = 514 nm at 110 mW cm^{-2}) and with voltage stepped from $V = -0.5$ V to $V = -1.0$ V (top panel).

voltage ($V = -1.0$ V), at which some photocurrent could be measured. The resulting photocurrent signal was recorded with an oscilloscope and is shown in Fig. 3-19 along with a plot of the applied voltage. The current decay was fitted using least squares and a single exponential yielded time constant $\tau = (3.3 \pm 0.1) \times 10^{-3}$ s, which is much longer than the time constant associated with the 3-dB roll off. While the time constant associated with incident light is related to the recombination time of carriers, the time constant with modulated applied voltage represents filling the of trap sites.

90

3.4 Thick-slab QD-PDs Containing Other Materials

To demonstrate that the QD-PD platform developed in this chapter can, in fact, be used for other materials, thick-slab QD-PDs based on CdTe and PbSe QDs and active to the low-energy side of the visible spectrum and into the infrared spectrum were fabricated. These devices were not extensively optimized for performance, and the data should be regarded as very preliminary.

3.4.1 CdTe QD-PD

Figure 3-20(a) shows a cartoon cutaway diagram of a CdTe QD-PD, fabricated analogously to the CdSe QD-PDs. One notable exception was that the top electrode was Au rather than Ag (and was evaporated in the Bawendi Lab evaporator). This was done because Au is thought to inject holes into CdTe QD films, which is critical for the photoconductivity mechanism in CdTe QD solids.[70]. CdTe QDs were synthesized using an established procedure. Briefly, a solution containing 0.318 g cadmium 2,4-pentanedionate (98%), 0.57 g 1,2-hexanedecanediol, and tri-n-octylphosphine (TOP) was degassed for 2 hr while being heated under nitrogen to 100 °C in an oil bath. Roughly 5 min after the solution was removed from the bath, 2.0 mL 1.5 M tri-n-butylphosphine telluride was added and the solution stirred. This solution was in turn injected into a 50-mL round-bottom flask containing 3.125 g tri-n-octylphosphine oxide (TOPO), 2.875 g hexylphosphonic acid, 1 mL TOP, and 0.4 g hexylphosphonic acid (which had been degased for 2 hr at 140 °C) held at 360 °C under nitrogen. Immediately after injection, the flask was held at 260 °C for 6 min to further grow the particles. One step that proved critical for the synthesis of high-quality particles was the passage of TOP (Strem, > 97%) through a basic alumina column, presumably removing phosphinic and phosphonic acid impurities.

External quantum efficiency $\eta_{eqe}(\lambda)$ was measured as a function of incident wavelength for the CdTe QD-PDs both as zero bias and with negative biases (applied to
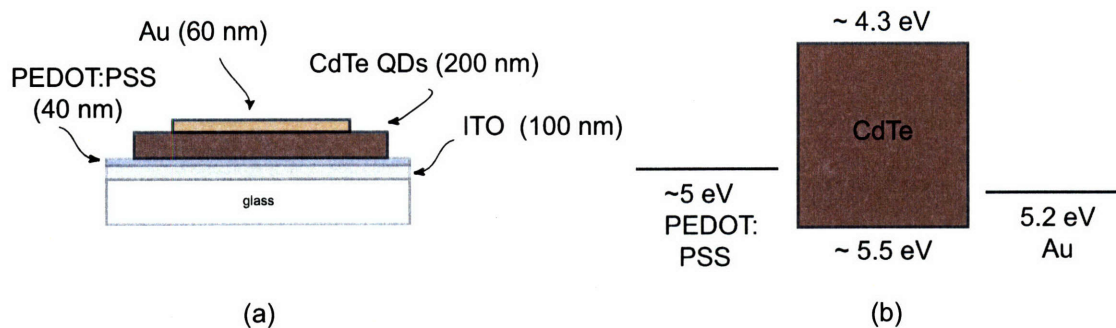
Figure 3-20: Cartoon cutaway (a) and energy-band structure (b) of CdTe QD-PD.
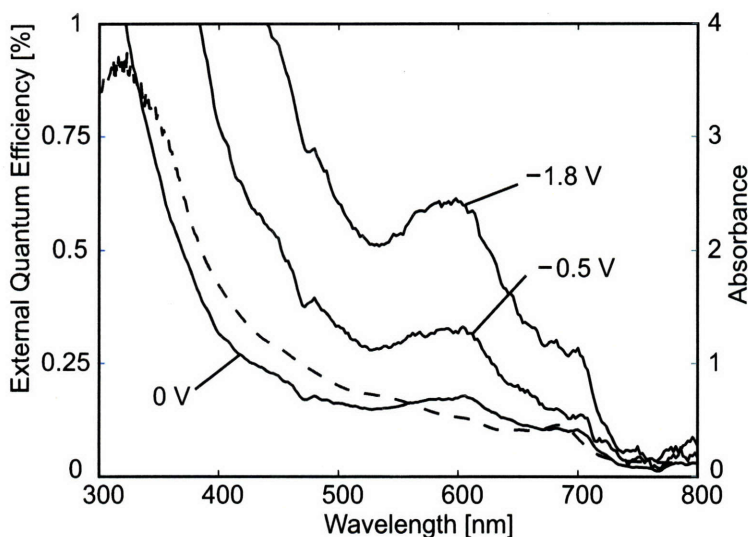
Figure 3-21: The zero-bias external quantum efficiency spectrum of a CdTe QD-PD agrees well with the absorbance spectrum of constituent CdTe QDs in solution (dashed) and displays band-edge $\eta_{eqe} \sim 0.1\%$.

top Au electrode, relative to ITO), as shown in Fig. 3-8. The zero-bias EQE spectrum matches well with the absorbance of the constituent CdTe QDs dispersed in hexane, with $0.10\% < \eta_{eqe} < 0.25\%$ throughout the visible spectrum and extending to $\lambda \approx 700$ nm. Interestingly, as the magnitude of applied bias is increased, a broad feature centered at $\lambda = 590$ nm appears and increases more quickly than other parts of the spectrum. It appears that there is a field-dependent enhancement mechanism, possibly based on a plasmon effect, evident in this device.
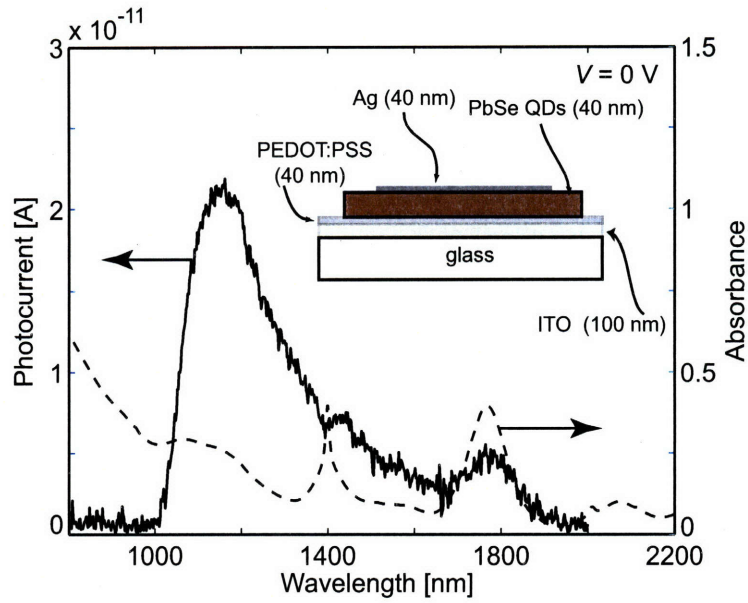
Figure 3-22: The zero-bias photocurrent spectrum of a PbSe QD-PD (solid) displays band-edge features consistent with the absorbance of constituent PbSe QDs in solution (dashed). The sharp peak at $\lambda = 1400$ nm is a combination of absorption from the constituent QDs and overtones of residual solvent. Inset is a cartoon cutaway of the PbSe QD-PD structure.

3.4.2   PbSe QD-PD

Thick-slab QD-PDs were also produced with PbSe QDs as the active material. From a synthesis, processing, and performance point of view, this is far more challenging than QD-PDs based on CdSe and CdTe QDs, and these challenges are discussed in more depth in Chapter 5. For the present discussion, we wish only to present Fig. 3-22, which shows photocurrent $I_{\mathrm{ph}}(\lambda)$ of the ITO/PEDOT/QD/Ag (cartoon cutaway shown inset). Band-edge $\eta_{\mathrm{eqe}}(\lambda)$ is very small ($\sim 0.001\%$), but the features at 1780 nm and 1420 nm in the photocurrent spectrum correspond to the first two absorbance features of PbSe QDs dispersed in 1,1,2-trichloro-1,2,2-trifluoroethane. The much sharper decrease in photocurrent as wavelength is increased (as compared to the decrease in absorbance) may be owing to both cavity effects and absorption by the ITO electrode, which can have appreciable absorption in the SW-IR.

93

3.5 Summary

We have developed a method to produce CdSe QD-PDs of sandwich geometry. These devices are solution-processable and have the potential to be made large in area and on flexible substrates. The active layer is a thick, close-packed, chemically annealed QD solid. These layered QD-PDs represent a minimal departure from the transverse bar electrode QD-PDs that have previously provided a wealth of insight into transport in CdSe QD solids.

Solution-phase treatments enable a number of desirable device performance characteristics, including

- room-temperature operation

- action spectra closely resembling QD core absorption

- external quantum efficiencies of 15-24% at -6 V

- internal quantum efficiencies ~ 70 % at -6 V

- stable detector response within ± 5 % at 0 V

- 50-kHz 3-dB bandwidth

- zero-bias detection limit with an upper limit of ~ 10 μW cm^2

The simple design of the present QD-PD structure provides a platform for studies of more complex QD-PD structures in both the visible and the IR regions of the spectrum.

Chapter 4

Multilayer QD-PDs

Post-deposition, solution-phase chemical annealing of QD solids[49, 48] has enabled the observation of unity internal quantum efficiency in a transverse, parallel bar electrode test structure[48]. In Chapter 3, QD solids were successfully incorporated into layered QD-PDs, otherwise making a minimal transformation in the device design, and $\eta_{iqe} = 70 \pm 10\%$ with $V < 10$ V was achieved. In this chapter, we describe the fabrication of more complex multilayer QD-PD structures, largely done in collaboration with Alexi C. Arango of the Bulović Group. While we continue to use both nascent and treated QD solids (in contrast to the polymer/nanocrystal blends used in other groups for QD-based photovoltaics[108]), we construct both single- and double- heterojunction structures with direct analogs in the solid-state[137] and organic-electronics[95] regimes. In § 4.1, we discuss materials used for new additional layers and potential benefits and drawbacks of adding layers between the optically active QD layer and the electrodes. Section 4.2 describes an effort to create a quasi-p-i-n, double-heterojunction device that was plagued by morphological problems. A more successful single-heterojuction device, analogous to a p-n junction, is discussed in § 4.3. Much of this work will appear in Ref. [51]. Finally, § 4.4 discusses new insight gained from these devices.

4.1 Multiple Layers

In this chapter, we define devices with "multiple layers" as those containing blocking layers or spacer layers—typically inorganic or organic semiconductor layers with little optical activity—positioned between the optically active QD solid and the electrodes. The use of blocking layers is far from unique to this work. Organic semiconductors are commonly used as blocking layers in OLEDs to confine charge, once injected from an electrode.[138] In QD-LEDs, a layer of TAZ[1] is often inserted between the QD monolayer and Alq$_3$[2] layers to prevent exciton generation deep in the Alq$_3$ layer, which would result in undesirable broadband, green organic emission.[31] In absorptive organic photodetector devices, organic semiconductors such as BCP[3] have been used as optically inactive spacer layers to move the critical heterojunction interface away from the metal electrode, where the optical field vanishes, and toward the $\lambda/4$ point. By providing better overlap between the optical field and the optically active layer, this increases η_{abs}, in turn increasing η_{eqe}.[95] An additional use of multiple layers is as a sacrificial or protecting layer in which a layer of semiconducting organic is minimally deposited on top of delicate layers of interest before a harsh process such as sputtering or evaporation of Au. These layers are understood to be destroyed and are usually not considered part of the finished device architecture.

Our interest in making QD-containing devices with multiple layers is two-fold. First, the inclusion of wide-band-gap organic or inorganic layers with much different electron and hole mobilities can act as charge blocking layers, relaxing the very strict morphological requirements of the QD layers discussed in Chapter 3. Similar polymer or organic protecting layers are not uncommon in the literature.[71] In addition to providing protection against catastrophic shorting, the insertion of hole- and electron-transporting layers can impart rectification in the device's current-voltage characteristics, making a hybrid structure somewhat akin to a solid-state p-i-n diode,

---

[1]Hole-blocking molecular organic semiconductor 3-[1,1'-biphenyl]-4-yl-5-[4-(1,1-dimethylethyl)phenyl]-4-phenyl-4H-1,2,4-triazole, CAS [150405-69-9].

[2]Electron-transporting molecular organic semiconductor tris(8-quinolinolato-κN1,κO8)-aluminum, CAS [2085-33-8].

[3]Semiconducting organic 2,9-dimethyl-4,7-diphenyl-1,10-phenanthroline, CAS [4733-39-5]
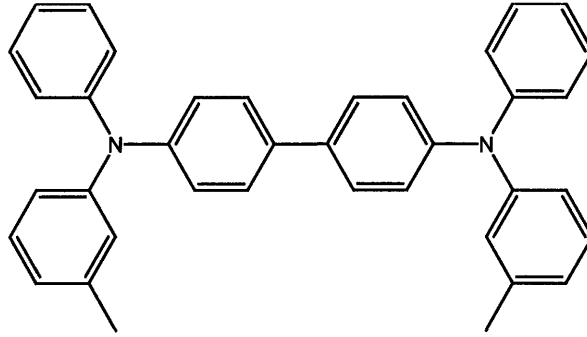
Figure 4-1: Chemical structure of TPD.

as shown in Fig. 4-2.

Second, the interfaces between blocking layers and the optically active layer can form a heterojunction, at which excitons are ionized, often critical for zero-bias operation. This is the design employed by almost all organic photodetectors,[95] and this principle has been shown to be central to QDs in polymer-blend solar cells.[98, 108] While an assumption in Chapter 3 was that our device was behaving largely as a photoconductive device (like its close relative in the transverse channel geometry), it is likely that QD-based heterojunctions are more appropriately interpreted as photodiodes. The two materials used in this chapter as blocking layers are n-type TiO_2 and p-type TPD.

TPD. TPD, or N,N'-diphenyl-N,N'-bis(3-methylphenyl)-4,4'-diamine, is a hole-conducting molecular organic ($\mu_h \sim 10^{-3}$ cm^2 V^{-1} s^{-1}) first investigated for use in xerography[139] and very commonly used in OLEDs since.[34] Like most molecular organics, TPD is usually thermally evaporated, and crystallinity in TPD is not desirable. An ionization energy E_{ip} of 5.4 eV and electron affinity E_{ea} of 2.1 eV give TPD a large band gap ($E_{ip} - E_{ea} > 3$ eV), making it especially well suited for use with a CdSe QD device, in which the band-edge response is in the middle of the visible spectrum. The chemical structure of TPD is shown in Fig. 4-1, and the position of its energy bands in Fig. 4-3

Titanium oxide. Titanium oxide, or TiO_2, is a wide-band-gap, n-type, electron-conducting layer for which the electron mobility is sensitive to its morphology and crystallinity. For TiO_2, $E_{ip} = 4.2$ eV and $E_{ea} = 7.4$ eV. While nanoporous titania

is well known from its role in the Grätzel solar cell design,[88] inorganic materials in general are not widely used as transport materials in organic or QD optoelectronics. However, they are gaining increased attention largely owing to their stability and the potential to support much higher current densities than their organic counterparts. Although sol-gel depositions were used initially,[132] RF sputtering was ultimately the deposition method used. Figure 4-3(b) shows the position of the band of TiO_2 relative to vacuum.

There are are least three potential drawbacks of multilayer QD-PD device structures.

- Added complexity to the device fabrication process. While high-quality blocking layers can help prevent catastrophic shorting, more layers require more time and equipment, coupled with the consistent deposition of high-quality layers. Smooth, defect-free TiO_2 and TPD layers were difficult to achieve in the quasi-*p-i-n* devices discussed in § 4.2.

- Added complexity to device interpretation. Uncertainty in how the applied potential is dropped across differing layers, coupled with the creation of multiple interfaces, make any sensible detailed interpretation even more challenging than in the simpler device architecture developed in Chapter 3.

- Reduced generality for potential use in other parts of the spectrum. As is evident in Fig. 4-12, blocking layers can (and, in general, do) have spectral overlap with the absorption spectrum of the active QD layer. While this would likely be less of an issue with SW-IR QD-PDs based on PbSe or PbS QDs, the narrow band gaps and unknown position relative to vacuum for these materials could make energy alignment challenging.

4.2   Quasi-*p-i-n* QD-PD

In this section, we discuss the fabrication and characteristics of a device with the composition $ITO/TiO_2/CdSe$ QD/TPD/Ag. Figure 4-3 shows a cutaway view (a)
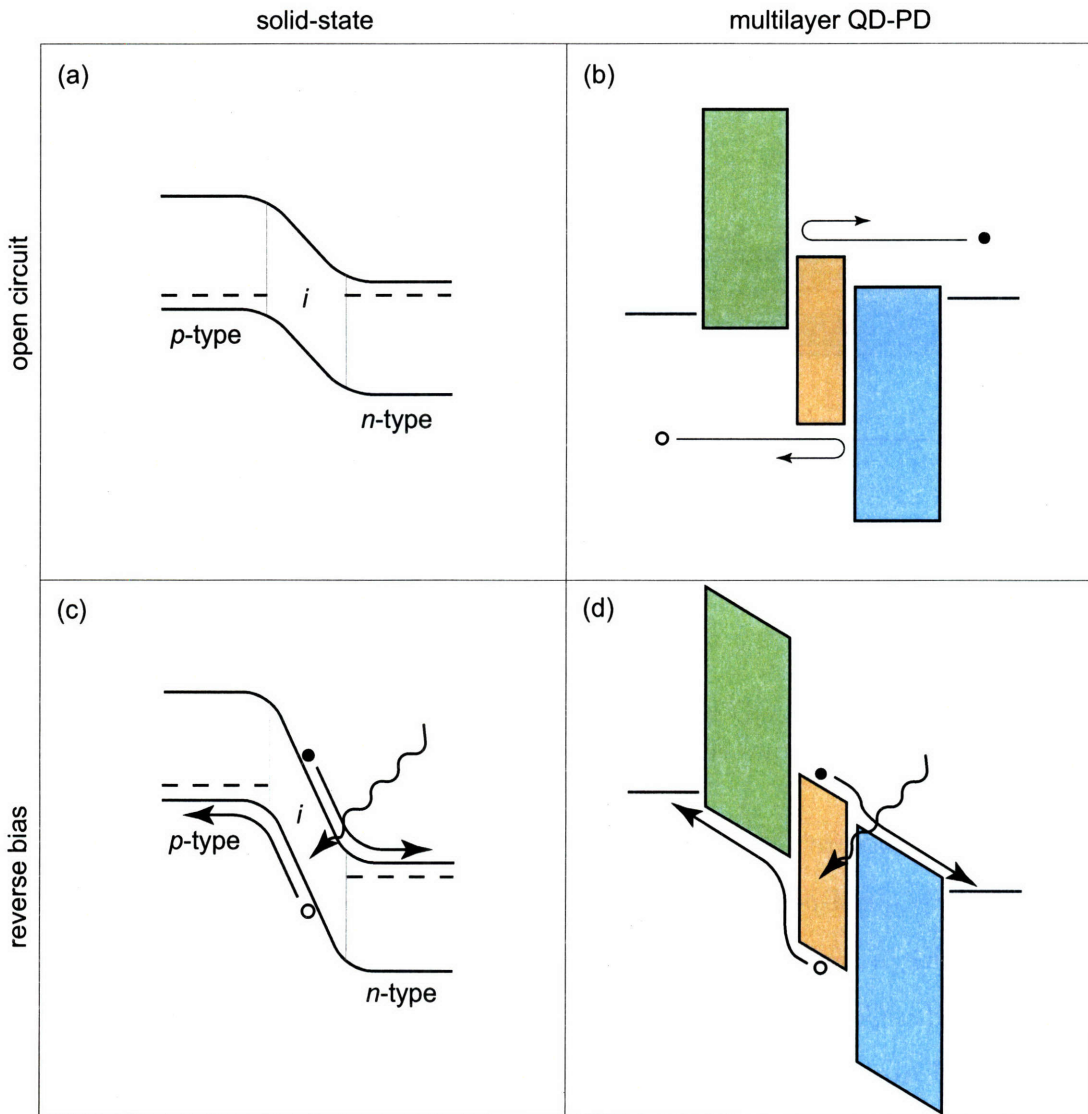
Figure 4-2: Comparison of multilayer QD-PDs with p-i-n-junction devices. Panel (a) shows an open-circuit p-i-n diode, with the intrinsic part of the device indicated by the thin, vertical gray lines. A QD-PD analog is shown in (b), in which QDs play the role of the intrinsic layer and organic or inorganic transport layers the p-type and n-type layers. Note that in (b), neither electrons or holes can easily pass through the entire device structure. The p-i-n diode is under reverse bias in (c) and acting as a photodetector. The potential is essentially dropped across only the intrinsic layer, which can be quite large given sufficiently good transit times. The QD-PD under reverse bias in (d), like the p-i-n in (c), is extracting charge from photoexcitons created in the middle layer. However, an important difference is that because of the poor mobilities of the blocking layers in (d), the field is dropped across the p-type and n-type layers, as well.

99
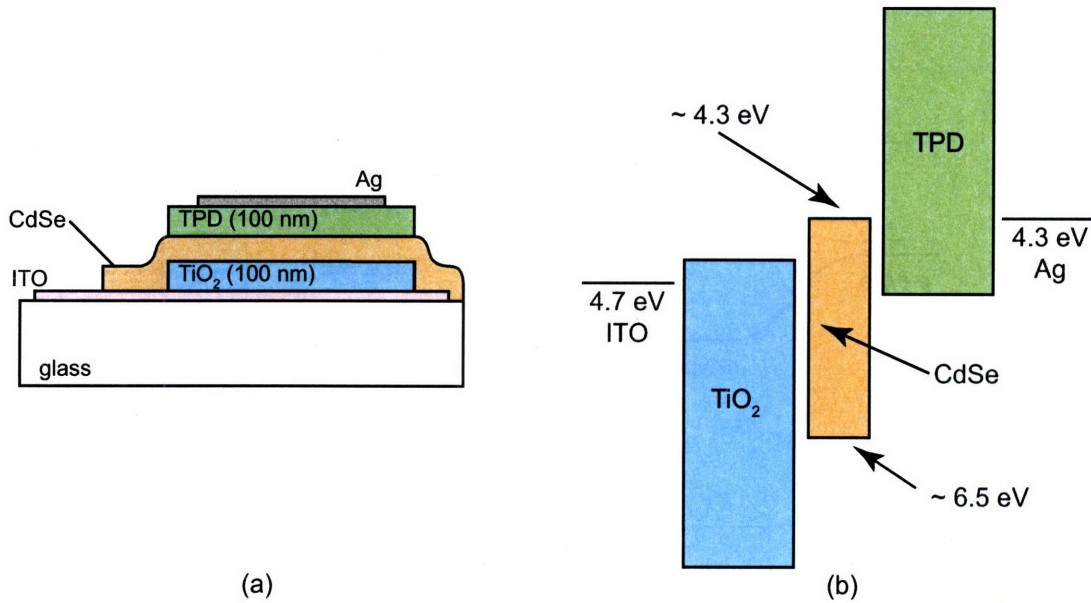
Figure 4-3: Quasi-*p-i-n* QD-PD. Panel (a) shows a cutaway cartoon of the quasi-*p-i-n* structure. Panel (b) shows the proposed energy structure.

and energy structure (b) for this device, henceforth referred to as the quasi-*p-i-n* QD-PD. Two quasi-*p-i-n* variants, one using *n*-butylamine-treated CdSe QD films and one using a nascent films, were produced in addition to a control structure, which lacked a CdSe QD layer. Though this design ought to perform well based on energy-band diagrams alone, the data in this section show that the devices are of little value, largely owing to widespread morphological problems with the TiO_2 and TPD layers.

4.2.1   Device Process

Glass/ITO. We purchased glass sheets on which ITO (115 nm) had already been sputtered, with sheet resistance of 55 Ω/square. The ITO was patterned as needed using a photolithography procedure and then cleaned, as described elsewhere.[132] Immediately prior to use, substrates were subjected to UV-ozone treatment for 5 min.

TiO_2. TiO_2 layers were RF magnetron sputtered using the integrated materials

100

deposition system in LOOE. Deposition parameters are given in Ref. [132]

CdSe QDs. CdSe QDs were synthesized and processed as described in Appendix A. CdSe films spin-cast were thinner than in Chapter 3 (80 nm vs. 200 nm), but the n-butylamine treatment procedures, when used, were identical.

TPD. The organic semiconductor TPD was used as a p-type blocking layer in this device structure. TPD, purchased from H. W. Sands and purified using train sublimation,[132] was thermally evaporated at a pressure $< 5 \times 10^{-6}$ and at a rate of ~ 1 Å s^{-1}. Thickness of the TPD layer was typically 100 nm.

Ag. The top Ag electrode was evaporated in the LOOE materials deposition system. Dynamic vacuum of $< 5 \times 10^{-6}$ Torr was maintained during evaporation, in which a 600 Å layer of Ag was deposited at a rate of ~ 2 Å/s. After evaporation, devices were stored in a nitrogen environment until characterization.

4.2.2 Quantum Efficiency Measurements

External quantum efficiency (EQE) spectra were recorded for a "control" quasi-p-i-n structure (containing no QD layer) and for two quasi-p-i-n designs containing nascent and n-butylamine treated 80-nm thick layers of CdSe QDs. The setup used was identical to that depicted in Fig. 3-8, and measurements were done at room temperature and in air. Figure 4-4(a) shows $\eta_{eqe}(\lambda)$ for the control device, and as expected, there is no device response for $\hbar\omega < 3.2$ eV, for which the constituent layers are transparent. This device is interesting in its own right because it is a quasi-p-n junction device somewhat akin to organic photodetectors and bears some correspondence to Grätzel solar cells.[88] Excitons generated in TPD within a diffusion length of the junction are dissociated at the TiO$_2$/TPD interface, and the resulting charge is transported through a single layer to the electrode.

Figure 4-4(b)-(d) show the $\eta_{abs}(\lambda)$, $\eta_{eqe}(\lambda)$, and η_{iqe}, respectively, for a quasi-p-i-n QD-PD containing an *untreated* CdSe QD layer 80 nm thick. Across the visible spectrum $\eta_{eqe} < 0.006\%$, indicating very inefficient exciton separation in and transport through the moderately thick, untreated QD layer. Internal quantum efficiency η_{iqe}, calculated from $\eta_{abs}(\lambda)$ and η_{iqe}, is less than 0.04%. In contrast, Fig. 4-4(e)-(g) show

film absorption, $\eta_{eqe}(\lambda)$, and η_{iqe} for a quasi-p-i-n device in which the active layer is an n-butylamine-treated CdSe QD film (80 nm thick prior to treatment). While the film absorption is unchanged, η_{eqe} is nearly 0.1% at the band edge, and η_{iqe} is calculated to be $0.8 \pm 0.2\%$ across the spectrum.

Despite the addition of the p and n layers, which introduce heterojunction interfaces on either side of the QD film, the quasi-p-i-n devices containing moderately thick 80-nm CdSe QD layers behave very much like the QD-PDs in Chapter 3. This is supported by the observations (1) that zero-bias η_{iqe} is nearly identical between the thick-slab QD-PD and the quasi-p-i-n device containing a treated film and (2) that treatment of the film resulted in a qualitative change in the behavior of the device, increasing band-edge η_{eqe} by more than an order of magnitude.

4.2.3 *I-V* Characteristics

The *I-V* characteristics for the quasi-p-i-n control device in the dark (dashed) and under white-light illumination (solid) are shown in Fig. 4-5. This device proved to be unstable with applied voltage $|V| > 0.5$ V, which is the reason for the very limited voltage range covered. The dark current curve reflects the instrument noise level, showing that over the very limited range covered, there is negligible leakage current through the device. Under illumination, the photocurrent is saturated for $V < 0.2$ V, and surprisingly, $V_{oc} \approx 0.4$ V despite the fact that (nominally) TiO_2 and Ag have the same work function (4.2 eV). One explanation for this might be the presence of a dipole at the TiO_2/TPD interface resulting from the accumulation of dissociated carriers.[140, 141]

Current-voltage characteristics for quasi-p-i-n devices containing both nascent and n-butylamine-treated QD films were recorded with a Keithley 2400 source-measure unit (SMU) in an nitrogen atmosphere and with a broad-band white-light source of unmeasured power. As Fig. 4-4 shows, the TPD and TiO_2 layers are active only under illumination with $\hbar\omega > 3.2$ eV, and to ensure that little UV light was incident on the device during these measurements, excitation was done through an acrylic sheet. Figure 4-6(a) shows *I-V* curves for an untreated device. As discussed in Ref.
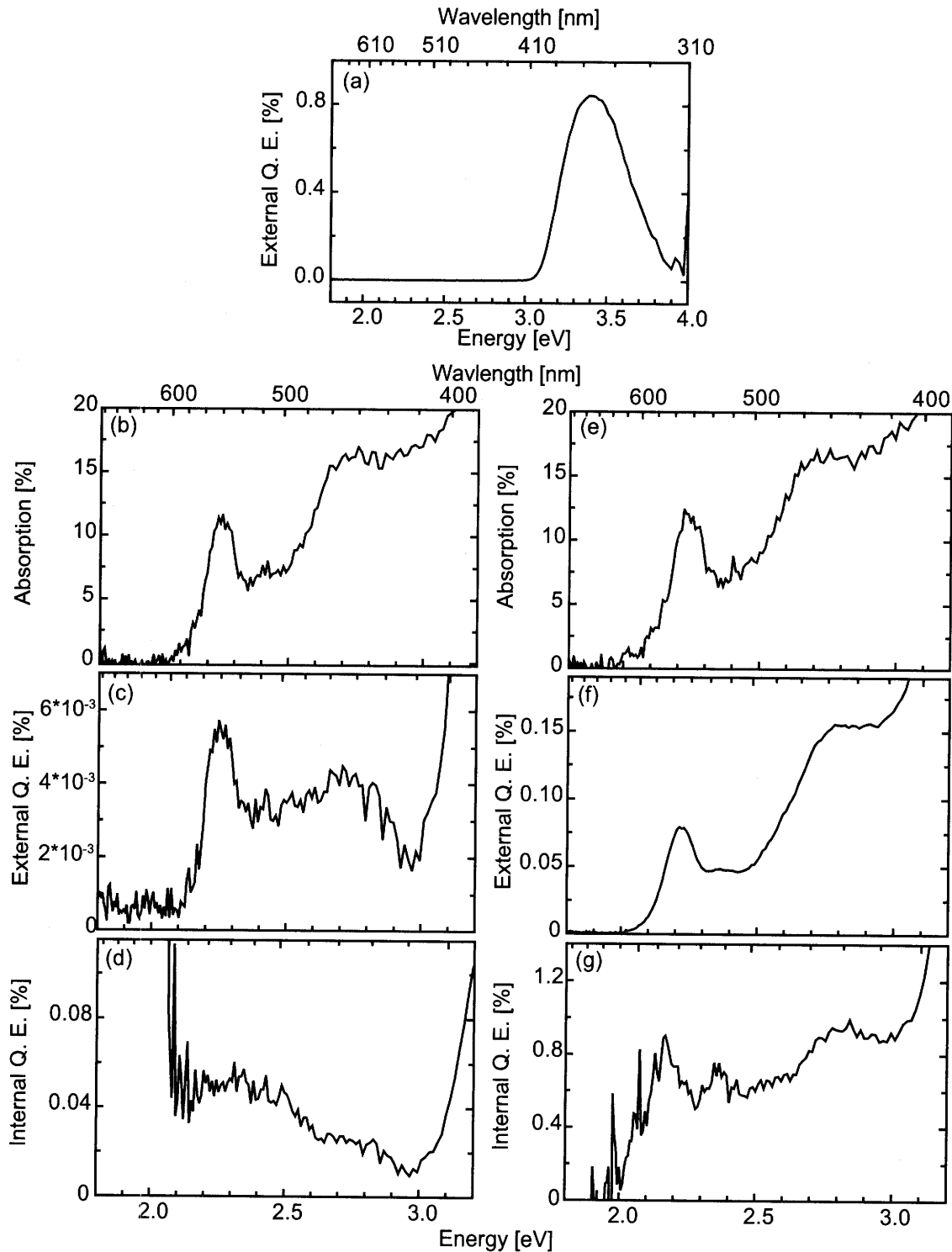
Figure 4-4: External quantum efficiency spectra for control (a), untreated (c), and treated (f) quasi-p-i-n QD-PDs. Absorption spectra for films (not measured in situ in full device structures) are shown in (b) and (e) for untreated and treated devices, respectively. Internal quantum efficiency spectra are shown for untreated (d) and treated (g) devices, and as expected, they do not exhibit a strong wavelength dependence.
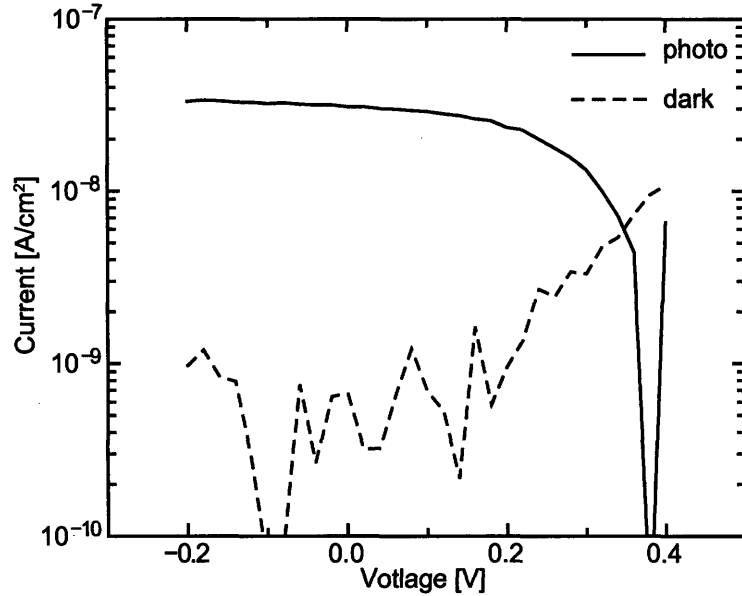
Figure 4-5: Photo (solid) and dark (dashed) current-voltage characteristics of quasi-p-i-n QD-PD control device, recorded in a N_2 environment with a broadband white-light source (power unknown). The photocurrent I-V curves reveal that $V_{oc} \approx 0.4$ V.

[132], interpretation of these curves is complicated by a current offset for this SMU that gives the dark trace an apparent asymmetry. While the trace recorded under illumination shows hysteresis, it is also shifted from its proper position. Regardless of the ambiguities associated with this offset, we can see (1) that there is an offset of roughly 0.4 V between the dark current minimum and the photocurrent minimum and (2) that the photoresponse of this device is very weak, barely emerging from the dark current trace, limited in this case by the 2-GΩ internal impedance of the SMU.

While the dark I-V curve in Fig. 4-6(b) also displays an artificially large dark current, the photocurrent effect is more pronounced with the device containing a treated CdSe QD layer, and clear rectification is observed. In forward bias (defined as Ag electrode relative to ITO electrode), current at the dark current level is observed, but in reverse bias, a significant photoeffect (more than an order of magnitude above what is seen in the untreated device) is observed. The open-circuit voltage V_{oc} is roughly 0.4 V, in very good agreement with that seen in the control device. However, one subtlety to note is that, on the low-voltage side of V_{oc}, the current rises more gradually in Fig. 4-6(b) than in Fig. 4-5, indicated by a much larger series resistance
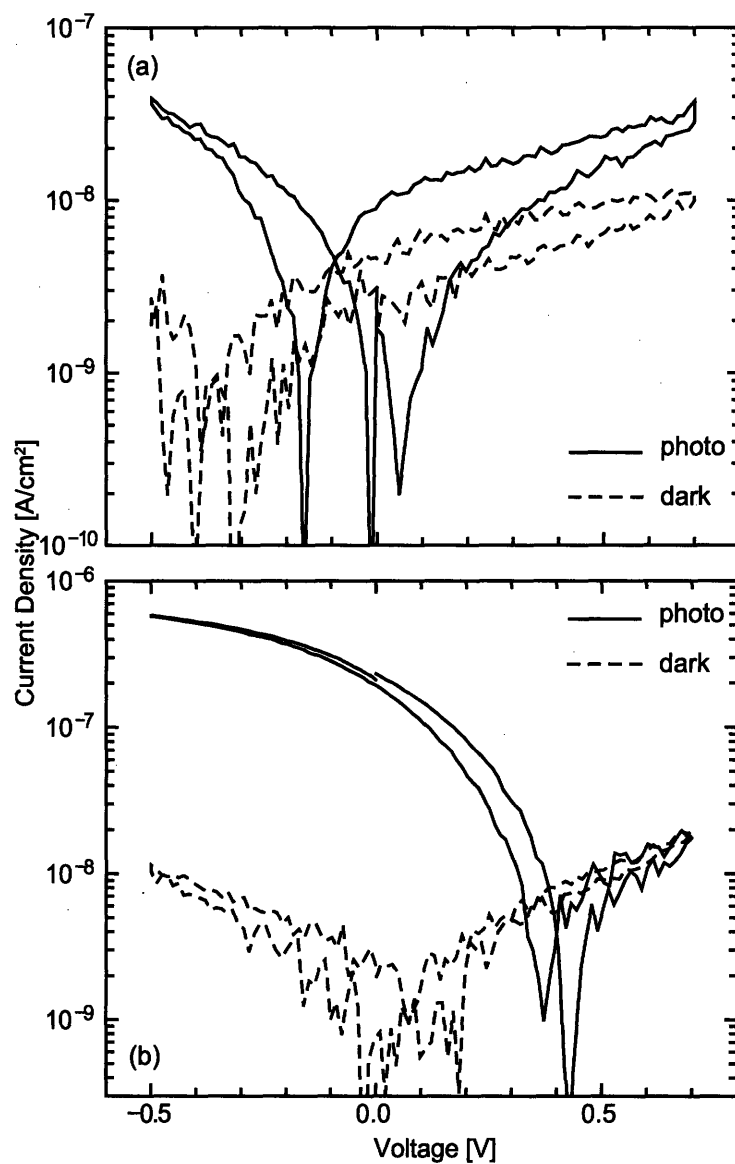
Figure 4-6: Quasi-p-i-n current-voltage characteristics of QD-PDs containing nascent (a) and n-butylamine-treated (b) CdSe QD films 80 nm in thickness. In (a), the solid photocurrent plot shows considerable hysteresis and little photoeffect. Panel (b) shows I-V curves under dark (dashed) and illuminated (solid) conditions.

105

in the treated-film quasi-p-i-n than in the corresponding control device.[132] This is consistent with the presence of the QD layer (which, even though treated, is still quite resistive).

4.3   Quasi-n-p Structure

A quasi-n-p device, with structure ITO/PEDOT:PSS/TPD/CdSe QD/ITO (shown in Fig. 4-7), is the product of an effort to invert the ITO/TiO$_2$/CdSe QD/TPD/Ag structure discussed in section § 4.2, which was hindered by poor morphology in both the metal oxide and semiconductor organic layers.[132] The original intention was to produce the double-heterojunction device ITO/PEDOT:PSS/TPD/CdSe QD/TiO$_2$/-ITO, but the introduction of oxygen during the use of the sputtering process was observed to foul the underlying QD and TPD layers, resulting in shorted devices. Subsequently, ITO/PEDOT:PSS/TPD/CdSe QD/SnO$_2$/ITO and ITO/PEDOT:PSS/-TPD/CdSe QD/ITO were both produced through RF sputtering using argon only (no oxygen introduced), and the devices performed nearly identically. The simpler ITO/PEDOT:PSS/TPD/CdSe QD/ITO design was adopted for pursuit because of its simplicity.

4.3.1   Device Process

Glass/ITO. We purchased glass sheets on which ITO (115 nm) had already been sputtered, with sheet resistance of 55 Ω/square. The ITO was patterned as needed using a photolithography procedure and then cleaned, as described elsewhere.[132] Immediately before further use, substrates were exposed to oxygen plasma for 5 min.

PEDOT:PSS PEDOT:PSS (Baytron P VP CH 8000) was used as purchased and was spin cast onto a glass/ITO substrate (4 000 RPM, 10 000 RPM/s) after filtration through a 0.45-μm PVDF syringe filter. Baking at 200 °C 5-10 min cross-linked the PEDOT:PSS layer. Glass/ITO/PEDOT:PSS substrates were then introduced to a nitrogen environment, and all subsequent fabrication steps were done either in nitrogen or vacuum.
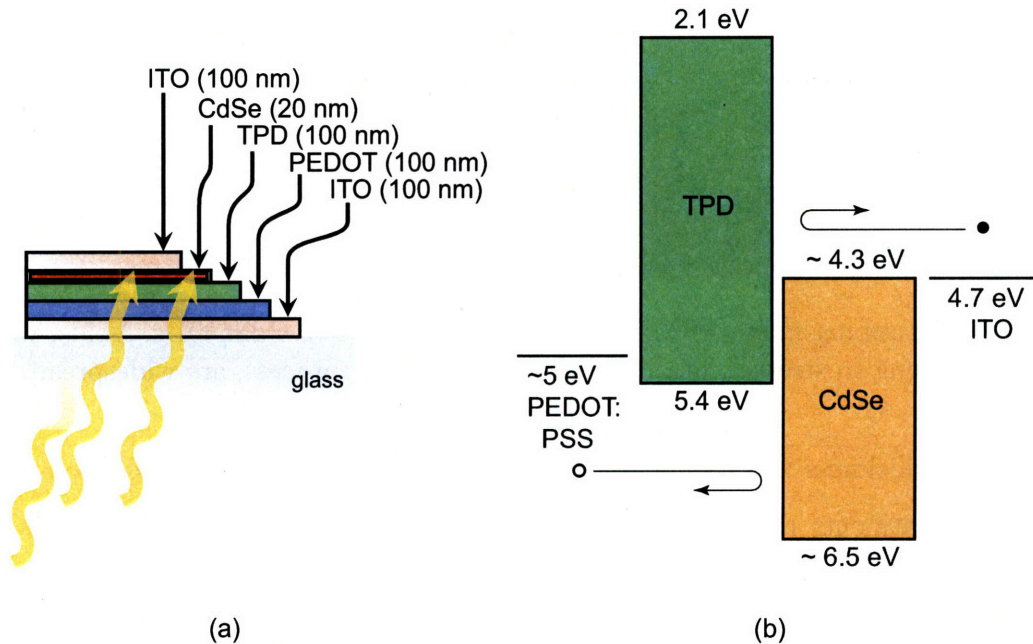
Figure 4-7: Cartoon cutaway view (a) and proposed energy (b) for quasi-*n*-*p* QD-PD. Despite the lack of a dedicated *n*-type layer in this design, this device should exhibit rectification through (1) the electron-blocking nature of TPD and (2) the difficulty of injecting holes into ITO.

TPD. The organic semiconductor TPD was used as a *p*-type blocking layer in this device structure. TPD, purchased from H. W. Sands and purified using train sublimation[132] was thermally evaporated at a pressure $< 5 \times 10^{-6}$ and at a rate of ~ 1 Å s^{-1}. Thickness was typically 100 nm.

CdSe QDs. Ideally, one would like to be able to spin cast the QD layer directly on top of the existing partial device structure (ITO/PEDOT:PSS/TPD). However, in this case, the top layer of the partial device, the molecular organic semiconductor TPD, would be dissolved or chemically damaged by the solvent used for spin casting QDs. Hence, for this device design, an alternative QD deposition method was required. We chose to use elastomeric stamping, which has previously been used successfully with QD-LED fabrication.[134, 126] In the variation used here, a slab of polydimethylsiloxane (PDMS) was cast and cut into small (1 cm $\times$ 1 cm $\times$ 0.5 cm) pieces such that the large faces on an each individual piece were either from the bottom or top face of the large mold and hence very smooth. A QD layer of

107
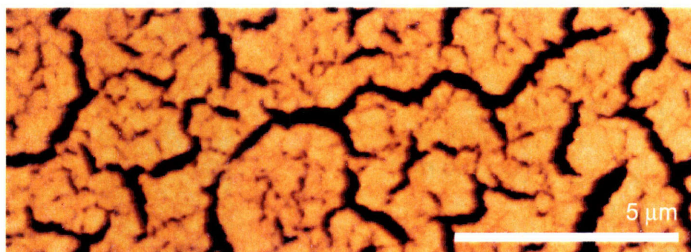
Figure 4-8: Tapping-mode AFM image of stamped layer of CdSe QDs. Voids, which are likely owing to stresses introduced by the stamping process, are widespread.

the desired thickness was then spin-cast onto the PDMS stamp. Any solution-phase chemical treatments applied to the QD film were done at this stage (again, so as not to expose the molecular organic TPD layer to solvent). With some pressure applied, the dried layer was then brought into intimate contact with the partial device structure (glass/ITO/PEDOT:PSS/TPD), and the QD layer was almost completely transferred to the partial device structure from the stamp. An AFM image of the resulting top layer is shown in Fig. 4-8. Despite the widespread appearance of voids, presumably caused by stresses within the film during the stamping process, devices were not shorted owing to the the presence of the electron-blocking TPD layer.

ITO. ITO was RF sputtered directly on top of the CdSe QD layer. A special sputtering procedure was employed in order to avoid damaging the delicate TPD and CdSe QD layers in the normally harsh sputtering environment. First, with a pressure of 5 mTorr Ar and power of 12 W, ITO was sputtered at a rate of 0.05 Å s^{-1} to build up a layer 100 to 200 Å thick. Following this, Ar pressure was lowered to 3 mTorr, power was increased to 55 W, and another 1300 Å ITO were sputtered at a rate of 0.6 Å s^{-1}.

4.3.2   Current-Voltage Characteristics

I-V characteristics were measured at room temperature in an inert environment in the LOOE MBraun glove box system using a Keithley 6487 picoammeter. Devices were never removed from nitrogen atmosphere so that devices could potentially be kept for months without air degradation and tested at a later date. Figure 4-9 shows dark *I-*
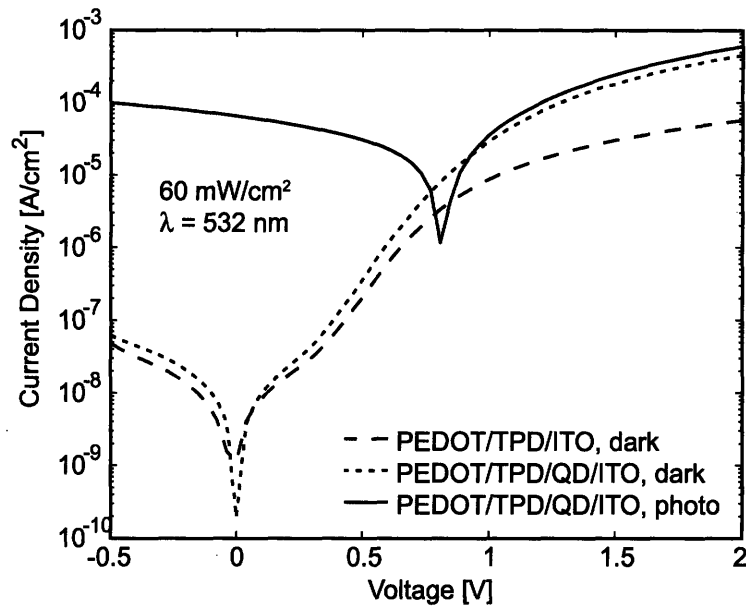
Figure 4-9: Current-voltage characteristics of the quasi-n-p and related devices. The dotted and dashed lines are for quasi-n-p and ITO/PEDOT:PSS/TPD/ITO devices, respectively, in the dark. The expected rectification and moderate injection in forward bias is observed. The solid line represents I-V characteristics of the quasi-n-p device under 60 mW cm^{-2} at $\lambda = 532$ nm.

V characteristics for the reference device (dotted) and the quasi-n-p device (dashed) and I-V characteristics for the quasi-n-p device under 60 mW cm^{-2} illumination at $\lambda = 532$ nm from an LED (Lamina, Light Engine operating at 2 A of current). The top (ITO) electrode was held at ground while the bottom ITO/PEDOT:PSS electrode is connected to the positive lead. Both dark plots show the expected rectification and some appreciable charge injection at more significant forward bias. Interestingly, between 0.5 V and 2.0 V, the quasi-n-p device actually exhibits *increased* current despite the addition of the somewhat resistive CdSe QD layer. An explanation for this is that the position of the CdSe QD conduction band enhances electron injection and subsequent recombination at the TPD/CdSe QD interface [Fig. 4-10(c)].

4.3.3   Open-Circuit Voltage under Modulated Illumination

Figure 4-10 contains three cartoons that depict charge transport behavior. Under zero bias or reverse bias and with illumination, the charge collection mechanism shown in
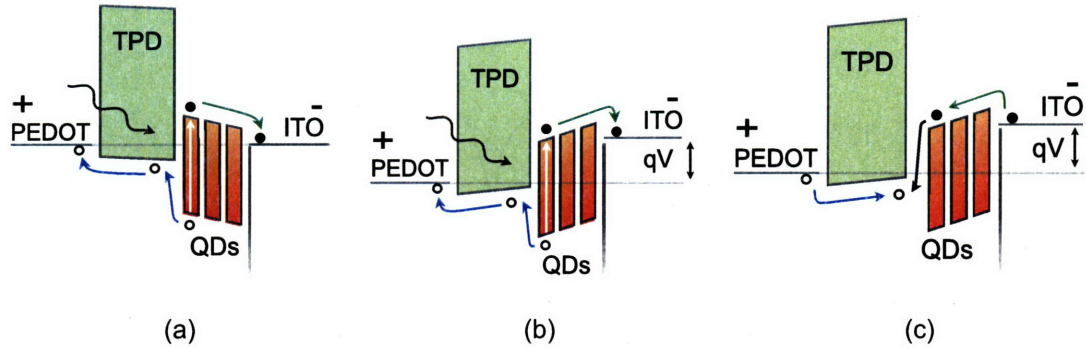
Figure 4-10: Three mechanisms of charge injection into and extraction from the quasi-n-p QD-PD. Panel (a) shows zero-bias extraction of photoexcitons ionized at the TPD/QD heterojunction interface. In reverse bias, this process is even more favorable. Panel (b) depicts that even in slight forward bias, photocurrent extraction is possible. Forward-bias current injection (present independent of illumination), shown in (c), competes with (b) in forward bias. When the two are equal and opposite and the voltage V_{oc}. At $V > V_{oc}$, the injection mechanism in (c) dominates.

Fig. 4-10(a) occurs. However, under forward bias with continuous illumination, two mechanisms—one extracting dissociated photoexcitons [Fig. 4-10(b)], I_{photo}, and one injecting charge [Fig. 4-10(c)], $I_{forward}$—are active. The applied bias at which these two processes cancel each other, resulting in $I = 0$, is V_{oc}. However, by measuring I-V curves using a lock-in amplifier and under modulated excitation, it is possible to extract I_{photo} from the inherently DC $I_{forward}$.[142] This allows us to observe directly the photoinduced built-in potential, or V_{bi}, which is the bias at which I_{photo} [represented by the mechanism in Fig. 4-10(a) and (b)] is completely suppressed. That is, it is the voltage at which diffusion of photogenerated carriers away from the heterojunction interface is exactly balanced by the applied field,[141, 140] and hence the rate of interfacial separation at the heterojunction interface must be equal to the rate of interfacial recombination. Figure 4-11 shows η_{eqe} as a function of voltage at $\lambda = 532$ nm at three representative intensities. While the observed value V_{bi} is invariant at 1.2 V over three orders of magnitude, V_{oc} increases roughly as the logarithm of intensity (Fig. 4-11, inset).
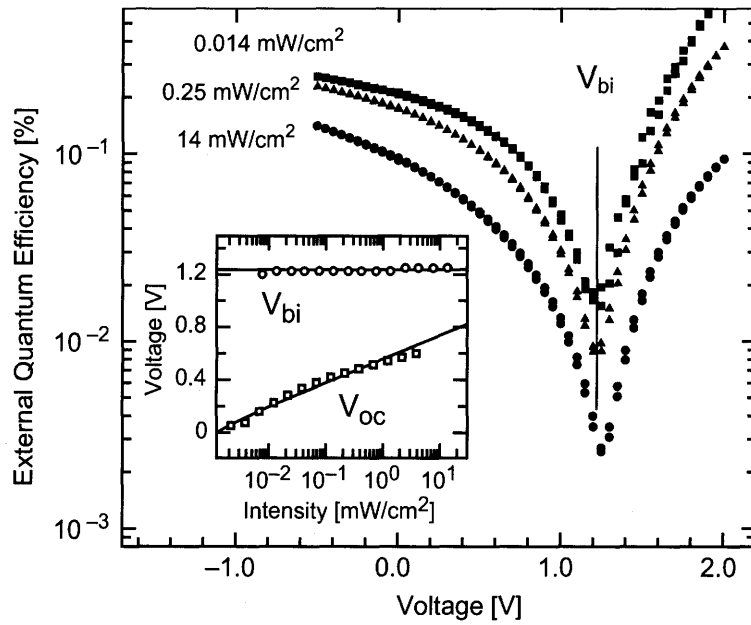
Figure 4-11: Quantum efficiency versus applied bias for quasi-n-p QD-PD, illuminated at $\lambda = 532$ nm at 0.014 mW cm^{-2} (squares), 0.25 mW cm^{-2} (triangles), and 14 mW cm^{-2} (circles). At each voltage step, the chopped photocurrent is measured after a settling-time delay of two seconds. The sharp minimum at 1.2 V occurs as the photocurrent switches polarity (observable as a sharp change in phase, data not shown). This bias point is take to be the built-in potential V_{bi} and is intensity independent (see inset) unlike V_{oc}, which grows roughly as the logarithm intensity.
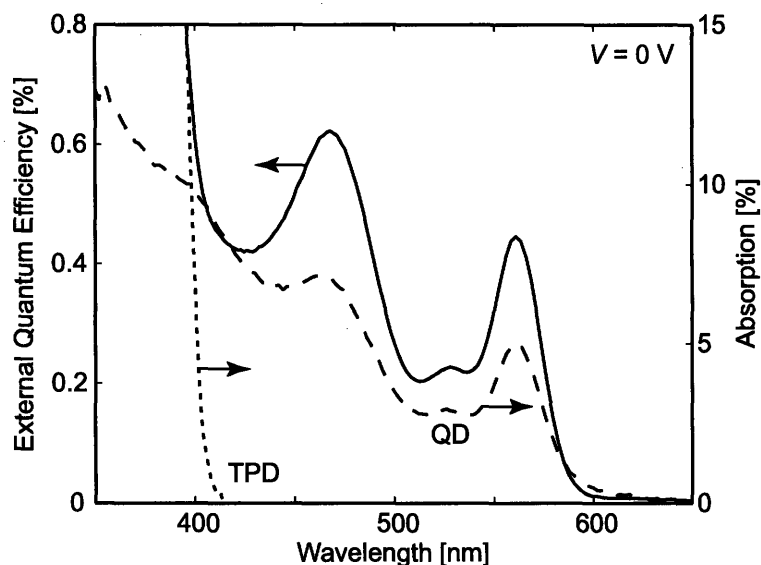
Figure 4-12: Zero-bias external quantum efficiency for ITO/PEDOT:PSS/TPD/QD/-ITO quasi-n-$p$device containing a 20-nm thick CdSe QD film. At the band edge η_{eqe} > 0.4%, which together with an in situ absorption efficiency of 5%, implies that η_{iqe} ~ 9% for λ > 400 nm. For λ > 400 nm, for which the TPD layer is transparent, the device response mirrors the core absorption of the constituent QDs. For λ < 400 nm, the device response is dominated by the absorbance of the much thicker TPD layer.

4.3.4 Quantum Efficiency Measurements

Zero-bias external quantum efficiency spectra were recorded for this device at room temperature. A setup similar to Fig. 3-8(a) was used, except that in this case, measurement was performed in an inert-atmosphere glove box using light from a Xe lamp and a monochromator external to the glove box. Figure 4-12 shows the zero-bias $\eta_{eqe}(\lambda)$ for the quasi-n-p device structure. For λ > 400 nm, for which the TPD layer is transparent, the device response mirrors the core absorption of the constituent QDs. The band-edge η_{eqe} for the device is > 0.4%, and an in situ absorption efficiency was measured to be 5% at the band edge, which implies that η_{iqe} is 9% across for λ > 400 nm. For λ < 400 nm, the device response is dominated by the absorbance of the much thicker TPD layer.

4.4 Discussion

The quasi-*p-i-n* devices discussed in § 4.2 were only marginally successful, owing to the difficulty in depositing high-quality TiO_2 (*n*-type) and TPD (*p*-type) layers, which were expected to play a crucial role as blocking layers. While significantly surpassed in performance by other designs, the quasi-*p-i-n* design demonstrates a straightforward attempt to mimic a solid-state *p-i-n* photodiode.

The quasi-*n-p* device discussed in § 4.3 was considerably more successful. While perhaps not an ideal photodetector itself (owing to limited absorption of the thin QD layer), this design can provide us with insight regarding (1) the importance of interfaces in the zero-bias operation of the thick-slab QD-PDs described in Chapter 3 and (2) the optimal thickness for a heterojunction device designed to operate at zero-bias.

4.4.1 Insight into Thick-Slab QD-PDs

The initial intention in Chapter 3 was to create a device platform that represents a straightforward geometric transformation from the transverse channel electrode test geometry to a layered, sandwich device much larger in area. Our initial expectation was that the device would also be operated in a similar way, at voltage extremes. (Indeed, at $V = -6$ V we measured $\eta_{iqe} = 70 \pm 10\%$.) Ultimately, many of the attractive device metrics reported in Chapter 3 were recorded at $V = 0$ V because of the relative lack of dark current (and the noise and instabilities associated with dark current) at this voltage. Thus, it is useful to learn more about the nature of zero-bias operation in thick-slab QD-PDs.

Figure 4-13(a) depicts a thick-slab QD-PD under illumination above the QD band gap. Although the optical field (and hence absorption) is likely suppressed near the metal electrode,[95] one can assume that photoexcitons are created more or less throughout the 200-nm thick QD film. In zero-bias operation, we observed $\eta_{iqe} < 1\%$. There are two exciton ionization and charge collection limits consistent with this observation. In the first case, depicted in Fig. 4-13(b), only photoexcitons generated

in the shaded area near the PEDOT:PSS/QD interface are ionized—at or very near to the interface—followed by hole collection by the PEDOT:PSS electrode and electron transport through the thick CdSe layer to the silver electrode. This is essentially a heterojunction-interface-driven regime common to organic photodetectors. In the other extreme [Fig. 4-13(c)], photoexcitons throughout the 200-nm thick QD film are ionized uniformly by the slight internal field, estimated to be on the order of 5×10^4 V cm^{-1}, followed by transport of electrons and holes to the Ag and PEDOT:- PSS electrodes, respectively.

To test which case applies, it would be ideal to make a modified thick-slab QD-PD that, instead of containing a film of CdSe QDs 200 nm thick, contains a much thinner film of QDs (20 nm, say). That is, we would like to make a device that is nearly "all interface" and see whether the zero-bias $\eta_{eqe}(\lambda)$ scales with thickness of the film or is largely invariant. Unfortunately, such a thin film of QDs (whether spun-cast or deposited otherwise) will almost invariably be plagued by shorts, making this experiment infeasible. However, the quasi-n-p QD-PD discussed in § 4.3 can perhaps be of use. Because the evaporated TPD layer in this design is free of catastrophic defects and provides the needed barrier between electrodes, the quasi-n-p QD-PD enables us to introduce any thickness of QDs we choose regardless of morphological fidelity.

The limiting behavior shown in Fig. 4-13(b) involves the PEDOT:PSS/QD heterojunction interface, and it is important that the energetics of this interface be roughly preserved for a realistic comparison. The valence band energy level of the organic TPD layer (~ 5.4 eV) is similar to that of the polymer PEDOT:PSS layer (~ 5 eV), creating a similar heterojunction interface with the QD layer so this requirement is approximately met.

When the zero-bias $\eta_{eqe}(\lambda)$ of the thick-slab QD-PD (Chapter 3) is compared to that of its thin-film counterpart (Fig. 4-14), we see that both η_{iqe} *and* $\eta_{eqe}(\lambda)$ in the quasi-n-p device are greater than in the thick-slab QD-PD *despite* the fact that the QD film is only 10% as thick. This strongly suggests that zero-bias operation relies heavily on a thin layer of QD solid near the PEDOT:PSS/QD interface. Further-

(a)

(b)

(c)
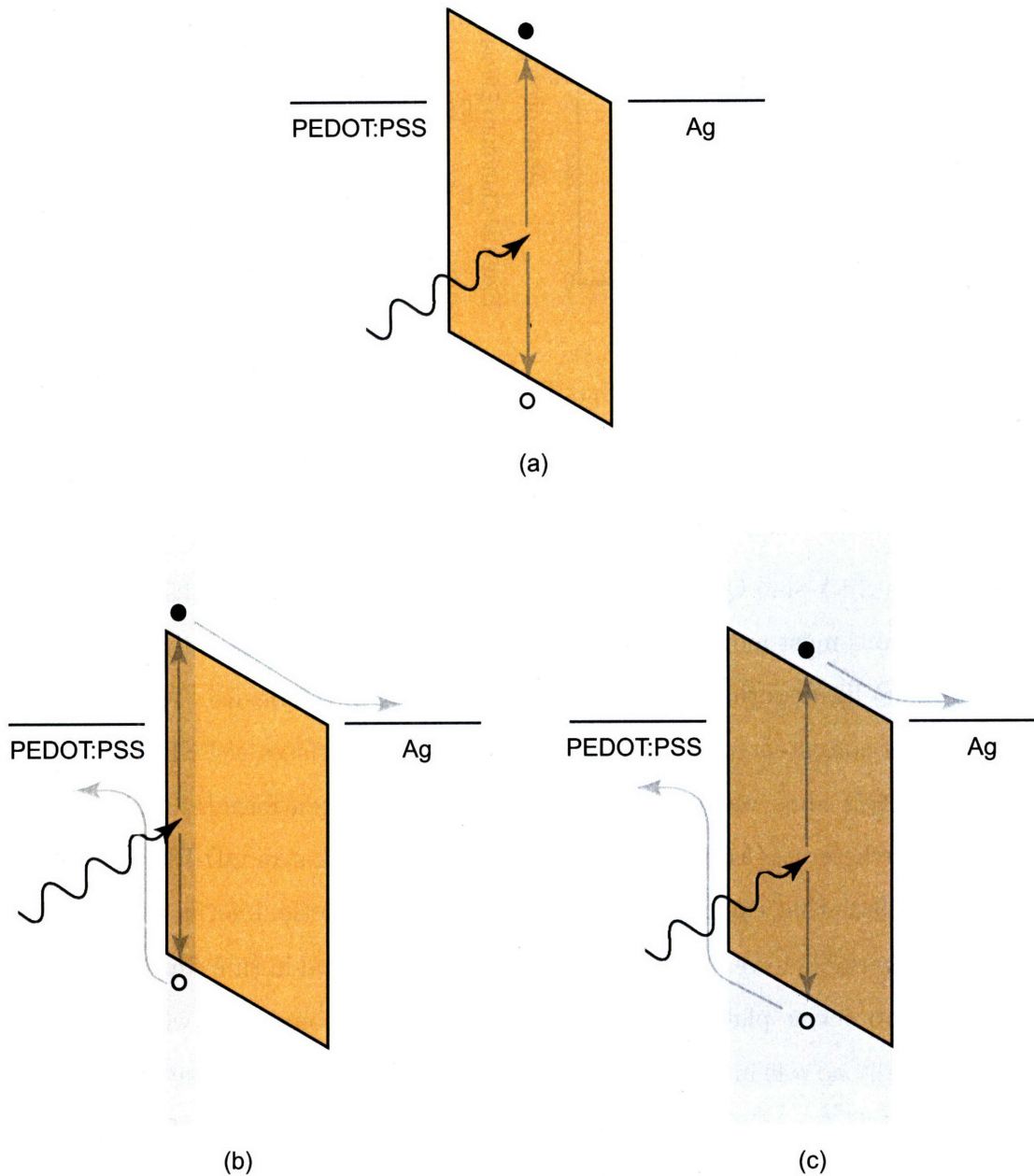
Figure 4-13: Panel (a) depicts the case in which the thick-slab QD-PD is operating under illumination at zero bias. Two charge collection schemes are consistent with zero bias operation. Panel (b) shows an extreme in which the PEDOT:PSS/QD interface plays a critical role in charge separation, and only photoexcitons near the interface give rise to photocurrent. Panel (c) shows the other extreme, in which photoexcitons are separated and collected more or less uniformly throughout the film.
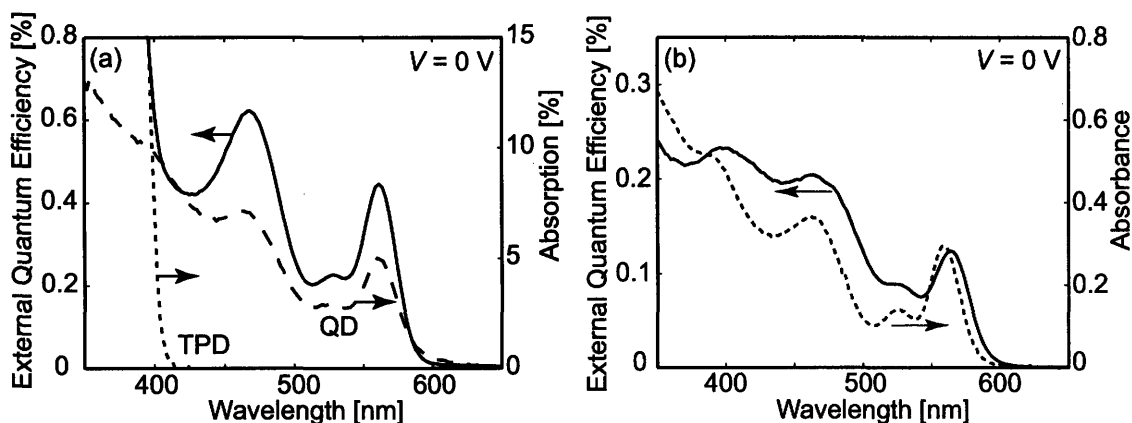
Figure 4-14: Comparison of zero-bias EQE spectra for quasi-n-p (a) and thick-slab (b) QD-PDs. The band-edge η_{eqe} is > 0.4% in (a) compared with < 0.15% in (b). For (a), η_{iqe} was calculated to be 9% based on device absorption compared to $0.6 \pm 0.1\%$ for (b).

more, in the thick-slab QD-PD, the thickness of the films (creating distance through which electrons must move through the device after being generated from excitons at the interface) likely actually diminishes the efficiency of the device. This qualitative conclusion is consistent with a recent study in which interfaces of PEDOT:PSS with graded-size QD films were studied with a more robust platform.[143] However, at larger bias, where $\eta_{eqe}(\lambda)$ was much increased for the thick-slab QD-PD, it is reasonable to conclude that exciton ionization is not confined to the interface region.

While interfaces have long been understood to be critical in thin-film devices,[144] the thick-slab device platform was derived from a test geometry in which interfaces play essentially no role in exciton dissociation.[47, 48] This result reminds us of the importance of interfaces, providing insight into the zero-bias operation of the thick-slab QD-PD, and is potentially useful in designing future generations of devices designed to operate at $V = 0$ V.

4.4.2 Device Performance with Thickness

The section immediately preceeding demonstrated that interfaces play a prominent role in exciton dissociation at $V = 0$ V. This was enabled by a thick TPD layer in the quasi-n-p QD-PD architecture, which allows functioning devices containing QD
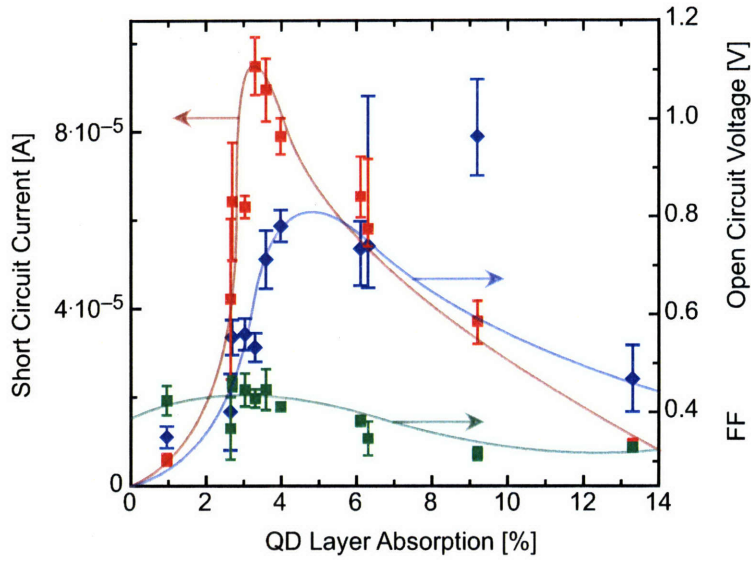
Figure 4-15: QD-PD performance as a function of film absorbance, which is roughly proportional to film thickness. Short-circuit current I_{sc}, fill factor, and open-circuit voltage V_{oc} are all maximized with absorption in the 3 to 5% range, corresponding to a QD film thicknesses of ~ 10 to 17 nm.

layers of arbitrary thickness to be fabricated. The quasi-n-p platform is, therefore, ideally suited to serve as a platform to study the dependence of metrics like η_{eqe}, η_{iqe} and V_{oc} on the thickness of the constituent QD layer.

Figure 4-15 shows preliminary data for such a study, in which several devices were fabricated with η_{abs} ranging from 1% to 13%, corresponding to QD-layer thickness ranging from ~ 4 nm to ~ 40 nm. *I-V* curves were recorded under illumination (94 mW cm^{-2}) at $\lambda = 532$ nm. In this initial plot, metrics particularly relevant to photovoltaics I_{sc}, V_{oc}, and fill factor (FF) are plotted (I_{sc} is proportional to η_{eqe}). Both V_{oc} and I_{sc} are maximzed in the 3 to 5% range, which corresponds to two or three "monolayers" of QDs in thickness.

This interface-thickness study is ongoing, and more devices are planned to better define the dependence of photovoltaic metrics and photodetector metrics on QD film thickness. While simple planar devices are limited in their overall efficiency owing to relatively low η_{abs}, study of optimal interface thickness may help guide the design of interface-based devices containing more complicated interfaces with high-aspect-ratio features and hence increased η_{abs}.

THIS PAGE INTENTIONALLY LEFT BLANK

Chapter 5

Photodetection with PbSe QDs

This chapter is the first of three relating to efforts with PbSe QDs. In this chapter, we describe the synthesis of PbSe QDs and early efforts to incorporate this material into both transverse and layered photodetector structures. In Chapter 6, we discuss a project that illuminated the mechanisms of monomer formation in PbSe syntheses and enabled rational doping modifications of PbSe QD preps which, in turn, allowed for several-fold improvements in particle yield. In the final chapter, we report a brief effort with the Frangioni Group at Harvard Medical School in which PbSe QDs were used to investigate the feasibility of in vivo imaging using the window 1225 nm $<$ $\lambda <$ 1370 nm, whose utility had been strongly suggested previously.[145]

After the initial successes enjoyed with QD-LEDs active in the visible range,[31] a QD material active in the SW-IR was sought. While the primary interest was the SW-IR (and, in particular, the $\lambda = 1.3$ μm and $\lambda = 1.55$ μm wavelengths important for communication), it was also sensible to seek a material that could be tuned well into the mid-IR for potential use in the 3 μm $< \lambda < 5$ μm atmospheric window. While both PbSe and PbS were candidates, a high-quality synthesis of PbSe had already been reported,[41] and, perhaps more importantly, the bulk band gap of PbSe is smaller than that of PbS (0.27 eV compared to 0.41 eV)[146]. This, coupled with the observation that excitons in PbSe have a larger Bohr radius than in PbS (46 nm compared to 20 nm),[1] suggested that PbSe could potentially be tuned over a much

---

[1]Calculated using ϵ, $m_{\perp,n}$, $m_{\parallel,n}$, $m_{\perp,p}$, $m_{\parallel,p}$ from Ref. [146].

wider range of wavelengths (both 1 μm $< \lambda <$ 2.5 μm and 3 μm $< \lambda <$ 5 μm), thus being a more versatile QD material.

Despite the demonstration that PbSe QDs could, in fact, be incorporated into the existing QD-LED architecture with very modest success,[32] nanocrystalline PbSe has generally proved to be a difficult material to incorporate into optoelectronic devices, largely owing to its considerable sensitivity to air, difficulty of exchanging surface ligands, and resistance to overcoating. Early efforts to record current-voltage characteristics for PbSe QDs and to make layered photodetector structures are reported in the following sections. At the end of the chapter, we briefly discuss recent work in our group and others[71] in which PbS is being revisited as a material for use in both interdigitated and layered photodetector structures.

5.1 PbSe QD Syntheses and Processing

Three different variants of the same PbSe QD synthesis were performed, using both coordinating and noncoordinating solvents as the dominent component of the growth solution.[126] The three syntheses, named for the solvent used, were the diphenylether synthesis (DPE), the tri-n-octylphosphine synthesis (TOP), and the octadecene synthesis (ODE). While each has benefits and drawbacks, the procedures are similar enough that they are described only once in the text that follows. Further differences are summarized in Table 5.1, and each of the procedures are more extensively discussed elsewhere [126]. We also describe in this section the air-free workup required to make the samples suitable for incorporation in optoelectronic devices.

380 mg (1 mmol) Pb(OAc)$_2$·3H$_2$O (Alfa) was added to a 50-mL round-bottom flask containing 0.63 mL (2 mmol) oleic acid (TCI) and the solvent for which the particular synthesis is named. The oleic acid, susceptible to oxidation with time, was stored in a freezer in an inert environment prior to use. This mixture of solvents was heated to the degassing temperature under N$_2$, and degassing under vacuum began very slowly to minimize bubbling in the pot and the resultant deposition of the lead salt above the solution line in the flask. Degassing continued for 2 hr before the flask was put

	DPE synthesis[a,b]	TOP synthesis[c]	ODE synthesis[d]
flask volume [mL]	15-25	8-12	15-30
degassing temp. [° C]	71	100	100
injection temp. [° C]	120-180	130	150-230
grow-out time [min]	2-5	3-4	4-6
wavelength [nm]	1400-1700[e]	> 1400	1500-2200
sensitivity to impurities	moderate	high	moderate
stability in growth sol.	poor	poor	good

[a]DPE is a solid at room temperature, and the entire bottle (with cap loosened) was gently heated in a water bath to melt the solid and allow for extraction of the requisite volume with a syringe.

[b]PbSe QD solids made from the DPE synthesis, even thrice flocculated and redispersed, were often cloudy.

[c]*Highly* sensitive to batch of TOP. One batch of TOP proved to be excellent for making high-quality, monodisperse PbSe QDs. Using QDs Jonathan S. Steckel made this way, Seth A. Coe-Sullivan and Steckel were able to produce high-quality 2D hexagonally close-packed structures with single "crystals" several μm across.[126]

[d]Degassing very predictably contained two pressure spikes. The first (smaller) spike corresponded to the solvent being degassed, and the second (larger) spike, which occurred $\sim$ 15 min into degassing corresponded to the formation of $Pb(oleate)_2$ and acetic acid, the latter of which was pulled off and collected in the trap.

[e]Can be extended to 1150-1700 nm with fortuitous batch of TOP.

Table 5.1: Summary comparison of three methods of making PbSe QDs.

under N_2 again and heated to the injection temperature, at which point 5 mL 1.0 M TOPSe (5 mmol Se) at room temperature were injected with vigorous stirring. The heating mantle was left in place and temperature slowly increased toward the injection temperature for several minutes to allow for further, controlled particle growth before being removed and allowing the flask to cool to room temperature. Generally, owing to the instability of the resulting QDs in their growth solution, the contents of the flask were carefully transferred (air-free) within 30 min of injection to two nitrogen-filled 20-mL flasks, which were then pumped into the 4-glove MBraun glove box for further processing. Overall yields were typically $\leq$ 20%.[2] Again, specifics of each of these three related procedures are provided in Table 5.1.

[2]Ref. [126] reports routine yields 30 to 50%. However, the present author consistently experienced lower yields, and perhaps this discrepancy can be explained through the particular batches of TOP used to prepare TOPSe.

5.1.1 PbSe QD Processing

All processing of PbSe QDs was carried out air-free in the 4-glove MBraun glove box. Typically, the PbSe growth solution was divided into two parts, and each was poured into two 50-mL plastic centrifuge tubes. An excess (at least 3:1 of original volume) of a combination methanol and butanol (butanol was added as needed to provide miscibility with the growth solution) was added, and the tubes were spun in a centrifuge (5 min, 3900 RPM) inside the glove box. The supernatant was poured off and the compact rinsed with methanol and drained. The PbSe QD solid in each tube was then dissolved with a minimal amount (usually < 2 mL) of 1,1,2-trichloro-1,2,2-trifluoroethane (CAS [76-13-1]), or TCFE, and the solutions were filtered with a 200-nm syringe filter into 20-mL glass vials, the type of vessels used for the remainder of the processing. Methanol is miscible with TCFE, and sufficient methanol was added to turn the dark, nearly black solution into a opaque, lighter brown solution, indicating a "hard" flocculation.[3] With QDs processed for use in optoelectronic devices, one more iteration of flocculation, redispersion, and filtration was performed (this time with a 100-nm filter, which was sometimes challenging), followed by a final redispersion in TCFE. The vial was then removed from the glove box, and the solvent was gently evaporated on a Schlenk line, never pulling very long after the pressure had decreased to 750 or 500 mTorr. The dried QDs were then returned to the glove box for storage until use. Two examples of this might be dispersion of a small quantity in a 9:1 hexane:octane mixture for drop casting or using the entire solid for preparation of a maximally concentrated solution for spin-casting QD layers for layered QD-PDs.

At times, PbSe QDs were processed without knowledge of their spectral characteristics. In these situations, after the third iteration of flocculation and dispersion in the glove box, roughly one sixth of the processed material was set aside for use in absorption and emission spectroscopy (with absorption spectroscopy requiring the commitment of a considerable amount of material).[4] However, because of the com-

---

[3]Unlike with CdSe QDs in hexane/butanol,[59] it is very difficult to produce with methanol a "soft" flocculation of PbSe QDs in TCFE. As a result, hard flocculations were used at all times for PbSe QDs, even for material intended for use in optoelectronic devices.

[4]Absorbance was measured using a Cary 5000 equipped with an extended InGaAs detector. For

mitment of resources associated with PbSe processing, absorption spectroscopy was sometimes performed *prior* to processing to determine if the batch was worth processing. (This was the often done for PbSe QDs prepared for use in the work in Chapter 7, in which case a fairly specific size of QD was required.) In this latter regime, 2 to 3 mL of growth solution were extracted from flask (while still on the Schlenk line) and quickly processed in air by doing two flocculations/redispersions with the methanol/TCFE system before being dispersed in 2.5 mL TCFE in a cuvette. The remainder of the batch could then be processed air-free if deemed appropriate.

In 2005, it became much more difficult to procure TCFE, presumably owing to its status as a chlorofluorocarbon, and a new processing method, based on hexane and acetone, was developed to allow for conservation of TCFE. While anhydrous hexane is easily purchased and passed into the glove box, "anhydrous" acetone was prepared in our lab by briefly "degassing" acetone at room temperature several times before transferring it to a bottle containing a generous layer of appropriate molecular sieves (Aldrich) that had just been activated. The sealed bottle was then passed into the glove box.

Using this method, the initial crash-out is the same as described above, but for subsequent iterations, the redispersions were performed with a minimal amount of hexane, and flocculation was done with acetone. Unlike the TCFE/methanol system, the flocculation point for hexane/acetone was much less well defined, and supernatant generally was colored even after the addition of considerable excess acetone. A final redispersion (this time in hexane) was dried as before. The advantage of this method is that the financially and environmentally costly TCFE can be used only for dispersions prepared for absorption or emission spectroscopy. However, one disadvantage of this method is that the yield of the processing procedure is probably < 50% of the yield for the traditional TCFE procedure, amplifying the problem of poor yields in PbSe QD syntheses.

---

emission, the excitation source was a HeNe laser ($\lambda = 633$ nm), and the resulting emission was dispersed on a 512×1 InGaAs linear array using an Acton 300i monochromator equipped with a 100 g mm^{-1} grating blazed at $\lambda = 1600$ nm.

5.2 PbSe QD Current-Voltage Studies

In this section, we report first steps toward investigations parallel to previous, extensive *I-V* photoconductivity studies on CdSe QD solids in this lab.[46, 47, 59] The goals were (1) to develop a processing method to produce PbSe QDs suitable for inclusion in optoelectronic devices, and (2) to discover chemical annealing procedures that would increase photoconductivity by orders of magnitude *and* qualitatively change the shape of the *I-V* characteristics, ideally demonstrating current saturation (indicating $\eta_{iqe} = 1$) as was observed in the CdSe system after treatment with *n*-butylamine.[48]. Because very specific observations were sought, some modest improvements in photocurrent observed after methanol exposure (a method now reported in the literature for photocurrent improvement in PbS QD solids) were disregarded.

5.2.1 Current-Voltage Studies of Untreated Films

PbSe QDs were synthesized and processed air-free as reported in § 5.1. A small quantity of the QD "powder" was dissolved in a 9:1 hexane:octane solution and was drop-cast on transverse channel geometry "chips" of the type used for CdSe photoconductivity studies.[59, 48] Both 1- and 2-μm channels were patterned on these chips, and 2-μm channels were used for these studies owing an excess in our lab of chips with "good" 2-μm channels and shorted 1-μm channels. Chips were cleaned with water, acetone, and isopropanol and were thoroughly dried before being glued into 28-pin DIPs with silver paint. Three sets of bar electrodes (corresponding to three channels) were then wired to the DIP using fine gold wire with the wire-bonder available at the MIT Microsystems Technology Laboratory (MTL). The assembled chips were introduced to an inert-atmosphere glove-box, PbSe QD films were drop-cast, and films were allowed to dry at room temperature over night.

PbSe QD transverse channel devices in DIPs were loaded into a cryostat[131] in the glove box, and the entire sealed assembly was removed from the glove box and then evacuated to a pressure of $\sim$ 1 mTorr using an oil diffusion pump backed by a mechanical pump. The cryostat was typically under dynamic vacuum for the entirety
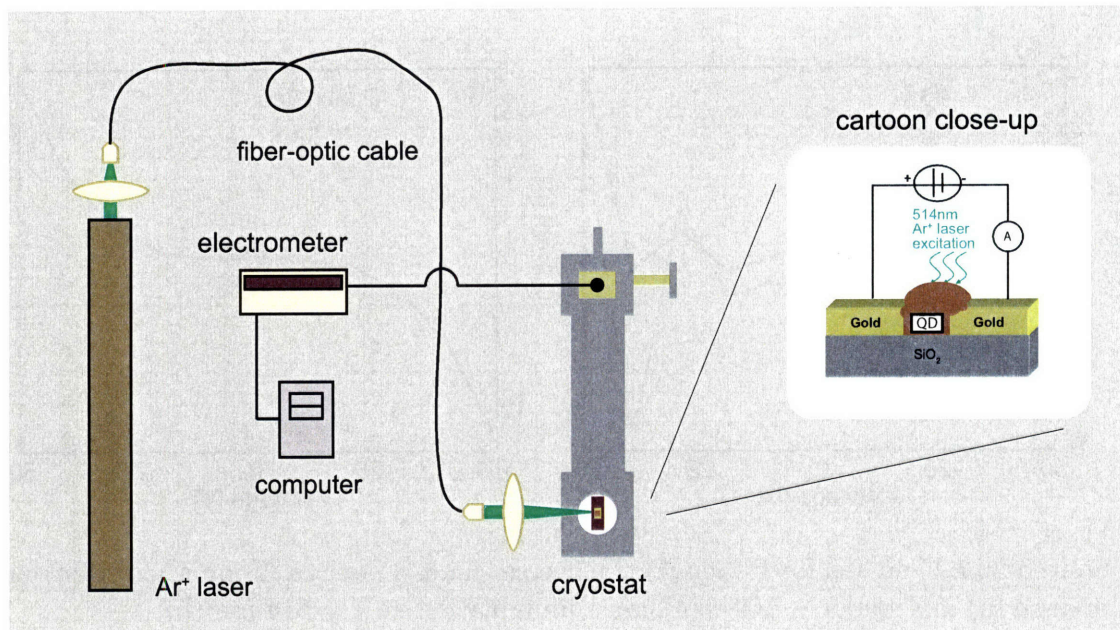
Figure 5-1: *I-V* measurement setup for transverse channel devices.

of photoconductivity experiments. Liquid nitrogen was sometimes introduced into the cryostat to cool the cold finger (equipped with a resistance heater) to 77 K. Otherwise, measurements were taken at ambient temperatures.

Figure 5-1 depicts the setup used for simple dark current and photocurrent measurements on transverse channel devices. Briefly, either in a dark room or under illumination at ~ 100 mW cm^{-2} with an Ar$^+$ laser at $\lambda = 514$ nm, voltage was applied and current measured with a Keithley 6517 electrometer. Coaxial cables connected to the cryostat cables were additionally shielded with metal sheathing, attached to the laser table, which was used in this setup as the single source of electrical ground. The electrometer was operated by a computer through a LabVIEW interface, and generally a scan was started at 0 V, increased to the maximum positive voltage by set increments (waiting 30 s at each voltage for the current to settle), and decreased to the (negative) voltage extreme before returning to 0 V and terminating the scan.

Figure 5-2(a) and (b) show typical current-voltage characteristics for a PbSe QD film at 77 K in the dark and under illumination, respectively. As was reported for CdSe QDs,[59] the absolute magnitude of the current-voltage characteristics was observed to vary by an order of magnitude or more depending on the QD synthesis used
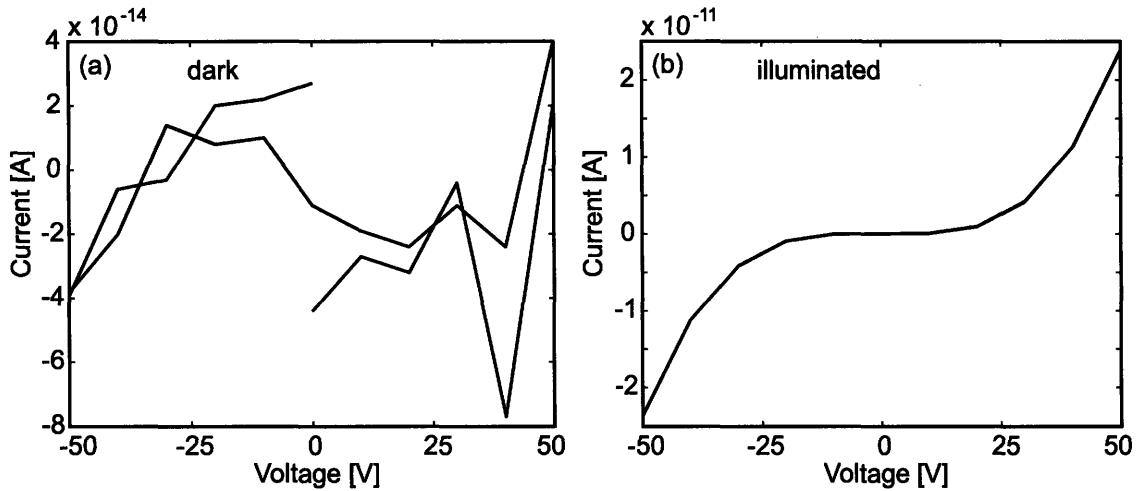
Figure 5-2: *I-V* curves for PbSe QD transverse channel devices (2 μm separation) in the dark (a) and under $\sim$ 100 mW cm^{-1} illumination at $\lambda = 514$ nm (b).

and the exact processing conditions. The plots in Fig. 5-2 are representative.[5] The dark current plot in Fig. 5-2(a) represent noise more than anything else; no injected current is evident. In Fig. 5-2, photocurrent is observed and reaches 25 pA at 50 V, at which point the applied field is 2.5 $\times$ 10^5 V cm^{-1}. Also similar to untreated CdSe QD films is the general shape of the *I-V* curves, which is everywhere a general exponential shape. This is indicative of exciton dissociation efficiency $\eta_d < 1$.[48] Photocurrent levels recorded at 300 K were, in general, roughly one order of magnitude lower than at 77 K, presumably owing to more efficient geminate recombination of photoexcitons.[131]

Also of interest in the transverse channel geometry is the ability to produce a plot like that shown in Fig. 2-2 (for CdSe QDs) in which the photocurrent as a function of incident wavelength, $I_{photo}(\lambda)$, is shown to be in good agreement with the absorbance spectrum of the constituent QDs. Using a tungsten lamp and near-IR monochromator (shown in Fig. 5-9 and discussed further below), near-IR light incident on a 2-μm channel device ($V = 100$ V applied) was swept from $\lambda = 2.0$ μm to $\lambda = 1.0$ μm, and the resulting photocurrent excitation trace is shown with the

---

[5]All *I-V* curves shown in this chapter are actual data. Dark current data were *not* subtracted from corresponding current-voltage data recorded under illumination to produce "corrected" photocurrent vs. voltage plots.
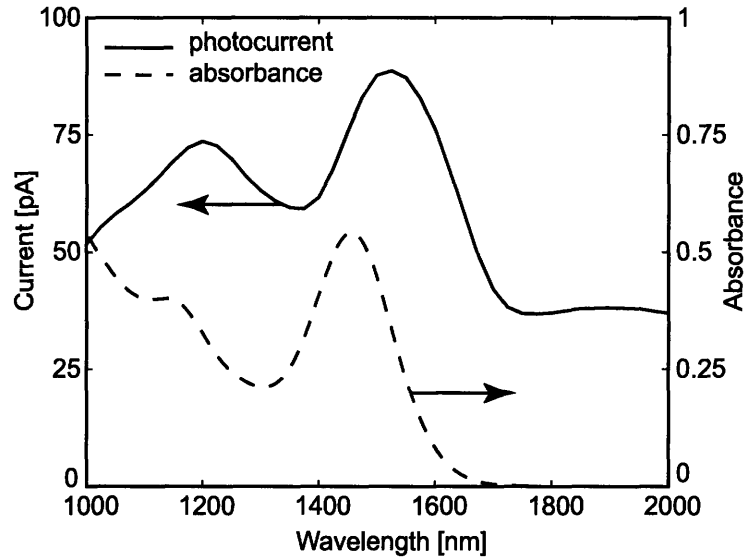
Figure 5-3: Photocurrent spectrum (solid) at $V = 100$ V for a transverse 2-μm bar electrode gap device compared to the absorbance spectrum (dashed) of the constituent PbSe QDs. There is good agreement between the two spectra, with the DC current offset being attributed to dark current. The slight shift of the photocurrent spectrum to lower energy is attributed to some combination of red shift in the film and possible miscalibration of the monochromator at the time of the experiment.

solid line in Fig. 5-3. The photocurrent excitation spectrum compares well with the dashed absorbance spectrum of the constituent PbSe QDs.

5.2.2   Methanol and Sodium-Hydroxide Treatments

While photocurrent was sufficient to be detected in PbSe QD films in the 2-μm channel design (Fig. 5-2), η_d was still clearly less than unity and photocurrent levels were low (even compared to devices containing nascent CdSe QD solids). We were thus motivated to pursue solution-phase chemical treatments, initially reported in Ref. [49] and at the time under investigation in our lab [48]. The treatment that showed the most promise at the time in CdSe QD films was methanol saturated with sodium hydroxide,[6] and results of this treatment are discussed here.

PbSe QDs were synthesized and processed as described above, and QD solids were

---

[6]Since the time of this work, 0.1-M n-butylamine in acetonitrile has superseded NaOH-saturated methanol as the treatment of choice for CdSe QDs. These two treatments give similar improvements in observed photocurrent, but more hysteresis and less reproducibility was observed for the latter treatment, making it less desirable.

127

drop-cast. Current-voltage characteristics were measured for the untreated films to establish a point of reference. Afterward, the cryostat was passed back into a glove box and the measurement chip removed. Sodium hydroxide was added to anhydrous methanol (in an inert environment) to the point of saturation, and the chip was submerged in the solution for 10 min and then rinsed with methanol. ("Control" treatments, in which the PbSe QD films were treated with methanol only, were also performed.) The chip was then heated to 70 °C for 1 hr and loaded back into the cryostat for measurement.

Methanol-only treatments. Figure 5-4 shows the effect of a methanol-only treatment on dark current and photocurrent in a 2-μm channel device. In Fig. 5-4(a), we see pre-treatment dark current, which can be understood to be largely instrument noise for $|V| < 80$ V, at which point there is some measurable current, presumably owing to injection into the PbSe QD film from the gold electrodes.[7] Under illumination with ~ 100 mW cm^{-2} at $\lambda = 514$ nm, photocurrent reaches 200 pA at $|V| = 100$ V, but the shape of the curve indicates that the photoexciton ionization efficiency η_d is still less than unity for all voltages applied. Figure 5-4(c) shows that after treatment with methanol, dark current increases by two or three orders of magnitude, perhaps supporting the suspicion that charge injection from Au into PbSe QD is possible. (The voltage range was limited to $|V| \leq 50$ V for this particular scan owing to the concern that the device might short if the usual $|V| \leq 100$ V range was used.) Finally, Fig. 5-4(d) shows the photocurrent (same excitation as control device) after treatment with methanol. The photocurrent increases by nearly two orders of magnitude, and reaches > 10 nA at $|V| = 100$ V. Comparing this magnitude to the saturated current in Ref. [48] suggests a gain in excess of unity, which is consistent with recent studies of CdTe QD solids, in which holes are injected by gold contacts.[70] The shape of the current-voltage plot, "less" exponential than the control plot (but neither linear nor saturating), is also interesting but not easily explained.

---

[7]While Au electrodes are understood to be non-injecting, or "blocking" for CdSe QD solids,[48] they may be capable of injecting one or both carriers into PbSe QD solids, for which the absolute position of the band gap is unknown. Au electrodes are known to inject holes into CdTe QD solids.[70]
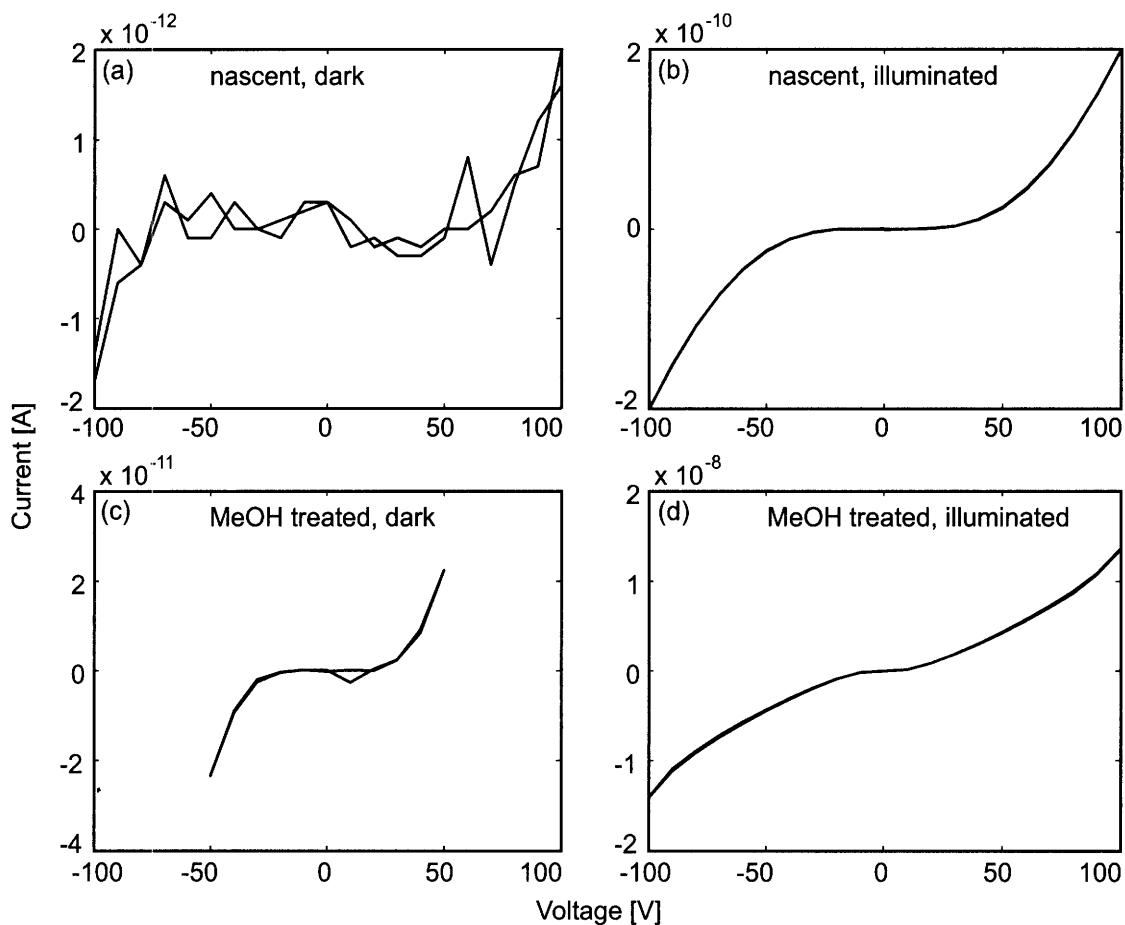
Figure 5-4: Dark and illuminated (~ 100 mW cm^{-2} at $\lambda = 514$ nm) current-voltage traces for PbSe QD films at 77 K prior to treatment [panels (a) and (b)] and after treatment with methanol [panels (c) and (d)]. Increases of two or three orders of magnitude are observed with in both dark current [panels (a) and (c)] and photocurrent [panels (b) and (d)] plots. While the shape of the I-V trace in (d) exhibits an interesting shape, not being as strongly exponential as plots is usually observed, no "saturated" region, corresponding to exciton dissociation efficiency $\eta_d = 1$, is observed.
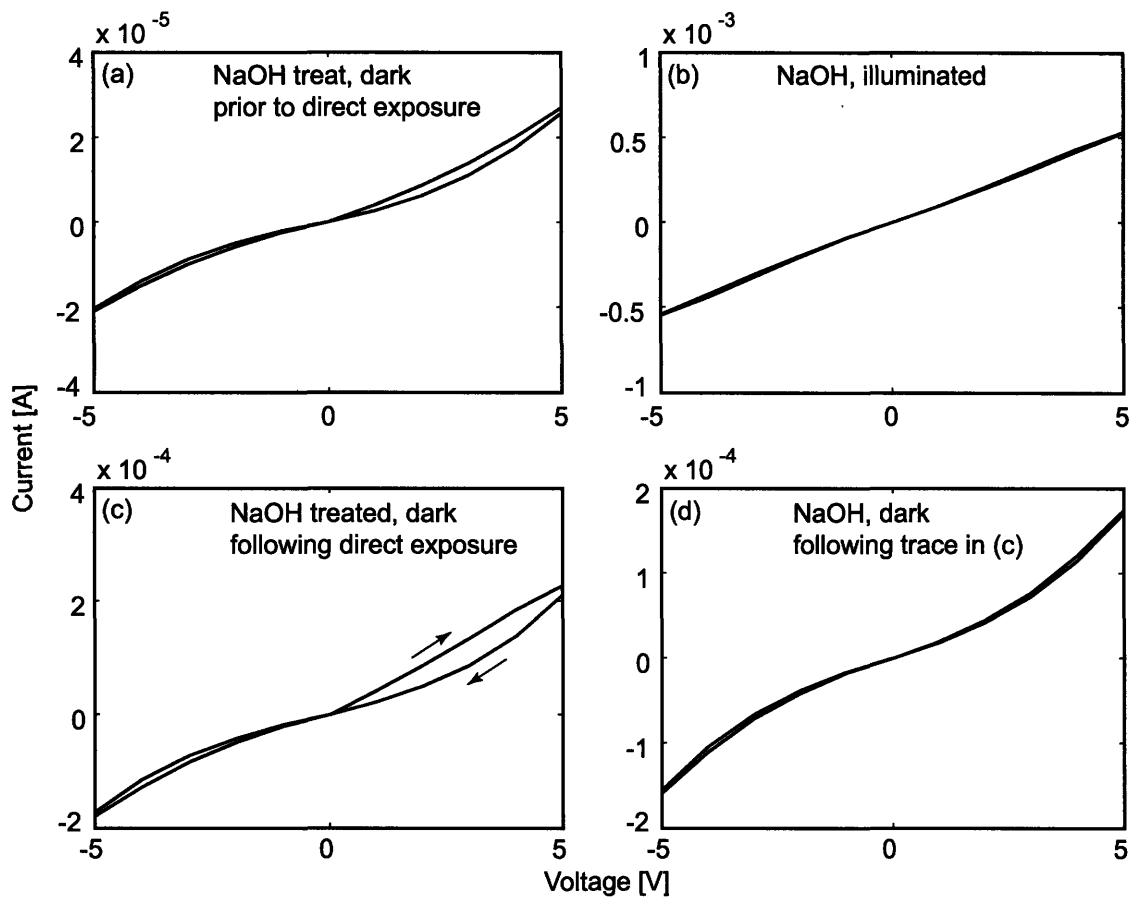
Figure 5-5: A sequence of room-temperature *I-V* characteristics after treatment with methanol saturated with NaOH. Of particular note are the very modest voltages used ($|V| < 5$ V) and very high current levels observed. Panel (a) shows initial dark current plot; (b) shows current until ~ 100 mW cm^{-2} at $\lambda = 514$ nm, which has nearly a linear shape; (c) shows dark current, immediately following (b), showing an increase by an order of magnitude and considerable hysteresis on the upward voltage sweep; (d) shows a second dark trace, immediately following (c), in which the current level is reduced by roughly 20% and the hysterisis is not observed.

NaOH-in-methanol treatments. Current-voltage characteristics for PbSe QD solids treated with NaOH-saturated methanol are shown in Figure 5-5(a)-(d). [Untreated, reference films are consistent with those in Fig. 5-4(a)-(b).] One feature of note about the data shown in Fig. 5-5 is the very limited voltage range used—applied voltage is limited to $|V| \leq 5$ V. Figure 5-4(a) shows dark current prior to prolonged exposure to ~ 100 mW cm^{-2} at $\lambda = 514$ nm. Some weak hysteresis is observed, and $I_{dark}(5 \text{ V}) > 20$ μA. Figure 5-4(b) shows the (nearly linear) photocurrent trace, reaching 500 μA at $|V| = 5$ V. Work with NaOH-treated PbSe QD films was hindered by large persistent photocurrents, and Fig. 5-5(c)-(d) illustrate this elevated dark current level, with the first dark current trace immediately after illumination (c), showing some hysteresis on the first upward sweep, followed by (d), a second dark current plot with no hysteresis but current levels nearly an order of magnitude higher than those seen in Fig. 5-5(a). [In fact, it is likely that the "initial" dark current trace shown in Fig. 5-5(a) was, in fact, representative of some persistent photocurrent, in part supported by the hysteresis seen in the first upward voltage sweep.] This lengthy persistence of photocurrent gave rise to badly drifting measurements and caused this treatment method to be judged dubious at the time.

Spectroscopic effects of treatments on thin films. The effect of methanol and NaOH treatments on the absorption and emission of PbSe QD films was studied by drop-casting films—identical in preparation to those used in photocurrent studies—on glass slides, allowing them to dry, and performing analogous treatments. Because of the air sensitivity of the samples, drop-casting and treatments were carried out in an inert atmosphere, and films were sealed using a cover slip and UV-curable epoxy available in the LOOE system. The absorption and emission comparisons are shown in Fig. 5-6. In Fig. 5-6(a), we see that the band-edge absorption features of the untreated film and methanol-treated films are in good agreement, whereas the corresponding feature for the NaOH-treated film is slightly broadened and shifted ~ 50 nm to higher wavelength. This is consistent with the interpretation that there is more significant aggregation (and core-to-core contact) in the NaOH-treated film than in the other two. The increase in overall absorbance with severity of treat-
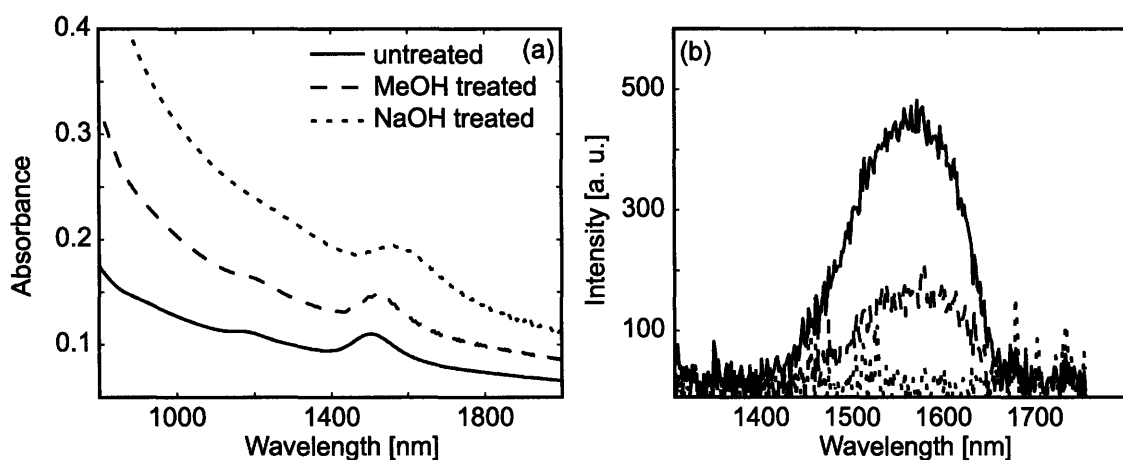
Figure 5-6: Absorbance (a) and photoluminescence (b) spectra of PbSe QD films either untreated (solid) or after treatment with methanol (dashed) or NaOH in methanol (dotted). In panel (a), the absorbance of the untreated and methanol-treated films is in rough agreement, whereas the band-edge peak of the NaOH-treated film is shifted to the red roughly 50 nm, presumably owing to "necking." The increasing overall absorbance untreated → methanol-treated → NaOH-treated is attributed to increased film scatter. The photoluminescence spectra in panel (b), while noisy, show a decrease in fluorescence untreated → methanol-treated → NaOH-treated, which we attribute to more and more ligand being stripped from the surfaces of the QDs with harsher treatments.
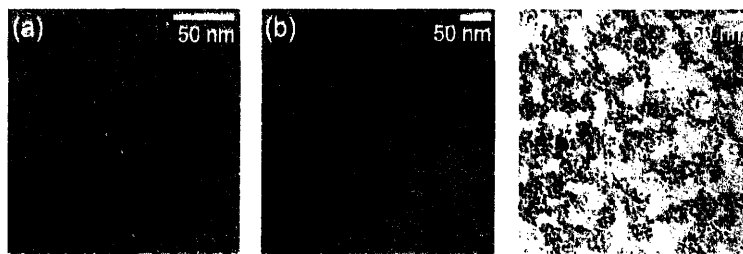
Figure 5-7: TEM images of monolayers or sub-monolayers of PbSe QDs before treatment (a) and after treatment with methanol (b) and methanol saturated with NaOH (c). Considerable aggregation is observed in panels (b) and (c), with (c) demonstrating few remaining isolated particles. (Electron microscopy courtesy of John P. Zimmer. Panels (a) and (b) were produced with JEOL 2000; panel (c) was recorded with JEOL 200.)

ment reflects an increase in the opacity (scatter) of the films after treatment. In Fig. 5-6(b), emission spectra from three analogous films are shown. Excitation was done with a HeNe laser, and emission was dispersed and detected with a 512-pixel InGaAs linear array interfaced with an Acton 300i spectrometer. The untreated film exhibited luminescence roughly three times as great as the methanol-treated film, which may be slightly red-shifted, and the NaOH treated film shows essentially no detectable photoluminescence. This is again consistent with the interpretation that the NaOH treatment is stripping surface ligands severely, followed by intimate PbSe QD aggregation.

Transmission electron microscopy (TEM). TEM was performed on PbSe QD films drop-cast on TEM grids, some of which were then treated with either methanol alone or methanol saturated with NaOH. While the untreated film in Fig. 5-7(a) shows close packing, with cores separated by > 1 nm, the treated samples in (b) and particularly in (c) show significant aggregation, indicating that both the methanol and NaOH treatments are removing capping ligands to a great extent. This is consistent with the fluorescence decrease seen in Fig. 5-6. While this was regarded as a drawback of the treatments at the time, more recent work with PbS QDs has shown significant promise for methanol-treated films in which similar "necking" (or core-to-core contact) is observed.[147]

133
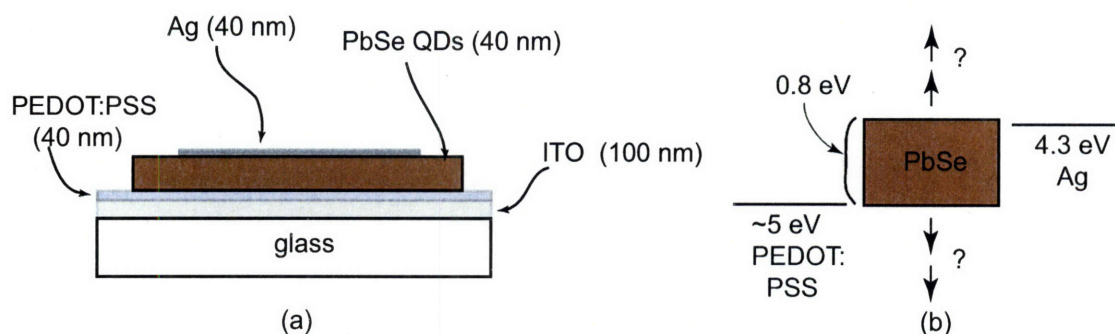
Figure 5-8: Cartoons of layered PbSe QD-PD cutaway (a) and proposed band structure (b). While the band gap of PbSe either in bulk or nanocrystalline form is trivial to determine, the position of the band gap *relative to vacuum* is unknown. Panel (b) reflects this uncertainty, which makes more difficult the rational design of devices containing PbSe QDs.

5.3 Layered PbSe QD Structures

The eventual goal of the work discussed in § 5.2 was to develop the conductivity-enhancing chemical treatments necessary to use PbSe QDs as a material set that could be substituted at will for CdSe QDs in any existing device structure. While these goals were not achieved, layered QD-PDs based on the thick-slab design in Chapter 3 were nonetheless constructed, and these brief efforts are discussed in this section. Device throughput, already a challenge because of the dispersed lab spaces and diverse tasks almost entirely under the responsibility of a single researcher, was made even more difficult by (1) the relatively low yields ($\leq 10\%$) of PbSe QD syntheses compared to CdSe syntheses (yields $\sim 50\%$) and (2) the necessity to handle all manipulations of PbSe QDs air-free. This made the "search" phase of the project (in which no data even of diagnostic value is collected) exceedingly taxing and discouraging. Below we describe the fabrication of thick-slab PbSe QD-PDs and some of the few measurements that yielded sensible results.

5.3.1 Design and Fabrication

Layered PbSe QD-PDs were constructed having the layered structure depicted in the cutaway cartoon in Fig. 5-8(a). The patterning of the ITO, the preparation of the

PEDOT:PSS layer, the spin-coating and treatment of the QDs, and the evaporation of the top Ag electrode were all essentially identical to procedures outlined in § 3.2. Typically, an entire processed PbSe QD batch synthesis was processed according to (§ 5.1) and was dissolved in the minimal amount of chloroform ($\sim$ 0.15 mL) to spin-cast films on one or two half-inch substrates. This is in contrast to CdSe QDs, for which the concentration of films was consistently calibrated using absorbance measurements and in which one synthesis could produce at least three such device runs. Despite the effort to create maximally thick PbSe QD films, the most significant difference between CdSe QD-PD and PbSe QD-PD structures, evident from Fig. 5-8(a), was the thickness of the QD layer (measured via profilometry to be $\sim$ 40 nm versus $\sim$ 200 nm for CdSe).[8]

While there was no evidence that treatment with n-butylamine in acetonitrile would enhance the photoconductivity of PbSe QD solids,[9] the procedure was performed nonetheless. Treatments, in general, had the effect of making the PbSe QD films more reflective in the visible spectrum.

Figure 5-8(b) depicts an energy band structure for the resulting device. In general, one can estimate the position of confined band gaps based on bulk values and the relative electron and hole effective masses. (This is routinely done for CdSe QDs.) In contrast to CdSe QDs, however, the position of the band gap of bulk PbSe relative to vacuum is not known, making such an estimate impossible. One possibility for the position (which would work well for our detector design) is shown in Fig. 5-8(b), but there could be considerable deviation from this guess. Hence, the interpretation of the zero-bias response with modulated illumination and the response under swept bias with continuous illumination is particularly challenging.

---

[8]While profilometry measurement consistently indicated the PbSe films were a factor of five thinner than CdSe films, profiles were not ideal. Unlike n-butylamine-treated CdSe QD films, which were not scratched by the profilometer stylus, PbSe QD films did exhibit some scoring, perhaps indicating a somewhat compromised measurement.

[9]While PbSe QDs were responsive to methanol and NaOH treatments, it is reasonable to assume that treatments that are effectively an in situ ligand exchange—such as the n-butylamine treatment—would be largely ineffective. To the author's knowledge, no one in the Bawendi Lab has ever been able to effectively ligand-exchange PbSe QDs.
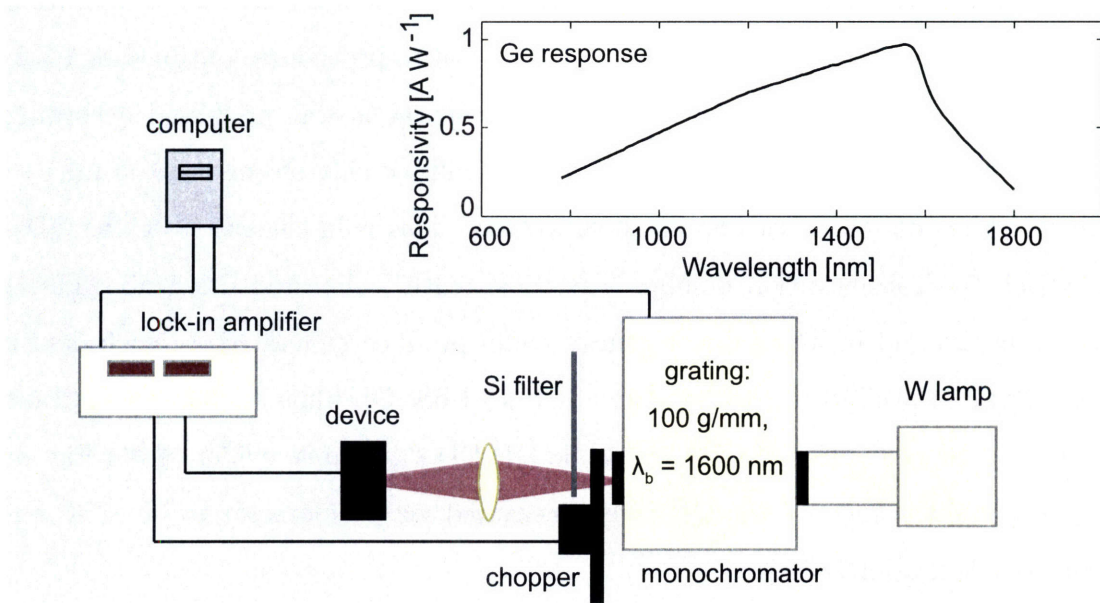
Figure 5-9: Experimental setup with which $\eta_{eqe}(\lambda)$ was measured for the PbSe QD-PD. Light from a W lamp dispersed by an infrared monochromator was modulated and filtered with silicon before falling either on a calibrated Ge photodetector or a PbSe QD-PD.

5.3.2 Device Characteristics

The extent to which PbSe QD-PDs were characterized was limited by the difficult task of producing working devices. External quantum efficiency was measured using the setup shown in Fig. 5-9. Emission from a tungsten filament lamp interfaced with an Acton 300i monochromator (equipped with a 100 grooves mm^{-1} grating, blazed at $\lambda = 1600$ nm) was used to access 1.0 μm $< \lambda < 1.8$ μm. A silicon wafer polished on both sides was used as a filter to remove higher-order output from the monochromator, and this filtered light was focused either on a calibrated germanium detector or a PbSe QD-PD pixel. Light was chopped at $f < 100$ Hz, and a lock-in amplifier was used to collect photocurrent signal.

Despite the very low overall external quantum efficiency observed ($\eta_{eqe} < 0.001\%$ at the band edge), Fig. 5-10 shows good agreement between features in the absorbance spectrum of the constituent PbSe QDs near the band edge. (The sharp decrease in photocurrent for $\lambda < 1100$ nm is owing to the silicon filter at the exit slit of the
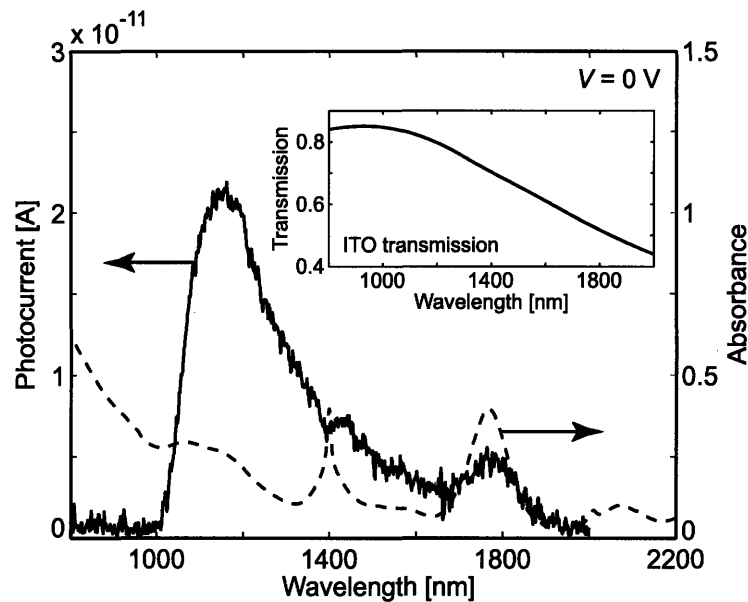
Figure 5-10: The zero-bias photocurrent excitation spectrum of a PbSe QD-PD displays band-edge features consistent with the absorbance of constituent PbSe QDs in solution. The sharp peak at $\lambda = 1400$ nm is a combination of absorption from the constituent QDs and overtones of residual solvent. The inset plot shows the transmission spectrum of an ITO-coated glass substrate, showing a significant increase in absorption and reflectance from $\lambda = 1000$ nm $\rightarrow$ 2000 nm.

monochromator.) One puzzling feature is the significant falloff in photocurrent from $\lambda = 1100$ nm $\rightarrow$ 1800 nm, which is even more severe for $\eta_{eqe}(\lambda)$ than in the plot of $I_{photo}(\lambda)$ shown. If anything, one would expect η_{eqe} to *increase* as wavelength increases toward the band edge owing to more efficient geminate recombination higher in the exciton manifold.[47] One cause of this falloff could be reduced transmission of ITO, which is known absorb in the near-IR depending on composition.[148] The inset to Fig. 5-10 shows the transmission spectrum of a glass/ITO substrate, measured at normal incidence with a Cary 5000 spectrophotometer. It shows a two-fold reduction in transmission from > 80% to just over 40% from $\lambda = 1000$ nm to 2000 nm. Another contribution to the band-edge falloff in η_{eqe} could be decreasing overlap, as wavelength increases, between the optical field and the PbSe QD film, which is in close proximity to the metal electrode, where the optical field is suppressed.[95]

Current-voltage characteristics were measured sparingly for PbSe QD-PDs because experience with CdSe QD-PDs indicated that high-quality *I-V* results were a
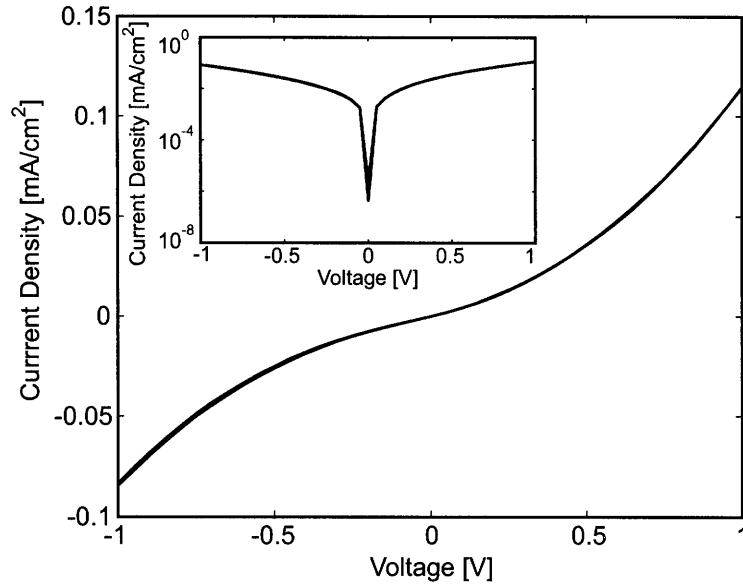
Figure 5-11: Current-voltage curve (dark) for PbSe QD-PD. Though the curve is not linear and very steep (which together would indicate catastrophic shorting), it is two to three orders of magnitude higher than a working CdSe QD-PD across the same voltage range. This may indicate ease of charge injection into the film.

more stringent test of a device pixel than was the ability to produce an $\eta_{eqe}(\lambda)$ with modulated illumination at zero bias. Those PbSe QD-PDs that were measured under constant illumination while sweeping applied voltage with an HP 4156c semiconductor parameter analyzer never exhibited a measurable photoeffect.

Figure 5-11 shows a typical dark current trace for a PbSe QD-PD (semilog plot inset) over a very limited voltage range ($|V| \leq 1$ V). Unlike I-V traces measured in the channel geometry, the bias was scanned from -1 V and increased to 1 V before returning to -1 V. No hysteresis was observed. While the dark current levels observed were two-to-three orders of magnitude higher than with similar CdSe QD-PD devices, there is curvature in the shape of the I-V plot, indicating that perhaps the devices were, in fact, *not* catastrophically shorted. This may be indicative of facile hole injection from Au electrodes into the PbSe QD film, as observed with CdTe QDs.[70]

5.4   Conclusions from Work with PbSe QDs

In this highly descriptive chapter, we discuss first-pass efforts to understand the photoconductivity of PbSe QD solids in a channel geometry and to incorporate the material in an existing layered QD-PD architecture. A person familiar with the successes producing both n-FETs and p-FETs with PbSe QDs, as described in Ref. [61], for example, might wonder why the work with PbSe QDs described here was shallow and relatively fruitless. The best explanation available seems to be a combination of inexperience, mindset, and throughput.

Data from PbSe QDs in the transverse channel geometry (§ 5.2) were thought to be of limited value because at the time this work was done, the desire was specifically to develop a treatment for PbSe that showed controlled photocurrent enhancement consistent with what was observed in CdSe QDs.[48] Because Au electrodes serve as blocking, non-injecting contacts in the CdSe QD system, the sort of increase in photocurrent (and dark conductivity) the NaOH treatments imparted on the PbSe QDs films were not recognized as sensible, potentially interesting results. Additionally, the persistent photocurrents seen in the treated films were difficult to work with experimentally and were also unfamiliar. Since this time, the observation and interpretation of the injection of holes into CdTe [70] and PbS[147] QD solids has made the PbSe QD results seem more reasonable. The NaOH treatment, which was at the time dismissed as too harsh, seems to induce behavior similar to what is reported in methanol-treated PbS QDs, both in terms of "necking" observed in TEM images and large photoconductive gains.[147]

In the layered geometry, we learned that the insertion of a new, SW-IR-active material into a platform developed for annealed CdSe QD solids was not trivial, and there were a number of possible factors contributing to this:

- ITO exhibits appreciable absorption for $\lambda > 1$ μm, requiring that a new "transparent" electrode be found. A system based on silicon was developed but never implemented owing to its complexity.

- Single PbSe QD batch syntheses were apparently not sufficient to create spin-

cast films 200 nm thick.

- The absolute energy levels of PbSe QDs are unknown, and there is perhaps some evidence that appreciable charge injection does occur.

- The longer wavelength of SW-IR light (compared to visible light) perhaps led to very poor optical overlap of incident light with the active PbSe QD layer within the device.

- Perhaps most importantly, unlike the n-butylamine-treated CdSe QD solid—which exhibited unity quantum efficiency in the transverse channel structure—we did not have in hand a treatment method that produced a PbSe QD solid suitable for inclusion in a detector structure.

Certainly some of these problems can be overcome, but they all require considerable screening of parameter space. While the same sort of screening was feasible (though arduous) for the CdSe QD system, the added barriers associated with PbSe QD devices made the requisite screening essentially intractable.

5.5 Current Work in the SW-IR

The current work[10] in this group to develop SW-IR-active photodetectors focuses on PbS QD solids in a transverse channel geometry. This work has been catalyzed by strong claims in Ref. [147], in which devices containing methanol-treated PbS QD solids drop-cast on gold interdigitated electrodes are reported to exhibit detectivities on the same order as cooled InGaAs infrared photodetectors. (While a discussion of detectivity, and more generally, noise, is beyond the scope of this thesis, Appendix C reviews the original thrust of the detectivity metric, often overlooked today.) The goal of the current work is to confirm the reported results and understand the system more thoroughly, particularly the sources of noise for these unconventional detectors. This work represents a departure from previous strategy both in terms of material and device geometry.

---

[10]Led by Scott M. Geyer.

Since the development of PbSe QDs in our group,[32, 126] straightforward PbS QD syntheses have been developed.[42] While PbS QDs can be tuned over 700 nm < λ < 1.7 μm, a more limited SW-IR range than PbSe QDs, the wavelength window required for nightglow imaging remains accessible. In addition, PbS QDs have proven to be more stable in air and more receptive to ligand exchange than their PbSe QD counterparts, simplifying their processing and likely making PbS superior to PbSe as a quantum-dot material for searching parameter space in the SW-IR.

Though there have been reports of layered PbS QD-based photodetectors,[127, 71] it seems to be increasingly recognized that layered structures containing QD solids are rather difficult to produce consistently. Even when produced successfully, their behavior is subject to domination by local, unknown features. While considerable device surface area is sacrificed (even with interdigitated electrodes) by returning to a transverse channel geometry, yield is much higher and interfaces are better understood.

THIS PAGE INTENTIONALLY LEFT BLANK

Chapter 6

Mechanistic Study of Lead Chalcogenide Quantum-Dot Formation

Significant advances in the synthesis of colloidal semiconductor quantum dots (QDs) have made possible the preparation of samples with narrow size distributions and high quantum yields. Most procedures involve the rapid injection of precursors into a heated mixture of solvents and ligands; organo-phosphines, organo-phosphine oxides and carboxylic acids are often used during the preparation of II-VI, III-V, and IV-VI QDs.[149, 9, 41, 7, 40, 150] The formation of QDs in solution is driven by the supersaturation of "monomers" which undergo a nucleation and growth process. Despite the large number of methods developed that produce high quality nanoparticles, progress toward understanding nucleation and growth has been limited to measurement of the size and yield.[151, 152] Very little specific information is known regarding the mechanism by which monomers are generated in solution.

A related issue about which little is known is the role of impurities in the starting materials used in QD syntheses. While variations in different lots of starting materials have plagued the synthetic efforts of this group periodically, detailed studies of the effects of impurities have never been undertaken. Two important reagents to which syntheses are especially sensitive are tri-n-octylphosphine (TOP) and tri-n-

octylphosphine oxide (TOPO), and some efforts have been made locally over the years to purify these compounds. TOP has been distilled repeatedly (to remove primary and secondary phosphines as well as shorter chain tertiary phosphines) and has been filtered through a basic alumina column (to remove phosphonic and phosphinic acids often present). TOPO has also been distilled for use in large quantities in overcoating procedures. These purification efforts have been met with mixed success (measured by synthetic results).

A more troubling idea, for which there is considerable evidence, is that these impurities are actually critical for the success (yield, luminescence, tunability, size distribution) of particular QD syntheses. Figure 6-1 shows ^{31}P NMR spectra of two nominally identical lots of TOP, marked as > 97%, from Strem Chemical. As can be seen, Fig. 6-1(a) contains many more impurities and at a higher level, but it was this lot of TOP that actually allowed much broader tunability and superior size distributions for the diphenylether PbSe synthesis (§ 5.1).

Studying semiconductor monomer formation indirectly by monitoring ^{31}P NMR spectra in a model synthetic system would not only provide mechanistic insight but could also allow us to learn about the roles of phosphorous-containing impurity species of potential importance. Much of this chapter is in pursuit of these ideas.

6.1 ^{31}P NMR Study

In this study, we used ^{31}P NMR spectroscopy to monitor key compounds (alkylphosphines and alkylphosphine oxides) involved in the formation of PbSe QDs. Lead selenide QDs are typically synthesized by rapidly injecting TOPSe into a heated solution containing the lead precursor, Pb(oleate)$_2$.[153, 32] Because of relatively low injection temperatures, the PbSe system is ideal for mechanistic studies aimed at gaining insight into QD chemistries. Based on ^{31}P NMR of the reaction solution, we propose that the two mechanisms in Fig. 6-2 occur simultaneously to generate monomers during the synthesis of PbSe QDs.

It is possible that analogous mechanisms occur in other QD syntheses using

144
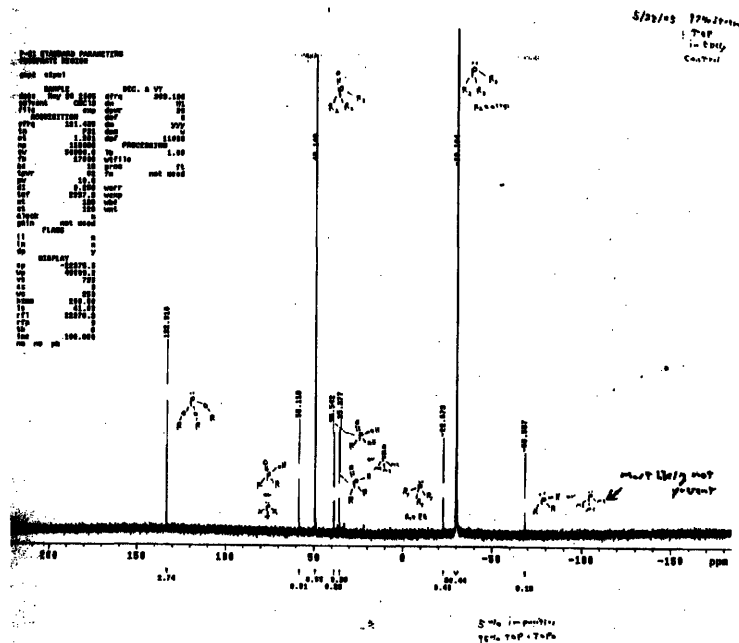
(a)
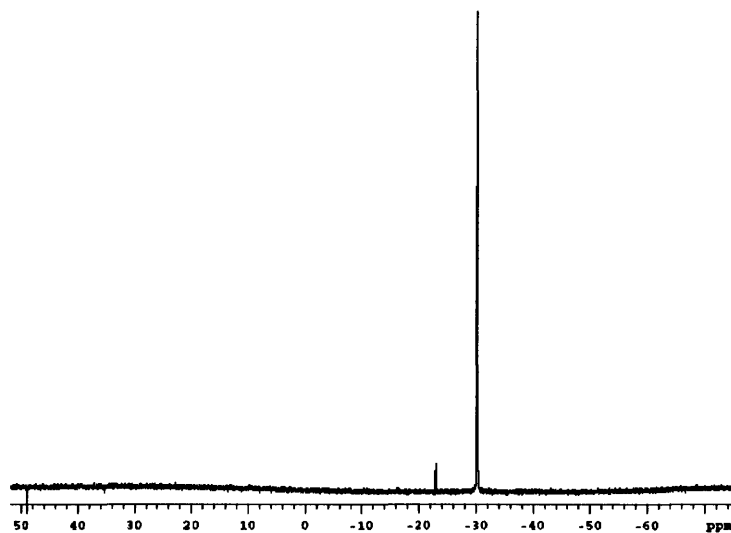
(b)

Figure 6-1: ^{31}P NMR spectra of two lots of Strem 97% TOP. Note that the axes of the two spectra cover different ppm ranges. Clearly, the lot in (a) contains many impurities than (b) and is actually calculated to be only $\sim$ 95% pure. The lot in (b) is much cleaner, containing only TOP ($\delta = -30$ ppm), TOPO ($\delta = 49$ ppm), and the poorly phased peak at $\delta = -23$ ppm, assigned to be triethylphosphine. Panel (a) courtesy of Jonathan S. Steckel.

$$(R_aCOO)_2Pb \ + \ Se=P(R_b)_3 \ \longrightarrow \ \left[PbSe\right] + \ O=P(R_b)_3 \ + \ (R_aCO)_2O \qquad \text{(a)}$$

$$(R_aCOO)_2Pb \ + \ PH(R_c)_2 \ \longrightarrow \left[Pb^0\right] \ + \ O=PH(R_c)_2 \ + (R_aCO)_2O$$

$$\left[Pb^0\right] \ + \ Se=P(R_b)_3 \ \longrightarrow \ \left[PbSe\right] \ + \ P(R_b)_3 \qquad \text{(b)}$$
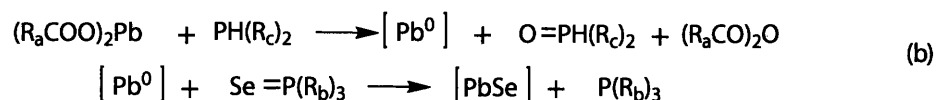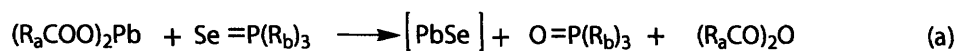
Figure 6-2: Reaction summary of overall reactions in which Se is delivered as Se^{2-} (a) and as Se^0 (b). The latter requires reduction of Pb^{2+} before the reaction can proceed.

metal salts and phosphine chalcogenides. Because of the weak P–X (X = Se, Te) bond,[154, 155] $R_3P=X$ can be regarded either as a source of X^0 or X^{2-}. In Fig. 6-2(a), tri-n-octylphosphine selenide (TOP=Se) delivers selenium as a Se^{2-} species, resulting in the production of monomer, tri-n-octylphosphine oxide (TOP=O), and an anhydride. In Fig. 6-2(b), TOP=Se can be regarded as delivering Se^0 to a reduced Pb^0 species, resulting in the formation of monomer, an anhydride, and free TOP. Once the monomer concentration increases above the solubility limit (supersaturation), the monomers combine by a nucleation and growth process to form QDs. The monomer is a transient species that is likely a PbSe unit stabilized by a number of ligands present in solution, and we label it as [PbSe] in our mechanisms.

6.1.1 Results and Discussion

The basic model system we used to study the formation of PbSe QDs consisted of Pb(oleate)$_2$ and TOPSe (pure TOPSe, with no free TOP) in 1-octadecene.[41, 152] Concentrations and reaction times in our experiments were optimized for ^{31}P NMR signal and not size distribution. Figure 6-3 shows the results of an experiment designed to elucidate mechanism in Fig. 6-2(a) in which our model system was held at an elevated temperature for four lengths of time (10, 20, 30, and 40 minutes). The growth solution for each time span was then quenched thermally and by dilution. The ^{31}P NMR spectra reveal that the TOPO concentration increased over time (Fig. 6-3, inset). We attribute the slight shift in TOPO chemical shift to a change in the local environment as QDs are being formed in large amounts. Flame atomic absorption spectroscopy was also performed on these same samples, and PbSe reaction yield was
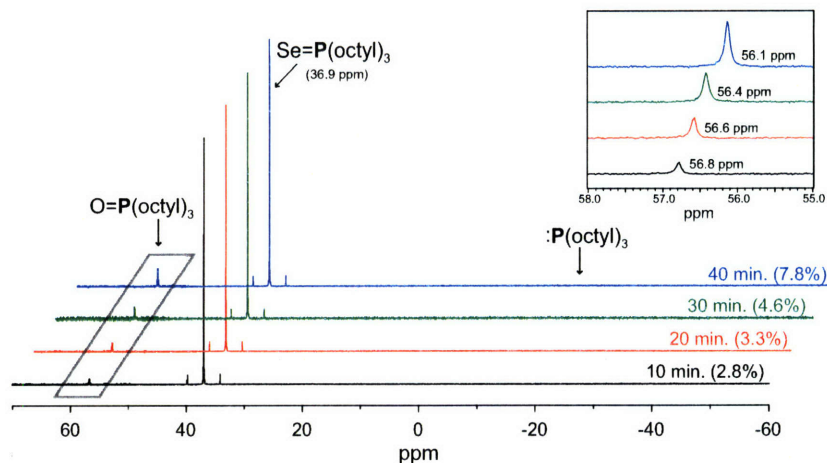
Figure 6-3: ^{31}P NMR spectra of four PbSe QD samples grown over 40 minutes at 170 °C with the corresponding reaction yields (from flame atomic-absorption spectroscopy) shown in parentheses. No free TOP was observed in the injection solution or throughout the run. The inset shows the detail view of the TOPO region.

found to increase correspondingly with the TOPO concentration.

Figure 6-4 shows in more detail our first proposed mechanism Fig. 6-2(a), in which TOPSe reacts directly with the Pb^{2+} center to produce TOPO, an oleate anhydride, and PbSe monomer. The Pb center remains Pb^{2+}, while the Se is delivered formally as a Se^{2-} species. It is important to note that only TOPO and the anhydride are formed in Fig. 6-4, consistent with the observation that no free TOP is generated (Fig. 6-3).

Semiconductor QD preparations often involve a significant amount of free organophosphine, which has been shown to act as a reducing agent. For example, triphenylphosphine reduces divalent palladium in the complex Pd(OAc)$_2$ through oxidation to triphenylphosphine oxide.[156] In a second experiment, designed to probe proposed mechanism Fig. 6-2(b), diphenylphosphine (DPP) was added to our model system, and products and reaction yield were studied. When diphenylphosphine was added to the TOPSe solution during the QD synthesis (Pb:Se:DPP mole ratio of 1:1:0.3), we observed the complete oxidation of DPP to DPP=O (Fig. 6-5) and a resulting significant increase in the PbSe QD reaction yield (54% compared to 2.8% with no DPP (Fig. 6-5)). The ^{31}P NMR spectra in Fig. 6-5 also show peaks corresponding to TOP and TOPO (small), the latter of which indicates that the reaction in Fig. 6-4 is

147

$(R_aCOO)_2Pb$ + $Se{=}P(R_b)_3$ $\longrightarrow$ $\left[R_aCOO\text{ - }Pb\text{ -}Se\text{ }{-}P(R_b)_3\right]^{\oplus}$ + $\overset{\ominus}{O}\underset{R_a}{\overset{O}{\wedge}}$

$\left[R_aCOO\text{ - }Pb\text{ -}Se\overset{}{-}P(R_b)_3\right]^{\oplus}$ + $\overset{\ominus}{O}\overset{O}{R_a}$ $\longrightarrow$ $R_a\overset{O}{\wedge}O{-}\overset{\oplus}{P}(R_b)_3$ + $R_a\overset{O}{\wedge}O{-}Pb{-}Se^{\ominus}$

$R_a\overset{O}{\wedge}O{-}Pb{-}Se^{\ominus}$ + $R_a\overset{O}{\wedge}O{-}\overset{\oplus}{P}(R_b)_3$ $\longrightarrow$ $\underset{R_a\text{-}C(O)\text{-}O}{\overset{R_a\text{-}C(O)\text{-}O}{\diagdown}}P(R_b)_3$ + $\left[PbSe\right]$

$\underset{R_a\text{-}C(O)\text{-}O}{\overset{R_a\text{-}C(O)\text{-}O}{\diagdown}}P(R_b)_3$ $\longrightarrow$ $O{=}P(R_b)_3$ + $R_a\overset{O}{\wedge}O\overset{O}{\wedge}R_a$
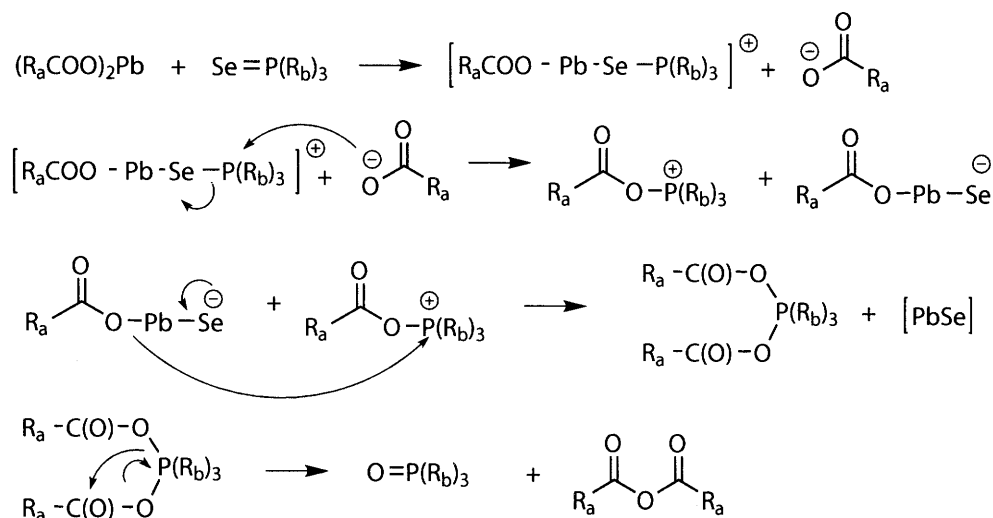
Figure 6-4: Proposed scheme for the Se^{2-} mechanism. $R_3P{=}Se$ (TOPSe) and metal carboxylates ($Pb(oleate)_2$) react to form monomer ([PbSe]). The [PbSe] species is likely stabilized by the presence of free ligands in solution ($R_3P{=}O$ and $R_3P{=}Se$). $R_a = (CH_2)_7CH{=}CH(CH_2)_7CH_3$, $R_b = octyl$.

proceeding to some extent, as well.

Figure 6-6 describes our second proposed mechanism (2) in more detail. Pb^{2+} is reduced by DPP, giving a Pb^0 species and DPPO. The Pb^0 species then reacts with TOPSe to liberate TOP and form PbSe. In contrast to Fig. 6-4, the Se can be regarded as being delivered to Pb^0 as a Se^0 species (TOP: + Se^0). Though TOP is a weaker reducing agent than DPP, TOP likely plays the role of DPP (Fig. 6-6) to some extent because it is often present in large excess in QD syntheses. Heating $Pb(oleate)_2$ with either TOP or DPP provided further evidence that organo-phosphines serve as reducing agents in QD synthesis. We found that substantial amounts of solid Pb^0 forms at 250-320 °C in the presence of TOP and at 180 °C in the DPP case.

Dialkylphosphines can be impurities in TOP, and they can also be generated in situ during the synthesis through a β-hydride elimination mechanism. The mechanism in Fig. 6-6 can help explain the empirical observation that different lots of TOP or specific heating times sometimes have profound effects on the reaction yield, size, and size distribution of resulting QDs.

148
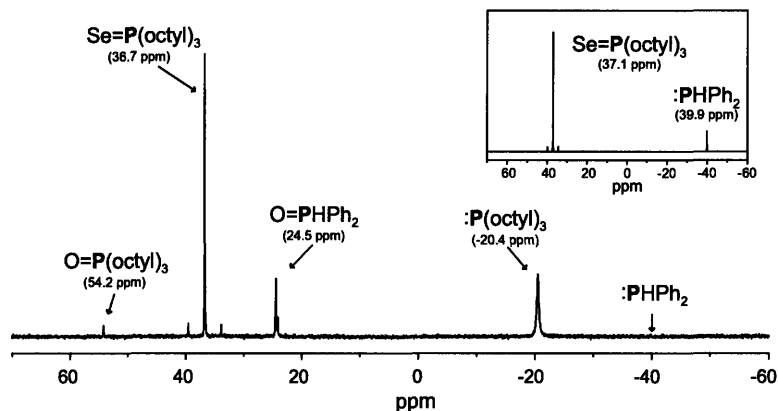
Figure 6-5: ^{31}P NMR spectrum of the growth solution of PbSe QDs synthesized using TOPSe doped with diphenylphosphine. The inset shows the ^{31}P NMR spectrum of the TOPSe/DPP solution before combining and reacting with the Pb(oleate)$_2$ solution. Reaction performed at 170 °C for 10 min.
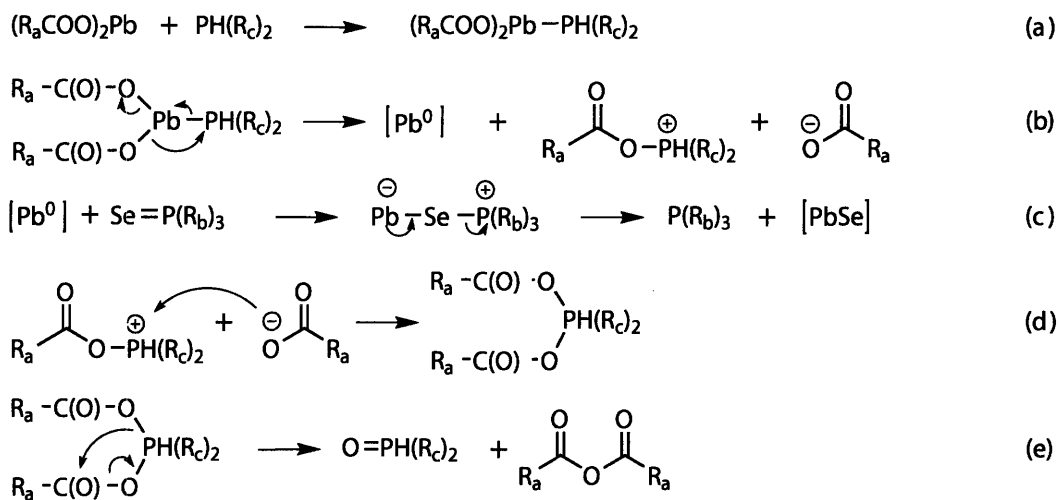
Figure 6-6: Proposed scheme for the Se^0 mechanism. R$_3$P=Se (TOPSe), a metal carboxylate (Pb(oleate)$_2$), and a reducing agent (diphenylphosphine) react to form monomer ([PbSe]). The [PbSe] species is likely stabilized by the presence of free ligands in solution (R$_3$P, R$_2$HP, R$_2$P=O, and R$_3$P=Se). R$_a$ = (CH$_2$)$_7$CH=CH(CH$_2$)$_7$CH$_3$, R$_b$ = octyl, and R$_c$ = phenyl.

149

6.1.2 Experimental Details

General. Lead (II) acetate trihydrate (99.999%), diphenylphosphine (> 90%), and anhydrous chloroform (> 99%) were purchased from Aldrich. Oleic acid (> 99%) was obtained from TCI America, octadecene (> 95%) from Fluka, tri-n-octylphosphine (97%) from Strem, and selenium shot (99.999%) from Alfa Aesar. All reagents were used as received. All ^{31}P NMR spectra were acquired on a Varian Mercury 300 MHz NMR spectrometer with an Oxford Instruments Ltd. superconducting magnet and a switchable probe ($^{1}H/^{19}F/^{13}C/^{31}P$). For each spectrum, 256 transients were acquired and referenced to an external phosphoric acid standard. Flame atomic absorption spectroscopy (FAA) was performed using a Perkin-Elmer Analyst 300. Near-IR absorption data were acquired on a Cary 5000 UV-Vis-NIR spectrophotometer. Optical absorption spectra were recorded with an HP/Agilent 8453 diode array spectrometer. Electrospray mass spectrometry (ESI-MS) was performed using a 4.7 T Bruker ApexIV FT-ICR-MS with an Apollo ESI source. Fourier transform infrared (FT-IR) spectra were obtained using a Perkin-Elmer System 2000.

Pb(oleate)$_2$ Characterization. Pb(oleate)$_2$ is produced when Pb(OAc)$_2$·3H$_2$O and oleic acid are together heated under vacuum. The presence of acetic acid was confirmed by the odor in the vacuum trap and by analysis of trap contents using ^{1}H NMR. A number of solvents are commonly used in PbSe syntheses: diphenylether (DPE), octadecene (ODE), dioctylether (DOE), squalene, and tri-n-octylphosphine (TOP). When the degassed lead precursor solution is left at room temperature, a white waxy precipitate forms over time in all solvents except TOP. This white waxy precipitate was isolated from the solvent and was soluble in TOP, chloroform, dichloromethane, and toluene. FT-IR spectroscopy, mass spectrometry, and elemental analysis confirmed the identity of the white waxy substance to be Pb(oleate)$_2$. FT-IR spectra (sample film on PTFE card) recorded for oleic acid and the white waxy solid are shown in Fig. 6-7. A broad O−H stretch at ∼ 3000 cm^{-1} and the O−H out-of-plane bending at 934 cm^{-1} seen in the oleic acid spectrum are absent in the spectrum of the white solid. Also, the C=O stretch disappears in the white
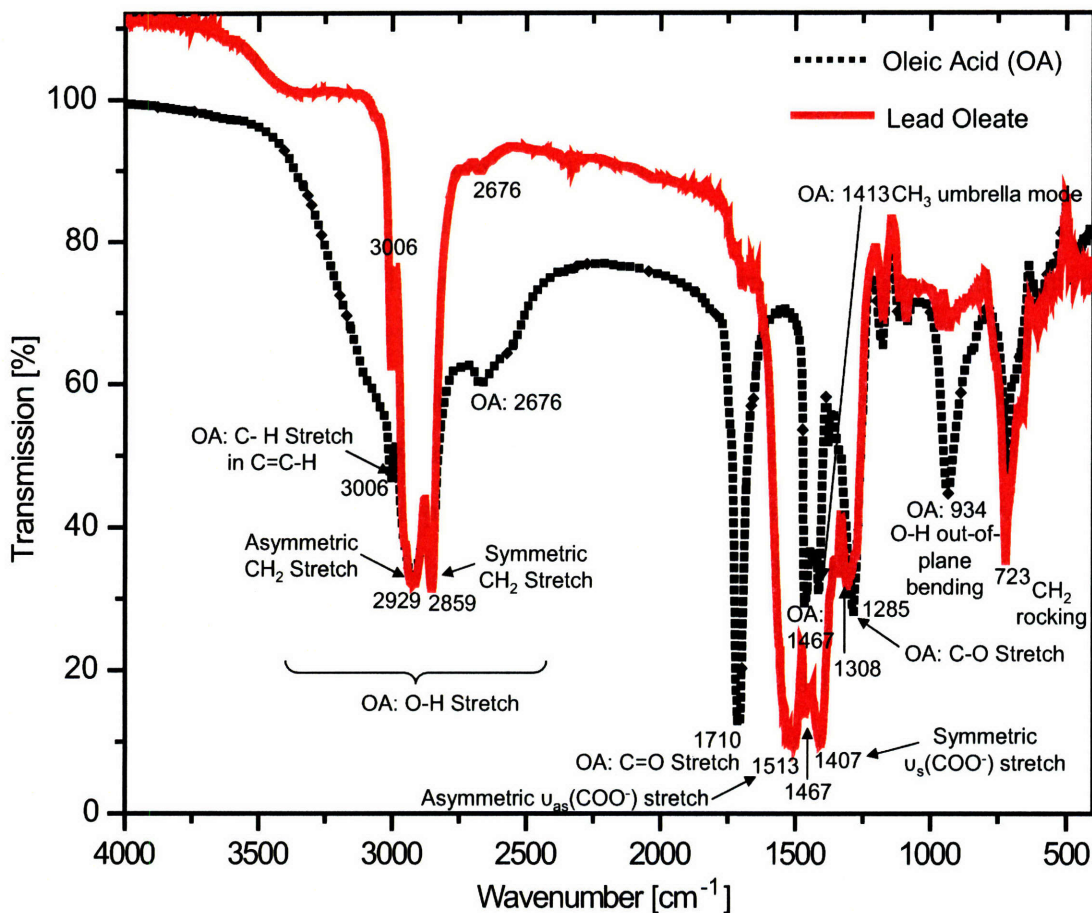
Figure 6-7: FT-IR spectra of oleic acid (black, dotted) and Pb(oleate)$_2$ (red, solid).

solid spectrum while two new C−O stretches appear at 1513 and 1407 cm^{-1}. When the head of a carboxylic acid is associated with a metal atom, the interaction is categorized as four types: monodentate, bridging bidentate, chelating bidentate, and ionic. The wavenumber separation (Δ) between the symmetric ν_s(COO−) stretch and the asymmetric ν_{as}(COO−) stretch IR bands can be used to diagnose the type of interaction. Large Δ (200-300 cm^{-1}) correspond to a monodentate interaction, medium Δ (140-190 cm^{-1}) correspond to a bridging bidentate interaction, and small Δ (< 110 cm^{-1}) correspond to a chelating bidentate interaction.[157] Here we see a difference of $\Delta = (1513 - 1407)$ cm^{-1} = 106 cm^{-1}, corresponding to the chelating bidentate species as we would expect in lead oleate. ESI-MS calcd m/z for $C_{36}H_{66}O_4PbH^+$ ([M$^+$H$^+$]): 771.5; Found: 771. Anal. calcd. for $C_{36}H_{66}O_4Pb$: C, 56.1; H, 8.6; Pb, 26.9; Found: C, 55.1; H, 8.7; Pb, 24.2.

Investigation of mechanism involving Se^{2-}. Tri-*n*-octylphosphine selenide (TOPSe, 2.24 M) was made by stirring excess elemental selenium shot in tri-*n*-octylphosphine (TOP) for several days. 0.5 mmol Pb(OAc)$_2$·3H$_2$O and 1 mmol oleic acid in 2.5 mL of octadecene were degassed under vacuum for 4 hours at 100 °C. During this time, Pb(oleate)$_2$ formed, accompanied by the removal of acetic acid. 0.5 mL (0.089 mmol of Pb(oleate)$_2$) of this solution was put in each of four NMR tubes along with 37 μL 2.24 M TOPSe (0.082 mmol of Se). The four NMR tubes were sealed under nitrogen, the solutions mixed via tube inversion, and placed into an oil bath at 170 °C. The initially clear solutions quickly (after a couple of seconds) turned dark brown and then black over time as the PbSe QDs formed. The first tube was taken out of the oil bath after 10 minutes, the second after 20 minutes, the third after 30 minutes, and the fourth after 40 minutes. 0.3 mL of anhydrous chloroform was added to each tube after removal. [We found that the addition of chloroform further solvated tri-*n*-octylphosphine oxide (TOPO), providing sharper NMR peaks.] The ^{31}P NMR spectrum of each tube was acquired within an hour, followed by the isolation via centrifugation and complete digestion of the PbSe QDs for reaction yield determination.

Investigation of mechanism involving Se^0. The Pb(oleate)$_2$ solution was prepared as described above. 2.24 M TOPSe was doped with 30 mol percent diphenyl-phosphine (DPP) before being added to the lead solution in an NMR tube. 0.5 mL of the Pb(oleate)$_2$ solution (0.089 mmol) and 40 μL of the doped TOPSe solution (0.089 mmol Se, 0.027 mmol of DPP) were mixed in an NMR tube, which was sealed and placed into an oil bath at 170 °C for 10 minutes. The entire experiment, including heating, was performed inside a glove box. When the NMR tube was removed from the oil bath, 0.3 mL of anhydrous chloroform was added, the tube was sealed and removed from the glove box, and the ^{31}P NMR spectrum was acquired.

Yield Determination. Reaction yields for our mechanism experiments, which were optimized for analysis with ^{31}P NMR and not QD quality, could not be calculated from the absorption spectra owing to poor size distributions and ill-defined first-absorption features. Yields were therefore determined by FAA spectroscopy. The

QDs were first isolated from solution using centrifugation (6000 rpm). They were then digested using HNO_3, and the solution was diluted with water for analysis

6.2 Cd(oleate)$_2$ Study

Curious to see if direct observation of metal reduction by TOP or DPP (as observed above for lead) was readily observable for other metals relevant to QD syntheses, such as cadmium, we carried out a number of experiments under similar conditions aimed at observing plating of Cd^0. Details of all that did not work is summarized here, but a few important constraints were learned, which guided the most definitive experiment, described below.

- Cadmium salts such as Cd(stearate)$_2$, chosen instead of Cd(oleate)$_2$ for this system, can decompose at high temperatures ($\sim$ 300 °C), especially when no excess acid is present.

- Cd(stearate)$_2$, when added as such and in high concentration, exhibited gel formation. This is consistent with observations of John P. Zimmer, who reported similar gel formation when sodium stearate was used as a ligand source in cobalt nanoparticle syntheses.

- While it would be ideal to use a stoichiometric ratio of cadmium and acid to produce the cadmium salt—so as to leave no excess acid—this reaction did not go to completion. This reason, coupled with the first point, necessitated the use of an excess of acid.

With these guidelines, the following procedure was carried out: 128 mg CdO (Aldrich > 99%) and 1.14 g stearic acid, representing a 1 mmol:4 mmol cadmium-to-stearate ratio, were added to 10 mL ODE (Fluka) in a 50-mL round-bottom flask. The mixture was heated to 240 °C (under N_2, without first degasing), at which point the solution cleared (from being a blood-red color), indicating the complete formation of Cd(stearate)$_2$. The temperature was then lowered to 200 °C for the remainder of the experiment to minimize risk of decomposition. A first quantity of DPP (0.175 mL, 1

DPP/Pb	reaction yield [%]	number of QDs	first abs peak
—	2.3	1.81×10^{16}	1358
0.08	11.6	3.09×10^{16}	1736
0.15	16.2	4.53×10^{16}	1716

Table 6.1: Results of three batch PbSe QD preparations using 0, 0.08, and 0.15 mmol of diphenylphosphine (DPP) doped into the 1 M TOPSe injection solution.

mmol) was added to the flask, and no formation of Cd^0 was observed over a period of 6 hr. A second quantity of DPP (0.70 mL, 4 mmol) was then added. This excess was to ensure that the presence of excess acid was not consuming the phosphine. Still, no Cd^0 was observed even 10 hr after this second injection, and when the flask was allowed to cool and was exposed to air. The scent of DPP was apparent at this point, indicating that an excess of DPP remained throughout the experiment.

This simple experiment indicates strongly that cadmium salts are reduced by secondary and tertiary phosphines not nearly as readily as are lead salts, weakening the potential generality of our mechanism. Still, it is possible that the reaction in Fig. 6-2(b) plays a role in monomer formation in CdSe syntheses, and the doping experiments in § 6.3 seem to suggest that this is, in fact, the case.

6.3 Doping

With an understanding of the role of each species in the monomer-formation chemistry, we can begin to rationally modify batch QD reactions. For instance, by changing the reducing agent, the rate of the reaction in Fig. 6-2(b) can be varied to provide more control over the system, perhaps changing QD yield or nanoparticle size.

6.3.1 Doping PbSe QD Syntheses with Diphenylphosphine

Table 1 shows the results of three batch preparations of PbSe QDs in which DPP was added to TOPSe before injection, increasing markedly the number of QDs formed and the overall reaction yields. The presence of DPP increases the supersaturation rate of monomers, thereby increasing the nucleation rate.
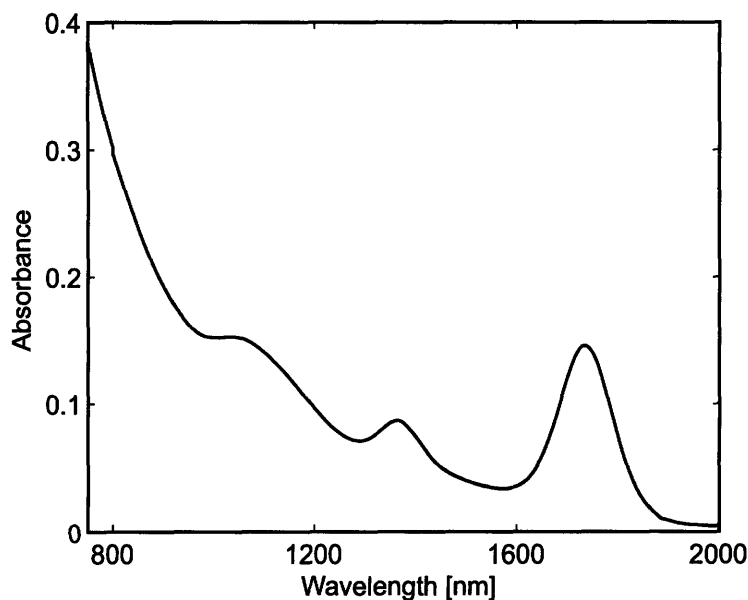
Figure 6-8: Representative absorption spectrum of PbSe QDs produced with batch synthesis using TOPSe doped with DPP (in this case, 0.08 mmol).

Batch synthesis modified with diphenylphosphine (DPP). 1 mmol lead acetate trihydrate, 3 mmol oleic acid, and 20 mL diphenylether were degassed under vacuum in a 50-mL round-bottom flask at 71 °C for 2 hours. 5 mL 1 M TOPSe (either undoped or doped with 0.08 or 0.15 mmol DPP) was injected into the Pb(oleate)$_2$ solution at 135 °C, followed by growth in which the temperature slowly increased toward the temperature of injection. After 2 minutes, the heating mantle was removed, allowing the solution to cool to room temperature. A representative absorption spectrum is shown in Fig. 6-8.

Yield Determination. Batch syntheses modified by doping TOPSe with DPP resulted in monodisperse samples with well-defined absorption features. Reaction yields for these samples could be extracted directly from the QD absorption spectra as follows: First, a 2-3 mL portion of growth solution was removed and these QDs were precipitated twice with methanol and finally redispersed in 1,1,2-trichloro-1,2,2-trifluoroethane, which has no absorption features in the 1000-2000 nm window. An absorption spectrum was recorded, and from the position of the band-edge absorption peak, the QD diameter was determined.[32] A small aliquot of growth solution was then diluted at a known factor in hexane, and the absorption at 400 nm was measured.

155

Based on both calculated and experimental values for absorption cross section per QD at 400 nm (below), QD concentrations (and hence yields) were calculated.

Absorption Cross-Section. The absorption cross-section at 400 nm was calculated using Eq. 6.1, based on Ref. [158].

$$C_{\text{abs}} = \frac{2\pi}{m_3\lambda}9m_3^4\frac{2n_1k_1}{(n_1^2 - k_1^2 + 2m_3^2)^2 + 4(n_1k_1)^2}\frac{4}{3}\pi a^3 \qquad (6.1)$$

C_{abs} is proportional to the product of the bulk semiconductor absorption coefficient $(2n_1k_1)$ and a local field factor that is equal to the ratio of the applied electric field to the electric field inside the QD. The parameters n and k are components of the complex refractive index for bulk PbSe,[159] m_3 is refractive index of hexane, λ is excitation wavelength, and a is the QD radius. The calculated per-particle absorption cross section (in cm^2) for PbSe at 400 nm was found to be $C_{\text{abs}} = (6.55 \times 10^5)a^3$ cm^2.

We confirmed the validity of Eq. 6.1 by directly measuring the single-exciton saturation curve of 4.5 nm diameter QDs. The QDs, dispersed in hexanes, were excited with a frequency doubled, regeneratively amplified titanium-sapphire laser (100 fs pulse width at 400 nm, 1-kHz repetition rate). The photoluminescence spectra were collected (Princeton Instruments OMA V 512-pixel InGaAs linear array interfaced with an Acton 300i spectrometer) at various pump powers, yielding the saturation curve shown in Fig. 6-9. Fitting the curve[160] gives an experimentally determined value of $C_{\text{abs}} = 1.05 \times 10^{-14}$ cm^2 at 400 nm. Substitution of the QD size into equation 6.1 gives a calculated value of $C_{\text{abs}} = 7.46 \times 10^{-15}$ cm^2, which is in good agreement with the experimental value.

6.3.2 Doping CdSe QD Syntheses with Diphenylphosphine

Despite the inconclusive results in our efforts to reduce Cd^{2+} (from Cd(oleate)$_2$) to Cd^0, we set out to determine the effects of doping CdSe syntheses with DPP. An increase in yield would indicate the participation of the reaction in Fig. 6-2(b) in semiconductor monomer formation in the CdSe system, making our mechanistic study more generally relevant.

$C_{abs} = 1.05 \times 10^{-14} cm^2$ at 400 nm

emission centered at 1436 nm

PbSe in hexane
1, 0.6, 0.4 mW
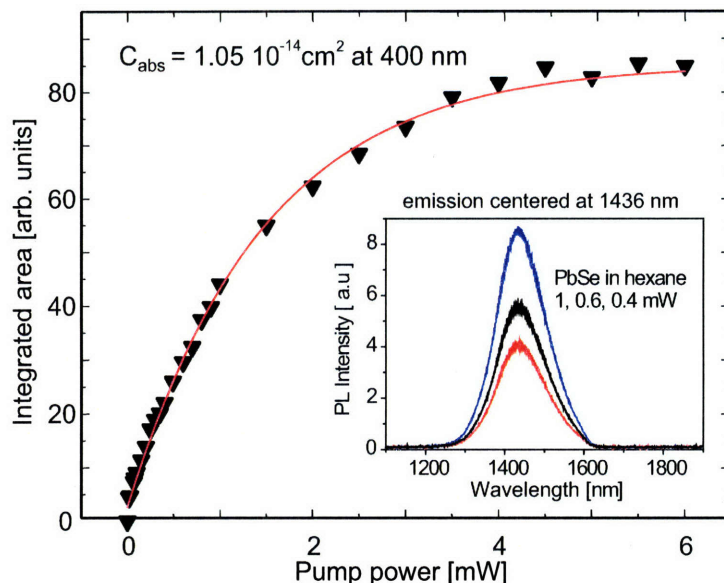
Figure 6-9: Single-exciton saturation curve of 4.5-nm PbSe QDs excited with 400-nm laser light of varying intensity.

DPP/Cd	reaction yield [%]	number of QDs	FWHM [nm]
—	55	4.7×10^{17}	33
0.21	70	6.0×10^{17}	27

Table 6.2: Results of two batch CdSe QD preparations undoped and with 0.21 mmol of diphenylphosphine (DPP) doped into the 1.5 M TOPSe injection solution.

Two CdSe syntheses (using the general method outlined in Appendix A) were carried out. In one, 40 mg DPP was added to the 1.5 M TOPSe component of the precursor injection mixture, which represented a DPP:Cd ratio of 1:5. Figure 6-10 shows a comparison of undoped and doped syntheses (absorbance samples were diluted equally from equal growth solution volumes), and a modest increase in yield is apparent. The yield was determined using absorbance values at $\lambda = 350$ nm in conjunction with the cross section calculations in Ref. [158], which is facilitated in our group through a widely-circulated spreadsheet usually used in the overcoating process. The results of the yield calculation are given in Table 6.2.

This increase in yield was more modest than those seen in the PbSe system (Table 6.1). However, because the undoped yield was already > 50%, large gains in yield were not possible, and it is intuitive that gains in this already efficient system would

157
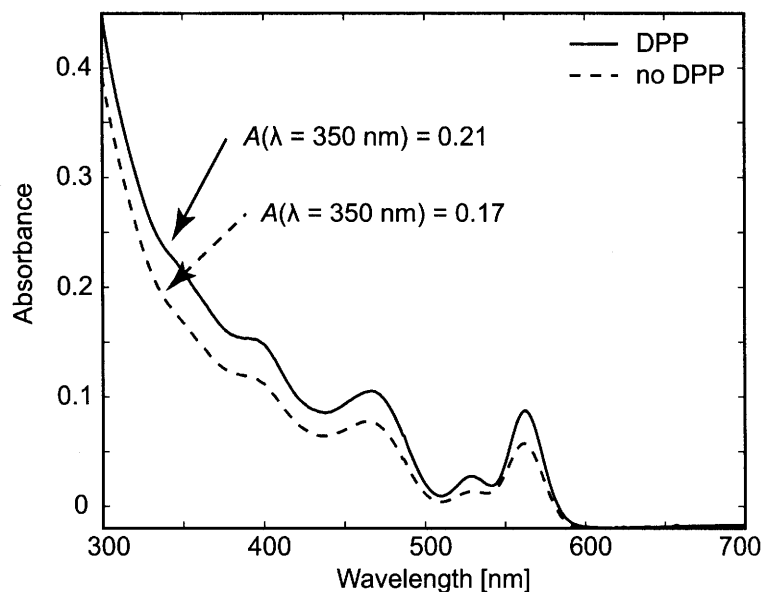
Figure 6-10: CdSe with (solid) and without (dashed) doping with DPP. The increase in $A(\lambda = 350$ nm$)$ is indicative of a modest increase in synthesis yield. Interestingly, while the position of the band-edge absorption does not change, the size distribution is improved in the doped synthesis (undoped: FWHM = 33 nm, doped: FWHM = 27 nm).

be modest. Despite the modest increase in yield, it is surprising that the center of the band-edge absorption peak ($\lambda = 562$ nm) is unchanged. In the CdSe system, perhaps a more significant improvement associated with DPP doping is the noticable improvement in size distribution, turning an average synthesis (FWHM = 33 nm) into essentially the synthetic limit (FWHM = 27 nm) for this size of CdSe QDs.

6.4 Summary

In summary, a model PbSe QD synthesis was used as a model system to study the mechanisms through which semiconductor monomers form in systems based on lead carboxylates and organo-phosphines. Based on our experimental results, we propose that two mechanisms occur simultaneously. One practical example of this understanding is our ability to increase significantly the reaction yield of the PbSe QD synthesis while maintaining the size distribution. Similar, more modest increases in yield have been observed in CdSe QD syntheses as well, suggesting some generality

to the mechanistic insight gained.

THIS PAGE INTENTIONALLY LEFT BLANK

Chapter 7

In Vivo Imaging in the 1225 nm $< \lambda <$ 1370 nm Window

In this chapter, we discuss an effort to evaluate the feasibility of using the 1225 nm $<$ $\lambda <$ 1370 nm spectral window for in vivo imaging. While this work, done in collaboration with the Frangioni Group (Beth Israel Deaconess Medical Center (BIDMC), Harvard Medical School), constituted a brief project primarily designed to inform a funding proposal in preparation, important conclusions were drawn which are counter to ideas now commonly accepted in the literature.[1] To fully understand the work reported here, the reader is encouraged to be familiar with Ref. [145] and the model used therein[164].

7.1   Background

During the past decade, interest in using colloidal quantum dots (QDs) in a variety of biomedical imaging applications has steadily increased.[165, 166, 24, 167] QDs exhibit continuous, increasing absorption profiles to the high-energy side of their emission peak (allowing for greater flexibility in excitation sources), they exhibit large single-photon and two-photon absorption cross sections, and they do not readily

---

[1]In particular, that SW-IR QD materials PbS and PbSe hold great promise for biological imaging.[161, 162, 163]
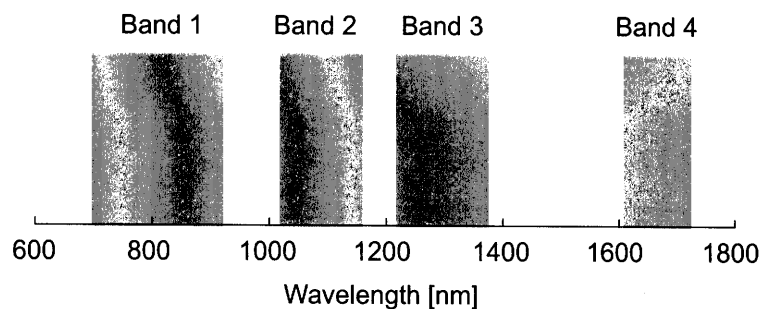
Figure 7-1: NIR and SW-IR bands of relatively good transmission in mammalian tissue.

photobleach as do their organic-dye counterparts. Further, the ability to tune the emission wavelength independent of surface functionality independently has allowed for a number of imaging constructs to be developed,[168] both in the visible and in the near-IR (NIR).

The NIR is of particular interest for imaging in mammalian tissues because this wavelength range contains four wavelength windows, or bands, depicted in Fig. 7-1, over which mammalian tissue is relatively transparent. Band 1 ranges from 690 nm $<$ $\lambda < 925$ nm and is strongly influenced on the high-energy side by hemoglobin absorption. Bands 2-4, representing 1025 nm $< \lambda <$ 1150 nm, 1225 nm $< \lambda <$ 1370 nm, and 1610 nm $< \lambda <$ 1710 nm, respectively, are essentially limited by water absorption bands.[145] Considerable work has been done in Band 1.[145, 24, 25] CdTe/CdSe heterostructure QDs passivated with oligomeric phosphines,[169, 170] and more recently (InAs)ZnSe QDs passivated with DHLA-PEG, have been used to demonstrate sentinel lymph node mapping,[24] and multiple lymph node mapping accompanied by extravasation,[25], respectively. However, particles emitting in Band 1 have yet to be crafted such that their hydrodynamic diameter remains small enough ($\sim$ 5 nm) to allow for efficient excretion.

Working in Band 1 is convenient for the following reasons:

- There are several QD materials that can be made to emit in Band 1, including CdTe/CdSe, InAs, and PbS, as well as more complicated constructs such as $InAs_xP_{1-x}/InP/ZnSe$,[171] many of which can now be made routinely.

162

- Most QD materials appropriate for Band 1 can be overcoated, which is critical for maintaining high luminescence efficiency in biological environments.

- Excitation and collection wavelength ranges for Band 1 are similar enough to those used with standard organic dyes that filter sets needed for work in Band I are widely available.

- Because $\lambda < 1000$ nm for Band 1, a silicon detector array can be used to detect emission. These cameras are relatively cheap, widely available, and optimized for room-temperature operation.

Despite these attractive practical aspects, it has been predicated theoretically, based on the Jacques model,[164] that in some instances operation in Band 3 might be preferable to Band 1.[145] Band 3 has the general benefit of reduced scatter (longer λ) and because of its spectral separation from the short wavelength side of Band 1, where hemoglobin absorption dominates, Band 3 may be superior in bloodier fields (high Hg-to-H_2O concentration ratios). Thus, we seek to experimentally verify the claim, now widely cited in the literature,[161, 162, 163] that Band 3 is a promising wavelength range for in vivo imaging.

7.2 Experimental

The flexibility in our experimental approach to this proof-of-principle problem was limited by a number of factors:

- The experiments had to be executed within a few weeks' time using an existing imaging setup for Band 1 and a temporary, trial setup for Band 3. The platform used, therefore, had to be simple, had to allow for several potential iterations and refinements in a short period of time, and had to use QD materials readily available at the time.

- The only QD materials readily available that emitted in Band 3 were PbSe and PbS, neither of which could be overcoated. Hence, to retain photoluminescence

efficiency, QDs would have to remain in solution (in organic solvent) throughout the experiment.

- The key factor being tested was spectral properties of the QDs. Thus, we required an experimental method that allowed for a performance metric in which factors such as QD concentration, QD absorption cross section, and QD photoluminescence quantum yield could be eliminated from consideration.

- Finally, a practical consideration was that the platform be portable such that it could easily and quickly be moved between setups for Band 1 and Band 3, which were housed in two separate laboratory spaces at BIDMC.

The platform and procedure developed is shown in Fig. 7-2. A gelatin mammalian tissue phantom[172] developed in the Frangioni Group was poured into a petri dish such that a small well was formed. In a separate dish, a second slab of uniform thickness was cast. QDs in common organic solvents such as hexane or toluene could then be introduced to fill the well, and QD emission was imaged before and after covering the well with the second phantom slab. This top slab effectively created an inclusion of an organic QD-containing solution within an aqueous gelatin phantom matrix. Because images were recorded both before ("bare") and after ("covered") being covered with the top phantom slab, a metric could be applied that was insensitive to the concentration, absorption cross section, and photoluminescence quantum yield of the QDs. The setup was quickly prepared (< 1 hr) from stock phantom solution at BIDMC, and the setup could easily be carried in a box from one lab to another. This experimental platform and procedure satisfied all the constraints identified above.

7.2.1 Gelatin Tissue Phantom

A gelatin-based phantom was used to simulate the optical properties—that is, absorption and scatter—of mammalian tissue.[172] Sodium azide was added at 0.015 M to tris-buffered saline (TBS, pH 7.4). NF gelatin (EM) 10% w/v was added and dissolved with gentle heating to 37 °C. Powdered bovine hemoglobin (Sigma) was added

imaging optics
camera

excitation

excitation

well cast for QD
solution

top slab
7 mm thick

(a)

(b)

(c)

(d)
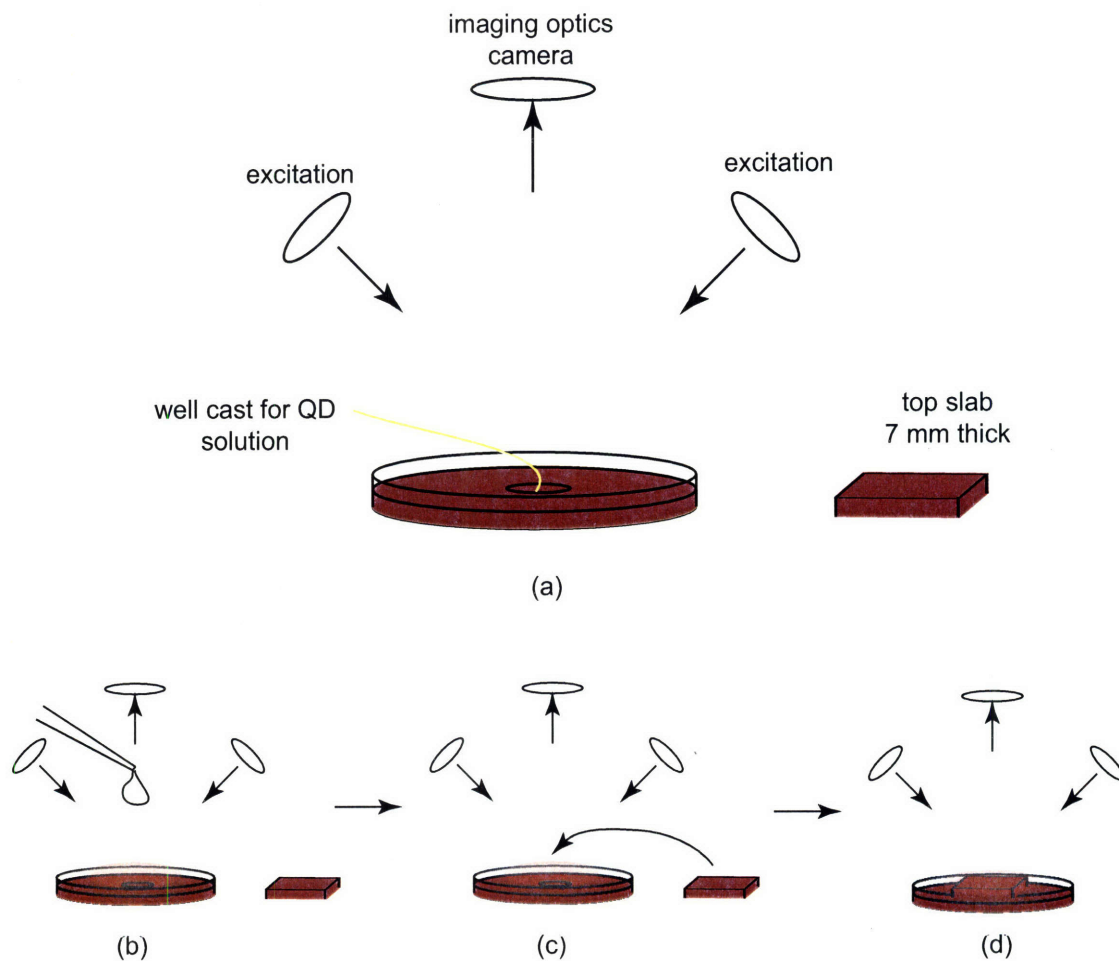
Figure 7-2: Cartoon depiction of experimental setup (a), involving a petri dish containing the gelatin phantom and well for QDs in hexane, an excitation source, and a camera capable of imaging emission in Band 1 or Band 3. In the experiment, QDs in hexane were quickly introduced into the gelatin well (b) and "bare" phantom image was recorded. The well was then covered with a second slab of phantom material, creating an enclosed well (c), which was followed quickly by another image (d) using the same excitation and collection setup as in (b).

to bring to the total hemoglobin concentration to either 170 or 340 μM. Sterile intralipid (1% v/v) was added, and the phantom mixture was left stirring at 37 °C until use. The sodium azide served to fix the ratio of oxyhemoglobin and deoxyhemoglobin to roughly 1:1.

"Melted" phantom at 37 °C bases was cast in either the base or the lid of 10 × 125 mm petri dishes and placed on a flat surface in a 4 °C refrigerator for 15-20 minutes to set. Casting of solvent wells occurred in two stages. First, a thin ($\sim$ 3 mm) bottom layer of uniform thickness was cast and allowed to become firm. Second, a 6-mL vial coated in nonstick cooking spray was held in the center of the dish, and a second 3-5 mm in thickness was poured around the base of the vial, and after the gelatin became firm, the vial was removed to created a void. Top slabs (4 or 7 mm thick) were cast in petri dishes coated with nonstick cooking spray to facilitate their subsequent removal without tearing. Phantoms could typically be used for an hour or more at room temperature before softening necessitated additional cooling.

A single phantom base and top slab were used for any set of experiments in Band 1 and Band 3 that were directly compared. Between experiments in the two wavelength ranges, the base and top slab were thoroughly rinsed with hexane to remove residual QDs.

7.2.2   Quantum Dots Used

Three sets of QDs were used in our experiments, and their emission spectra are shown in Fig. 7-3. Initially, the QDs used for Band 1 were (InAs)ZdSe,[25] dispersed in hexane and were prepared by John P. Zimmer. Owing to time constraints and a shortage of As(TMS)$_3$ during this compressed effort, PbS QDs purchased from Evident Technologies (Troy, NY) were used in later iterations of the experiment. PbS QDs were dispersed in toluene and were further diluted with hexane for our use.

PbSe QDs were synthesized using the diphenylether synthesis (DPE) method[32] and were dispersed in hexane when used as emitters for Band 3. Synthesis of particles of appropriate size (ideally, with emission peak centered at $\lambda = 1320$ nm) proved to be very difficult with batches of starting materials in the lab at the time. In particular,
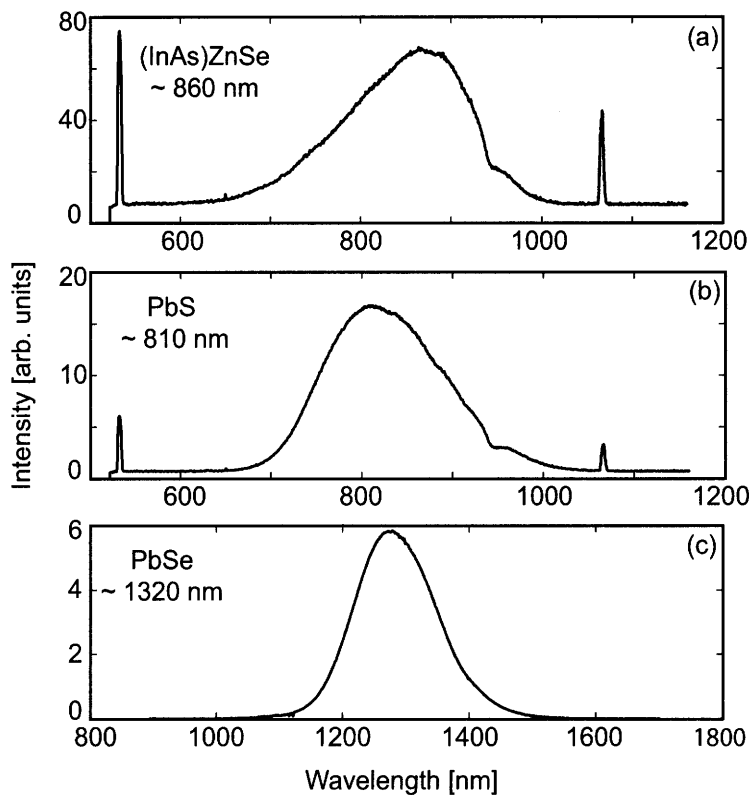
Figure 7-3: Emission spectra of NIR and IR QDs used in imaging experiments: (a) Emission spectrum of (InAs)CdSe QDs (prepared by John P. Zimmer) in hexane. (b) Emission spectrum of PbS QDs (Evident Technologies, Troy, NY) in toluene. (c) Emission spectrum of PbSe QDs in hexane. Emission spectra in (a) and (b), with excitation at $\lambda = 532$ nm, was recorded with an Ocean Optics Si array. The asymmetry exhibited for $\lambda \gtrsim 900$ nm is owing to descrease in detector sensitivity. The emission spectrum in (c) was recorded with a 512-pixel InGaAs linear array coupled to an Acton 300i spectrometer, and excitation at $\lambda = 633$ nm was used.

the batch of TOP, different than that used for the work in Ref. [32], disallowed synthesis of particles with emission peaks below $\lambda \sim 1450$ nm. Considerable work was done with other PbSe synthesis methods and toward the development of doped DPE methods (some of which were discussed in Chapter 6), but none of these allowed us synthesize high-quality QDs small enough to emit at $\lambda = 1320$ nm. Finally, and fortuitously, a bottle of a previous batch of TOP was found, and TOPSe prepared with this TOP allowed the requisite particles to be synthesized routinely. PbS QDs, which were just beginning to be synthesized in our lab when the work reported in this chapter was carried out, would now be another material with which to routinely produce particles that emit in Band 3.

PbSe QDs were processed more or less as specified in § 5.1, but generally no more than two flocculations were done and no more than one filtration (with a 200-nm filter) because photoluminescence efficiency (and not suitability for optoelectronic devices) was paramount in this case. After processing, QDs were stored in an inert atmosphere until use, at which point they were dispersed in anhydrous solvent, sealed, and removed from the glove box. No effort was made to match concentrations or absorption cross sections of QD solutions. Solutions were only exposed to air when finally delivered to the tissue phantom.

7.2.3 Imaging Setups

The Band-1 imaging apparatus consisted of a 640×480 pixel NIR silicon CCD array and a color video camera, likely the Hitachi HV-D27, as specified in Ref. [145]. This setup was already in place from ongoing in vivo work in Band 1. A cube containing filters spectrally divided the light into the two channels, likely using a $\lambda = 795$ nm long-pass filter. LabVIEW software was used to simultaneously collect 16-bit images from both channels and overlay them when needed. For this work, only the signal from the NIR silicon array was important.

The imaging apparatus used for Band 3 was transient. Again, LabVIEW was used to facilitate cameras collecting 16-bit grayscale images of two different portions of the spectrum, divided at a cube. (In this case, needless effort was expended

overlapping visible and Band-3 images. Visible images were irrelevant to this study.) Because little work is usually done in the region of Band 3, it is likely that the filters used to separate the spectrum were not ideal, and some leakage of excitation light (when broadband excitation was used) might have occurred. Visible light was imaged with a silicon array. SW-IR emission was detected with a 256 × 256 pixel, liquid-nitrogen-cooled InGaAs array. This camera was a prototype OMA V 2D on loan from Princeton Instruments and proved to be unwieldy. Because of the presence of the large nitrogen dewar, it was much more bulky than the silicon cameras used. The orientation in which we used it (with the array facing toward the floor) required the dewar to be held sideways, severely limiting the volume of nitrogen that could be added (and hence the length of time over which cooling could be achieved). Further, this orientation required the array to be disconnected and dismounted from the setup in order for the dewar to be refilled. Finally, there were unexpected software problems with the prototype that required phone assistance from PI representatives, further slowing progress. Nonetheless, some meaningful data were obtained. In all instances in both wavelength ranges, flat-fields were taken just prior to image capture.

7.3 Results and Discussion

7.3.1 Performance with dissimilar excitation

Figure 7-4 shows data from an early iteration of our proof-of-principle experiment. (InAs)ZnSe QDs are used as Band-1 emitters, and PbSe QDs emit in Band 3. In Fig. 7-4(a) and (c) are the images for the bare well of QDs in hexane and the same well covered with a 7-mm slab of tissue phantom. A drastic reduction in contrast with background is observed, but the well is still perceptible in the image. For Band 3, Fig. 7-4(b) shows very clearly the well when bare, but no hint of the image is evident when the well is covered in (d).

Though the conclusion of this initial set of images is intuitive, some simple processing was done to evaluate the images according to a more concrete metric. Images were

loaded into ImageJ (NIH), which interpolated the images to 8-bit from their native 16-bit format. For each image, a large area of background was selected, and the gray level over this range (from 1 to 256) was averaged to establish average background intensity $\bar{I}_{\text{bkgd}}$ for that image. Then, a similar analysis was done on a representative portion of the QD-filled well (if it was perceptible), and an average gray level was calculated from which $\bar{I}_{\text{bkgd}}$ was subtracted, resulting in $\bar{I}_{\text{QD}}$. The ratio $\bar{I}_{\text{QD}}/\bar{I}_{\text{bkgd}}$ the for each image provided a metric of how easily the QD-filled well could be distinguished from the other parts of the image. The computed $\bar{I}_{\text{QD}}/\bar{I}_{\text{bkgd}}$ values are shown, where calculable, associated with the images in Fig. 7-4. Ultimately, we would like to compare the reduction in $\bar{I}_{\text{QD}}/\bar{I}_{\text{bkgd}}$ upon coverage with the top slab, or

$$\gamma = \frac{\bar{I}_{\text{QD}}/\bar{I}_{\text{bkgd}}(\text{bare})}{\bar{I}_{\text{QD}}/\bar{I}_{\text{bkgd}}(\text{covered})}.$$

(7.1)

Clearly, because of the lack of processable data in Fig. 7-4, this metric cannot be computed here. This would seem to indicate that Band 3 is not at all suitable for in vivo imaging.

Upon further consideration, however, there were several infelicities with this early iteration of the experiment, most of which centered around the excitation of the phantoms. While excitation in Band-3 was performed using two light pipes illuminating the center of the petri dish containing the phantom, the excitation source in Band 1, used for numerous mouse and rat surgeries for some time, was much more robust. Figure 7-5 compares the excitation sources in Band 1 (a) and Band 3 (b), depicting the much more thorough illumination employed in the Band-1 setup. The larger illuminated area and more thorough set of illumination angles allows (1) for light to enter the side of the slab through the transparent glass petri dish and potentially be waveguided to the QD-containing well and (2) more extensive excitation of the QD-containing well from light incident on the entire top surface of the layered phantom assembly.

Another uncertainty in this comparison are the very different (and complex) excitation spectra used for these two samples. The theoretical model in Ref. [145] assumes

InAs QDs , NIR

PbSe QDs , InGaAs

(a)

(b)

Bare
QDs 20.5

Bare
QDs 10.7

(c)

(d)

Covered
QDs 0.4

Covered
No signal

bare:covered   ratio ~ 50

no signal

Figure 7-4: Images from initial phantom experiments for uncovered QD well, (a) and (b), and well covered with gelatin phantom slab 7 mm thick, (c) and (d). Images (a) and (c) were taken with intense, broad-band, white-light LED excitation, and emission recorded by a Si CCD camera. Comparison of $\bar{I}_{\mathrm{QD}}/\bar{I}_{\mathrm{bkgd}}$ for (a) and (b) yields a reduction in camera contrast by a factor of ~ 50. Images (b) and (d) were taken with varied excitation with $\lambda < 1200$ nm, and emission was recorded with a 256×256 InGaAs array detector. No signal is seen for the QD well covered with the phantom slab.
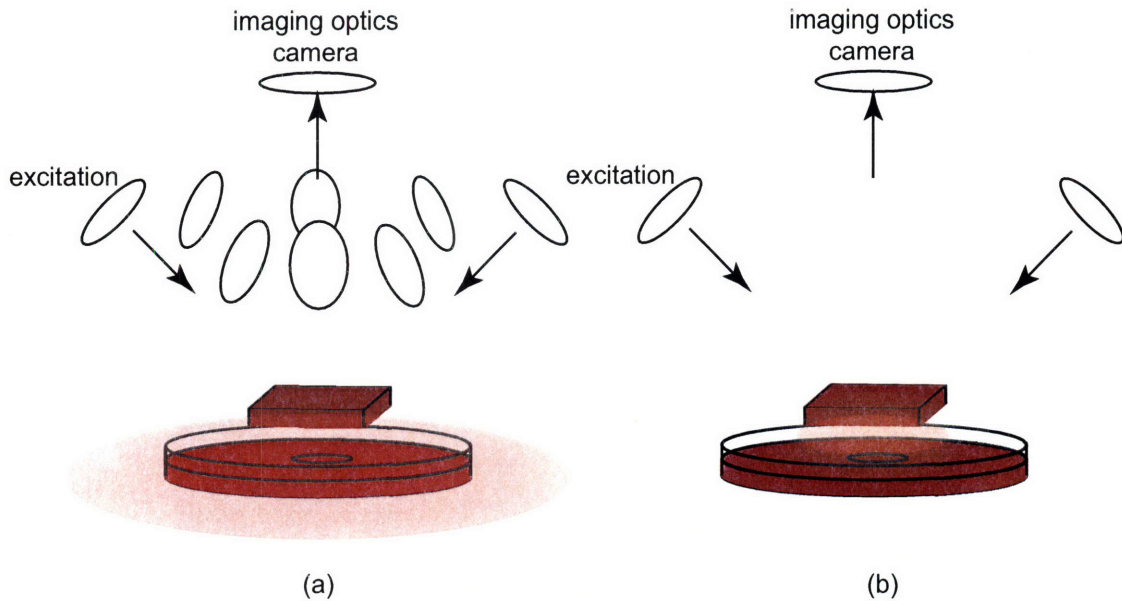
Figure 7-5: A comparison of excitation sources for Band 1 (a) and Band 3 (b) shows that sources used for Band 1 are much more intense and cover the top and sides of the oblate phantom more fully, allowing for many more excitation pathways.

a step function in photon density extending indefinitely to the high-energy side of the QD absorption band-edge, and this assumption was far from being satisfied in the excitation sources for either Band 1 or Band 3. Figure 7-6 shows the various excitation spectra obtained using different configurations of the light-pipe system used for excitation in Band 3.

7.3.2 Performance with identical excitation

To address the inconsistencies above, the following changes were made:

- A single $\lambda \sim 770$ nm laser excitation source (delivered via optical fiber) was used to excite both samples.

- More care was taken to match excitation geometry. The divergent beam emitted from the end of the fiber was held at 45° to the phantom surface and at a fixed distance 10-20 cm above the surface of the phantom.

- The top phantom slab was made large in area to essentially completely cover the bottom slab. It was also made thinner (4 mm rather than 7 mm) to allow

172
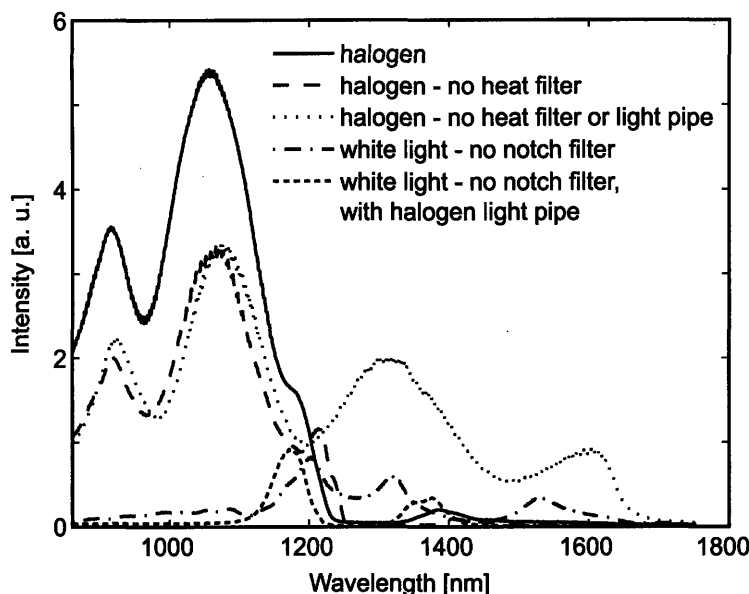
Figure 7-6: Excitation sources initially used for investigation of Band 3, measured with an Ocean Optics spectrometer equipped with an InGaAs detector. While the model in Ref.[145] assumes a step-function excitation, with constant intensity to the high-energy side of the absorbance band edge, these measured excitation spectra deviate strongly from the step function assumption, in some cases having significant emission across Band 3.

for more contrast in the images of the covered QD-containing well.

- The outer rim of the petri dish in which the phantom was contained was masked with transparent tape to eliminate the need to consider light entering the phantom this way.

Another modification, not made to address inconsistences but rather made out of necessity owing to shortage of (InAs)ZnSe QDs, was to use commercial PbS QDs in toluene (diluted with hexane) as the Band-1-active material. Still one more change was an increase in the overall hemoglobin (Hb) concentration in the tissue phantom from 170 μM to 340 μM, which was beginning to stress the Hb solubility limit. While 170 μM is apparently an "average" Hb concentration, 340 μM corresponds to bloodier fields, perhaps favoring Band 3 as predicted theoretically for high Hb-to-H_2O ratios.[145]

Images from the modified experiment are shown in Fig. 7-7(a)-(d), and in for both Band 1 and Band 3, the QD-containing well is perceptible in both the bare

PbS QDs , NIR   PbSe QDs , InGaAs

(a) Bare 34.5

(b) Bare 92.7

(c) Covered 1.27
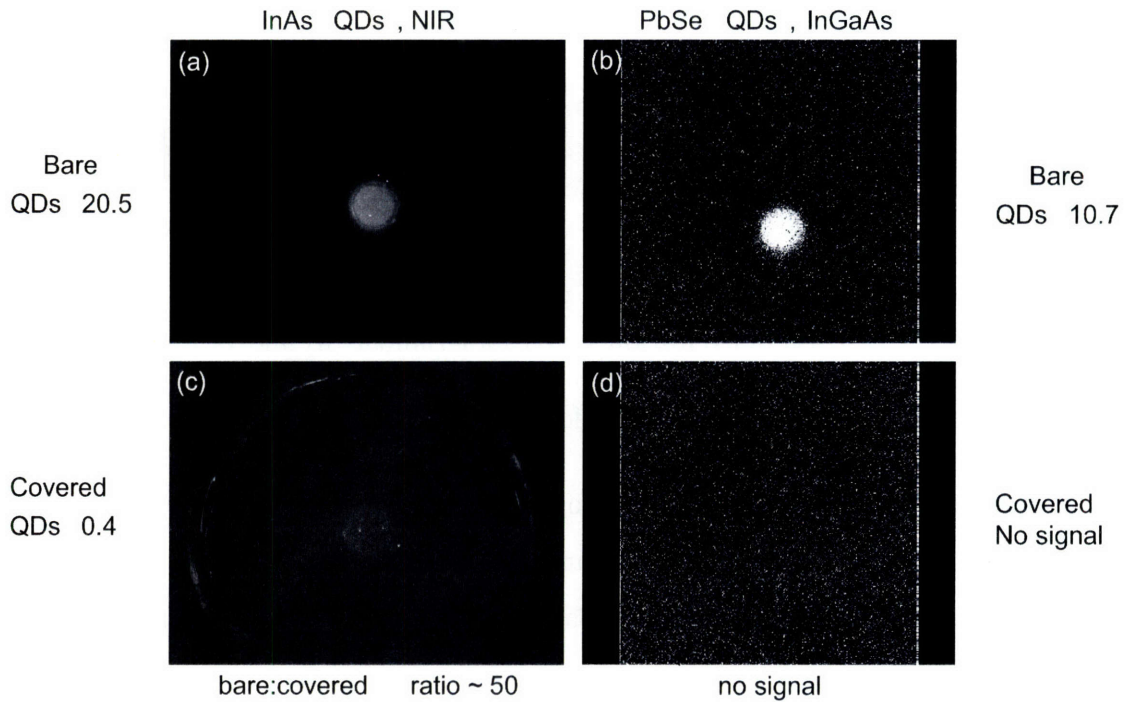
(d) Covered 4.0

Ratio 27.2   Ratio 23.2
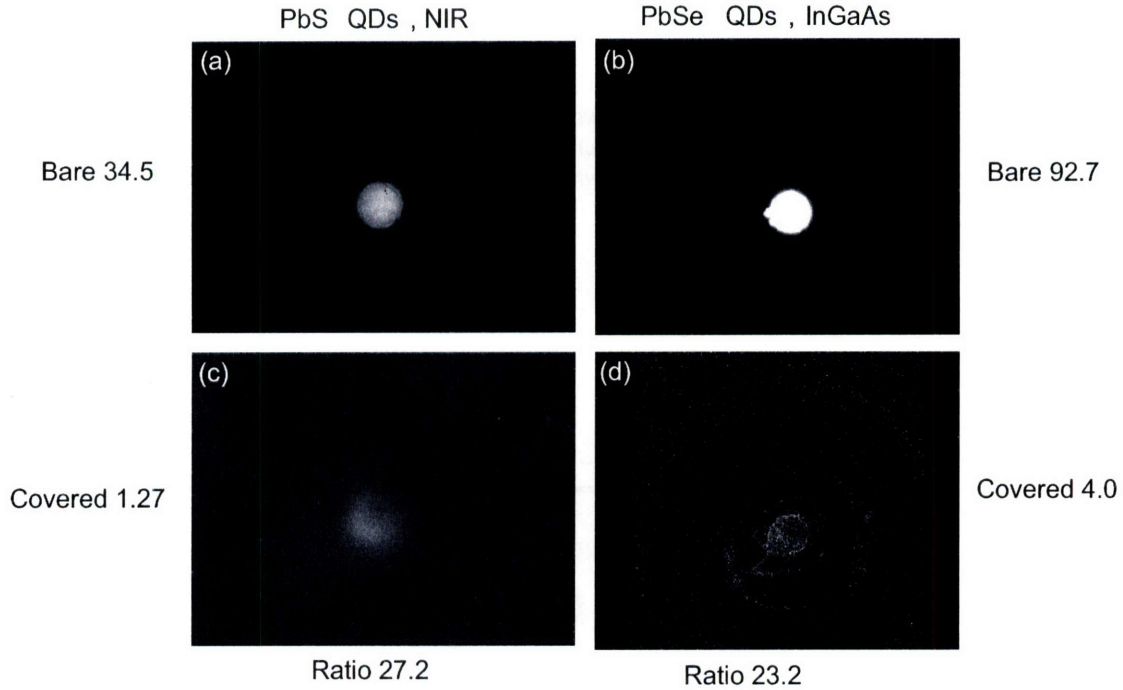
Figure 7-7: Images from refined phantom experiments for uncovered QD well, (a) and (b), and QD well covered with gelatin phantom slab 4 mm thick, (c) and (d). All images were taken with the same $\lambda \sim 770$ nm laser excitation source, held at 10-20 cm above the sample and at 45° to the phantom plane. Images (a) and (c) show a comparison of bare and covered QD well in Band 1, and the reduction in contrast, as measured by the $\bar{I}_{QD}/\bar{I}_{bkgd}$ metric, is 27.2. Images (b) and (d) show a comparison of bare and covered QD well in Band 3, and the reduction in contrast is 23.2.

and covered images. Using ImageJ and calculating the metric described above, the contrast reduction from bare to covered is $\gamma = 34.5/1.27 = 27.2$ for Band 1 and $\gamma = 92.7/4.0 = 23.2$ for Band 3. This suggests that under these refined experimental conditions, Band 3 is only roughly as good as Band 1 for imaging in (somewhat bloody) mammalian tissue.

A closer examination of Fig. 7-7 reveals that the contrast reduction ratio γ computed for Band 3 is too low and that the reduction is actually significantly higher. Despite efforts to ensure that the cameras used were never saturated, the QD-containing well in Fig. 7-7(b), recorded in Band 3 with the InGaAs detector array, is clearly saturated. In Fig. 7-8, linear gray-level data are extracted for the bare images for Band 1 (b) and Band 3 (d). Figure 7-8(d) shows severe saturation, indicating that $\bar{I}_{QD}/\bar{I}_{bkgd}$ for this image could be an order of magnitude higher or more. Taking this into
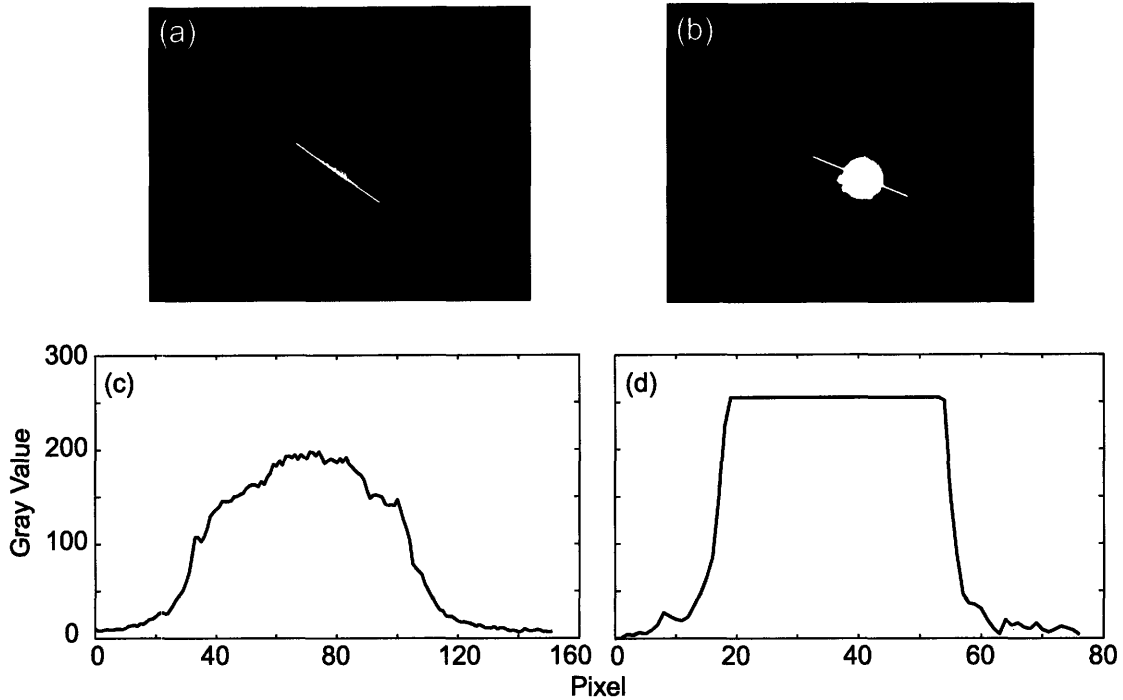
Figure 7-8: Comparison of uncovered QD well images in the refined experiment for Band 1 (a) and Band 3 (b). Panels (b) and (d) show gray-level profiles for (a) and (c) respectively, as indicated. This analysis reveals that the uncovered Band 3 image is saturated, somewhat compromising the value of our comparison. Both images were originally recorded using 16-bit cameras but were reduced to 8-bit for analysis in ImageJ.

account, the $\gamma = 23.2$ for Band 3 should be regarded as a very conservative lower estimate, suggesting that Band 1 is actually superior for this phantom and excitation scheme.

7.3.3 Future Experiments

A further refinement of this experiment was planned, but never executed, largely owing to the lack of availability of the OMA V 2D InGaAs array trial camera from Princeton Instruments. The goals of these experiments would be to (1) ensure that no parts of any images recorded were saturated, (2) modify excitation scheme to be band-specific, and (3) explore more fully the dependence of γ on phantom composition (Hb concentration, for the most part) and thickness of the top slab. Not only is the step-function in incident intensity used in Ref. [145] difficult to realize experimen-

175
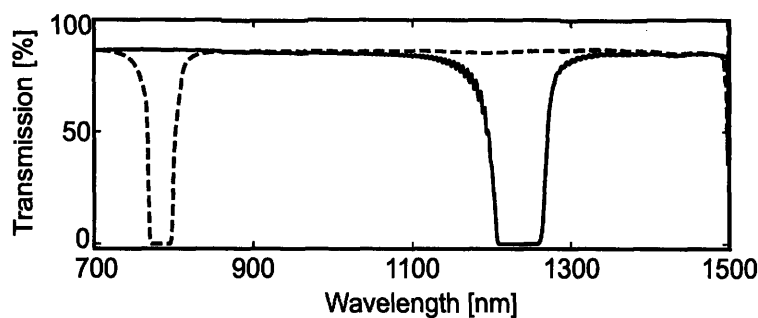
Figure 7-9: Transmission characteristics of holographic notch filters HNF-1250.0-1.5 (solid) and HNF-785.0-1.5 (dashed) from Kaiser Optical Systems. Shaded areas represent Bands 1 and 3. Transmission data recorded using Cary 5000 spectrophotometer with beam normal to filters.

tally, but one of the conclusions of the analysis is that, owing to absorbance far to the high-energy side of the QD band-edge, the continuous (and increasing) absorption manifold exhibited by QDs is largely nullified.[145] A more elegant approach would perhaps be to perform both excitation and image collection within a *single* band. Excitation with a laser source at the short-wavelength edge of a band coupled with QDs that fluorescence toward the longer-wavelength edge are needed to achieve this. In addition, excitation laser scatter needs to be filtered, and to this end, two holographic notch filter were purchased from Kaiser Optical Systems. Their transmission properties are shown in Fig. 7-9. Appropriate excitation laser sources for these filters are the Ti:saph (Band 1) and the idler output from the OPA on the RegA system (tuned for $\lambda \sim 1250$ nm, say).

7.3.4 Outlook for Band-3 In Vivo Imaging

Despite the remaining loose ends surround this experiment, we were able to produce a sufficiently definitive answer in a short period of time to be of use in crafting the funding proposal in question. Not only do our result indicate that Band 3 seem to be only similar, *at best*, to Band 1, but a number of practical difficulties make using Band 3 difficult:

- Cameras, used for detection in the Band 3 window, such as an InGaAs array, are not widely available, are expensive, and require liquid nitrogen cooling to

176

achieve reasonable signal-to-noise.

- QD materials that can be used routinely to achieve IR emission (PbSe, PbS) cannot currently be overcoated, essentially preventing their direct use in biological systems.

- Filters and optics designed for cut-off in or near Band 3 are rare and often have to be specially ordered.

In conclusion, Band 3 was modeled to be superior to Band 1 in bloodier field,[145] but the results in this chapter seem to indicate that, short of imaging in whole blood, Band 1 is superior and more easily facilitated in practice.

THIS PAGE INTENTIONALLY LEFT BLANK

Chapter 8

Concluding Remarks

Overall, the work presented in this thesis is quite multidisciplinary. Colloidal quantum dots were synthesized wet chemically on a Schlenk line, and they were processed in a way to render them suitable for inclusion in optoelectronic devices. Recent developments providing qualitative improvements in the photoconductivity of QD solids were exploited. Knowledge of basic organic-electronic device platforms and materials, in conjunction with understanding of simple device physics, guided both simple and more complex device design. Devices were fabricated, largely using the integrated materials processing system in the LOOE, and a number of metrics were measured on custom-built setups. Through these efforts, we demonstrated the feasibility of using QD solid (subjected to post-deposition chemical annealing) in layered geometries and have begun to investigate more complex device geometries. In related work, a first pass was made studying PbSe QD solids in both transverse and sandwich geometries, and PbSe QDs also served as the object of a synthetic mechanistic study and a biological imaging feasibility study.

The central photodetector project discussed in the thesis was unusual, at least in traditional academic science terms, because of the very strong emphasis placed on process development and the continued interplay between process and science. This is challenging in a setting in which everything is done in batch mode, and manpower is exceedingly limited. Only when process was optimized could significant scientific understanding potentially begin.

As stated in the introduction to this thesis, there were a number of real, practical challenges surrounding the photodetector project discussed, and ultimately, these challenges were never overcome. The spread of facilities used, the extensive use of student-run, shared facilities, and limited quantity of our QD material (coupled with very high consumption during device fabrication), led to experimental throughput that was not sufficient to address the heavy burden that this work placed on perfecting device processes. Typically, infelicities in process dominated any useful scientific insight that could be gleaned. It was perhaps the author's foolishness that led to continued pursuit of difficult layered structures, as opposed to abandoning this direction for something more robust.

I have three recommendations for future work in this vein, the first two of which have already been adopted by successors, in part owing to the actions of other groups. The recommendations are:

- Choose a simple, robust device platform, even if this means sacrificing some surface area or photovoltaic effect. One needs to be able to work in a regime in which meaningful data can be collected somewhat routinely. The interdigitated electrode design is a good candidate.

- Work in a wavelength range of potential application. While working with CdSe QDs (active the visible region) allowed us to exploit the extensive understanding of how to process and chemically anneal the material, the resulting devices are not compelling because of the immutable dominance of silicon photodetectors in the visible spectrum.

- Engage management. Because of the diverse nature of activities required in QD-PD development and the limited availability of QD material, progress will likely be optimized when a when a team of several people, with considered, unified goals, work together.

Despite the limits of this work and the occasional needless dissipation of resources, progress has been made—and the endless frontier of parameter space has become a bit smaller.

Appendix A

Synthesis and Processing of CdSe QDs for Use in QD-PDs

CdSe QDs used for the production of QD-PDs were "bare" cores produced by so-called "cadmium oleate" synthesis.[13] The procedural variant used is described below in detail.

To a 50-mL, three-neck, round-bottom flask (evacuated and back-filled with N_2 were added 8.0 mL oleylamine (Pfaultz & Bauer), 5.0 mL di-n-octylether (TCI), and 3.5 mL tri-n-octylphosphine (Strem, 97%). The flask was brought to 85 °C, and degasing was begun very slowly. Once vigorous bubbling subsided, degasing continued for at least 1 hr.

To a 20-mL septum-capped vial were added a small stir bar, 318 mg[1] (1 mmol) 98% cadmium pentanedionate (Lancaster or Alfa Aesar) and 0.62 mL[2] (2 mmol) > 99% oleic acid (TCI > 95%). The vial was evacuated and back-filled with N_2, after which 3.0 mL tri-octylphosphine (Strem, 97%) was added. The vial was then again evacuated. After bubbling stopped, the vial was lowered into a 100 °C bath of silicone oil. Degasing continued for at least two hours, after which the solution was clear and pinkish-orange in color.

6.0 mL 1.5 M (9 mmol) TOPSe was added to the above vial after the vial was back-

---

[1] 1 mmol Cd(acac)$_2$ is actually 311 mg. 318 mg was used to correct for the presence of $\sim$ 2% impurities.

[2] At times, 1.0 mL oleic acid was used. This was to ensure complete conversion to Cd(oleate)$_2$.

filled with N_2 and allowed to cool for 3-5 min.[3] The precursors were mixed, yielding 10 mL of injection solution. The flask was heated to 325-327 °C, at which point the heating mantle was removed and the precursors were rapidly injected. There was no grow-out. A typical absorption spectrum is shown in Fig. A. Changing the Cd:Se ratio did not affect appreciably the band-edge wavelength of this synthesis. However, "quenching" the reaction with an additional 10 mL of cold solvent immediately after injection of precursors as been effective in producing smaller QDs.

Once the growth solution cooled to under 100 °C, 5.0 mL butanol were added to the flask, and the resulting solution (roughly 30 mL in volume) were split between two 20-mL vials and stored in a lab drawer until needed.

As has been done with the more fundamental studies of photoconductivity of CdSe,[59] great care was taken in processing CdSe QDs for use in QD-PDs. Below is the typical processing procedure (a so-called "soft" crash-out) for processing CdSe cores that produced sufficient QD material for one or two half-inch thick-slab QD-PDs.

1. Two 5-mL aliquots of growth solution (with butanol added, as noted above) were put into two 20-mL vials. Methanol was delivered by buret into each vial (with stirring) until the solution became cloudy. An additional 1 mL of methanol was then added to each.

2. The vials were spun in a centrifuge for 5 min at 3900 RPM. The supernatant (slight QD color) was poured off, yielding a QD centrifugate of oily appearance on the bottom and wall of the vial. 2 mL anhydrous hexane (Aldrich, > 95%) were added to each vial, which were refrigerated 5-10 min.[4]

3. The vials were again spun for 5 min at 3900 RPM, and the supernatant was removed and filtered (using 200-nm syringe filters) into two new 20-mL vials. 2 mL butanol was added to each vial.

---

[3]This delay was to ensure that there was no nucleation in the vial upon mixing Cd and Se precursors.

[4]The refrigeration step is more important for a $Cd(OH)_2$-based $Cd(oleate)_2$ prep, in which there are more salts that need to be removed. It could perhaps be removed from the procedure for processing the synthesis outlined above.

4. Methanol was delivered by buret into each vial until the solution turned cloudy. Fifteen additional drops of methanol were then added to each.

5. The vials were spun for 5 min at 3900 RPM. The supernatant (considerable QD color) was poured off, yielding a QD centrifugate oily in appearance and confined to a small area at the bottom of the vial. 1.5 mL anhydrous hexane and 1.5 mL butanol was added to each. These solutions were in turn passed through 100-nm syringe filters into new 7-mL vials.

6. Methanol was delivered until each solution turned cloudy, and fifteen additional drops of methanol were then added. The vials were centrifuged a final time for 5 min at 3900 RPM.

7. The supernatant (considerable QD color) was poured off, and 0.5 mL anhydrous hexane was added to each vial. The solutions were combined in a 1-mL syringe and filtered through a 20-nm syringe filter into a new 7-mL vial equipped with a septum cap.

8. The mass of this resulting solution was measuring, and from this mass, the volume of the solution was calculated.[5] Then, 12.5 μL of this solution were added to 2.5 mL hexane (dilution by a factor of 200), and the resulting absorption spectrum was taken. Usually, the first peak had an absorption value of about 0.2.

9. Using the volume of the solution and absorbance value after 200 times dilution, the volume (of chloroform) needed to produce a 100-times dilution first absorbance maximum of 3.0 was calculated. Typically, this volume was 0.2-0.3 mL.[6]

10. A stir bar was added to the vial, and the hexane was evaporated on the vacuum line. The vial was back-filled with N_2 and transported to the LOOE growth lab in Building 13.

---

[5]The mass of the QDs was neglected in this calculation.

[6]I have concluded that the QD/chloroform solutions prepared by Wing-K. Woo and Jonathan S. Steckel for QD-LEDs can be approximately replicated by replacing the 3.0 absorption target by 0.5.
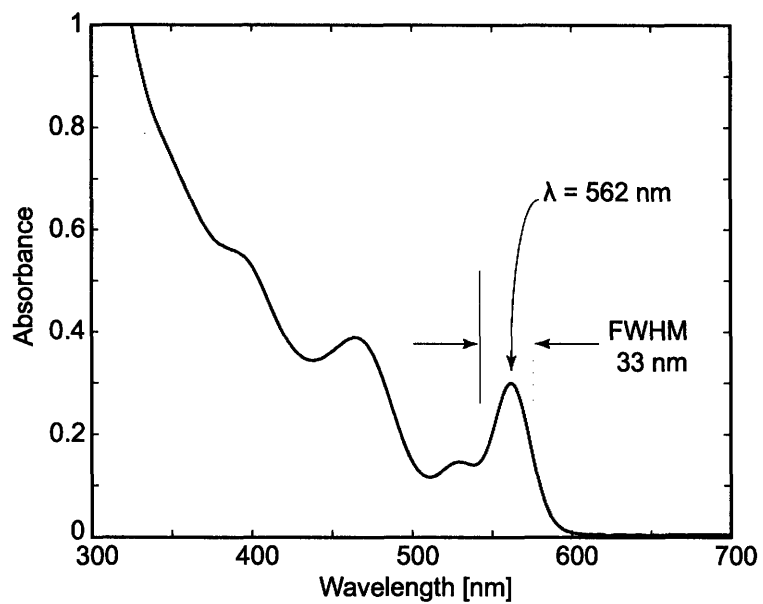
Figure A-1: Absorption spectrum of a typical synthesis of CdSe QDs.

Appendix B

InSb QDs: Attempts at Synthesis

In this brief appendix, we describe work carried out in 2004 by Bawendi Group post-doc Frédéric Dumestre toward the successful synthesis of useful InSb QDs, which were of interest because the small bulk band gap (0.17 eV) of InSb would allow colloidal QDs InSb to be tunable across 3 μm $< \lambda <$ 5 μm. Currently, this work has been nowhere reported and only exists in electronic presentation format. A summary is provided here, along with a description of instrumentation purchased to characterize InSb QDs spectrally.

B.1   InSb Syntheses

B.1.1   Synthesis with a Reductant

In the first synthetic approach, an In^{+III} and an Sb^{+III} compound were both used in the presence of a reducing agent. The injection mixture, containing 0.5 mmol In(Me)$_3$ in 1.5 mL TOP, 0.5 mmol Sb(Ph)$_3$ in 1.5 mL TOP, and 2 mmol HDDO in 1.5 mL TOP, was prepared and immediately injected into a flask containing 5 mmol HDA, 5 mmol oleic acid, and 3 g TOPO at 320 °C. Growth was carried out at 280 °C.

A representative TEM of the resulting solid is shown in Fig. B-1(a), and both nanoribbons and nanoparticles are present. STEM was used to map the elements in these structures and determined that while the nanoribbons contained both In and
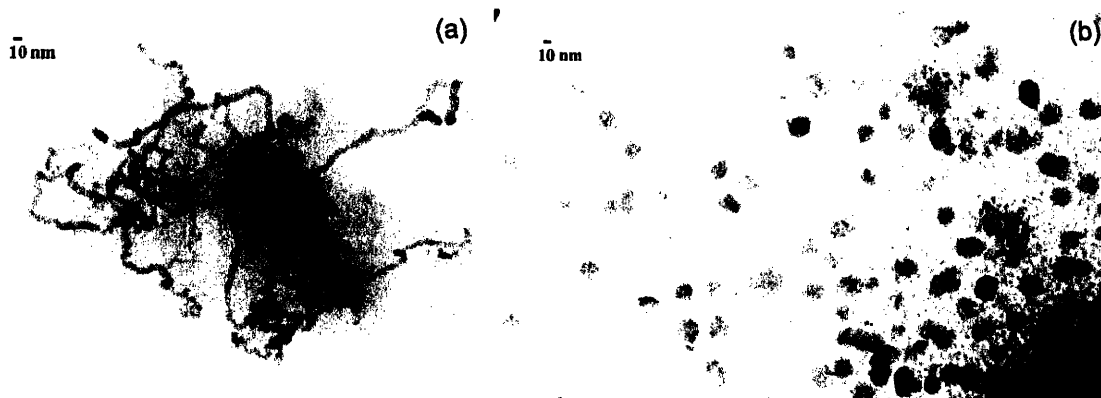
Figure B-1: TEM results from two InSb QD syntheses. Image (a) shows a mixture of In particles and InSb nanoribbons resulting from a synthesis using In(Me)$_3$ and Sb(Ph)$_3$ as starting materials, and image (b) shows polydisperse InSb nanoparticles resulting from the reaction of InCl$_3$ with Sb(TMS)$_3$.

Sb, the particles were contained only In.

B.1.2 Synthesis without a Reductant

In the second synthetic approach, In^{+III} and Sb^{-III} compounds were reacted directly. The indium source was InCl$_3$-TOP, and the antimony source was Sb(TMS)$_3$, an analog of the As(TMS)$_3$ used by our group in InAs QD syntheses[25]. Sb(TMS)$_3$ is highly sensitive to air and *exceedingly* difficult to make. In this reaction, 10 mL TOP were heated to 300 °C and 1.5 mL InCl$_3$-TOP,[1] 1.35 mmol In, and 0.68 mmol Sb(TMS)$_3$ were mixed and immediately injected. Growth followed at 260 °C.

The resulting nanoparticles are shown in Fig. B-1(b), suggesting a rather polydisperse size distribution. HRTEM seemed revealed lattice spacings for the small particles (3.65 Å) consistent with the InSb (111), 3.74 Å. However, the large particles had a smaller spacing (3.32 Å), perhaps indicating another compound. Filtration was carried out to separate the small nanoparticles from the larger ones, but the nanoparticles could not be dispersed in chloroform after this simple processing.

Ultimately, InSb particles processable in common solvents and with good monodispersity were never produced before Dumestre departed the Bawendi Group.

---

[1]Prepared with 15 mL TOP and 3 g InCl$_3$.

186

B.2 FT-IR Customized to 3 μm $< \lambda <$ 5 μm Range

Early in 2004, in preparation for characterization of QD materials with band-edge features in the 3 μm $< \lambda <$ 5 μm range, the author configured and purchased a Thermo-Nicolet Nexus 470 FT-IR spectrometer optimized for 3 μm $< \lambda <$ 5 μm (but capable of detecting 1 μm $< \lambda <$ 5 μm). This spectrometer which now resides in Bawendi Laser Lab B. Dispersive spectrometers equipped with extended InGaAs detectors (such as the Cary 5000) are limited to $\lambda <$ 3 μm, and those reaching longer in wavelength are rare. The FT-IR was customized for 3 μm $< \lambda <$ 5 μm by selecting a tungsten-halogen source, CaF_2 beam splitter, and DTGS detector. Because of the general lack of samples active for 3 μm $< \lambda <$ 5 μm and some displeasure with the noise level in this spectrometer, it has seen very light use.

THIS PAGE INTENTIONALLY LEFT BLANK

Appendix C

The Detectivity Metric D^*

While the bulk of the work reported in this thesis is oriented toward the development of working QD-PDs without strong consideration of all device metrics, a recent report of very high detectivities in the SW-IR demonstrated by PbS QD-PDs (using the more robust interdigitated transverse channel geometry)[147] has prompted work in our group to turn toward (1) experimental verification of the reported results and (2) development of a deeper understanding of noise sources in photodetectors. This work is being led by Scott M. Geyer. In this brief appendix, we explain the origin of the detectivity metric, which has become obscured today by its very wide use (both correctly and incorrectly) in the literature and in industry.

The metric D^*, or "dee-star," which we shall also call detectivity in this appendix, was first defined by R. Clark Jones of Polariod in the 1950s.[173] For a photon detector,[1] operating such that the photon noise is the dominant noise source, responsive quantum efficiency may be defined as

$$R(\lambda) = \frac{i_{\text{ph}}}{P(\lambda)}, \qquad (C.1)$$

where i_{ph} is photocurrent in amperes and $P(\lambda)$ the incident power in watts. While this metric is, in some sense, a figure of merit for a detector, it does not capture the

---

[1]Photon detectors include photodiodes, PMTs, human vision, and photographic film. This metric does not apply for thermal detectors such as bolometers and thermocouples.

entire picture, particularly with regard to fundamental photon noise. For example, phototubes and photomultiplier tubes have vastly different responsive quantum efficiencies, yet they contain the same kind of photosensitive surface and perhaps should exhibit the same photon noise characteristics.

For any operating photon detector, we can define N_i as the number of photons incident on the detector, and this value is easily measured. We can also measure N_a, the number of photons absorbed by the detector. However, not all of the absorbed photons necessarily give rise to detector output. Of the N_a (statistically independent) photons absorbed, only N_e, the number of *effective* photons, actually give rise to detector output. The ratio N_e/N_i, then provides a more fundamental kind of "detective" quantum efficiency that reflects how well the detector output preserves the statistical independence of the incident photons. Unfortunately, this is far from an operational metric because N_e cannot be directly measured.

To illustrate this subtlety more clearly, let us consider two photon detectors:

Case 1: An "ideal" photodetector in which $N_e = N_a$. That is, all absorbed photons (statistically independent) give rise to electrons in the circuitry.

Case 2: Altered "ideal" photodetector in which an absorptive OD = 0.3 filter is placed in front of the device and an amplifier with gain = 2 is added to the circuit.

Clearly, the responsive quantum efficiency R is equal for these devices. However, the signal in Case 2 will have twice the mean square noise current because fewer statistically independent photons contributed to signal current. We can define this noise current as the noise equivalent input (NEI), and in Case 2 NEI is twice that in Case 1.

Provided that photon noise is the dominant source of detector noise, the NEI can be measured experimentally, and is usually called noise equivalent power (NEP). This is done by dividing the integrated RMS noise current i_n (integrated over some frequency range of detector operation) by the responsive quantum efficiency R. We

can then define the detective quantum efficiency

$$D = \frac{R}{i_n} = \frac{1}{\text{NEP}}.$$

(C.2)

The metric D, then, behaves as an indicator of the "fundamental" quantum efficiency N_e/N_i. That is, in our simple example, $D(\text{Case 1}) = 2D(\text{Case 2})$.

We can make this metric more universal by normalizing for device area and for bandwidth over which noise current is integrated. If we return to Case 1 above and now compare two otherwise identical, ideal photodetectors of with areas A and nA (for some integer n), we can view the latter as multiple samplings of the former for which noise will increase with $n^{1/2}$. A similar additive argument pertains for frequency windows of different widths in the detector response spectrum in which we may choose to work. More specifically, NEP should scale as $(\Delta f)^{1/2}$ and, in fact, is often measured in this normalized sense directly. Hence, we can define the detectivity, or D^*, as

$$D^* = \frac{(A\Delta f)^{1/2}}{\text{NEP}}.$$

(C.3)

Normally, D^* is given in units of cm $\text{Hz}^{1/2}$ W^{-1}, also known as Jones.

During the last fifty years, the D^* metric has become somewhat clouded by imprecise or even evolving definitions. However, it is important to remember the idea that, most deeply, D^* applies to photon-noise-limited detectors and describes how badly a detector degrades the statistical independence of absorbed photons. The following two guidelines should be kept in mind:

- Any claims of a "dark" D^* measurement should be viewed with suspicion. Because D^* deals fundamentally the degradation of the statistical independence of photons, some photon source must be acknowledged, even if it is just a black-body source at 300 K.

- D^* is dependent on illumination source, center frequency, and frequency bandwidth. To avoid ambiguity, D^* should always be specified as $D^*(\lambda, f, \Delta f)$ or $D^*(T, f, \Delta f)$.[137]

191

THIS PAGE INTENTIONALLY LEFT BLANK

References

[1] J. H. Moore, C. C. Davis, and M. A. Coplan. *Building Scientific Apparatus.* Perseus Books, Cambridge, MA, 2003.

[2] *Manual of classification.* United States Patent and Trademark Office, 2007. Class Definition 977. http://www.uspto.gov/go/classification/uspc977/-defs977.htm.

[3] P. Walter, E. Welcomme, P. Hallegot, N. J. Zaluzec, C. Deeb, J. Castaing, P. Veyssiere, R. Breniaux, J. L. Leveque, and G. Tsoucaris. Early use of PbS nanotechnology for an ancient hair dyeing formula. *Nano Letters*, 6(10):2215–2219, 2006.

[4] D. Jembrih-Simburger, C. Neelmeijer, O. Schalm, P. Fredrickx, M. Schreiner, K. De Vis, M. Mader, D. Schryvers, and J. Caen. The colour of silver stained glass - analytical investigations carried out with XRF, SEM/EDX, TEM, and IBA. *Journal of Analytical Atomic Spectrometry*, 17(4):321–328, 2002.

[5] M. Reibold, P. Paufler, A. A. Levin, W. Kochmann, N. Patzke, and D. C. Meyer. Materials - carbon nanotubes in an ancient Damascus sabre. *Nature*, 444(7117):286–286, 2006.

[6] M. C. Roco. *Government Nanotechnology Funding: An International Outlook*, National Science Foundation, 2003. http://www.nano.gov/html/res/-IntlFundingRoco.htm.

[7] C. B. Murray, D. J. Norris, and M. G. Bawendi. Synthesis and characterization

of nearly monodisperse CdE (E = S, Se, Te) semiconductor nanocrystallites. *Journal of the American Chemical Society*, 115(19):8706–8715, 1993.

[8] M. G. Bawendi and N. E. Stott. U. S. Patent 6,576,291. Preparation of nanocrystallites , volume = 6576291, year = 2003.

[9] Z. A. Peng and X. G. Peng. Formation of high-quality CdTe, CdSe, and CdS nanocrystals using CdO as precursor. *Journal of the American Chemical Society*, 123(1):183–184, 2001.

[10] L. E. Brus. Electron electron and electron-hole interactions in small semiconductor crystallites - the size dependence of the lowest excited electronic state. *Journal of Chemical Physics*, 80(9):4403–4409, 1984.

[11] M. K. Kuno. *Band Edge Spectroscopy of CdSe Quantum Dots*. Ph.D. Thesis, Massachusetts Institute of Technology, 1998.

[12] B. R. Fisher. *Time Resolved Fluorescence of CdSe Nanocrystals using Single Molecule Spectroscopy*. Ph.D. Thesis, Massachusetts Institute of Technology, 2005.

[13] B. K. H. Yen, N. E. Stott, K. F. Jensen, and M. G. Bawendi. A continuous-flow microcapillary reactor for the preparation of a size series of CdSe nanocrystals. *Advanced Materials*, 15(21):1858–1862, 2003.

[14] D. J. Norris, A. L. Efros, M. Rosen, and M. G. Bawendi. Size dependence of exciton fine structure in CdSe quantum dots. *Physical Review B*, 53(24):16347–16354, 1996.

[15] A. Sacra, D. J. Norris, C. B. Murray, and M. G. Bawendi. Stark spectroscopy of CdSe nanocrystallites - the significance of transition linewidths. *Journal of Chemical Physics*, 103(13):5236–5245, 1995.

[16] V. I. Klimov. Optical nonlinearities and ultrafast carrier dynamics in semiconductor nanocrystals. *Journal of Physical Chemistry B*, 104(26):6112–6123, 2000.

[17] V. I. Klimov, A. A. Mikhailovsky, D. W. McBranch, C. A. Leatherdale, and M. G. Bawendi. Quantization of multiparticle Auger rates in semiconductor quantum dots. *Science*, 287(5455):1011–1013, 2000.

[18] S. A. Empedocles, D. J. Norris, and M. G. Bawendi. Photoluminescence spectroscopy of single CdSe nanocrystallite quantum dots. *Physical Review Letters*, 77(18):3873–3876, 1996.

[19] M. Nirmal, B. O. Dabbousi, M. G. Bawendi, J. J. Macklin, J. K. Trautman, T. D. Harris, and L. E. Brus. Fluorescence intermittency in single cadmium selenide nanocrystals. *Nature*, 383(6603):802–804, 1996.

[20] K. T. Shimizu, W. K. Woo, B. R. Fisher, H. J. Eisler, and M. G. Bawendi. Surface-enhanced emission from single semiconductor nanocrystals. *Physical Review Letters*, 89(11), 2002.

[21] B. Fisher, J. M. Caruge, D. Zehnder, and M. Bawendi. Room-temperature ordered photon emission from multiexciton states in single CdSe core-shell nanocrystals. *Physical Review Letters*, 94(8), 2005.

[22] R. D. Schaller and V. I. Klimov. High efficiency carrier multiplication in PbSe nanocrystals: Implications for solar energy conversion. *Physical Review Letters*, 92(18):186601, 2004.

[23] R. J. Ellingson, M. C. Beard, J. C. Johnson, P. R. Yu, O. I. Mićić, A. J. Nozik, A. Shabaev, and A. L. Efros. Highly efficient multiple exciton generation in colloidal PbSe and PbS quantum dots. *Nano Letters*, 5(5):865–871, 2005.

[24] S. Kim, Y. T. Lim, E. G. Soltesz, A. M. De Grand, J. Lee, A. Nakayama, J. A. Parker, T. Mihaljevic, R. G. Laurence, D. M. Dor, L. H. Cohn, M. G. Bawendi, and J. V. Frangioni. Near-infrared fluorescent type II quantum dots for sentinel lymph node mapping. *Nature Biotechnology*, 22(1):93–97, 2004.

[25] J. P. Zimmer, S. W. Kim, S. Ohnishi, E. Tanaka, J. V. Frangioni, and M. G. Bawendi. Size series of small indium arsenide-zinc selenide core-shell nanocrys-

tals and their application to in vivo imaging. *Journal of the American Chemical Society*, 128(8):2526–2527, 2006.

[26] Y. Chan, J. P. Zimmer, M. Stroh, J. S. Steckel, R. K. Jain, and M. G. Bawendi. Incorporation of luminescent nanocrystals into monodisperse core-shell silica microspheres. *Advanced Materials*, 16(23-24):2092–2097, 2004.

[27] Y. Arakawa and H. Sakaki. Multidimensional quantum well laser and temperature-dependence of its threshold current. *Applied Physics Letters*, 40(11):939–941, 1982.

[28] V. C. Sundar, H. J. Eisler, and M. G. Bawendi. Room-temperature, tunable gain media from novel II-VI nanocrystal-titania composite matrices. *Advanced Materials*, 14(10):739–743, 2002.

[29] Y. Chan, J. S. Steckel, P. T. Snee, J. M. Caruge, J. M. Hodgkiss, D. G. Nocera, and M. G. Bawendi. Blue semiconductor nanocrystal laser. *Applied Physics Letters*, 86(7), 2005.

[30] P. T. Snee, Y. H. Chan, D. G. Nocera, and M. G. Bawendi. Whispering-gallery-mode lasing from a semiconductor nanocrystal/microsphere resonator composite. *Advanced Materials*, 17(9):1131–1136, 2005.

[31] S. Coe, W. K. Woo, M. Bawendi, and V. Bulović. Electroluminescence from single monolayers of nanocrystals in molecular organic devices. *Nature*, 420(6917):800–803, 2002.

[32] J. S. Steckel, S. Coe-Sullivan, V. Bulović, and M. G. Bawendi. 1.3 μm to 1.55 μm tunable electroluminescence from PbSe quantum dots embedded within an organic device. *Advanced Materials*, 15(21):1862–1866, 2003.

[33] C. W. Tang and S. A. Vanslyke. Organic electroluminescent diodes. *Applied Physics Letters*, 51(12):913–915, 1987.

[34] V. Bulović, P. E. Burrows, and S. R. Forrest. Molecular organic light-emitting devices. In *Electroluminescence I*, volume 64 of *Semiconductors and Semimetals*, pages 255–306. Academic Press, Inc., New York, 2000.

[35] S. Coe-Sullivan, W. K. Woo, J. S. Steckel, M. Bawendi, and V. Bulović. Tuning the performance of hybrid organic/inorganic quantum dot light-emitting devices. *Organic Electronics*, 4(2-3):123–130, 2003.

[36] B. G. Streetman and S. Banerjee. *Solid State Electronic Devices*. Prentice Hall Series in Solid State Physical Electronics. Prentice Hall, Upper Saddle River, NJ, fifth edition, 2000.

[37] P. K. Kaiser and R. M. Boynton. *Human color vision*. Optical Society of America, Washington, DC, 1996.

[38] P. Peumans, V. Bulović, and S. R. Forrest. Efficient, high-bandwidth organic multilayer photodetectors. *Applied Physics Letters*, 76(26):3855–3857, 2000.

[39] G. Gaussorgues. *Infrared Thermography*. Microwave Technology Series. Chapman & Hall, London, 1994.

[40] D. Battaglia and X. G. Peng. Formation of high quality InP and InAs nanocrystals in a noncoordinating solvent. *Nano Letters*, 2(9):1027–1030, 2002.

[41] C. B. Murray, S. H. Sun, W. Gaschler, H. Doyle, T. A. Betley, and C. R. Kagan. Colloidal synthesis of nanocrystals and nanocrystal superlattices. *IBM Journal of Research and Development*, 45(1):47–56, 2001.

[42] M. A. Hines and G. D. Scholes. Colloidal PbS nanocrystals with size-tunable near-infrared emission: Observation of post-synthesis self-narrowing of the particle size distribution. *Advanced Materials*, 15(21):1844–1849, 2003.

[43] P. Rousselot, C. Lidman, J. G. Cuby, G. Moreels, and G. Monnet. Night-sky spectral atlas of OH emission lines in the near-infrared. *Astronomy and Astrophysics*, 354(3):1134–1150, 2000.

[44] K. G. Anlauf, R. G. MacDonald, and J. C. Polanyi. Infrared chemiluminescence from H + O_3 at low pressure. *Chemical Physics Letters*, 1(13):619–622, 1968.

[45] B. O. Dabbousi, C. B. Murray, M. F. Rubner, and M. G. Bawendi. Langmuir-Blodgett manipulation of size-selected CdSe nanocrystallites. *Chemistry of Materials*, 6(2):216–219, 1994.

[46] C. R. Kagan. *The Electronic and Optical Properties of Close Packed Cadmium Selenide Quantum Dot Solids*. Ph.D. Thesis, Massachusetts Institute of Technology, 1996.

[47] C. A. Leatherdale, C. R. Kagan, N. Y. Morgan, S. A. Empedocles, M. A. Kastner, and M. G. Bawendi. Photoconductivity in CdSe quantum dot solids. *Physical Review B*, 62(4):2669–2680, 2000.

[48] M. V. Jarosz, V. J. Porter, B. R. Fisher, M. A. Kastner, and M. G. Bawendi. Photoconductivity studies of treated CdSe quantum dot films exhibiting increased exciton ionization efficiency. *Physical Review B*, 70(19):195327, 2004.

[49] P. Guyot-Sionnest and C. Wang. Fast voltammetric and electrochromic response of semiconductor nanocrystal thin films. *Journal of Physical Chemistry B*, 107(30):7355–7359, 2003.

[50] D. C. Oertel, M. G. Bawendi, A. C. Arango, and V. Bulović. Photodetectors based on treated CdSe quantum-dot films. *Applied Physics Letters*, 87(21):213505, 2005.

[51] A. C. Arango, Y. Xu, V. Bulović, D. C. Oertel, and M. G. Bawendi. Quantum dot photovoltaics fabricated via microcontact printing. *in preparation*, 2007.

[52] J. S. Steckel, B. K. H. Yen, D. C. Oertel, and M. G. Bawendi. On the mechanism of lead chalcogenide nanocrystal formation. *Journal of the American Chemical Society*, 128(40):13032–13033, 2006.

[53] D. L. Klein, P. L. McEuen, J. E. B. Katari, R. Roth, and A. P. Alivisatos. An approach to electrical studies of single nanocrystals. *Applied Physics Letters*, 68(18):2574–2576, 1996.

[54] D. L. Klein, R. Roth, A. K. L. Lim, A. P. Alivisatos, and P. L. McEuen. A single-electron transistor made from a cadmium selenide nanocrystal. *Nature*, 389(6652):699–701, 1997.

[55] M. A. Kastner. Artificial atoms. *Physics Today*, 46(1):24–31, 1993.

[56] R. C. Ashoori. Electrons in artificial atoms. *Nature*, 379(6564):413–419, 1996.

[57] A. P. Alivisatos. Semiconductor clusters, nanocrystals, and quantum dots. *Science*, 271(5251):933–937, 1996.

[58] C. B. Murray, C. R. Kagan, and M. G. Bawendi. Self-organization of CdSe nanocrystallites into 3-dimensional quantum-dot superlattices. *Science*, 270(5240):1335–1338, 1995.

[59] M. V. Jarosz, N. E. Stott, M. Drndić, N. Y. Morgan, M. A. Kastner, and M. G. Bawendi. Observation of bimolecular carrier recombination dynamics in close-packed films of colloidal CdSe nanocrystals. *Journal of Physical Chemistry B*, 107(46):12585–12588, 2003.

[60] D. S. Ginger and N. C. Greenham. Charge injection and transport in films of CdSe nanocrystals. *Journal of Applied Physics*, 87(3):1361–1368, 2000.

[61] D. V. Talapin and C. B. Murray. PbSe nanocrystal solids for n- and p-channel thin film field-effect transistors. *Science*, 310(5745):86–89, 2005.

[62] M. Drndić, M. V. Jarosz, N. Y. Morgan, M. A. Kastner, and M. G. Bawendi. Transport properties of annealed CdSe colloidal nanocrystal solids. *Journal of Applied Physics*, 92(12):7498–7503, 2002.

[63] N. Y. Morgan, C. A. Leatherdale, M. Drndić, M. V. Jarosz, M. A. Kastner, and M. Bawendi. Electronic transport in films of colloidal CdSe nanocrystals. *Physical Review B*, 66(7):075339, 2002.

[64] D. S. Novikov, M. Drndić, L. S. Levitov, M. A. Kastner, M. V. Jarosz, and M. G. Bawendi. Levy statistics and anomalous transport in quantum-dot arrays. *Physical Review B*, 72(7):075309, 2005.

[65] T. D. Krauss and L. E. Brus. Charge, polarizability, and photoionization of single semiconductor nanocrystals. *Physical Review Letters*, 83(23):4840–4843, 1999.

[66] M. Drndić, R. Markov, M. V. Jarosz, M. G. Bawendi, M. A. Kastner, N. Markovic, and M. Tinkham. Imaging the charge transport in arrays of CdSe nanocrystals. *Applied Physics Letters*, 83(19):4008–4010, 2003.

[67] R. J. Ellingson, J. L. Blackburn, P. R. Yu, G. Rumbles, O. I. Mićić, and A. J. Nozik. Excitation energy dependent efficiency of charge carrier relaxation and photoluminescence in colloidal InP quantum dots. *Journal of Physical Chemistry B*, 106(32):7758–7765, 2002.

[68] Z. H. Hu, M. D. Fischbein, and M. Drndić. Local charge transport in two-dimensional PbSe nanocrystal arrays studied by electrostatic force microscopy. *Nano Letters*, 5(7):1463–1468, 2005.

[69] B. A. Ridley, B. Nivi, and J. M. Jacobson. All-inorganic field effect transistors fabricated by printing. *Science*, 286(5440):746–749, 1999.

[70] V. J. Porter, T. Mentzel, S. Charpentier, M. A. Kastner, and M. G. Bawendi. Temperature-, gate-, and photoinduced conductance of close-packed CdTe nanocrystal films. *Physical Review B*, 73:155303, 2006.

[71] A. Maria, P. W. Cyr, E. J. D. Klem, L. Levina, and E. H. Sargent. Solution-processed infrared photovoltaic devices with > 10% monochromatic internal quantum efficiency. *Applied Physics Letters*, 87(21):213112, 2005.

[72] S. C. Erwin, L. J. Zu, M. I. Haftel, A. L. Efros, T. A. Kennedy, and D. J. Norris. Doping semiconductor nanocrystals. *Nature*, 436(7047):91–94, 2005.

[73] M. Shim and P. Guyot-Sionnest. n-type colloidal semiconductor nanocrystals. *Nature*, 407(6807):981–983, 2000.

[74] M. Shim, C. J. Wang, and P. Guyot-Sionnest. Charge-tunable optical properties in colloidal semiconductor nanocrystals. *Journal of Physical Chemistry B*, 105(12):2369–2373, 2001.

[75] D. Yu, C. J. Wang, and P. Guyot-Sionnest. n-type conducting CdSe nanocrystal solids. *Science*, 300(5623):1277–1280, 2003.

[76] D. Yu, C. J. Wang, B. L. Wehrenberg, and P. Guyot-Sionnest. Variable range hopping conduction in semiconductor nanocrystal solids. *Physical Review Letters*, 92(21):216802, 2004.

[77] B. L. Wehrenberg, D. Yu, J. S. Ma, and P. Guyot-Sionnest. Conduction in charged PbSe nanocrystal films. *Journal of Physical Chemistry B*, 109(43):20192–20199, 2005.

[78] M. Shim, C. J. Wang, D. J. Norris, and P. Guyot-Sionnest. Doping and charging in colloidal semiconductor nanocrystals. *MRS Bulletin*, 26(12):1005–1008, 2001.

[79] C. J. Wang, M. Shim, and P. Guyot-Sionnest. Electrochromic nanocrystal quantum dots. *Science*, 291(5512):2390–2392, 2001.

[80] W. K. Woo, K. T. Shimizu, M. V. Jarosz, R. G. Neuhauser, C. A. Leatherdale, M. A. Rubner, and M. G. Bawendi. Reversible charging of CdSe nanocrystals in a simple solid-state device. *Advanced Materials*, 14(15):1068–1071, 2002.

[81] C. J. Wang, M. Shim, and P. Guyot-Sionnest. Electrochromic semiconductor nanocrystal films. *Applied Physics Letters*, 80(1):4–6, 2002.

[82] A. L. Roest, J. J. Kelly, D. Vanmaekelbergh, and E. A. Meulenkamp. Staircase in the electron mobility of a ZnO quantum dot assembly due to shell filling. *Physical Review Letters*, 89(3):036801, 2002.

[83] D. Vanmaekelbergh and P. Liljeroth. Electron-conducting quantum dot solids: novel materials based on colloidal semiconductor nanocrystals. *Chemical Society Reviews*, 34(4):299–312, 2005.

[84] A. Germeau, A. L. Roest, D. Vanmaekelbergh, G. Allan, C. Delerue, and E. A. Meulenkamp. Optical transitions in artificial few-electron atoms strongly confined inside ZnO nanocrystals. *Physical Review Letters*, 90(9):036801, 2003.

[85] B. L. Wehrenberg and P. Guyot-Sionnest. Electron and hole injection in PbSe quantum dot films. *Journal of the American Chemical Society*, 125(26):7806–7807, 2003.

[86] J. J. Urban, D. V. Talapin, E. V. Shevchenko, and C. B. Murray. Self-assembly of PbTe quantum dots into nanocrystal superlattices and glassy films. *Journal of the American Chemical Society*, 128(10):3248–3255, 2006.

[87] A. J. Nozik. Quantum dot solar cells. *Physica E-Low-Dimensional Systems & Nanostructures*, 14(1-2):115–120, 2002.

[88] B. O'Regan and M. Grätzel. A low-cost, high-efficiency solar-cell based on dye-sensitized colloidal TiO_2 films. *Nature*, 353(6346):737–740, 1991.

[89] D. Liu and P. V. Kamat. Photoelectrochemical behavior of thin CdSe and coupled TiO_2 CdSe semiconductor-films. *Journal of Physical Chemistry*, 97(41):10769–10773, 1993.

[90] R. Vogel, P. Hoyer, and H. Weller. Quantum-sized PbS, CdS, Ag_2S, Sb_2S_3, and Bi_2S_3 particles as sensitizers for various nanoporous wide-bandgap semiconductors. *Journal of Physical Chemistry*, 98(12):3183–3188, 1994.

[91] P. Hoyer and R. Könenkamp. Photoconduction in porous TiO$_2$ sensitized by PbS quantum dots. *Applied Physics Letters*, 66(3):349–351, 1995.

[92] A. Zaban, O. I. Mićić, B. A. Gregg, and A. J. Nozik. Photosensitization of nanoporous TiO$_2$ electrodes with InP quantum dots. *Langmuir*, 14(12):3153–3156, 1998.

[93] N. C. Greenham, X. G. Peng, and A. P. Alivisatos. Charge separation and transport in conjugated polymer cadmium selenide nanocrystal composites studied by photoluminescence quenching and photoconductivity. *Synthetic Metals*, 84(1-3):545–546, 1997.

[94] G. Yu, J. Gao, J. C. Hummelen, F. Wudl, and A. J. Heeger. Polymer photovoltaic cells - enhanced efficiencies via a network of internal donor-acceptor heterojunctions. *Science*, 270(5243):1789–1791, 1995.

[95] P. Peumans, A. Yakimov, and S. R. Forrest. Small molecular weight organic thin-film photodetectors and solar cells. *Journal of Applied Physics*, 93(7):3693–3723, 2003.

[96] Y. Wang and N. Herron. Photoconductivity of CdS nanocluster-doped polymers. *Chemical Physics Letters*, 200(1-2):71–75, 1992.

[97] Y. Wang and N. Herron. Semiconductor nanocrystals in carrier-transporting polymers. charge generation and charge transport. *Journal of Luminescence*, 70:48–59, 1996.

[98] N. C. Greenham, X. G. Peng, and A. P. Alivisatos. Charge separation and transport in conjugated-polymer/semiconductor-nanocrystal composites studied by photoluminescence quenching and photoconductivity. *Physical Review B*, 54(24):17628–17637, 1996.

[99] D. S. Ginger and N. C. Greenham. Charge separation in conjugated-polymer/nanocrystal blends. *Synthetic Metals*, 101(1-3):425–428, 1999.

[100] D. S. Ginger and N. C. Greenham. Photoinduced electron transfer from conjugated polymers to CdSe nanocrystals. *Physical Review B*, 59(16):10622–10629, 1999.

[101] D. S. Ginger and N. C. Greenham. Charge transport in semiconductor nanocrystals. *Synthetic Metals*, 124(1):117–120, 2001.

[102] T. W. F. Chang, S. Musikhin, L. Bakueva, L. Levina, M. A. Hines, P. W. Cyr, and E. H. Sargent. Efficient excitation transfer from polymer to nanocrystals. *Applied Physics Letters*, 84(21):4295–4297, 2004.

[103] G. Konstantatos, C. J. Huang, L. Levina, Z. H. Lu, and E. H. Sargent. Efficient infrared electroluminescent devices using solution-processed colloidal quantum dots. *Advanced Functional Materials*, 15(11):1865–1869, 2005.

[104] W. J. E. Beek, M. M. Wienk, and R. A. J. Janssen. Hybrid polymer solar cells based on zinc oxide. *Journal of Materials Chemistry*, 15(29):2985–2988, 2005.

[105] W. J. E. Beek, M. M. Wienk, and R. A. J. Janssen. Hybrid solar cells from regioregular polythiophene and ZnO nanoparticles. *Advanced Functional Materials*, 16:1112–1116, 2006.

[106] C. Y. Kwong, A. B. Djurisic, P. C. Chui, K. W. Cheng, and W. K. Chan. Influence of solvent on film morphology and device performance of poly(3-hexylthiophene): TiO$_2$ nanocomposite solar cells. *Chemical Physics Letters*, 384(4-6):372–375, 2004.

[107] A. A. R. Watt, D. Blake, J. H. Warner, E. A. Thomsen, E. L. Tavenner, H. Rubinsztein-Dunlop, and P. Meredith. Lead sulfide nanocrystal: conducting polymer solar cells. *Journal of Physics D-Applied Physics*, 38(12):2006–2012, 2005.

[108] W. U. Huynh, X. G. Peng, and A. P. Alivisatos. CdSe nanocrystal rods/-poly(3-hexylthiophene) composite photovoltaic devices. *Advanced Materials*, 11(11):923–927, 1999.

[109] W. U. Huynh, J. J. Dittmer, W. C. Libby, G. L. Whiting, and A. P. Alivisatos. Controlling the morphology of nanocrystal-polymer composites for solar cells. *Advanced Functional Materials*, 13(1):73–79, 2003.

[110] D. J. Milliron, A. P. Alivisatos, C. Pitois, C. Edder, and J. M. J. Frechet. Electroactive surfactant designed to mediate electron transfer between CdSe nanocrystals and organic semiconductors. *Advanced Materials*, 15(1):58–61, 2003.

[111] J. S. Liu, T. Tanaka, K. Sivula, A. P. Alivisatos, and J. M. J. Frechet. Employing end-functional polythiophene to control the morphology of nanocrystal-polymer composites in hybrid solar cells. *Journal of the American Chemical Society*, 126(21):6550–6551, 2004.

[112] W. U. Huynh, J. J. Dittmer, and A. P. Alivisatos. Hybrid nanorod-polymer solar cells. *Science*, 295(5564):2425–2427, 2002.

[113] W. U. Huynh, J. J. Dittmer, N. Teclemariam, D. J. Milliron, A. P. Alivisatos, and K. W. J. Barnham. Charge transport in hybrid nanorod-polymer composite photovoltaic cells. *Physical Review B*, 67(11):115326, 2003.

[114] I. Gur, N. A. Fromer, M. L. Geier, and A. P. Alivisatos. Air-stable all-inorganic nanocrystal solar cells processed from solution. *Science*, 310(5747):462–465, 2005.

[115] D. L. Schulz, M. Pehnt, D. H. Rose, E. Urgiles, A. F. Cahill, D. W. Niles, K. M. Jones, R. J. Ellingson, C. J. Curtis, and D. S. Ginley. CdTe thin films from nanoparticle precursors by spray deposition. *Chemistry of Materials*, 9(4):889–900, 1997.

[116] B. Q. Sun, E. Marx, and N. C. Greenham. Photovoltaic devices using blends of branched CdSe nanoparticles and conjugated polymers. *Nano Letters*, 3(7):961–963, 2003.

[117] L. Manna, D. J. Milliron, A. Meisel, E. C. Scher, and A. P. Alivisatos. Controlled growth of tetrapod-branched inorganic nanocrystals. *Nature Materials*, 2(6):382–385, 2003.

[118] B. Q. Sun, H. J. Snaith, A. S. Dhoot, S. Westenhoff, and N. C. Greenham. Vertically segregated hybrid blends for photovoltaic devices with improved efficiency. *Journal of Applied Physics*, 97(1), 2005.

[119] H. J. Snaith, G. L. Whiting, B. Q. Sun, N. C. Greenham, W. T. S. Huck, and R. H. Friend. Self-organization of nanocrystals in polymer brushes. application in heterojunction photovoltaic diodes. *Nano Letters*, 5(9):1653–1657, 2005.

[120] Y. Kang and D. Kim. Well-aligned CdS nanorod conjugated polymer solar cells. *Solar Energy Materials and Solar Cells*, 90(2):166–174, 2006.

[121] R. D. Schaller, M. A. Petruska, and V. I. Klimov. Effect of electronic structure on carrier multiplication efficiency: Comparative study of PbSe and CdSe nanocrystals. *Applied Physics Letters*, 87(25):253102, 2005.

[122] J. E. Murphy, M. C. Beard, A. G. Norman, S. P. Ahrenkiel, J. C. Johnson, P. R. Yu, O. I. Mićić, R. J. Ellingson, and A. J. Nozik. PbTe colloidal nanocrystals: Synthesis, characterization, and multiple exciton generation. *Journal of the American Chemical Society*, 128(10):3241–3247, 2006.

[123] R. D. Schaller, M. Sykora, J. M. Pietryga, and V. I. Klimov. Seven excitons at a cost of one: Redefining the limits for conversion efficiency of photons into charge carriers. *Nano Letters*, 6(3):424–429, 2006.

[124] R. D. Schaller, V. M. Agranovich, and V. I. Klimov. High-efficiency carrier multiplication through direct photogeneration of multi-excitons via virtual single-exciton states. *Nature Physics*, 1(3):189–194, 2005.

[125] D. F. Qi, M. Fischbein, M. Drndić, and S. Selmić. Efficient polymer-nanocrystal quantum-dot photodetectors. *Applied Physics Letters*, 86(9):093103, 2005.

[126] J. S. Steckel. *The Synthesis of Inorganic Semiconductor Nanocrystalline Materials For the Purpose of Creating Hybrid Organic/Inorganic Light-Emitting Devices.* Ph.D. Thesis, Massachusetts Institute of Technology, 2006.

[127] S. A. McDonald, G. Konstantatos, S. G. Zhang, P. W. Cyr, E. J. D. Klem, L. Levina, and E. H. Sargent. Solution-processed PbS quantum dot infrared photodetectors and photovoltaics. *Nature Materials*, 4(2):138–142, 2005.

[128] S. A. McDonald, P. W. Cyr, L. Levina, and E. H. Sargent. Photoconductivity from PbS-nanocrystal/semiconducting polymer composites for solution-processible, quantum-size tunable infrared photodetectors. *Applied Physics Letters*, 85(11):2089–2091, 2004.

[129] K. R. Choudhury, Y. Sahoo, T. Y. Ohulchanskyy, and P. N. Prasad. Efficient photoconductive devices at infrared wavelengths using quantum dot-polymer nanocomposites. *Applied Physics Letters*, 87(7):073110, 2005.

[130] K. R. Choudhury, Y. Sahoo, and P. N. Prasad. Hybrid quantum-dot-polymer nanocomposites for infrared photorefractivity at an optical communication wavelength. *Advanced Materials*, 17(23):2877–2881, 2005.

[131] C. A. Leatherdale. *Photophysics of Cadmium Selenide Quantum Dot Solids.* Ph.D. Thesis, Massachusetts Institute of Technology, 2000.

[132] Alexi C. Arango. *A quantum dot heterojunction photodetector.* S.m. thesis, Massachusetts Institute of Technology, 2004.

[133] N. Koch, A. Elschner, J. Schwartz, and A. Kahn. Organic molecular films on gold versus conducting polymer: Influence of injection barrier height and morphology on current-voltage characteristics. *Applied Physics Letters*, 82(14):2281–2283, 2003.

[134] S. Coe-Sullivan. *Hybrid organic/quantum dot thin film structures and devices.* Ph.D. Thesis, Massachusetts Institute of Technology, 2005.

[135] S. Coe-Sullivan. *Efficient light emitting devices utilizing CdSe(ZnS) quantum dots in organic host matrices.* M.s. thesis, Massachusetts Institute of Technology, 2002.

[136] H. Mattoussi, L. H. Radzilowski, B. O. Dabbousi, E. L. Thomas, M. G. Bawendi, and M. F. Rubner. Electroluminescence from heterostructures of poly(phenylene vinylene) and inorganic CdSe nanocrystals. *Journal of Applied Physics*, 83(12):7965–7974, 1998.

[137] S. M. Sze. *Physics of Semiconductor Devices.* John Wiley & Sons, New York, 1969.

[138] M. A. Baldo, D. F. O'Brien, and S. R. Forrest. U. S. Patent 6,097,147. Structure for high efficiency electroluminescent device, 2000.

[139] M. Stolka, J. F. Yanus, and D. M. Pai. Hole transport in solid-solutions of a diamine in polycarbonate. *Journal of Physical Chemistry*, 88(20):4707–4714, 1984.

[140] C. M. Ramsdale, J. A. Barker, A. C. Arias, J. D. MacKenzie, R. H. Friend, and N. C. Greenham. The origin of the open-circuit voltage in polyfluorene-based photovoltaic devices. *Journal of Applied Physics*, 92(8):4266–4270, 2002.

[141] B. A. Gregg. Excitonic solar cells. *Journal of Physical Chemistry B*, 107(20):4688–4698, 2003.

[142] P. Peumans and S. R. Forrest. Separation of geminate charge-pairs at donor-acceptor interfaces in disordered solids. *Chemical Physics Letters*, 398(1-3):27–31, 2004.

[143] E. A. Weiss, R. C. Chiechi, D. C. Bell, G. M. Whitesides, V. J. Porter, S. G. Geyer, and M. G. Bawendi. Charge transport through multi-size arrays of colloidal CdSe quantum dots with ITO/PEDOT:PSS and eutectic gallium/indium contacts: the role of the QD/electrode interfaces. *Journal of the American Chemical Society*, submitted, 2007.

[144] C. W. Tang. 2-layer organic photovoltaic cell. *Applied Physics Letters*, 48(2):183–185, 1986.

[145] Y. T. Lim, S. Kim, A. Nakayama, N. E. Stott, M. G. Bawendi, and J. V. Frangioni. Selection of quantum dot wavelengths for biomedical assays and imaging. *Molecular Imaging*, 2:50–64, 2003.

[146] K. H. Hellwege. *Numerical data and functional relationships in science and technology*, volume III17f. Springer-Verlag, Berlin, 1961.

[147] G. Konstantatos, I. Howard, A. Fischer, S. Hoogland, J. Clifford, E. Klem, L. Levina, and E. H. Sargent. Ultrasensitive solution-cast quantum dot photodetectors. *Nature*, 442(7099):180–183, 2006.

[148] H. Kim, C. M. Gilmore, A. Pique, J. S. Horwitz, H. Mattoussi, H. Murata, Z. H. Kafafi, and D. B. Chrisey. Electrical, optical, and structural properties of indium-tin-oxide thin films for organic light-emitting devices. *Journal of Applied Physics*, 86(11):6451–6461, 1999.

[149] L. H. Qu, Z. A. Peng, and X. G. Peng. Alternative routes toward high quality CdSe nanocrystals. *Nano Letters*, 1(6):333–337, 2001.

[150] X. G. Peng, J. Wickham, and A. P. Alivisatos. Kinetics of II-VI and III-V colloidal semiconductor nanocrystal growth: "focusing" of size distributions. *Journal of the American Chemical Society*, 120(21):5343–5344, 1998.

[151] L. H. Qu, W. W. Yu, and X. P. Peng. In situ observation of the nucleation and growth of CdSe nanocrystals. *Nano Letters*, 4(3):465–469, 2004.

[152] C. R. Bullen and P. Mulvaney. Nucleation and growth kinetics of CdSe nanocrystals in octadecene. *Nano Letters*, 4(12):2303–2307, 2004.

[153] F. Chen, K. L. Stokes, W. Zhou, J. Fang, and C. B. Murray. Synthesis and properties of lead selenide nanocrystal solids. *Materials Research Society Symposium Proceedings*, 691:G10.2, 2001.

[154] R. A. Zingaro, B. H. Steeves, and K. Irgolic. Phosphine tellurides. *Journal of Organometallic Chemistry*, 4:320, 1965.

[155] M. L. Steigerwald and C. R. Sprinkle. Application of phosphine tellurides to the preparation of Group-II-VI (2-16) semiconductor-materials. *Organometallics*, 7(1):245–246, 1988.

[156] C. Amatore, A. Jutand, and M. A. Mbarki. Evidence of the formation of zerovalent palladium from pd(oac)$_2$ and triphenylphosphine. *Organometallics*, 11(9):3009–3013, 1992.

[157] N. Q. Wu, L. Fu, M. Su, M. Aslam, K. C. Wong, and V. P. Dravid. Interaction of fatty acid monolayers with cobalt nanoparticles. *Nano Letters*, 4(2):383–386, 2004.

[158] C. A. Leatherdale, W. K. Woo, F. V. Mikulec, and M. G. Bawendi. On the absorption cross section of CdSe nanocrystal quantum dots. *Journal of Physical Chemistry B*, 106(31):7619–7622, 2002.

[159] E. D. Palik, editor. *Handbook of Optical Constants of Solids*. Academic Press, Orlando, 1985.

[160] J. M. Caruge, Y. T. Chan, V. Sundar, H. J. Eisler, and M. G. Bawendi. Transient photoluminescence and simultaneous amplified spontaneous emission from multiexciton states in CdSe quantum dots. *Physical Review B*, 70(8), 2004.

[161] X. H. Gao, L. L. Yang, J. A. Petros, F. F. Marshal, J. W. Simons, and S. M. Nie. In vivo molecular and cellular imaging with quantum dots. *Current Opinion in Biotechnology*, 16(1):63–72, 2005.

[162] E. H. Sargent. Infrared quantum dots. *Advanced Materials*, 17(5):515–522, 2005.

[163] K. T. Yong, Y. Sahoo, K. R. Choudhury, M. T. Swihart, J. R. Minter, and P. N. Prasad. Shape control of PbSe nanocrystals using noble metal seed particles. *Nano Letters*, 6(4):709–714, 2006.

[164] C. M. Gardner, S. L. Jacques, and A. J. Welch. Light transport in tissue: Accurate expressions for one-dimensional fluence rate and escape function based upon Monte Carlo simulation. *Lasers in Surgery and Medicine*, 18(2):129–138, 1996.

[165] B. Dubertret, P. Skourides, D. J. Norris, V. Noireaux, A. H. Brivanlou, and A. Libchaber. In vivo imaging of quantum dots encapsulated in phospholipid micelles. *Science*, 298(5599):1759–1762, 2002.

[166] X. H. Gao, Y. Y. Cui, R. M. Levenson, L. W. K. Chung, and S. M. Nie. In vivo cancer targeting and imaging with semiconductor quantum dots. *Nature Biotechnology*, 22(8):969–976, 2004.

[167] M. Stroh, J. P. Zimmer, D. G. Duda, T. S. Levchenko, K. S. Cohen, E. B. Brown, D. T. Scadden, V. P. Torchilin, M. G. Bawendi, D. Fukumura, and R. K. Jain. Quantum dots spectrally distinguish multiple species within the tumor milieu in vivo. *Nature Medicine*, 11(6):678–682, 2005.

[168] J. M. Klostranec and W. C. W. Chan. Quantum dots in biological and biomedical research: Recent progress and present challenges. *Advanced Materials*, 18(15):1953–1964, 2006.

[169] S. Kim, B. Fisher, H. J. Eisler, and M. Bawendi. Type-II quantum dots: CdTe/CdSe(core/shell) and CdSe/ZnTe(core/shell) heterostructures. *Journal of the American Chemical Society*, 125(38):11466–11467, 2003.

[170] S. Kim and M. G. Bawendi. Oligomeric ligands for luminescent and stable nanocrystal quantum dots. *Journal of the American Chemical Society*, 125(48):14652–14653, 2003.

[171] S. W. Kim, J. P. Zimmer, S. Ohnishi, J. B. Tracy, J. V. Frangioni, and M. G. Bawendi. Engineering $InAs_xP_{1-x}/InP/ZnSe$ III-V alloyed core/shell quantum dots for the near-infrared. *Journal of the American Chemical Society*, 127(30):10526–10532, 2005.

[172] A. M. De Grand, S. J. Lomnes, D. S. Lee, M. Pietrzykowski, S. Ohnishi, T. G. Morgan, A. Gogbashian, R. G. Laurence, and J. V. Frangioni. Tissue-like phantoms for near-infrared fluorescence imaging system assessment and the training of surgeons. *Journal of Biomedical Optics*, 11(1), 2006.

[173] R. C. Jones. Quantum efficiency of detectors for visible and infrared radiation. In L. Marton, editor, *Advances in Electronics and Electron Physics*, volume XI, pages 88–184. Academic Press, New York, 1959.

David C. Oertel

EDUCATION

Massachusetts Institute of Technology   June 2007
Cambridge, Massachusetts
Ph.D., Physical Chemistry
"Photodetectors Based on Colloidal Quantum Dots"
GPA 5.0/5.0

Oberlin College   May 2001
Oberlin, Ohio
B.A., Chemistry, Mathematics
GPA 4.07/4.0, Highest Honors in Chemistry

AWARDS

Fannie and John Hertz Foundation Fellowship (2001-2006)
Barry M. Goldwater Scholarship (2000-2001 academic year)
Ernest B. Yeager Award granted by the Society for Applied Spectroscopy (2001)
Oberlin College Harry N. Holmes Prize in Chemistry (2001)
Phi Beta Kappa (inducted 2000, junior year)
National Merit Corporation Scholarship (1997-1998 academic year)

EXPERIENCE

Department of Chemistry, Massachusetts Institute of Technology   2001-2007
Research Assistant

Synthesized and processed colloidal semiconductor nanocrystal materials (CdSe, CdTe, PbSe) for incorporation in optoelectronic devices. Designed, fabricated, and characterized visible and near-IR photodetectors based on nanocrystal solids.

Molecular Microspectroscopy Laboratory, Miami University   2001
Summer Researcher

Molecular microspectroscopy research under André J. Sommer
Analyzed and modeled degradation of infrared spectra at polymer/air interfaces
to establish resolution limits for samples with small feature sizes.

Department of Chemistry, Oberlin College   1999-2001
Research Student

Molecular spectroscopy research under Norman C. Craig
Analyzed high-resolution infrared spectra of fluorohydrocarbons and calculated
precise molecular structures based on detailed fittings of spectra

Oberlin College   1999-2001
Teaching Assistant and Grader

LEADERSHIP

Sidney-Pacific Graduate Residence, MIT   2002-2005
Various positions: Infrastructure Chair, Vice-President of Resources, Controller

Extensive experience developing and managing physical and financial resources of a new 700- bed residence with government of 50. Designed and implemented inventory system for physical resources; personally managed team of 10 committee chairs charged with developing and managing financial, physical, and aesthetic holdings; directly oversaw residence government budget and implemented widely used database-driven web interface for financial transactions.

Graduate Student Committee, Department of Chemistry, MIT   2003-2004
Co-Chair

AFFILIATIONS

American Chemical Society
Materials Research Society

PUBLICATIONS

J. S. Steckel, B. K. H. Yen, D. C. Oertel, and M. G. Bawendi.
On the Mechanism of Lead Chalcogenide Nanocrystal Formation.
Journal of the American Chemical Society, 128(40):13032-13033, 2006.

D. C. Oertel, M. G. Bawendi, A. C. Arango, and V. Bulović
Photodetectors based on treated CdSe quantum-dot films.
Applied Physics Letters, 87(21):213505, 2005.

N. C. Craig, C. M. Oertel, D. C. Oertel, M. J. Tubergen, R. J. Lavrich, and A. M. Chaka
Structure of cis,trans-1,4-Difluorobutadiene from Microwave Spectroscopy.
Journal of Physical Chemistry A, 106(16):4230-4235, 2002.

N. C. Craig, C. M. Oertel, D. C. Oertel, and M. Lock
Complete Structure of anti-1,1,2,2-Tetrafluoroethane by High-Resolution Infrared Spectroscopy.
Journal of Physical Chemistry A, 105(25):6008-6019, 2001.

REFERENCES

Moungi G. Bawendi
Professor
Department of Chemistry, MIT
77 Massachusetts Avenue, Room 6-221
Cambridge, MA 02139
617-253-9796
mgb@mit.edu

Vladimir Bulović
KDD Associate Professor of Communications and Technology
Department of Electrical Engineering and Computer Science, MIT
77 Massachusetts Avenue, Room 13-3138
Cambridge, MA 02139
617-253-7012
bulovic@mit.edu

Dr. Roger G. Mark, M.D., Ph.D.
Professor of Electrical Engineering
Distinguished Professor in Health Sciences and Technology, MIT
Housemaster, Sidney-Pacific Graduate Residence
77 Massachusetts Avenue, Room E25-506
Cambridge, MA 02139
617-253-7818
rgmark@mit.edu